



HAL
open science

Electronic transport in quantum confined systems

Maxime Berthe

► **To cite this version:**

Maxime Berthe. Electronic transport in quantum confined systems. Physics [physics]. Université des Sciences et Technologie de Lille - Lille I, 2007. English. NNT: . tel-00343378

HAL Id: tel-00343378

<https://theses.hal.science/tel-00343378>

Submitted on 1 Dec 2008

HAL is a multi-disciplinary open access archive for the deposit and dissemination of scientific research documents, whether they are published or not. The documents may come from teaching and research institutions in France or abroad, or from public or private research centers.

L'archive ouverte pluridisciplinaire **HAL**, est destinée au dépôt et à la diffusion de documents scientifiques de niveau recherche, publiés ou non, émanant des établissements d'enseignement et de recherche français ou étrangers, des laboratoires publics ou privés.

THÈSE

Présentée à

l'Université des Sciences et Technologies de Lille

**Ecole Doctorale Sciences de la Matière,
du Rayonnement et de l'Environnement**

Pour obtenir le titre de

DOCTEUR DE L'UNIVERSITÉ

Spécialité

SCIENCES DES MATÉRIAUX

Par

Maxime BERTHE

Electronic transport in quantum confined systems

Soutenue le 11 décembre 2007 devant la commission d'examen composée de:

B. DJAFARI-ROUHANI

S. ROUSSET

D. RODITCHEV

F. CHARRA

D. STIÉVENARD

H. SHIGEKAWA

B. GRANDIDIER

Président

Rapporteur

Rapporteur

Examineur

Directeur de thèse

Co-directeur de thèse

Co-directeur de thèse

Résumé

Depuis l'avènement des nanotechnologies, une grande quantité de matériaux sont façonnés à l'échelle du nanomètre par des techniques diverses et l'intégration de ces nanostructures demande une caractérisation de leur structure électronique. La microscopie à effet tunnel est adaptée à ces études car elle permet l'adressage de nanostructures uniques pour mesurer leur structure électronique. Nous rapportons ici l'étude du transport électronique dans deux types de nanostructures: des nanotubes de carbone simple paroi déposés sur une surface d'or et des atomes uniques de silicium sur un substrat de silicium.

Dans la première étude, le couplage faible entre un nanotube et le substrat permet d'accéder à la densité d'états unidimensionnelle des nanotubes et autorise la formation de défauts ponctuels, ayant des états localisés dans la bande interdite des nanotubes. Cette modification, réversible, de la structure atomique des nanotubes de carbone amène des opportunités concernant la modification contrôlée et à volonté de leurs propriétés électroniques.

La deuxième étude vise à caractériser la dynamique des porteurs dans une liaison pendante de silicium énergétiquement isolée de tout autre état électronique sur une surface Si(111). L'analyse du transport révèle un courant inélastique mettant en œuvre la recombinaison non radiative des électrons de la pointe avec des trous capturés par l'état de la liaison pendante, grâce à l'émission de vibrations. La spectroscopie à effet tunnel montre de plus que l'on peut caractériser l'efficacité de capture d'un état quantique unique, en connaissant son niveau d'énergie, sa fonction d'onde, sa section de capture et le couplage électron-phonon.

Summary

With the advent of nanotechnology, a broad range of materials can be shaped with nanometer scale dimensions involving different methods, and the integration of nanostructures into electronic devices needs to characterize their electronic structure. Scanning tunnelling microscopy is a well appropriate technique for such purpose because it allows a precise positioning of the probe above the nanostructures and has the ability to resolve their electronic structure. Through this work, we report on the electronic transport of two nanostructures: single wall carbon nanotubes deposited on a gold surface and single Si atoms on a silicon substrate. In the first study, the weak coupling of the nanotube with the gold substrate give access to the one-dimensional density of states of nanotubes and allows the formation of point defects, with localized states in the band gap of the nanotubes. Such an atomic scale, reversible, modification of the nanotube wall opens up opportunities to tailor single wall carbon nanotube electronic properties at will. The second study aims at characterizing the carrier dynamics of an isolated Si dangling bond state on a Si(111) surface, which is energetically decoupled from any other electronic states. Analysis of the transport reveals an inelastic current involving the non radiative recombination of electrons from the tip with holes captured by the dangling bond state, thanks to the emission of vibrations. By further scanning tunnelling spectroscopy experiments, we show that it is possible to characterize the trapping efficiency of a single quantum state, knowing its energy level, wave function, capture cross-section and electron-phonon coupling.

Remerciements

Cette thèse a été menée sur plusieurs sites dont je remercie les directeurs pour m'y avoir accueilli: Alain Cappy, directeur de l'Institut d'Electronique, de Microélectronique et de Nanotechnologie (IEMN), Léon Carrez et Pierre Giorgini, directeurs successifs de l'Institut Supérieur d'Electronique et du Numérique (ISEN) de Lille ainsi que Yoichi Iwasaki, président de l'université de Tsukuba au Japon.

Je remercie Bahram Djafari-Rouhani pour avoir accepté de présider le jury de ma thèse, Dimitri Roditchev et Sylvie Rousset pour s'être intéressés à mon travail en tant que rapporteurs et Fabrice Charra pour en être examinateur.

Merci infiniment à Didier Stiévenard de m'avoir accueilli dans le groupe Physique de l'IEMN et d'avoir dirigé mes travaux durant trois ans, j'admire son professionnalisme. Je suis profondément reconnaissant envers mes codirecteurs Bruno Grandidier et Hidemi Shigekawa. Merci pour leur clairvoyance, leur rigueur et leur bonne humeur. Mon travail leur doit beaucoup.

Merci à Dominique Deresmes, Jean-Philippe Nys et Osamu Takeuchi qui sont une véritable mine d'or dans les techniques expérimentales et qui ont fortement contribué à mon projet professionnel.

Je remercie aussi Florence Senez et Kazumi Akitsu pour leur disponibilité, leur efficacité et leur bonne humeur.

Un grand merci à toutes les personnes qui m'ont aidé et m'ont beaucoup appris: Luis Perdigao, Ana Urbieto, Ken Kanazawa, Arifumi Okada, Rares Stiufiuc, Loic Patout (et ses imitations!), Clément Schockaert et Gautier Mahieu.

Merci encore aux membre du laboratoire Shigekawa de l'université de Tsukuba (Japon) avec qui j'ai passé une année inoubliable: Terada-san, Yoshida-san, Taninaka-san, Aoyama-san, Kondo-san, Kanitani-san, Ebine-san et les autres.

Merci aussi aux membres de l'IEMN qui ont contribué à la bonne ambiance et au travail efficace: Francois, Sophie, Pierre, Thibaut, Mamadou, Tao, Karin, Jean-François, Patrick, Pierre-Adrien, Arnaud et les chefs: Christophe,

Arnaud, Isabelle, Thierry, Ludger, Heinrich.

J'adresse un merci supplémentaire à Madame Alexandre de la maison universitaire France-Japon à Strasbourg et aux gens qui m'ont aidé à partir au Japon.

Merci à tous mes amis, un peu trop nombreux pour les citer individuellement...

Merci spécialement à ma famille pour m'avoir encouragé et supporté tout au long de mes études.

Merci enfin à ma Chérie-Jolie, Emeline, pour m'avoir toujours encouragé et pour avoir été forte lorsque j'étais à dix mille kilomètres.

Contents

Introduction	11
1 Electronic transport in nanostructures weakly coupled to the leads	15
1.1 Introduction	15
1.2 Some theoretical backgrounds	16
1.2.1 The Double Barrier Tunnel Junction (DBTJ)	16
1.2.2 I-V characteristics	19
1.2.3 Coulomb interactions	24
1.3 Experimental characterization of a DBTJ	26
1.3.1 Double barrier structures prepared by lithography	26
1.3.2 In a STM junction	26
1.3.3 Recent examples of substrates designed for STM-DBTJ experiments	28
1.4 Conclusion	35
2 Scanning Tunneling Microscopy (STM) and Spectroscopy (STS)	37
2.1 The Tunnel Effect	37
2.2 STM	40
2.2.1 Distance Feedback	40
2.2.2 Lateral Resolution	43
2.2.3 The Omicron LT-STM	45
2.3 Tunneling Spectroscopy	50
2.3.1 Distance versus bias spectroscopy $Z(V)$	50
2.3.2 Current versus bias spectroscopy $I(V)$	51
2.3.3 Current versus distance spectroscopy $I(Z)$	59
2.4 Conclusion	59

CONTENTS

3	STM induced point defects in Single-Walled Carbon Nanotubes	61
3.1	Introduction	61
3.1.1	Identification of SWCNTs and their electronic properties	62
3.1.2	Preparation of the samples	67
3.1.3	Identification of SWCNT atomic structure	68
3.2	Creation and removal of defects on SWCNTs	69
3.3	Identification of the defect	72
3.4	Statistics of the defect creation and annihilation	74
3.5	Conclusion	75
4	Running current through an isolated localized state in silicon	77
4.1	Introduction	77
4.2	Electronic structure of the Si(111)-($\sqrt{3} \times \sqrt{3}$)R30°-B surface .	79
4.2.1	The Silicon(111) surface	79
4.2.2	Reconstructions of the Si(111) surface	80
4.2.3	Sample preparation	81
4.2.4	The Si(111)-($\sqrt{3} \times \sqrt{3}$)R30°-B surface investigated by STM	82
4.2.5	Conclusion	83
4.3	Identification of subsurface acceptors	85
4.4	Running current through an unpassivated silicon dangling bond	89
4.4.1	Establishing a current through an isolated dangling bond state	91
4.4.2	Shape of the differential conductance in the case of a strong electron-vibration coupling	94
4.4.3	Experimental evidence for the strong electron-phonon coupling	98
4.4.4	Comparison with theory	99
4.4.5	Conclusion	100
4.5	Probing the hole capture rate of a single Si dangling bond . .	100
4.5.1	STS at high tunneling currents	101
4.5.2	Saturation of the current through I-Z spectroscopy . .	104
4.6	Conclusion	109
	Conclusion	111
	A Résumé de la thèse	115
	B List of publications	129

Introduction

Energy consumption has always been a critical factor in the evolution of electronic devices. From the vacuum tube to the transistor and from the transistor to the microprocessor, the constant increase of the performances have been accompanied by a significant reduction of energy losses. Up to now, the challenge has been fulfilled, partly by the miniaturization of the active parts of the electronic components, and their size have now reached the nanometer scale.

But as the dimensions are decreased, new effects appear. The undulatory nature of the electrons, for example, allows them to cross nanometer sized dielectrics and causes tunnel current leaks that are not negligible anymore. Such a source of energy loss thus increases as the size of electronic devices decreases and may hinder further miniaturization. Conversely, the tunnel effect is also a great opportunity as quantum electron transport becomes a measurable signal that can be exploited in nano-electronic devices. The first use of quantum electron transport was done by L. Esaki when he designed the tunnel diode in 1958 [1] for which he won the Nobel prize in 1973. Such components involved planar junctions whose lateral size was not nanoscopic, but the speed of operation that has reached several hundreds of GHz was highly encouraging to think about their evolution.

While the tunnel effect has been successfully implemented in planar junctions, its application to lower dimensional systems whose size is in the nanometer scale in more than one dimension is not straightforward. Indeed, the reliability of systems like molecules or small edifices made of a finite number of atoms has not yet been investigated and one can wonder how much current they can stand before destruction. Furthermore supposing a certain current to be established through a nanostructure without destruction, the mechanisms at the origin of the current flow may be quite different from those found in classical components. The goal of this work is to investigate the electronic transport induced by the tunnel effect in small edifices in order to answer these questions.

Thanks to the advances of experimental techniques, notably the invention

INTRODUCTION

of the Scanning Tunneling Microscope (STM) [2, 3, 4], it has become possible to study the electronic transport across structures with reduced dimensions of the order of the nanometer. Confinement of the electrons in two or even three dimensions revealed atom-like properties of some nanostructures [5], allowing one to shape the matter at the smallest scale. Exploration of the properties of such nanostructures gives an insight into the possible future of electronics.

As the field of electronic transport across quantum systems attracts a lot of attention, I will analyze encouraging experimental tunneling investigations carried on nanostructures, after a recall on how the tunnel effect can be exploited as a signal in a device. We will see that the regime that has been investigated up to now is resonant tunneling, involving mainly elastic transport of the electrons. Indeed, inelastic phenomena are usually measured as an insignificant fraction of the signal, but some setups can exhalt them and thus provide a better knowledge of the physical properties of nanostructures. Thus, the first chapter aims at highlighting the possibility of exhalting the intrinsic behaviour of a nanostructure thanks to subsequent decoupling from the leads.

In the second chapter, I will focus on the working principle of the tool used in my experiments: the low temperature STM. Details will be given on its ability to resolve the matter at the atomic scale and also on its application to transport measurements. Indeed, this microscope offers the unique advantage of being able to measure the electronic and vibrational structure of systems that can be as small as an atom thanks to its spectroscopic mode of operation. These properties make the STM a major instrument in the field of nanotechnology, which will be exploited for the electronic characterization of two different confined systems:

- In the third chapter, the characterization of a one-dimensional (1D) nanostructure –the Single-Walled Carbon NanoTube (SWCNT)– inserted between two metallic electrodes in a tunnel junction will be explained, the first electrode being the STM tip and the second electrode a gold sample. It will be shown that electronic transport in such a system is dictated by the 1D bandstructure of the SWCNT. The use of the STM as a manipulation tool at the atomic scale will be demonstrated through the creation and annihilation of defects on the wall of the SWCNTs. The influence of the defects on the transport properties of the SWCNT will be directly observed.
- A silicon atom holding a single electronic state energetically decoupled from any other state of a Si(111) surface will be taken as a study system

in the fourth chapter. The ability of the STM to characterize atomic-scale transport phenomena will reveal the vibrational excitation of the isolated atom when its equilibrium position is perturbed by the transit of an electron. Despite the aparent simplicity of such a system, we will see that the determination of the path taken by an electron is not straightforward and that the strong electron-phonon coupling allows a hole from the valence band to be captured by the adatom to recombine with the electron. Moreover, the control of the inelastic current will be demonstrated.

I will at last mention the first attempts in the use of substrates that should in principle lead to a stronger decoupling of nanostructures with respect to the leads.

Chapter 1

Electronic transport in nanostructures weakly coupled to the leads

1.1 Introduction

The evolution of the performances in electronics requires a constant miniaturization. Nevertheless, the statistic laws governing the electron transport reach a limit when the size of the components is barely bigger than a few atoms. At this scale, the low dimensionality of the edifices induces quantum phenomena like boundary effects, discretization of the energy levels and electron tunneling. The last phenomenon is at the origin of energy losses because the electrons can cross thin dielectric barriers and then give birth to a sink current.

The tunnel effect can nevertheless be taken as an advantage: in 1957, *L. Esaki* published the first conclusive experimental evidence for tunneling in a diode [1]. Esaki's tunnel diode had a large impact on the physics of semiconductors, leading to important developments such as the tunneling spectroscopy, and to increased understanding of tunneling phenomena in solids. *L. Esaki* [6], *I. Giaever* [7] and *B. Josephson* [8] received in 1973 the Nobel prize for their work about tunneling in semiconductors, superconductors and theoretical predictions of the properties of a supercurrent through a tunnel barrier, respectively. In 1963, *R. Davis* and *H. Hosack* introduced the concept of resonant tunneling in double barriers [9].

1.2 Some theoretical backgrounds

When the size of the active elements of an electronic device can be as small as a few nanometers, the concept developed by Esaki becomes the basis of every device.

The behaviour of electrons crossing a Double Barrier Tunnel Junction (DBTJ) have long been studied [9] for its negative differential resistance (NDR) that can be used to form oscillators or fast switches. Moreover, as the tunneling process relies on the dwelling time of electrons within the barrier, it is able to operate at very high frequencies. In this section, we will recall the basic theory to explain the electronic transport in a DBTJ.

1.2.1 The Double Barrier Tunnel Junction (DBTJ)

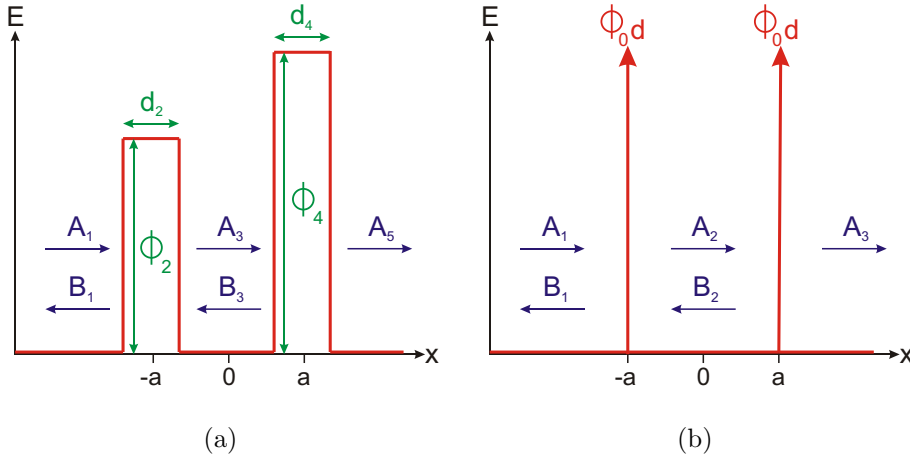


Figure 1.1: Energy diagram of the DBTJ without (a) and with (b) the Krönig and Penney approximation. A_i are the incident wave amplitudes and B_i are the reflected amplitudes.

The NDR effect arises as a variation of the transmission coefficient of the junction when the energy of the incoming electrons varies. Let us demonstrate this effect using a 1D model for a metallic particle in a well between two barriers, see Fig. 1.1(a).

For a simple barrier, the transmission depends exponentially on the product Kd , with d the barrier's thickness and $K = \sqrt{\frac{2m}{\hbar^2}(\Phi_0 - E)}$ the wave vector inside the barrier region. m is the mass of an electron, \hbar is the reduced Planck's constant, Φ_0 is the height of the potential barrier and E is the energy of the electron. In the case of the double barrier, the approximation of

1.2 Some theoretical backgrounds

Krönig and Penney [10], simplifies the problem: it approximates the tunnel barriers with two Dirac-like functions (see Fig. 1.1(b)).

For the demonstration, we will take two identical barriers.

Thus $d \rightarrow 0$, $\Phi_i \rightarrow \infty$ and $\Phi_i d = \Phi_0 d$ is constant.

$$V(x) = V_0 d (\delta(x+a) + \delta(x-a)) \quad (1.1)$$

Outside of the barriers, three regions can be distinguished and the general solution of the Schrödinger equation in these regions is:

$$\begin{aligned} \varphi_1(x) &= A_1 e^{ikx} + B_1 e^{-ikx} \\ \varphi_2(x) &= A_2 e^{ikx} + B_2 e^{-ikx} \\ \varphi_3(x) &= A_3 e^{ikx} \end{aligned} \quad (1.2)$$

where $k = \sqrt{\frac{2m}{\hbar^2} E}$.

In those infinitely thin barriers, the continuity of the wave functions requires:

- φ is continuous in $x_0 = -a$ and $x_0 = a$:

$$\varphi(x_{0+}) = \varphi(x_{0-}) \quad (1.3)$$

- $\frac{\partial \varphi}{\partial x}$ is discontinuous in $x_0 = -a$ and $x_0 = a$:

$$\frac{\partial \varphi}{\partial x}(x_{0+}) - \frac{\partial \varphi}{\partial x}(x_{0-}) = \frac{2m\Phi_0 d}{\hbar^2} \varphi(x_0) \quad (1.4)$$

One can prove (1.4) by integration of the Schrödinger equation:

$$\frac{-\hbar^2}{2m} \frac{\partial^2 \psi}{\partial x^2} + \Phi_0 \psi = E \psi \quad (1.5)$$

Let us integrate between $a - d/2$ and $a + d/2$:

$$\frac{-\hbar^2}{2m} \int_{a-d/2}^{a+d/2} \frac{\partial^2 \psi}{\partial x^2} dx + \int_{a-d/2}^{a+d/2} \Phi_0 \psi dx = E \int_{a-d/2}^{a+d/2} \psi dx \quad (1.6)$$

when $d \rightarrow 0$ then $\psi \sim \text{Constant}$ and $\psi(a - d/2) = \psi(a + d/2)$

thus

$$\left(\frac{\partial \psi}{\partial x} \Big|_{a+d/2} - \frac{\partial \psi}{\partial x} \Big|_{a-d/2} \right) = (\Phi_0 - E) \frac{2md}{\hbar^2} \psi(a) \quad (1.7)$$

CHAPTER 1. ELECTRONIC TRANSPORT IN NANOSTRUCTURES WEAKLY COUPLED TO THE LEADS

with $\Phi_0 \gg E$ when $d \rightarrow 0$

After a few algebraic manipulations, (1.3) and (1.4) associated with (1.3) give the following system as matching conditions:

$$\begin{aligned}
 \alpha \frac{B_1}{A_1} - \frac{1}{\alpha} \frac{A_2}{A_1} - \alpha \frac{B_2}{A_1} &= -\frac{1}{\alpha} \\
 \alpha \frac{A_2}{A_1} + \frac{1}{\alpha} \frac{B_2}{A_1} - \alpha \frac{A_3}{A_1} &= 0 \\
 \alpha(1+M) \frac{B_1}{A_1} + \frac{1}{\alpha} \frac{A_2}{A_1} - \alpha \frac{B_2}{A_1} &= \frac{1}{\alpha}(1-M) \\
 -\alpha \frac{A_2}{A_1} + \frac{1}{\alpha} \frac{B_2}{A_1} + \alpha(1+M) \frac{A_3}{A_1} &= 0
 \end{aligned} \tag{1.8}$$

with $M = \frac{2im\Phi_0 d}{\hbar^2 k}$ and $\alpha = e^{ika}$

The interesting quantity in our case is the transmission coefficient: the amount of the outgoing flow of electrons over the incident flow.

$$T(E) = \frac{|A_3 e^{ikx}|^2}{|A_1 e^{ikx}|^2} = \left| \frac{A_3}{A_1} \right|^2 \tag{1.9}$$

The resolution of (1.9) gives

$$\frac{A_3}{A_1} = \frac{4}{(M+2)^2 - \alpha^4 M^2} \tag{1.10}$$

Then,

$$T(E) = \frac{1}{1 + \frac{|M|^2}{4} (2 \cos(2ka) + |M| \sin(2ka))^2} \tag{1.11}$$

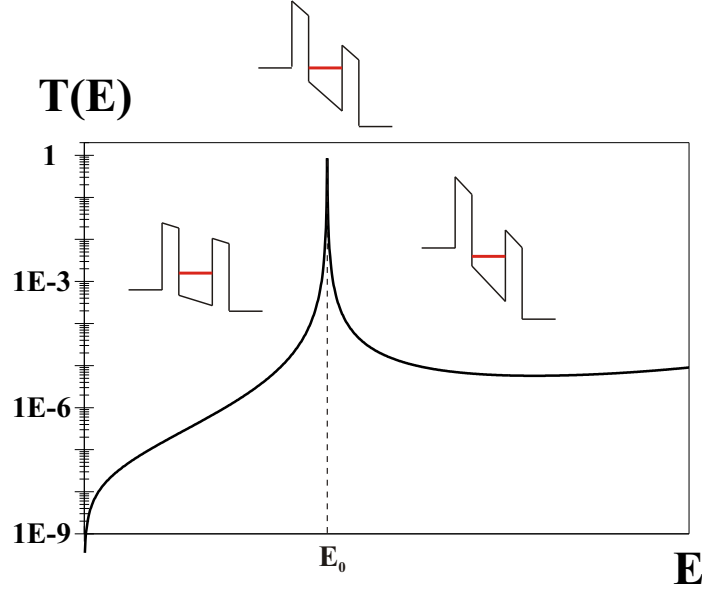


Figure 1.2: Explanation of the NDR effect in a DBTJ. Here, the width of the quantum well is $2a = 2\text{nm}$ and the width of each barrier is $d = 0.8\text{nm}$

At $\tan(2ka) = -\frac{2}{|M|}$, there is a sharp resonance in (1.11). In fact, at this energy position, the transmission coefficient even reaches 1, independently of the thickness of the barriers (but keeping in mind that $d \ll a$), meaning perfect transparency.

Fig. 1.2 gives an example of the variation of the transmission coefficient as a function of the energy, where one can see the sharpness of the curve at resonance. In fact, the sharp peak of the transmission coefficient corresponds to a path for resonant tunneling through the ground state of the quantum well situated between the barriers of the DBTJ. Though the above equation (1.11) was calculated in a case where the electrodes are not polarized, it gives a qualitative understanding of the electron tunneling through a DBTJ.

1.2.2 I-V characteristics

Let us call the electrodes corresponding to region 1 and 3 respectively the emitter and the collector. The total current J flowing from the emitter to the collector is:

$$J = J_{emitter \rightarrow collector} - J_{collector \rightarrow emitter} \quad (1.12)$$

CHAPTER 1. ELECTRONIC TRANSPORT IN
NANOSTRUCTURES WEAKLY COUPLED TO THE LEADS

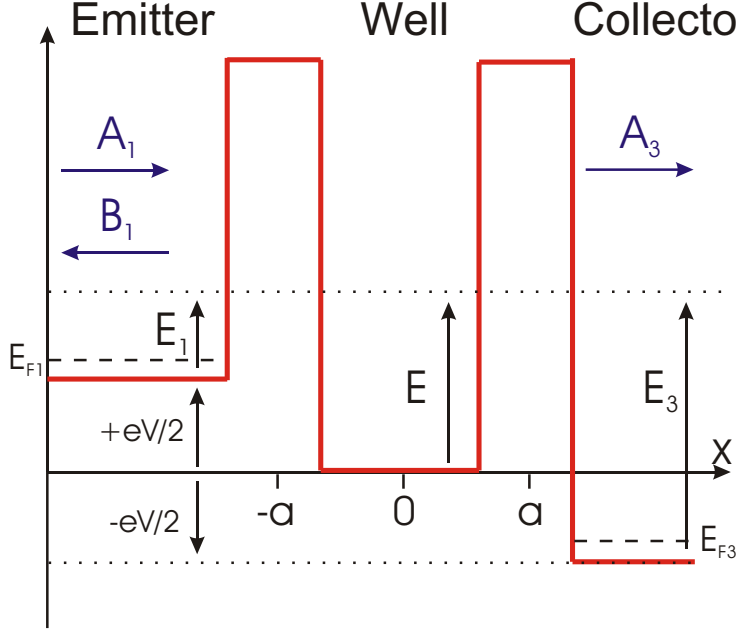


Figure 1.3: Polarized DBTJ. eV is the bias, A_i are the incident wave amplitudes and B_i are the reflected amplitudes.

Both contributions $J_{emitter \rightarrow collector}$ and $J_{collector \rightarrow emitter}$ are the sum of the electron tunneling events over all the states of the electrodes (we will consider a constant density of states ρ in both electrodes, this is coherent with metallic electrodes at small biases. For simplicity, we will set $\rho = 1$). For instance, one event from the emitter to the collector is described by:

- The probability of finding an occupied electronic state on the emitter at the energy $E_{emitter}$, given by the Fermi-Dirac statistics:

$$f_{emitter}(E_{emitter}) = \frac{1}{1 + \exp\left(\frac{E_{emitter} - E_{F_{emitter}}}{k_B T}\right)} \quad (1.13)$$

where $E_{F_{emitter}}$ is the Fermi level, k_B is Boltzman's constant and T is the temperature;

- The probability of finding an empty electronic state on the collector at the energy $E_{collector}$, also given by the Fermi-Dirac statistics:

$$1 - f_{collector}(E_{collector}) \quad (1.14)$$

- The tunneling probability, given by the coefficient of transmission $T(E)$

Thus

$$\begin{aligned}
 J_{emitter \rightarrow collector} &= \int_{-\infty}^{\infty} f_{emitter}(E_{emitter})(1 - f_{collector}(E_{collector}))T(E) dE \\
 J_{collector \rightarrow emitter} &= \int_{-\infty}^{\infty} f_{collector}(E_{collector})(1 - f_{emitter}(E_{emitter}))T(E) dE
 \end{aligned} \tag{1.15}$$

And after summation,

$$J = \int_{-\infty}^{\infty} [f_{emitter}(E_{emitter}) - f_{collector}(E_{collector})]T(E) dE \tag{1.16}$$

When the electrodes are not polarized, no current can flow through because $J_{emitter \rightarrow collector} = J_{collector \rightarrow emitter}$. On the other hand, when a polarization eV is applied on the system, the transmission coefficient $T(E)$ is modified in the following way:

With a polarization eV , one can write:

- In the emitter:

$$E_{emitter} = E - \frac{eV}{2} = \frac{\hbar^2}{2m}k_1^2 \quad \text{and} \quad \psi(x) = A_1e^{ik_1x} + B_1e^{-ik_1x} \tag{1.17}$$

- In the collector:

$$E_{collector} = E + \frac{eV}{2} = \frac{\hbar^2}{2m}k_3^2 \quad \text{and} \quad \psi(x) = A_3e^{ik_3x} \tag{1.18}$$

In quantum mechanics, the current of particles is given by:

$$j = -\frac{i\hbar}{2m}(\psi^* \frac{\partial \psi}{\partial x} - \psi \frac{\partial \psi^*}{\partial x}) \tag{1.19}$$

When applied to eq. (1.17) and eq. (1.18), this equation gives:

$$j_1 = \frac{\hbar k_1}{m}(|A_1|^2 - |B_1|^2) \tag{1.20}$$

$$j_3 = \frac{\hbar k_3}{m}|A_3|^2 \tag{1.21}$$

Moreover, in the permanent regime, $j_1 = j_3$ leads to:

$$1 = \frac{k_3}{k_1} \frac{|A_3|^2}{|A_1|^2} + \frac{|B_1|^2}{|A_1|^2} \tag{1.22}$$

CHAPTER 1. ELECTRONIC TRANSPORT IN NANOSTRUCTURES WEAKLY COUPLED TO THE LEADS

In the above expression, one can identify:

$$T(E) = \frac{k_3 |A_3|^2}{k_1 |A_1|^2} \quad (1.23)$$

$$R(E) = \frac{|B_1|^2}{|A_1|^2} \quad (1.24)$$

the transmission and reflection coefficients.

Eq. (1.17) and eq. (1.18) also give

$$\frac{k_3}{k_1} = \sqrt{\frac{E + \frac{eV}{2}}{E - \frac{eV}{2}}} = \sqrt{1 + \frac{eV}{E - \frac{eV}{2}}} \quad (1.25)$$

For a small bias, the shape of the barriers does not change significantly, thus one can include equation (1.11) into the bias dependent $T(E)$ and one gets:

$$T(E) = \sqrt{1 + \frac{eV}{E - \frac{eV}{2}}} \times \frac{1}{1 + \frac{|M|^2}{4} (2 \cos(2ka) + |M| \sin(2ka))^2} \quad (1.26)$$

At small values of eV , the expression of $T(E)$ is not very different from the unpolarized case, as a result, we again expect sharp resonance in $T(E)$. Abrupt changes are thus expected in the I-V characteristics of DBTJ.

Temperature effects

The current flowing through a DBTJ, has a sharp behaviour against energy. Nevertheless, the temperature influences the I-V characteristics. Indeed, $f_{emitter}(E_{emitter}) - f_{collector}(E_{collector})$ defines an integration window in the expression of the current (eq. (1.16)):

- At $T = 0K$, the Fermi-Dirac distribution is a step function, which means that transport occurs only at resonance.
- As T increases, $f_{emitter}(E_{emitter}) - f_{collector}(E_{collector})$ becomes smoother: the energy distribution of the electrons broadens and more states around the Fermi level in the emitter and collector are involved in the transport when they become resonant with the quantum state of the well in the DBTJ. Figure 1.4 illustrates this broadening with curves calculated at $T = 10K$, $T = 77K$ and $T = 300K$.

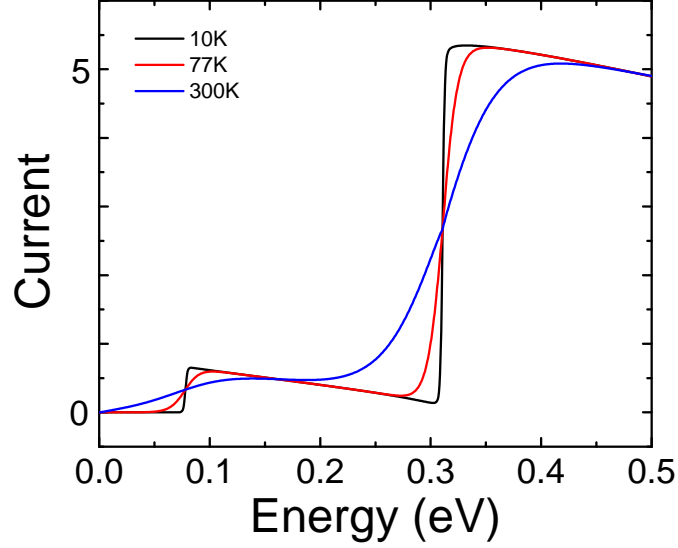


Figure 1.4: Calculated I-V characteristics of a DBTJ from 0 to 500meV at 10K, 77K and 300K. The expression for the current is eq. (1.16) with $T(E)$ taken from eq. (1.26). The parameters are: Barrier Width $d = 0.5nm$, Well Width $a = 1.5nm$, Barrier Height $\Phi_0 = 4.5eV$

Other causes of broadening

Generally, the width of the peaks observed in the I-V characteristics are larger than the width expected if only the thermal excitation of the electrons is taken into account. Indeed an electron can interact with phonons in the well of the DBTJ and the inelastic scattering produces transmissions sidebands. Depending on the geometry and the chemical nature of the materials located between both barriers, a structure with reduced sizes can lead to a splitting of localised states, generally degenerate in the bulk materials. Coupling between the states (for example intervalley coupling) induces also a broadening of the transmission peak when the spectral resolution is not high enough. Finally, another cause of broadening is the effect of the transition time across the DBTJ: following a consequence of Heisenberg's principle, fast decaying processes lead to an uncertainty on their energy. The minimum width of a peak, called "natural linewidth", is defined by:

$$\Delta E \geq \frac{\hbar}{2\Delta t} \quad (1.27)$$

Thus, the slower the process, the sharper the peak.

CHAPTER 1. ELECTRONIC TRANSPORT IN NANOSTRUCTURES WEAKLY COUPLED TO THE LEADS

1.2.3 Coulomb interactions

When a nanostructure is placed in the center of a DBTJ, and its localized states are only weakly coupled to the leads, the time that an electron leaves the nanostructure may be longer than the time required to have an electron tunneling from the emitter into the nanostructure: Coulomb interactions may become relevant. We can understand this effect from classical physics.

Fig. 1.5 shows the equivalent circuit for a DBTJ. Each tunneling junction is modeled with a capacitor and a resistor in parallel. The charges on the junctions and on the nanostructure can be written as:

$$\begin{aligned} q_1 &= C_1 V_1 \\ q_2 &= C_2 V_2 \\ q &= -ne = q_2 - q_1 = C_2 V_2 - C_1 V_1 \end{aligned} \quad (1.28)$$

with $n = n_1 - n_2$ the number of electrons in the nanostructure.

Using the above set of expressions and $V_{bias} = V_1 + V_2$ gives:

$$\begin{aligned} V_1 &= \frac{C_2 V_{bias} + ne}{C_1 + C_2} \\ V_2 &= \frac{C_1 V_{bias} - ne}{C_1 + C_2} \end{aligned} \quad (1.29)$$

As a result, the electrostatic energy as a function of the number of electrons in the nanostructure is:

$$E(n) = \frac{q_1^2}{2C_1} + \frac{q_2^2}{2C_2} = \frac{C_1 (C_2 V_{bias} + ne)^2 + C_2 (C_1 V_{bias} - ne)^2}{2(C_1 + C_2)^2} \quad (1.30)$$

In order to simplify the explanation, let us take a symmetric system:

$$C_1 = C_2 = C \quad (1.31)$$

In this case, the electrostatic energy of the nanostructure is:

$$E(n) = \frac{1}{4} \left(C V_{bias}^2 + \frac{(ne)^2}{C} \right) \quad (1.32)$$

For an electron tunneling event, the work of the source must equal the variation of the electrostatic energy of the system:

$$\begin{aligned} [(n+1) - n] \frac{eV_{bias}}{2} &= E(n+1) - E(n) \\ V_{bias} &= (2n+1) \frac{e}{2C} \end{aligned} \quad (1.33)$$

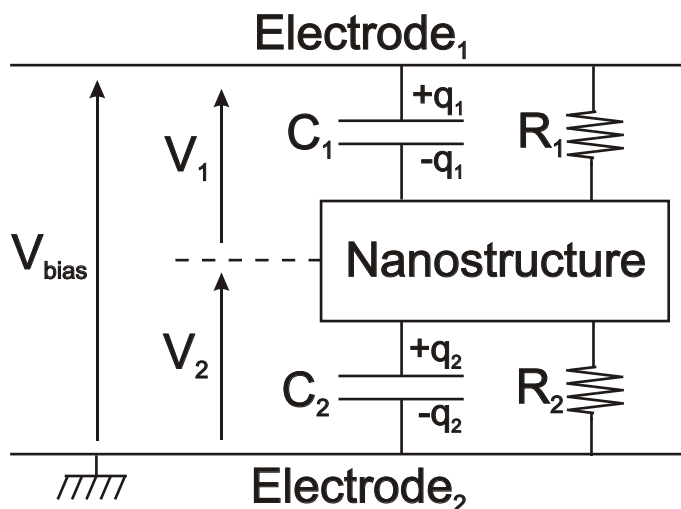


Figure 1.5: Equivalent circuit for a DBTJ. Two tunneling junctions (C_1, R_1) and (C_2, R_2) are put in series with a nanostructure in between. $Electrode_1$ is polarized at V_{bias} with respect to the ground.

Thus eq. (1.33) gives the values of V_{bias} for which no charge accumulates into the nanostructure. In other words, resonant tunneling happens. For other values of V_{bias} , inelastic processes are needed to transfer all the electrons from one electrode to another.

The resulting $I(V)$ characteristics is called the Coulomb staircase, and one has to note that if

$$\frac{k_B T}{e} \leq V_{bias(0)} = \frac{e}{2C} \quad (1.34)$$

with k_B Boltzman's constant and T the temperature, then no current can flow: this is the Coulomb blockade of conductance.

What happens if the system is not symmetric? The results stated above are valid for symmetric junctions, ie when $R_1 = R_2$ and $C_1 = C_2$. But if one junction is less transparent than the other, for example the junction 2, it will limit the transfer rate of the electrons. Every electron transferred to the nanostructure via the junction 1 will be stored until it can escape and as a result, the nanostructure will become charged. The $I(V)$ characteristics will still be a staircase-like curve but, depending on the relative transparency of the barriers, charging or uncharging of the nanostructure will occur as a function of the bias.

1.3 Experimental characterization of a DBTJ

The observation of the above behaviours through experimental DBTJs remains a field where great improvements are possible. Indeed, the insertion of externally synthesized nanostructure, like molecules and nanocrystals, between two electrodes is a challenging task.

1.3.1 Double barrier structures prepared by lithography

Indeed, when one thinks of electronic devices, the first idea is to build a structure that will be integrated in an ensemble. A common and easily integrable approach is to make the electrodes by lithography, which is already used in the conception of classical electronics and then drop the nanostructure between these electrodes. One can easily understand the challenge of placing a nanometer-sized particle in such a small gap!

In 2000, Park et al. reported the *Nanomechanical oscillations in a single- C_{60} transistor* [11] by placing C_{60} molecules in nano-gap electrodes fabricated by the electromigration technique [12]. They were able to detect molecules “in a significant fraction of the C_{60} devices” only. Seven years later the reliance of such devices is still a challenging task: Shibata et al. are able to bridge nanogaps with InAs quantum dots with an effectiveness of 5% [13].

If this approach is the most readily usable in integrated devices, it still lacks of reproducibility. Moreover, the width of the gap between the electrodes cannot be tuned. Instead of trying to deposit the nanostructures between fixed electrodes, another approach would be the use of mobile electrodes to connect fixed nanostructures.

1.3.2 In a STM junction

Among the techniques used to measure transport properties of nanostructures, Scanning Probe Microscopies (SPM) may not be the most suitable for directly applicable designs. Nevertheless, they offer the unique advantage to locate easily nanostructures and to precisely tailor the thickness of one the tunneling barriers.

In particular, the Scanning Tunneling Microscope (STM) is well suited for transport experiments on nanostructures, it relies on the use of a scanning electrode over a flat sample acting as the other electrode. Thus, nanostructures deposited on the flat sample can be connected to the other electrode with an effectiveness of 100%.

1.3 Experimental characterization of a DBTJ

The substrate must be able to carry electrons in order to establish a current with the tip. Consequently, metals and semiconductors are the most common substrates used for STM experiments. Moreover, their crystalline structure is very convenient for atomic scale metric measurements, provided that they are observable. Indeed, STM images reflect the local density of states of the underlying surface and on metals, the valence s and p electrons are more delocalized than on semiconductors. The effect is known as Smoluchowski smoothing [14] and affects the lateral resolution on metallic surfaces. Therefore, atomic resolution is not straightforward on metals because the corrugation is considerably reduced [15].

STM has long been known for its ability to identify surface reconstructions [4] and their spatially resolved density of states [16]. When adsorbates are present on the surface, the imaging process is more complicated. For example, the adsorption site of the adsorbate influences the STM image, Weiss and Eigler report that it "may limit the usefulness of the scanning tunneling microscope in elucidating the structures of adsorbed molecules" [17].

Moreover, when adsorbates are deposited on a surface, diffusion of the species can hinder imaging of individual objects. For metallic substrates, it happens most of the time and experiments are only possible at low temperature. When C60 are deposited on metals, they chemically react with the surface, thus a charge transfer occurs and creates hybrid states [18] [19] [20] This hybridization is dependant on the adsorption site and the orientation of the molecule. Because of these factors, it is important to control the interactions of molecules with the substrate.

In the case of semiconducting samples, room temperature experiments on single objects are possible because of the high reactivity of the surface [21, 22]. But this behaviour is not the best solution because too strong substrate-adsorbate interactions prevent from molecule-molecule interactions such as self-organization.

For all these reasons, the substrate is of first importance in the investigation of the properties of nano-objects. A metallic substrate is an easy solution to contact nanometric edifices but it doesn't give a good resolution in spectroscopic mode [23] and only low-temperature experiments are possible. A semiconducting substrate is better for spectroscopy thanks to its energy gap but the reactivity of the surface is likely to modify the electronic structure of the adsorbate.

A wise solution to avoid these phenomena is to decouple physically the nanostructure from the substrate. The resulting configuration is a Tip-Insulator-Nanostructure-Insulator-Substrate in which the nanostructure is isolated by two potential barriers, one on each side.

CHAPTER 1. ELECTRONIC TRANSPORT IN NANOSTRUCTURES WEAKLY COUPLED TO THE LEADS

1.3.3 Recent examples of substrates designed for STM-DBTJ experiments

When a DBTJ is implemented in a STM, the distance between the tip and the nanostructure is well defined and easily reconfigurable. Meanwhile, the quality of the other junction is of crucial importance. The interest of decoupling the molecule from the substrate is clearly demonstrated by Silien et al. [23]: they have shown that the spatial resolution and the spectral linewidth on molecular orbitals of C_{60} molecules are improved when the molecules are separated of the *Cu* metallic substrate by a K layer. A simple, but not easy, way to reduce the interactions with the substrate is indeed to separate the adsorbates from the surface. The separation must be big enough to decouple the adsorbate states from the surface states, and small enough to allow tunneling of the electrons to the substrate. Several methods are commonly used and will be described in the following paragraphs: insulating layers on metallic substrates, insulating layers on semiconducting substrates and, ultimately, vacuum.

Insulating materials have always been of prime interest in electricity, electronics, and more recently in nanotechnology where they aim at separating electrically conductive parts and/or play the role of dielectrics.

At the nanometric scale, insulating materials have another interesting property: they are transparent for tunneling electrons [24]. Thus, the controlled growth of ultrathin insulating layers on (semi)conducting substrates is an increasingly growing field of research. Since the end of the eighties, the growth of several types of insulating materials have been tested on both metals and semiconductors, and some studies investigated the properties of molecules deposited on such structures.

On metals

The growth of a variety of ultrathin insulating layers has been investigated on a lot of metal substrates. Most of the insulators are metal oxides, some examples are

- Al_2O_3 on $Ni_3Al(111)$ [25, 26], $NiAl(111)$ [27], $NiAl(110)$ [28, 29], $Re(0001)$ [30], $Nb(110)/Sapphire(0001)$ [31]
- NiO on $Ni(100)$ [32], $Ag(001)$ [33, 34]
- CoO on $Ag(001)$ [34, 35, 36]
- FeO on $Ag(001)$ [37]

1.3 Experimental characterization of a DBTJ

- Ga_2O_3 [38]
- CeO_2 on $Pt(111)$ [39], $CeO_2(111)$ [40]
- MgO on $Fe(001)$ [41, 42, 43], $Mo(001)$ [44, 45, 46, 30], $Ag(001)$ [47, 48, 49, 50]
- $NaCl$ on $Al(111)$ and $Al(100)$ [51], $Cu(100)$ [52], $Cu(111)$ [53], $Cu(211)$ [54], $Cu(311)$ [55], $Cu(532)$ [56], $Ag(111)$

The growth of insulators on metallic surfaces has shown that a few monolayers are usually enough to exhibit almost the same properties as bulk insulating materials [41], but sometimes it does not give satisfying results for the growth of uniform layers. For example, NiO and $Ni(100)$ have a misfit of almost 20% [57], therefore the growth results in the formation of crystallites including many defects. In this case, the existence of a gap could not be concluded in the observation of differential conductance spectra.

Until now, the best results obtained with nanostructures on ultrathin insulating films by STM are on Al_2O_3 grown on $NiAl(110)$ [29, 58, 59] and $NaCl$ on $Cu(111)$ [60, 61].

CHAPTER 1. ELECTRONIC TRANSPORT IN NANOSTRUCTURES WEAKLY COUPLED TO THE LEADS

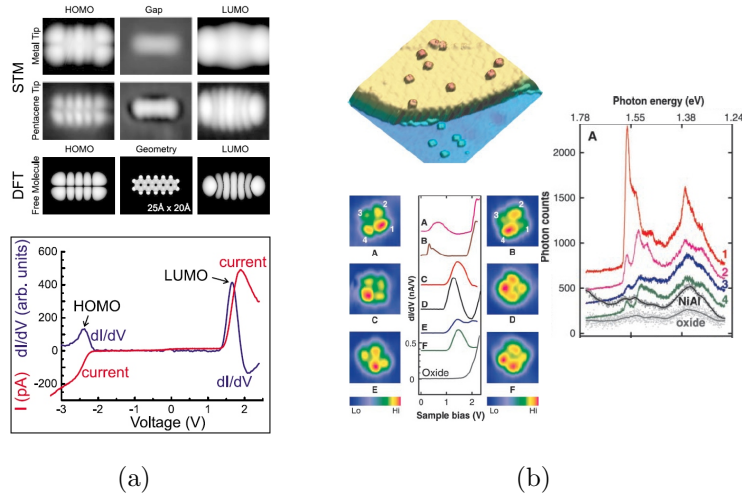


Figure 1.6: (a) *Molecules on Insulating Films: Scanning-Tunneling Microscopy Imaging of Individual Molecular Orbitals* [61] Top part: STM images acquired with a metal and a pentacene tip, on a pentacene molecule deposited on $\text{NaCl}/\text{Cu}(111)$ compared to contours of constant orbital probability distribution of the free molecule. The geometry of the free pentacene molecule is displayed in the lower center image. Bottom part: dI/dV spectroscopy at the center of a pentacene molecule on NaCl . The dI/dV signal shows two distinct peaks that can be attributed to the negative and positive ion resonance states, and a broad gap of low conductance in between the peaks. (b) *Vibrationally Resolved Fluorescence Excited with Submolecular Precision* [29] Top Left: STM topograph of a partially oxidized $\text{NiAl}(110)$ surface with ZnEtIOI molecules adsorbed at 13 K. The image size is 350 by 350 Å. Bottom Left: (A to F, left and right panels) STM images of ZnEtIOI molecules in different conformations on $\text{Al}_2\text{O}_3/\text{NiAl}(110)$, with (center panel) the corresponding dI/dV spectra. All images sizes are 32 by 32 Å; $V_{\text{bias}} = 2.35\text{V}$ and $I = 0.1\text{nA}$. Depending on the molecular adsorption site and conformation, the apparent relative height of the molecules lobes can be different. Molecules A and B luminesced, whereas no emission was detected for molecules C to F in the spectral range from 500 nm to 1000 nm. The presence of a low-energy peak in the dI/dV spectrum has been found to be necessary for a molecule to be optically active in the detection range. Right: Light-emission spectra acquired on the different lobes of molecule A, together with spectra acquired on bare NiAl and $\text{Al}_2\text{O}_3/\text{NiAl}(110)$ surface. The spectra are indexed according to the lobe numbering patterns seen on Bottom Left, respectively, and are offset vertically for clarity. The spectra were acquired at $V_{\text{bias}} = 2.35\text{V}$, $I = 0.5\text{nA}$, with an exposure time of 100 s; the NiAl and oxide spectra have been multiplied by factors of 4 and 15, respectively.

These surfaces are indeed interesting for the formation of structures where a molecule is inserted into the DBTJ:

- *Repp et al.* demonstrated the direct imaging of the unperturbed molecular orbitals of individual pentacene molecules by means of low-temperature scanning-tunneling microscopy on ultrathin insulating NaCl films deposited on $\text{Cu}(111)$ [61]. Fig. 1.6(a) shows the images obtained on the molecules and the comparison with theoretical calculations of the shape of the molecular orbitals. STS spectra show the peaks attributed to the orbitals. Those peaks are not observed on a bare $\text{Cu}(111)$ surface.
- *Qiu et al.* focused their study on the fluorescence of molecules vibrationally excited [29]. Fig. 1.6(b) shows individual molecules deposited

1.3 Experimental characterization of a DBTJ

on a $Al_2O_3/NiAl(110)$ surface, four lobes identify each molecule and its conformation on the surface. In contrast, when molecules adsorb on the $NiAl(110)$ surface, no light emission is measured. The conductivity depends on this conformation as well as the emission of light. The graph on the right of Fig. 1.6(b) gives this light emission for each lobe of molecule A and shows that they have their own light emission properties.

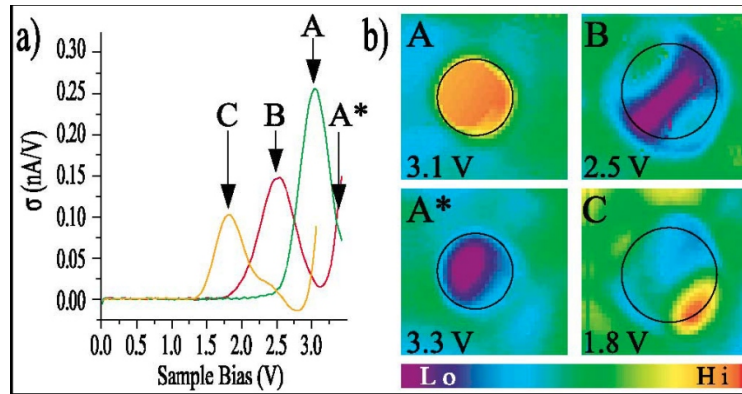


Figure 1.7: Influence of a Heterogeneous Al_2O_3 Surface on the Electronic Properties of Single Pd Atoms [62] (a) dI/dV spectra and (b) conductivity images of three Pd atoms on different Al_2O_3 adsorption sites ($35\text{\AA} \times 35\text{\AA}$, $I = 0.1\text{nA}$). To compare the spatial distribution of conducting channels, the apparent size of atoms in topographic images is marked by circles.

Nevertheless, several drawbacks are worth to be emphasized:

- The structure of these insulators can be complex to predict and difficult to measure by STM because of the large bandgap. For example, X-ray Diffraction experiments done by *Stierle et al.* proved that the structure of Al_2O_3 ultrathin layers on $NiAl(110)$ [63] is strongly distorted and recent ab-initio calculations even predicted it to be $Al_{10}O_{13}/NiAl(110)$ rather than Al_2O_3 [64]. As a result, the deposited nanostructures have different possible conformations with different possible electronic characteristics. For example, *Nilius et al.* [62] did STS on single Pd atoms deposited on the heterogeneous $Al_2O_3/NiAl(110)$ surface. Fig. 1.7 shows strong differences in the conduction of each adatom positioned on different lattice sites, without any good knowledge of the adsorption site. In this figure, the atoms A to C look different on the STM images and their differential conductance spectra are respectively shifted towards the Fermi level because of increasing couplings. The explanation

CHAPTER 1. ELECTRONIC TRANSPORT IN NANOSTRUCTURES WEAKLY COUPLED TO THE LEADS

is that they are respectively positioned on a regular oxide site, near a defect site and directly on a defect site.

- The tunneling processes involved in such junctions, even with nanostructures decoupled from the metallic surface, are always resonant. These systems allow a very good measurement of unperturbed molecular states thanks to decoupling from the substrate's continuum like in Fig. 1.6, but electronic transitions between molecular orbitals remain very limited. Fig. 1.8(a) shows the pathes followed by electrons in a junction where a nanostructure is deposited on a metallic sample covered by an insulating layer. When the energy of the tip becomes resonant with a discrete state of the nanostructure, the electrons tunnel to this state but then have a high probability to be transferred directly to the empty electronic states of the metallic sample. Of course, some electrons can release part of their energy by inelastic processes like vibrations [58] or radiative intra-orbital recombinations [29] but these contributions are limited compared to the direct path.

In order to increase the contribution of the inelastic processes, it would be interesting to use samples that have no resonant states with the nanostructure. In other words, it would be interesting to use insulating or semiconducting substrates.

As we need a current flow, semiconducting samples are more appropriate.

The schematic diagram of the tunnel junction in such a configuration is drawn on Fig. 1.8(b) where the electrons tunnel to a state of the nanostructure resonant with the energy of the tip. Inside the nanostructure, the electron relaxes and is then transmitted to the sample.

A few results have been obtained for the growth of insulating layers on semiconducting samples and are described in the following section.

1.3 Experimental characterization of a DBTJ

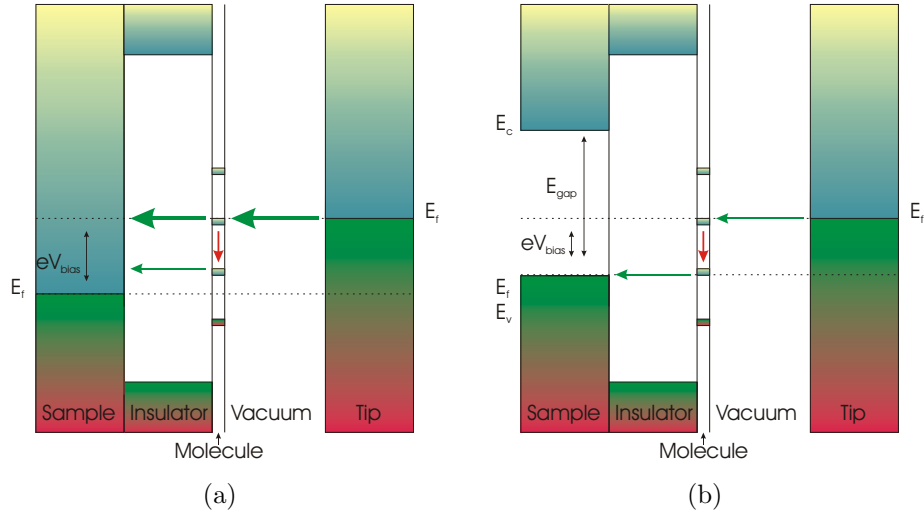


Figure 1.8: Schematic diagram of the tunnel junction in two different configurations: (a) a tip-vacuum-nanostructure-insulator-metal interface allows the electronic decoupling of nanostructures and the study of their electronic properties through resonant tunneling, i.e. the states of the nanostructure provide preferential paths for tunneling to the substrate but the recombinations inside the nanostructure itself are very limited; (b) a tip-vacuum-nanostructure-insulator-semiconductor interface, if well designed, binds the electrons to recombine inside the nanostructure before tunneling into the substrate states, as a result, inelastic phenomena are likely to be emphasized.

On semiconductors

- On $Si(111)$, the epitaxy of CaF_2 has been investigated in the early days of STM by Ph. Avouris and R. Wolkow [65] to demonstrate the imaging of insulators. They found the formation of a small gap insulating CaF interface on Si followed by the growth of layers of CaF_2 with a gap of 12eV, the top of the valence band being at -8.5eV and the bottom of the conduction band at approximately +3.5eV. The surface forms CaF/CaF_2 stripes on stepped $Si(111)$ surfaces [66] and was used for the "Chemical imaging of insulators by STM" [67]. This stripe pattern was even used by Rauscher et al. as a template for the fabrication of one-dimensional molecular structures thanks to the distinct chemical reactivities of CaF and CaF_2 [68]. More recent SPM studies focus on the varying properties of this surface with increasing thickness [69, 70].
- References [71, 72, 73, 74] investigate the growth modes of CaF_2 by Molecular Beam Epitaxy (MBE) at various substrate temperatures during deposition. CaF_2 deposited at low temperatures (i.e. 400 to 500°C) on $Si(001)$ forms square nanoscale islands but at higher substrate temperatures (700 to 750°C), the molecules dissociate and Ca reacts with the Si surface atoms until 1ML coverage [74] but after,

CHAPTER 1. ELECTRONIC TRANSPORT IN NANOSTRUCTURES WEAKLY COUPLED TO THE LEADS

elongated islands are the preferential growth mode.

- The growth of SrF_2 on $Si(001)$ undergoes the same behaviour as CaF_2 on the same surface but, as the lattice mismatch is much stronger, some interface disorder has been observed with high coverages [75].
- Glöckler et al. studied $NaCl$ on $Ge(100)$ by STM with atomic resolution [76] and they give the evidence of a carpet-like growth mode on the Ge atomic steps [77].

This section and the previous one, on the decoupling of nano-objects from the leads by an ultra-thin insulating layer, show the feasibility of well characterized transport measurement setups for nanostructures. Ultra-thin insulating layers indeed allow very good decoupling properties by forming a tunneling barrier between the nanostructure and the sample. A challenging task is to find the broadest bandgap materials for these layers in order to approach the quality of a vacuum barrier. But for some kinds of nanostructures, The perfect vacuum barriers are already used: 1D nanostructures like carbon nanotubes can be suspended over trenches.

By vacuum

The length of carbon nanotubes allows their suspension over wide trenches. The best example of what can be done is the "Electrical generation and absorption of phonons in carbon nanotubes" by LeRoy et al. [78]. In their experiment, they grow single-wall carbon nanotubes (SWCNTs) by chemical vapour deposition on a patterned Pt sample and are able to scan on SWCNTs over the trenches with atomic resolution (Fig. 1.9). Fig. 1.9(d) shows STS experiment along the suspended and supported parts of the nanotube. Regularly spaced horizontal lines over the suspended part of the nanotube reveal charging effects (Coulomb staircase) that are quenched over the supported part. On each side of the principal lines, sidelines appear only in the middle of the suspended part of the CNT and are secondary peaks reflecting inelastic phenomena associated with the emission and absorption of phonons. These peaks were not observed on the supported parts of the SWCNTs.

These solutions are smart, but they each concern only one type of molecule and there may be some problems of integration with other parts. A more versatile tentative is thus the growth of an insulating layer on the surface of the substrate.

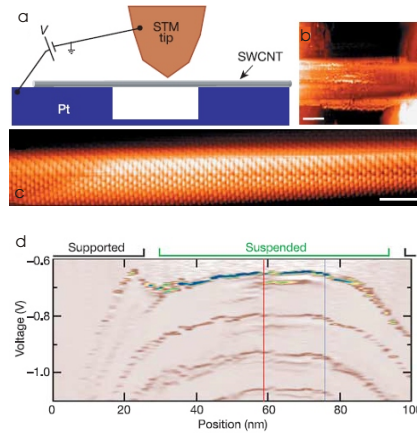


Figure 1.9: Electrical generation and absorption of phonons in carbon nanotubes [78] Measurement set-up and topographic images. (a) Schematic diagram showing the set-up for performing spectroscopy on suspended SWCNTs. A voltage is applied to the substrate with respect to the tip, and the current flowing from the substrate through the SWCNT to the tip is measured. (b) STM image of a nanotube crossing a trench. Scale bar, 25 nm. The apparent width of the 2-nm-diameter tube is enlarged by tip convolution. (c) High-resolution image of the suspended portion of the SWCNT showing atomic resolution. Scale bar, 2 nm. The STM images were taken with a feedback current of 300 pA at -1 V. All of the measurements were performed at 5 K in an ultrahigh-vacuum STM. (d) Spatially resolved spectroscopy along the suspended semiconducting SWCNT shown in (b). Plot of the normalized differential conductance (colour scale) as a function of voltage and position. Sharp spikes are visible at all positions due to the Coulomb staircase, while extra peaks are visible only in the centre of the suspended region. The differential conductance was measured using lock-in detection with a 2 mV r.m.s. excitation voltage. The setpoint current was 300 pA at -1.25 V. The coloured lines above the graph indicate the regions where the SWCNT is supported (black) and suspended (green).

1.4 Conclusion

In this first chapter, we have introduced the concept of Double Barrier Tunneling Junction and shown examples of characterized DBTJ systems. The DBTJ is adapted to the study of electronic transport through nanoscopic objects:

- Thanks to its ability of decoupling them from the leads;
- Because it gives spectroscopic informations on the nanostructure, provided the tunneling barriers were well dimensioned.

We have pointed out the performances of STM in the case of metallic substrates as one of the leads of the DBTJ:

- Because it is possible to create a DBTJ easily by placing a nanostructure between the tip and the substrate (ie on the path of tunnel electrons)

CHAPTER 1. ELECTRONIC TRANSPORT IN NANOSTRUCTURES WEAKLY COUPLED TO THE LEADS

- Because the width of one barrier can be configured at will by tuning the tip-nanostructure distance.
- Because STMs are nowadays especially designed to measure spectroscopic informations through I-V characteristics, Density Of States (DOS) spectroscopy and even vibrational spectroscopy by IETS (Inelastic Electron Tunneling Spectroscopy)
- And because STM also gives access to atomically resolved topographic images.

In the next chapters, we will investigate two different cases: a nanotube deposited on a gold surface and a silicon dangling bond state at the Si surface. Depending on the strength of the electronic coupling with one lead, we will see that we can modify a single-walled carbon nanotube or control the inelastic current through an isolated dangling bond state.

Chapter 2

Scanning Tunneling Microscopy (STM) and Spectroscopy (STS)

2.1 The Tunnel Effect

In 1905, Einstein postulated the existence of photons, quanta of light energy E with a wave-like behaviour of frequency ν such that

$$E = h\nu \tag{2.1}$$

h being Planck's constant, the equation is called "Equation of Planck-Einstein".

In 1924, Louis de Broglie postulated that not only light, but every piece of matter also has an undulatory nature. He generalized the relation of Planck-Einstein (eq.(2.1)) with the following expression:

$$\lambda = \frac{h}{p} \tag{2.2}$$

with p the quantity of movement and h Planck's constant.

The phenomenon was rapidly confirmed by diffraction experiments on electrons, protons, and even molecules by Estermann and Stern in 1929. De Broglie received the Nobel prize the same year for his discovery.

This theory had several important consequences, especially on the use of electrons in microscopy: as their wavelength is smaller than the wavelength of photons, they can be focused on small objects with a better resolution, in electronic microscopes and, later, Scanning Electron Microscopes (SEM).

Another phenomenon resulting from the wave-particle duality is the fact that every particle of energy E can penetrate into a barrier of energy $\Phi_0 > E$, and even cross it if the barrier is thin enough. This is called the tunnel effect

CHAPTER 2. SCANNING TUNNELING MICROSCOPY (STM) AND SPECTROSCOPY (STS)

and this effect was exploited for the first time with electrons in 1957 when Leo Esaki created the tunnel diode for which he won the Nobel prize in 1973.

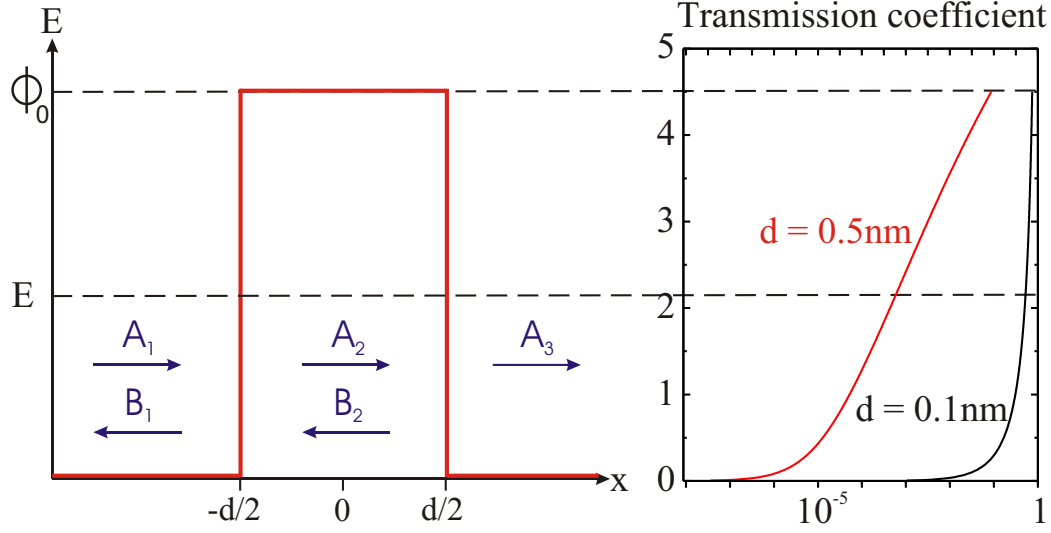


Figure 2.1: (left) schematized 1D tunnel barrier of width d in the x direction, the y and z directions are infinite. An incident electronic plane wave packet of energy E and amplitude A_1 hits the barrier of energy $\Phi_0 > E$. A part of the wave is reflected (amplitude B_1) and a part crosses the barrier (A_3). Inside the barrier, evanescent waves of amplitudes A_2 and B_2 take part in the tunnel process; (right) The graph corresponds to the energy E vs transfer coefficient $T = \left| \frac{\vec{A}_3}{\vec{A}_1} \right|^2$ for two barrier thicknesses of $d = 0.5nm$ and $d = 0.1nm$. For the present example, the energy barrier height is $\Phi_0 = 4.5eV$

Following is a demonstration of the strong dependence of electron tunneling on the thickness of the barrier. Two metallic electrodes are separated by a square potential barrier in the one-dimensional case as shown in Fig. 2.1. The electrons of energy $E < \Phi_0$ are described by their wave functions ψ_1 , ψ_2 and ψ_3 that verify Schrödinger's equation in their respective region:

$$\begin{aligned}
 \frac{-\hbar^2}{2m} \frac{\partial^2 \psi_1}{\partial x^2} &= E\psi_1 \\
 \frac{-\hbar^2}{2m} \frac{\partial^2 \psi_2}{\partial x^2} + \Phi_0 \psi &= E\psi_2 \\
 \frac{-\hbar^2}{2m} \frac{\partial^2 \psi_3}{\partial x^2} &= E\psi_3
 \end{aligned} \tag{2.3}$$

The general solutions in this case are:

$$\begin{aligned}
 \varphi_1(x) &= A_1 e^{ikx} + B_1 e^{-ikx} \\
 \varphi_2(x) &= A_2 e^{\alpha x} + B_2 e^{-\alpha x} \\
 \varphi_3(x) &= A_3 e^{ikx}
 \end{aligned} \tag{2.4}$$

with A_i and B_i the incident and reflected part of each wave in region $i = 1, 2, 3$, $k = \sqrt{\frac{2m}{\hbar^2} E}$ and $\alpha = \sqrt{\frac{2m}{\hbar^2} (\Phi_0 - E)}$

The probability that an electron crosses the barrier is given by:

$$T(E) = \left| \frac{A_3}{A_1} \right|^2 \quad (2.5)$$

In $x_0 = \pm \frac{d}{2}$, the wave function and its derivative are continuous. As a result, one gets a system of 4 equations to find the values of A_1, B_1, A_2, B_2 as a function of A_3 .

After resolution of the system, one gets the expression:

$$T(E) = \left| \frac{A_3}{A_1} \right|^2 = \frac{1}{1 + \frac{\Phi_0^2}{4E(\Phi_0 - E)} sh^2(\alpha d)} \quad (2.6)$$

The fact that $T(E)$ is not zero shows that electrons are able to cross a vacuum barrier thanks to their undulatory nature. Moreover, the probability of crossing the barrier depends on its thickness d : as T varies in an exponential way, we have a very sensitive thickness-dependent feedback signal.

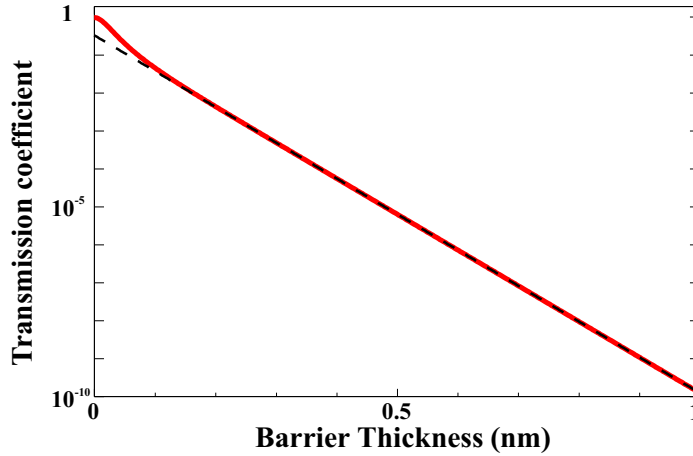


Figure 2.2: (red curve) Equation (2.6) vs barrier thickness at an energy of 0.1eV; (black dashed curve) Equation (2.7) vs barrier thickness at an energy of 0.1eV. The vertical axis has a logarithmic scale.

As an example, the red curve shown on Fig. 2.2 was computed from eq.(2.6) with tungsten electrodes (in this case, $\Phi_0 = 4.5eV$) at an energy of $E = 0.1eV$. The shape of the curve clearly shows an exponential behaviour

CHAPTER 2. SCANNING TUNNELING MICROSCOPY (STM) AND SPECTROSCOPY (STS)

when $d > 1\text{\AA}$. Indeed, at small energies, $\alpha = \sqrt{\frac{2m}{\hbar^2}(\Phi_0 - E)} \approx 1\text{\AA}^{-1}$. As a result, when the barrier d increases of 1\AA , the transmission coefficient decreases by e^{-2} . The transmission coefficient expression can thus be simplified to:

$$T(E) \simeq \frac{16E(\Phi_0 - E)}{\Phi_0^2} \exp(-2d\sqrt{\frac{2m}{\hbar^2}(\Phi_0 - E)}) \quad (2.7)$$

What is shown to be equivalent to (2.6) on Fig. 2.2 when $d > 1\text{\AA}$. Moreover, one can see the slope of 1 decade every 1\AA .

This variation of the current versus distance was measured by G. Binnig and H. Rohrer when they demonstrated the Tunneling through a controllable vacuum gap in 1982 [3]. This first report rapidly gave birth to the Scanning Tunneling Microscope, or STM [2, 4]. In fact, Young et al. [79] built in 1971 an instrument called the Topographiner which experimentally proved the transition between field emission (When the energy of the electrons is higher than the barrier) and electron tunneling but they could never demonstrate an atomic resolution and the project was abandoned. The next part demonstrates the ability of such a tool to achieve atomic resolution.

2.2 STM

The principle of the STM lies on the tunnel effect, described above, between two metallic or semiconducting electrodes. Fig. 2.3 shows both electrodes : a very sharp tip is the probe that analyzes the topography of the other electrode, an atomically flat sample. In the previous section, none of the electrodes were polarized, as a result the number of electrons going from the left to the right must be equal to the number going in the other direction. Now, in order to measure the distance between both electrodes, a current is established by polarizing one electrode with respect to the other.

2.2.1 Distance Feedback

Let us demonstrate that the value of the current has indeed a very good sensitivity against distance variations.

In order to calculate the current at a bias eV applied on the sample, one needs to integrate the Transmission coefficient $T(E, eV)$ of the electrons across the barrier to all the energy states in the sample between energies ranging from $E_{FSample}$ to $E_{FTip} = E_{FSample} + eV$ at $T = 0K$.

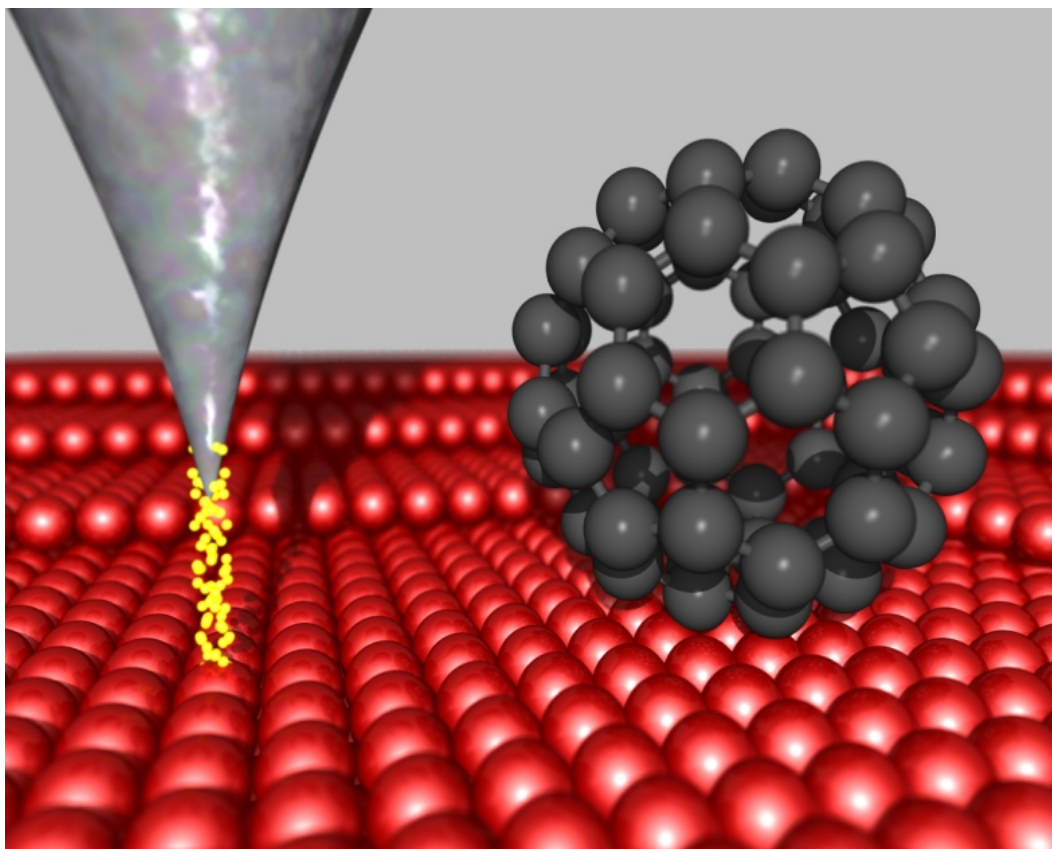


Figure 2.3: Scheme of a STM at the atomic scale: A metallic tip is approached close to an atomically flat (semi)conducting surface. Typically, the tip is connected to the ground and the sample is polarized with respect to the tip. As the distance between those two electrodes is very small (a few Angströms), electrons can tunnel from one electrode to the other and can be used as a feedback for distance regulation. The tip is mounted on piezoelectric ceramics, able to scan the surface with a sub-nanometer precision. The electrons can also tunnel through nano-materials deposited on the surface, like the C_{60} fullerene on the image.

$$I = \int_0^{eV} T(E, eV) \rho_{tip}(E - eV) \rho_{sample}(E) dE \quad (2.8)$$

with ρ_{tip} and ρ_{sample} the local density of electronic states of respectively the tip and the sample.

Some approximations are usually taken as they greatly simplify the calculation and understanding:

1. The polarization of the electrodes is usually small compared to the height of the tunneling barrier. In such a configuration, the trapezoidal barrier can be assimilated to a square barrier (cf Fig. 2.4) with the

CHAPTER 2. SCANNING TUNNELING MICROSCOPY (STM) AND SPECTROSCOPY (STS)

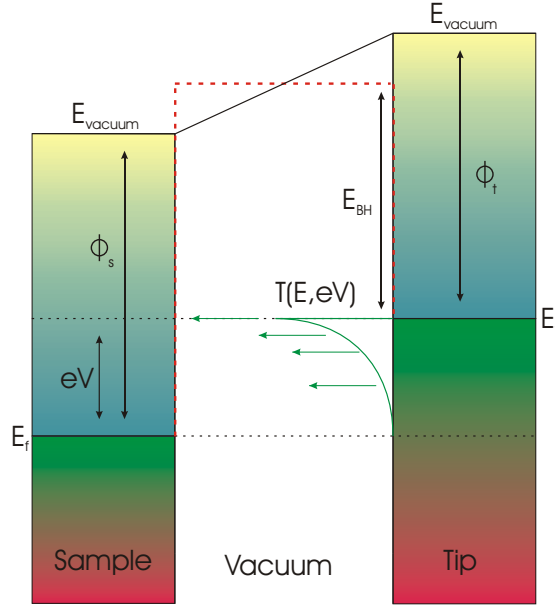


Figure 2.4: Schematic diagram of the tunnel junction in a STM. At zero bias, the height of the barrier seen by the electrons is approximated by a square barrier of height $\Phi = \frac{\Phi_{tip} + \Phi_{sample}}{2}$, which is the mean of the work functions of the electrodes. When a bias eV is applied on the sample, the barrier becomes more and more trapezoidal. If eV is small compared to ϕ , then the barrier seen by the electrons can still be considered as square, with a height $E_{BH} = \frac{\Phi_{tip} + \Phi_{sample}}{2} - eV/2$ (red dashed line).

following characteristics:

$$E_{BH} = \frac{\Phi_{tip} + \Phi_{sample}}{2} - \frac{eV}{2} \quad (2.9)$$

and equation (2.6), which does not take into account the polarization of the electrodes, is valid for the calculation of the current if E_{BH} is taken as the height of the barrier.

2. The distance d between both electrodes is expected to be in the order of a few Angströms. In this configuration, it was previously seen that equation (2.6) becomes equation (2.7):

$$T(E) \approx \frac{16E(E_{BH} - E + eV)}{E_{BH}^2} \exp\left(-2d\sqrt{\frac{2m}{\hbar^2}(E_{BH} - E + eV)}\right) \quad (2.10)$$

Thus, equation (2.10) is injected into equation (2.8) and one finds

$$I \approx \int_0^{eV} \frac{16E(E_{BH} - E + eV)}{E_{BH}^2} \exp\left(-2d\sqrt{\frac{2m}{\hbar^2}(E_{BH} - E + eV)}\right) \rho_{tip}(E - eV) \rho_{sample}(E) dE \quad (2.11)$$

and for biases much lower than the average barrier height, it becomes:

$$I \approx 16 \exp\left(-2d\sqrt{\frac{2m}{\hbar^2}E_{BH}}\right) \int_0^{eV} \frac{E - eV}{E_{BH}} \rho_{tip}(E - eV) \rho_{sample}(E) dE \quad (2.12)$$

The above equation demonstrates the exponential dependence of the current against distance. For instance, tungsten electrodes, which have a work function of $\Phi = 4.5eV$, will give $\sqrt{\frac{2m}{\hbar^2}E_{BH}} \approx 1\text{\AA}^{-1}$. It means that an increase of 1\AA of the tip-sample distance leads to a change of the current by a factor $e^{-2} \approx 0.1$.

Such exponential dependance of the current provides enough precision to detect atomic-scale vertical variations, but a microscope should also be able to discriminate one atom and its neighbour. The next part demonstrates the lateral resolution of the STM.

2.2.2 Lateral Resolution

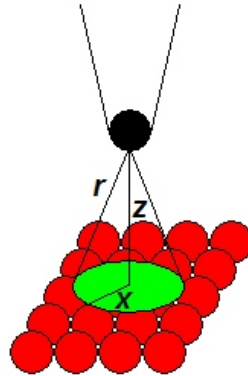


Figure 2.5: Lateral resolution of the STM

As seen with Equation(2.12), the current is exponentially dependent on the distance between the electrodes. As a consequence, we can assume that

CHAPTER 2. SCANNING TUNNELING MICROSCOPY (STM) AND SPECTROSCOPY (STS)

only the last atom of the tip contributes to the current. Let us suppose that this atom has a wave function of s type, described by:

$$|\Psi|^2 = \frac{e^{-2\alpha r}}{r^2} \quad (2.13)$$

with $r = \sqrt{x^2 + z^2}$, as seen in Fig. 2.5.

As $z \gg x$, r is approximated by

$$r \approx z + \frac{x^2}{2z} \quad (2.14)$$

Thus:

$$|\Psi|^2 \approx \frac{e^{-2\alpha z}}{z^2} e^{-\alpha \frac{x^2}{z}} \quad (2.15)$$

which is a gaussian function in x , of full width at half maximum equal to:

$$\Delta x \approx \sqrt{\frac{2z}{\alpha}} \quad (2.16)$$

The height of the tip is

$$z = R + d \quad (2.17)$$

Where R is the radius of curvature of the apex of the tip, and d is the tip-sample distance. For tungsten and with a low bias, we already know that $\alpha \approx 1\text{\AA}^{-1}$. As seen in controlled contact experiments [80, 81, 82], the tip sample distance in scanning conditions is $d = 4\text{\AA}$ to $d = 8\text{\AA}$. Following Tersoff and Hamann's *Theory of the scanning tunneling microscope*, [83] the height of the tip can be taken equal to the radius of curvature R of the tip (several nanometers), compared to the tip-sample separation. Thus they found a lateral resolution of

$$\Delta x \approx 1.4\sqrt{R} \quad (2.18)$$

It corresponds to $\Delta x = 14\text{\AA}$ for a very sharp tip with a radius of curvature of $R = 100\text{\AA}$. Although giving a good appreciation, the value is far higher than the experimentally achieved resolutions. In fact, the atomic resolution is often the consequence of atomic-sized protrusions at the apex of the tip. These protrusions have a very small radius of curvature. If one takes a tip-sample distance $d = 5\text{\AA}$ [80, 81, 82] and an equal value for the radius of the apex protrusion $R = 5\text{\AA}$, the resolution to be achieved is $\Delta x \approx 1.4\sqrt{10}\text{\AA} \approx 4.4\text{\AA}$.

Sacks calculated more realistic results [84]: taking into account tip-sample couplings and other symmetries of the orbitals like p or d orbitals instead of a s orbital, he could explain the high experimental resolutions.

Thus, the tunnel current established between the tip and the surface is a good feedback value for distance regulation, and the beam is quite narrow to provide good lateral resolution. In order to reproduce topography images at the atomic scale, the two electrodes are mounted on a moving stage, motorized by piezoelectric ceramics in the three spatial directions X, Y and Z. Fig. 2.6 gives an example of such a setup, where the sample is fixed and the tip is collecting the tunnel current at every (X,Y) location of the sample in order to reproduce the topography, $Z(X,Y)$ on a computer screen. This is the first, historical, mode of operation of the STM. Nevertheless, other modes, called spectroscopic modes, exist and will be explained right after the description of the microscopes used in this thesis.

2.2.3 The Omicron LT-STM

The microscopes used in this thesis are Low-Temperature STM (LT-STM) from Omicron GmbH. Not only is it able to reproduce atomic-scale images, it does it in a Ultra-High Vacuum (UHV) chamber (base pressure: $7.10^{-11}Torr$) in order to avoid any pollution, and also works at low temperature. The UHV chambers are made of stainless steel and contain several apertures in order to connect them to other chambers. Copper gaskets are used in order to avoid leaks.

I worked on two LT-STMs: the microscope of the Physics group of IEMN at the University of Lille 1 (France) and the one of Shigekawa Laboratory at the University of Tsukuba (Japan). They are very similar and have the same characteristics so I will describe them at the same time and state the differences only when needed.

Three autonomous chambers compose the system:

The load-lock chamber

The load-lock chamber interfaces the UHV chambers with outside. In Lille, this chamber contains a sliding transfer rod on which three samples can be placed whereas in Tsukuba, it has only one place. Samples are entered in this chamber through a viewport that can be opened. This viewport has a viton gasket instead of a copper gasket. The main advantage is that it does not need to be replaced every time the viewport is opened. The drawbacks are: the maximum bake-out temperature is $120^{\circ}C$ and the vacuum level is limited, but it can achieve $P < 1.10^{-8}T$, which is enough for this chamber.

CHAPTER 2. SCANNING TUNNELING MICROSCOPY (STM) AND SPECTROSCOPY (STS)

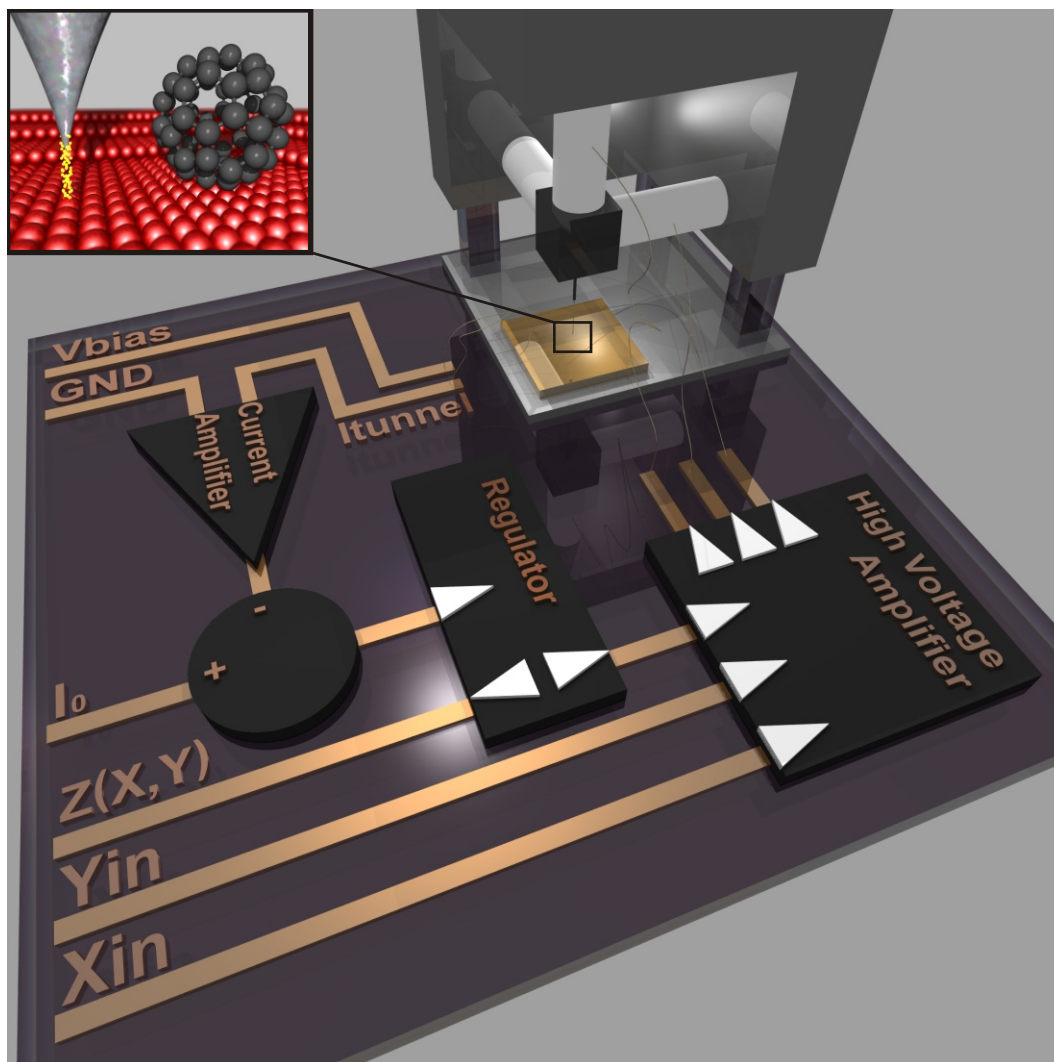


Figure 2.6: Simplified Schematics of a STM. On the top right corner, the tip is mounted on a piezo tripod (the three white cylinders, respectively X, Y and Z) over the sample to be analysed. The polarization is done through the inputs V_{bias} and GND, respectively connected to the sample and to the tip. The tunnel current is collected on the tip side and amplified by a current amplifier. The output signal is then compared to the reference current I_0 to produce the error signal that will drive the regulator. This stage has two outputs: the first one gives $Z(X,Y)$, the topography information while the other output regulates the tip-sample distance through the elongation or contraction of the Z piezo. In order to allow lateral movements of the tip, the two inputs X_{in} and Y_{in} drive the X and Y piezo motion. If zooming on the tunnel junction was possible, one would see a figure similar to Fig. 2.3, here added as an inset.

When new materials are put into this chamber, it is always pumped down to High Vacuum thanks to a turbomolecular pump and baked-out at 120°C during 9 hours in order to remove the most common contaminants of air, like water.

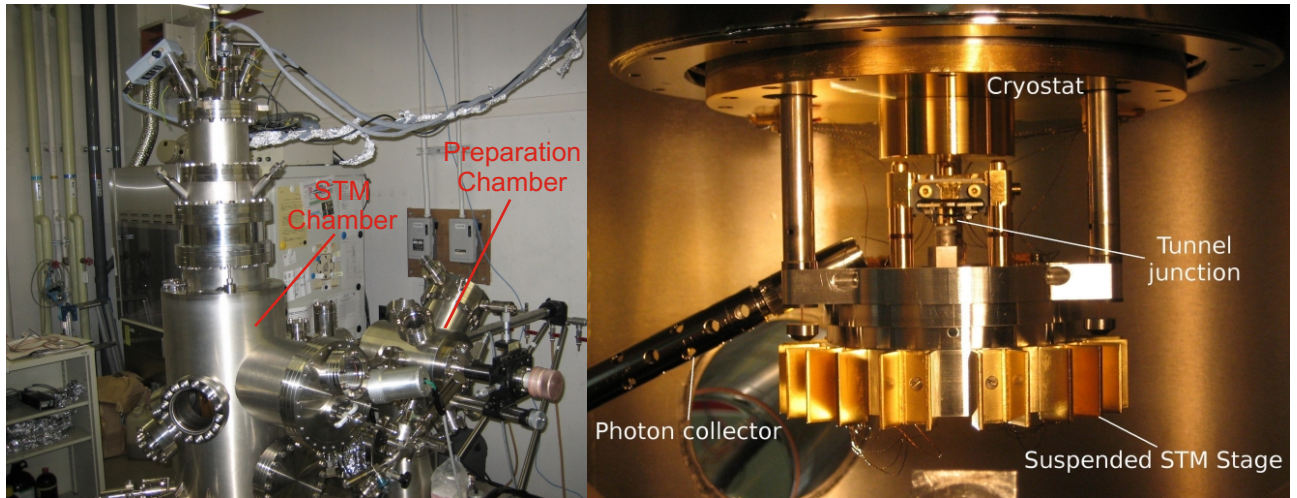


Figure 2.7: (right) Outside view of the Omicron LT-STM; (left) inside view of the STM chamber in an Omicron LT-STM with an additional photon collecting tube.

The preparation chamber

The preparation chamber is maintained in UHV by an ion getter pump and a Titanium Sublimation Pump (TSP). The base vacuum in this chamber is $5.10^{-11}T$. When the load-lock chamber and the preparation chamber are both pumped down, the valve can be opened, the transfer rod of the load-lock can enter the preparation chamber and the samples can be transferred to a second sliding transfer rod located in the preparation chamber. The chamber contains a sample storing stage with 5 slots and a manipulator.

The manipulator can receive one sample, is able to move in the 3 directions and rotate around its axis. As a result, the sample mounted on the manipulator can be placed in front of other equipments that will be described below. The manipulator also have a resistive heater, a thermocouple and different electrical connections: the sample can be either polarized or a current can be established through it, for example when a resistive sample needs to be heated.

Indeed, the manipulator is of critical importance for the preparation of samples and tips:

- We use polycrystalline tungsten tips that are electrochemically etched in a solution of NaOH before loading them into UHV.

Once it is on the manipulator, the tungsten wire of the tip is connected to a finger at the ground potential and the manipulator is polarized. As a result, the wire is heated by Joule effect. The tip is heated to high temperatures (orange color, $\approx 1000K$) in order to get rid of the

CHAPTER 2. SCANNING TUNNELING MICROSCOPY (STM) AND SPECTROSCOPY (STS)

oxide layer. At last, it is flashed to orange-yellow color a few times. The flashes aim at stabilizing the emission current of the tip.

- Resistive samples like semiconductors also need to be heated in order to remove their native oxide layer, to clean them and to reconstruct their surface without defects. For such a purpose, we take advantage of the resistive nature of the sample by polarizing one end of the sample against the other with the manipulator. The sample is thus heated by Joule effect. More details on the sample preparation will be given in the appropriate chapters.
- The procedure for cleaning metallic samples is quite different as they are not resistive. Usually, metals are cleaned by repeated cycles of ion sputtering and heating. The ion sputtering aims at removing the contaminants. It is usually done with Argon and the ion gun facing the manipulator. As the sputtering step damages the surface, it needs to be reconstructed by heating with the resistive heater of the manipulator. Because heating also induces a migration of the contaminants to the surface, the cycle has to be repeated several times in order to deplete the sample from contaminants.

An extra place that is used as an oven for molecules is located below the manipulator. A clean, freshly prepared semiconductor sample can be set on this place and molecules are deposited on the sample. The sample is then heated by Joule effect and the molecules are sublimated. If another sample is put in front of the oven, the molecules are deposited on this sample with a controllable rate. A mass spectrometer is able to monitor the presence of molecules in the atmosphere of the chamber.

The preparation chamber also contains a gaz inlet and a tungsten filament. This setting is used for special surface reconstructions like hydrogenation or nitridation. The hydrogen or nitrogen gas is cracked by the filament heated to high temperature and the resulting ions are attracted by an electric field created by polarizing the sample.

The STM chamber

As for the preparation chamber, UHV is maintained by an ion getter pump and a TSP. The base pressure in this chamber at room temperature after bake-out is $7 \cdot 10^{-11} Torr$. Up to six samples and tips can be stored in a carousel and a wobblestick is used for the transfers from the carousel to the STM. Two cryostats are connected to the STM to cool down the system. One cryostat (outer) acts like a shield and is filled with Nitrogen only, whereas the

second cryostat (inner) can be refilled with Nitrogen or Helium depending on the temperature range to be used.

Thanks to the cryostats and a heating device, the microscope can be operated over a broad range of temperatures, going from 4K to 300K, but it is most of the time set to 4K (liquid Helium temperature) or 77K (liquid Nitrogen temperature). At low temperature, the cryostats act as cryogenic traps for remaining contaminants in the chamber and the pressure slightly increases with time with the number of heating-cool down cycles.

- The outer cryostat is always filled with liquid nitrogen and is empty within 16 hours.
- The inner cryostat can be filled with liquid Nitrogen. In this case the temperature is 77K and refilling occurs every 3 days. If it is filled with liquid Helium, the temperature is 4.8K and the consumption reaches 4 liters in 24hours when we continuously work with the same tip and sample.

In Tsukuba, I have worked on the design of a photon detection system to be focused on the tunnel junction. This system can be viewed on Fig. 2.7 and is made of 2 lenses mounted on a metallic tube. One end of the tube is approached close to the tunnel junction in the UHV chamber thanks to a (z, θ) manipulator on which is connected the other end of the tube. At this end, a $0.6mm$ optical fiber collects the lights emitted by the tunnel junction and brings it to a spectrometer (Acton Research SpectraPro-2300i) on which a CCD (Princeton Spec-10 CCD: LN2 cooled and back illuminated) measures the spectrum of light. As the tube with the lenses is not cooled, and as it has to be approached close to the tunnel junction, thermal radiations heat up the system and, when the inner cryostat is filled with liquid Helium, the temperature of the tunnel junction is 20K and the cryostat is empty within 4 hours.

On some kinds of variable temperature microscopes, only the sample is cold, therefore the piezo motors and the tip are at room temperature. This has two inconvenients: lateral drift by the piezos and thermal broadening against the energy when doing spectroscopy. The main advantage of the LT-STM is that all the active parts are thermalized: the tip, the sample and the piezo motors are kept at the same temperature. Thus, better results at a fixed temperature can be obtained. Also, when the system is cooled down to only a few Kelvin, there is almost no more lateral drift and the loop can be opened (ie no more distance regulation) for more than half an hour without any measurable motion of the tip compared to the sample.

CHAPTER 2. SCANNING TUNNELING MICROSCOPY (STM) AND SPECTROSCOPY (STS)

The STM is made of a fix sample and a moving tip. Two types of movements are allowed:

- Coarse positioning is done through a “stick and slip” piezoelectric system. It makes possible to move the tip in the three directions X, Y and Z of respectively $5mm$, $5mm$ and $10mm$.
- Fine movements and image scans are made thanks to a piezoelectric tube on which the tip is mounted. At room temperature, it can move over an area of $10\mu m \times 10\mu m$ and the tip is able to move in the Z direction of $1\mu m$. As temperature deacreses, the sensitivity of the piezo decreases and as a result, for the same excitation, a smaller area is covered: at 4K, the tube is able to scan only $1.8\mu m \times 1.8\mu m$ laterally and $0.2\mu m$ in Z. The vertical resolution is better than $10pm$ in Z.

In order to be able to handle such a high resolution, the STM must be isolated of any vibration. As the STM is under vacuum, there is no coupling with vibrations coming from the air, like acoustic waves, but vibrations of the floor can be transmitted to the UHV chamber. For this reason, the STM is mounted on an Eddy current (aka Foucault current) damping system.

The stability brought by the cooling system and the damping system makes the LT-STM an ideal machine for spectroscopy of nanoscale objects.

2.3 Tunneling Spectroscopy

Equation (2.12) shows that the tunnel current I depends on the bias V and the tip-sample distance d . In the common, topographic, mode of operation, V is fixed by the experimentator and the desired current I is regulated against d by the feedback loop at every point scanned by the tip. In the spectroscopic mode, the tip is stopped at one specific place and one of the three values d , I , V is ramped while one other is kept constant and the last one is measured. The absolute Tip-sample distance d is not easy to determine and it is usually replaced by Z , the relative height of the tip to a reference. Theoretically, six types of spectroscopy can be done: $I(Z)$, $I(V)$, $Z(V)$, $Z(I)$, $V(Z)$, $V(I)$. In reality, only the three first are used as the other ones don't give much information.

2.3.1 Distance versus bias spectroscopy $Z(V)$

This mode is easy to understand as it uses the same distance feedback as in the topographic mode. The feedback loop is kept closed while V is

swept from one value to another. As a result, the regulator adjusts Z in order to keep I constant. The tip-sample distance variations Z are stored as a function of V .

This mode is often used to measure the height of the tunnel barrier: when eV becomes comparable to $\Phi = \frac{\Phi_{tip} + \Phi_{sample}}{2}$, the shape of the barrier progressively becomes triangular and when eV becomes greater than Φ , oscillations of the tip-sample distance are detected because of field emission resonances. The first experiments to show resonances due to localized states in the barrier were done by Binnig and Rohrer [85].

Even though this mode is also able to detect changes of the tip and sample conductivity ρ_{tip} and ρ_{sample} , it is not broadly used because its resolution is limited by the feedback loop. For example, it is not possible to do spectroscopy at both negative and positive bias in the same spectrum because at zero volts, the tip and the sample would enter into contact. On the contrary, $I(V)$ spectroscopy, which is described below, works with an open loop.

2.3.2 Current versus bias spectroscopy $I(V)$

When the feedback loop is opened, the tip-sample distance is kept constant and it is still possible to measure the tunnel current. The first study was done by Feenstra, Thompson and Fein [86].

Elastic spectroscopy

As seen previously, the tip is considered atomically sharp, with a s -like orbital for the apex atom. In these conditions, and if we assume that the density of states for the tip is constant, we get:

$$I \propto \rho_{tip} \int_0^{eV} T(E, eV) \rho_{sample}(E) dE \quad (2.19)$$

thus

$$\frac{\partial I}{\partial V} \propto e \rho_{tip} \rho_{sample}(eV) T(eV, eV) + e \rho_{tip} \int_0^{eV} \frac{d}{deV} [T(E, eV)] \rho_{sample}(E) dE \quad (2.20)$$

The above expression is dependent on the sample density of states, but the exponential increase of the signal against bias due to the influence of the transmission coefficient $T(E, eV)$ induces a larger contribution of the states lying at higher energy with respect to the states closer to the Fermi level. This effect may be negligible for metals, but becomes significant for semiconductors, where higher biases are used. Feenstra et al. [87] have shown that

CHAPTER 2. SCANNING TUNNELING MICROSCOPY (STM) AND SPECTROSCOPY (STS)

the differential conductance can be normalized by the ratio I/V in order to cancel the exponential dependence because of $T(E, eV)$:

$$\frac{\frac{\partial I}{\partial V}}{\frac{I}{V}} \propto \frac{\rho_{sample}(eV) + \int_0^{eV} \frac{\partial}{\partial eV} [T(E, eV)] \frac{\rho_{sample}(E)}{T(eV, eV)} dE}{\frac{1}{eV} \int_0^{eV} \frac{T(E, eV)}{T(eV, eV)} \rho_{sample}(E) dE} \quad (2.21)$$

The second term of the numerator is a slowly varying background term and as a result, the variations of $\frac{\partial I}{\partial V}$ as a function of V are mainly related to $\rho_{sample}(eV)$. Thus

$$\frac{\frac{\partial I}{\partial V}}{\frac{I}{V}} \propto \rho_{sample}(eV) \quad (2.22)$$

This relation shows that it is possible to get a measure of the Local Density Of States (LDOS) of the sample, independent of the tip-sample separation, from $I(V)$ curves. The technique works well with metals and small band gap materials. Nevertheless, for materials with a wide band gap, two problems occur and need a further treatment:

- The value $\frac{I}{V}$ is decreasing faster than $\frac{\partial I}{\partial V}$ when $V \rightarrow 0$. As a result, the ratio $\frac{\frac{\partial I}{\partial V}}{\frac{I}{V}}$ is divergent at the edges of the gap [88]. This issue can be solved by broadening $\frac{I}{V}$, for example with an exponential convolution [89]:

$$\overline{\frac{I}{V}} \equiv \int_{-\infty}^{+\infty} \frac{I(V')}{V'} \exp\left[-\frac{|V' - V|}{\Delta V}\right] dE \quad (2.23)$$

We generally chose ΔV of the order of the band gap of the sample in order to avoid a significant amplification of the noise level in the band gap. This process does not induce any shift of the peaks position and yields thus a qualitative knowledge of the LDOS as it suppresses the divergence in the band gap region.

- The value $\frac{\frac{\partial I}{\partial V}}{\frac{I}{V}}$ indeed gives a measure of the sample's density of states that is independent of the tip-sample distance but not of the signal

to noise ratio. As a result, where I is smaller than the noise level, $\frac{\partial I}{\partial V}$ gives incoherent values. In order to overcome the decrease of $\frac{\partial I}{\partial V}$ sensitivity in the energy gap region of semiconductors, the tip can be brought closer to the surface [88]. The goal is to counterbalance the exponential dependence of the current against distance:

$$I \propto \exp\left(-2d\sqrt{\frac{2m}{\hbar^2}}\sqrt{\Phi - \frac{|eV|}{2}}\right) \quad (2.24)$$

In order to annihilate the distance dependence, one has to find a variation of the tip-sample distance which keeps the current constant during the measurement of a spectrum. This can be achieved if one sets:

$$d(V)\sqrt{1 - \frac{|eV|}{2\Phi}} = d_0 \quad (2.25)$$

where d_0 is a constant corresponding to the tip-sample distance at $V=0$. for small values of V (smaller than Φ), an expansion gives:

$$d(V) = d_0 \left(1 + \frac{|eV|}{4\Phi}\right) \quad (2.26)$$

Then, in order to gain sensitivity in the band gap region of semiconductors, the tip can be approached closer to the sample following a linear ramp against V . With $d_0 = 10\text{\AA}$ and $\Phi = 4.5\text{eV}$, the slope to be counterbalanced is $0.56\text{\AA}/V$.

Temperature broadening

When the temperature is not $0K$, the electrons can gain a thermal energy, what allows them to fill electronic states higher than the Fermi level. The resulting energy distribution follows the law of Fermi-Dirac and the current is broadened by this function. It has been seen in the previous chapter (1.2.2 on page 22) that the total current flowing through the junction is the difference between the current from the tip to the sample and from the sample to the tip. After summation, one obtains the following expression:

$$I \propto \int_{-\infty}^{+\infty} [f_{sample}(E) - f_{tip}(E - eV)]T(E, eV)\rho_{tip}(E - eV)\rho_{sample}(E) dE \quad (2.27)$$

CHAPTER 2. SCANNING TUNNELING MICROSCOPY (STM) AND SPECTROSCOPY (STS)

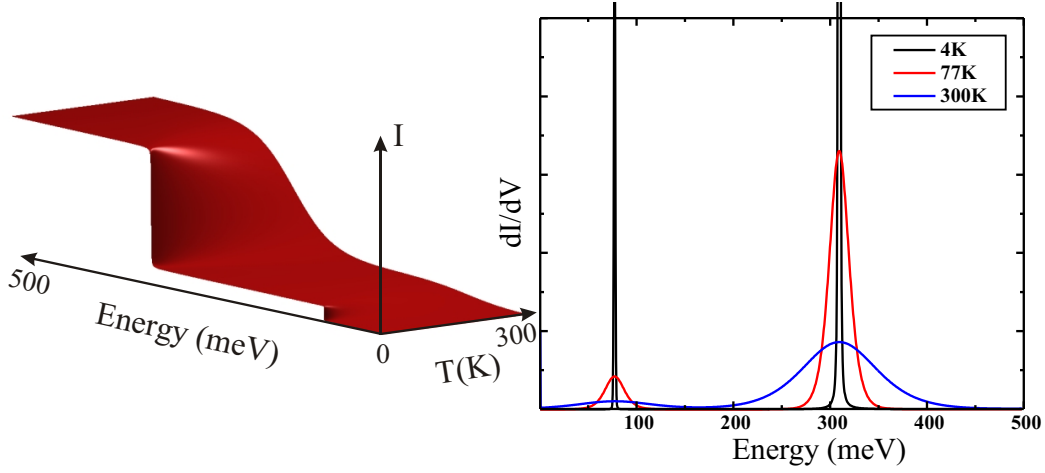


Figure 2.8: Calculated effect of the temperature on the tunneling spectrum of a 1D tunnel structure made of a tungsten electrode (barrier height of 4.5eV at zero bias) system with two energy states at 80 and 310meV. Left: 3D plot of the current against temperature, T and energy E . Right: plot of the derivative of the current at 4K, 77K and 300K illustrating the temperature broadening. We assume that the density of states is constant in the metallic electrode.

with $f_n(E) = \frac{1}{1 + \exp\left(\frac{E - E_{F_n}}{k_B T}\right)}$ the Fermi-Dirac function, k_B is Boltzman's constant.

$T(E, eV)$ adds a background to the spectra, but its influence can be neglected in the case of small energies. Thus, assuming a constant density of states in the tip (this is consistent with small energies compared to the barrier height), the derivative of the current against bias is:

$$\frac{\partial I}{\partial V} \propto \rho_{tip} \int_{-\infty}^{+\infty} \frac{\partial f_{tip}}{\partial V}(E - eV) \rho_{sample}(E) dE \quad (2.28)$$

The above equation shows that the measured $\frac{\partial I}{\partial V}$ spectra correspond in fact to a convolution between the derivative of the Fermi-Dirac function of the tip at this temperature and the LDOS of the sample. The expression of $\frac{\partial f_{tip}}{\partial V}(E + eV)$ is:

$$\frac{\partial f_{tip}}{\partial V}(E - eV) = \frac{-1}{k_B T} \frac{\exp\left(\frac{E - eV - E_F}{k_B T}\right)}{\left[1 + \exp\left(\frac{E - eV - E_F}{k_B T}\right)\right]^2} \quad (2.29)$$

Fig. 2.8 shows an example of the temperature broadening effect on calculated spectra of the tunnel current. The very sharp peaks that would be obtained at $T = 0K$ are progressively smoothed by expression (2.29) which has a width at half maximum $fwhm = 3.2k_B T$.

The lock-in amplifier

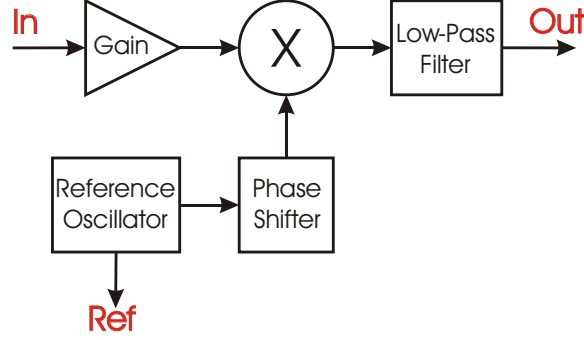


Figure 2.9: Functional bloc diagram of a lock-in amplifier

As seen previously (equation(2.22)), the derivative of the current is needed to get spectroscopic informations on the LDOS of the sample. A simple way is to numerically derivate the current. This method is fast and easy but noisy: due to mechanical instabilities and electronic amplifiers, a wide-band noise is inherently included in the measurement and amplifies with the derivation of the current. The major contribution of the noise is a low frequency $1/f$ noise that cannot be removed from numerically calculated derivatives.

On the other hand, lock-in amplifiers use a technique known as phase sensitive detection to measure small ac signals by transposing and filtering only the interesting part of the signal to a reference frequency. The process is analogous to radio broadcast, where a carrier signal of well known frequency is modulated by the interesting signal.

When the polarization eV is modulated by a sinusoidal carrier of small amplitude $eV_{mod} \sin(\omega_{mod}t + \varphi)$, the tunneling current can be expanded into the following Taylor series:

$$I(eV + eV_{mod} \sin(\omega_{mod}t + \varphi)) = \sum_{n=0}^{\infty} \frac{I^{(n)}(eV)}{n!} [eV_{mod} \sin(\omega_{mod}t + \varphi)]^n \quad (2.30)$$

If the frequency of modulation $f_{mod} = \frac{\omega_{mod}}{2\pi}$ is set high compared to the speed of the current feedback loop, the oscillations will not perturb the STM image or spectrum. Typically, a frequency of modulation f_{mod} in the range of $500Hz \rightarrow 10kHz$ is suitable.

CHAPTER 2. SCANNING TUNNELING MICROSCOPY (STM) AND SPECTROSCOPY (STS)

Thus, at the second order:

$$\begin{aligned}
 I(eV + eV_{mod} \sin(\omega_{mod}t + \varphi)) = & \\
 & I(eV) + I''(eV) \frac{e^2 V_{mod}^2}{4} \\
 & + I'(eV) eV_{mod} \sin(\omega_{mod}t + \varphi) \\
 & - I''(eV) \frac{e^2 V_{mod}^2}{4} \cos(2\omega_{mod}t + 2\varphi) + o(e^2 V_{mod}^2 \sin^2(\omega_{mod}t + \varphi)) \quad (2.31)
 \end{aligned}$$

Which means that when the bias is modulated, the first and the second derivatives of the current are carried respectively by its first and second harmonics. As seen on Fig. 2.9, the lock-in measures the amplitude of the harmonics based on the following method:

1. The modulated signal In is amplified. Let us take a gain of 1 and the signal $In = I(eV + eV_{mod} \sin(\omega_{mod}t + \varphi)) + K \sin(\omega_{noise}t + \varphi_{noise})$ in which the second term can be any noise contribution.
2. A multiplier mixes the input with the reference signal $\sin(\omega_{mod}t + \varphi_{ref})$. As a result, the interesting part of the signal is shifted to a dc value and any other contribution with a different frequency is kept as an ac signal:

$$\begin{aligned}
 In \times \sin(\omega_{mod}t + \varphi_{ref}) = & \\
 & I'(eV) \frac{eV_{mod}}{2} \cos(\varphi - \varphi_{ref}) \\
 + & \left[I(eV) + I''(eV) \frac{e^2 V_{mod}^2}{4} + o(e^2 V_{mod}^2 \sin^2(\omega_{mod}t + \varphi)) \right] \sin(\omega_{mod}t + \varphi_{ref}) \\
 - & I''(eV) \frac{e^2 V_{mod}^2}{8} \sin(\omega_{mod}t + 2\varphi - \varphi_{ref}) \\
 - & I'(eV) \frac{eV_{mod}}{2} \cos(2\omega_{mod}t + \varphi + \varphi_{ref}) \\
 + & I''(eV) \frac{e^2 V_{mod}^2}{8} \sin(3\omega_{mod}t + 2\varphi + \varphi_{ref}) \\
 + & \frac{K}{2} [\cos((\omega_{noise} - \omega_{mod})t + (\varphi_{noise} - \varphi_{ref})) \\
 & - \cos((\omega_{noise} + \omega_{mod})t + \varphi_{noise} + \varphi_{ref})] \quad (2.32)
 \end{aligned}$$

3. A narrow low-pass filter keeps only the dc part of the signal. Provided $\omega_{noise} \neq \omega_{mod}$:

$$Out = I'(eV) \frac{eV_{mod}}{2} \cos(\varphi - \varphi_{ref}) \quad (2.33)$$

which is proportional to the derivative of the tunneling current.

But using a lock-in amplifier has a drawback: the tip-sample system and the wires that connect it to the preamplifier form a capacitance. As a result, the modulation creates a parasitical sinusoidal current of the same frequency as the modulation. This current can be huge compared to the tunnel current and hinders the dynamical resolution of the lock-in. Hopefully, it is phase shifted because of the capacitive nature of the system and can be removed easily by adding the opposite signal, derivated from the reference.

Moreover, the amplitude of the modulation has to be chosen carefully: indeed, the integration over time of the modulation signal gives a half round shaped curve of diameter $2eV_{mod}$ against energy. Klein et al. [90] have shown that the measured $\frac{dI}{dV}$ is broadened because it is a convolution of this curve, called the “instrumental resolution function”, with the real LDOS spectrum. As long as eV_{mod} remains smaller than the desired energy resolution, the spectrum will not be significantly broadened but in some case, the Signal/Noise (S/N) ratio may require an increase of the modulation amplitude in order to extract the signal.

Such a case does not often happen for the first derivative, but in the following part, the second derivative will be computed and requires a particular attention on the S/N due to its weakness.

Inelastic spectroscopy

The major part of the electrons cross the tunnel barrier without energy loss, but a small amount can also release some of their energy due to scattering events. For example, if we consider a molecule in a tunneling junction, electrons from the tip can be transferred to the molecule and lose part of their energy before tunneling to the sample electrode. This loss of energy can occur with the emission of photons or vibrations. This process involves an inelastic electron tunneling event and the detection technique to characterize this event is called Inelastic Electron Tunneling Spectroscopy (IETS).

This technique is, in fact, older than STM: it was developed by Jaklevic and Lambe in 1966 [91] while they were working on M-I-M (Metal-Insulator-Metal) junctions. At low temperature, they saw conductance jumps that could be identified as peaks on the second derivative of the tunneling current. These jumps correspond to the opening of new channels for the electrons when their energy eV is high enough to excite a vibrational mode $h\nu_0$. Thus, when $eV \geq h\nu_0$, the slope of the current changes, causing a step in the differential conductance and a peak on the second derivative (see Fig. 2.10).

The lock-in can also be used to detect IETS spectra if it is locked on the

CHAPTER 2. SCANNING TUNNELING MICROSCOPY (STM) AND SPECTROSCOPY (STS)

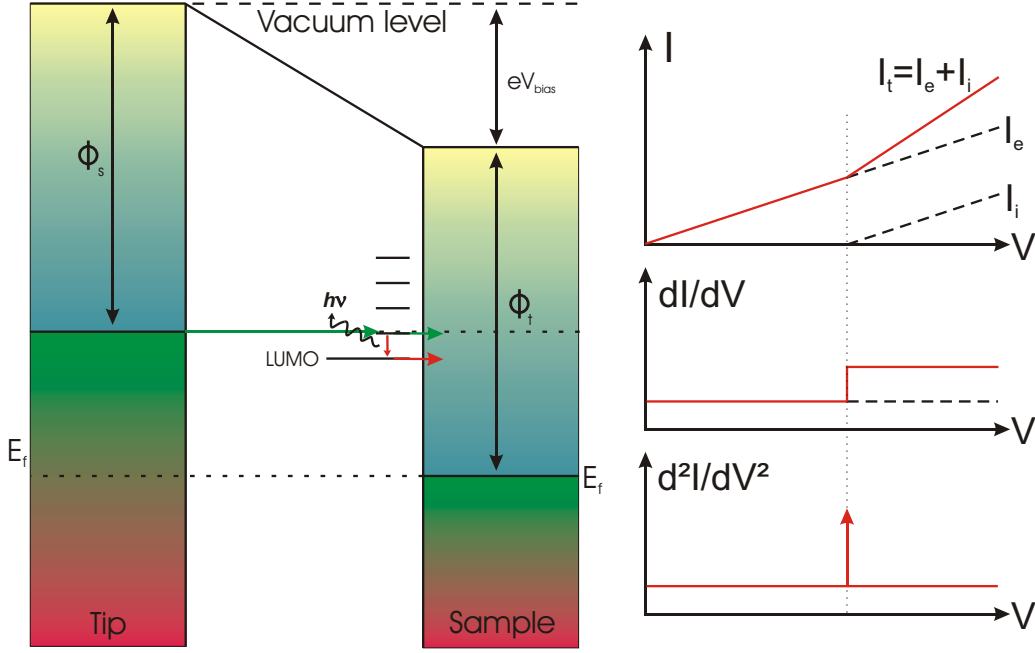


Figure 2.10: Inelastic electron tunneling process

second harmonic of the modulation ($2f$ mode):

$$\begin{aligned}
 & I n \times \sin(2\omega_{mod}t + \varphi_{ref}) = \\
 & - I''(eV) \frac{e^2 V_{mod}^2}{8} \sin(2\varphi - \varphi_{ref}) \\
 & + I'(eV) \frac{eV_{mod}}{2} \cos(\omega_{mod}t + \varphi - \varphi_{ref}) \\
 & + \left[I(eV) + I''(eV) \frac{e^2 V_{mod}^2}{4} + o(e^2 V_{mod}^2 \sin^2(\omega_{mod}t + \varphi)) \right] \sin(2\omega_{mod}t + \varphi_{ref}) \\
 & - I'(eV) \frac{eV_{mod}}{2} \cos(3\omega_{mod}t + \varphi + \varphi_{ref}) \\
 & + I''(eV) \frac{e^2 V_{mod}^2}{8} \sin(4\omega_{mod}t + 2\varphi + \varphi_{ref}) \\
 & + \frac{K}{2} [\cos((\omega_{noise} - 2\omega_{mod})t + (\varphi_{noise} - \varphi_{ref})) \\
 & \quad - \cos((\omega_{noise} + 2\omega_{mod})t + \varphi_{noise} + \varphi_{ref})] \tag{2.34}
 \end{aligned}$$

If $\omega_{noise} \neq 2\omega_{mod}$, the dc part of the signal is:

$$- I''(eV) \frac{e^2 V_{mod}^2}{8} \sin(2\varphi - \varphi_{ref}) \tag{2.35}$$

It is proportional to the second derivative of the tunnel current and can be isolated with a narrow low-pass filter. Again, the spectrum is convoluted with an “instrumental resolution function” [90] of width $fwhm = 1.22eV_{mod}$.

Lambe and Jackevic have also shown in 1968 [92] that the second derivative is broadened with a $fwhm = 5.44k_B T$ due to the spread of the electron energy distribution with the temperature. As a consequence, it is crucial to work at low temperature for IETS.

2.3.3 Current versus distance spectroscopy I(Z)

As seen in Equation (2.12), the current is exponentially dependent on the tip-sample distance. The decay constant K is related to the work function of the tip and the sample:

$$I \propto e^{-2Kd} \quad (2.36)$$

where $K = \sqrt{\frac{2m}{\hbar^2} \left(\frac{\Phi_{tip} + \Phi_{sample}}{2} - \frac{eV}{2} \right)}$

This spectroscopy mode is useful to identify the work function of the tip or the sample. In order to do it, the tip is immobilized over the surface and the feedback loop is opened. The tip-sample distance d is then ramped at a constant bias V and the tunnel current I is measured.

2.4 Conclusion

This chapter reviewed the underlying phenomena of Scanning Tunneling Microscopy and Scanning Tunneling Spectroscopy: the tunnel effect, which explains why a current can be established between two electrodes that are not in contact. The exponential dependence of this current against distance and its extreme localization make it possible to study surfaces at the atomic scale and even probe the density of states through the spectroscopic mode of the STM.

High resolution in energy can however only be reached at low temperatures. The following chapters will widely use the spectroscopic techniques described above to investigate the transport processes through different quantum confined systems put in an ultra-high vacuum environment, for cleanliness.

Chapter 3

STM induced point defects in Single-Walled Carbon Nanotubes

3.1 Introduction

Discovered in 1952 by Radushkevich and Lukyanovich [93] in time of the Cold War, in an article written in russian, carbon nanotubes, Fig. 3.1(a), did not have many assets for a worldwide distribution. For this reason, the report of Sumio Iijima in 1991 [94], Fig. 3.1(b), is often associated with the discovery of the Multi-Walled Carbon Nanotube (MWCNT) [97]. This article had a great impact as it gave the starting point for the development of one of the most famous bricks used in nanoscience. Only two years later, Iijima et al. [95], Fig. 3.1(c), and Bethune et al. [96], Fig. 3.1(d), both discovered the Single-Walled Carbon Nanotube (SWCNT) which is made of a single rolled up sheet of graphene. SWCNTs can be smaller than one nanometer in diameter and longer than a micrometer.

Owing to their unique aspect ratio, SWCNTs have attracted considerable attention in the study of transport across one-dimensional systems [94, 98, 99, 100]. They are good candidates for nano-electronic devices [101] as they can be either metallic or semiconducting. Unfortunately, it has not yet been possible to grow them selectively so far, preventing the preparation of a large set of similar devices for a given batch of SWCNTs.

As a result, the electronic properties of each SWCNT must be identified prior to their use in a device. One way to determine the properties of individual SWCNTs consists in placing them in the tunneling junction between a tip and a metallic surface in a STM. Such a configuration is sim-

CHAPTER 3. STM INDUCED POINT DEFECTS IN SINGLE-WALLED CARBON NANOTUBES

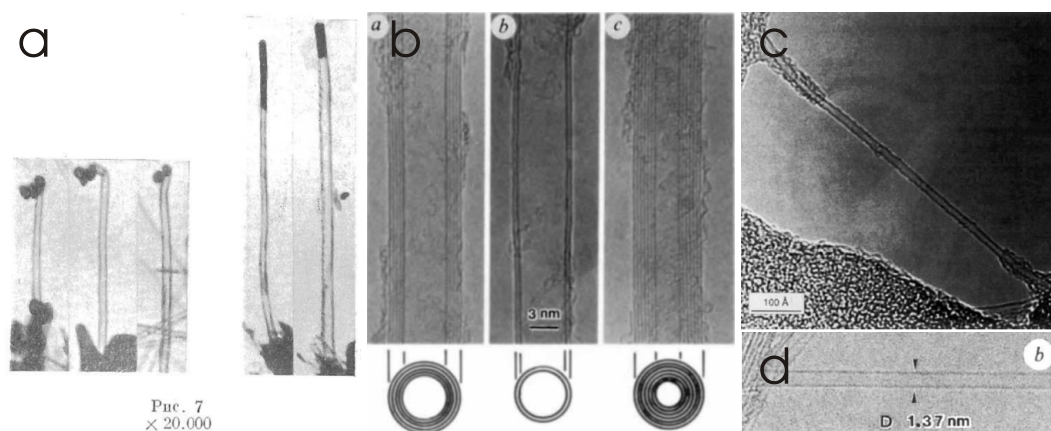


Figure 3.1: TEM observations (a) of the first Carbon Nanotubes (CNT) by Radushkevich and Lukyanovich [93] in 1952, (b) of the Multi-Walled CNT by Iijima in 1991 [94] and of the first SWCNT (c) by Iijima et al. [95] and (d) by Bethune et al. [96]

ilar to an asymmetric Double Barrier Tunnel Junction (DBTJ) where the barrier between the tip and the nanotube is much thicker than the barrier between the nanotube and the metallic contact. This method of identification has been used to study transport through SWCNTs and, depending on the length of the nanotube, it was possible to reveal standing waves [102, 103] or vibrationally assisted transport [78]. In this chapter, we will investigate the electronic properties of SWCNTs by Scanning Tunneling Spectroscopy (STS). We will show that we can indeed characterize the electronic structure of individual SWCNTs by STS when they are adsorbed on a gold surface. Furthermore, we will describe a method to selectively modify the electronic properties of semiconductor SWNTs by the creation and annihilation of point defects on their surface with a STM tip. The fabrication of the defects is detected from the measurements of the tip height variation, when the sample voltage is increased to a few volts maintaining the tunneling current constant. While spatially resolved tunneling spectroscopy reveals the formation of Stone-Wales defects, such defects can be removed by applying a similar voltage ramp, demonstrating the reversibility of the process.

3.1.1 Identification of SWCNTs and their electronic properties

A SWCNT is the result of rolling a graphene sheet up on itself in order to form a cylinder by connecting equivalent sites. The electronic properties of carbon nanotubes can therefore be derived from the properties of graphene and the way it is rolled up. Using tight-binding calculations allows a good

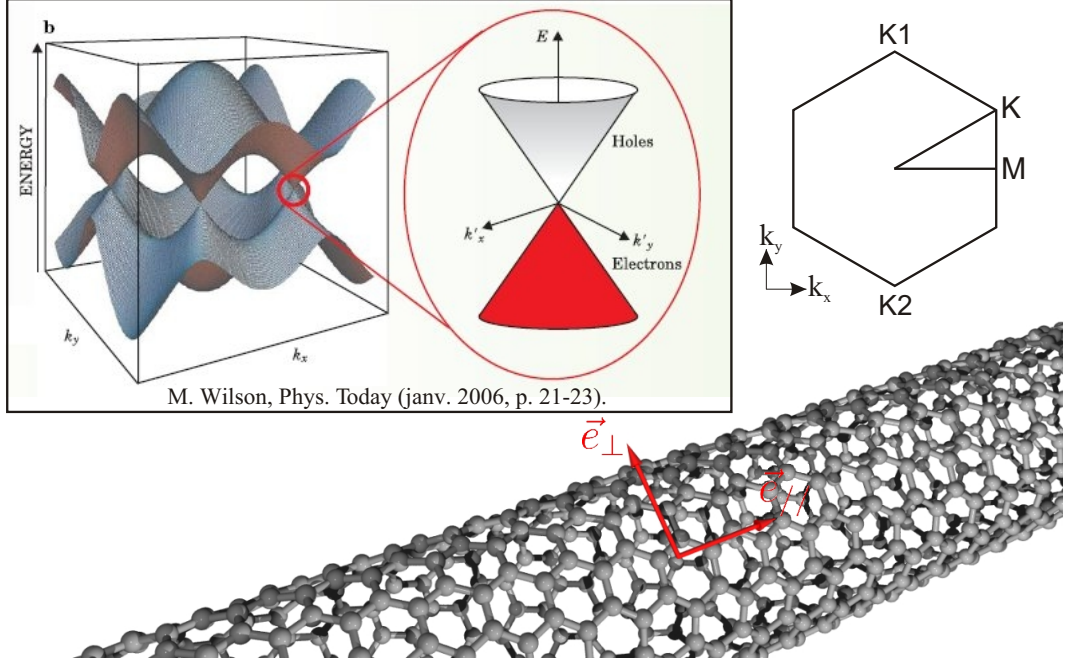


Figure 3.2: Tight-binding energy dispersion for graphene in its first Brillouin zone. The coordinates of K_1 and K_2 are $(k_x, k_y) = (0, \pm \frac{4\pi}{3})a^{-1}$ with $a = 2.46\text{\AA}$ the lattice constant.

understanding of their electrical nature [104] [105] [98] [106].

In graphene, the bonds between carbon atoms form a hexagonal lattice. Three of the four valence electrons of each carbon atom participate in the C-C σ bonding with sp_2 hybrid orbitals and the fourth electron carries a p_z orbital. The electronic interaction between these p_z orbitals leads to delocalized states responsible for the electrical conductivity of graphene. Such states are built from the linear combination of the p_z orbitals and the eigenenergies are written [107]:

$$E(k_x, k_y) = \pm \gamma_0 \left[1 + 4 \cos \left(\frac{\sqrt{3}k_x a}{2} \right) \cos \left(\frac{k_y a}{2} \right) + 4 \cos \left(\frac{k_y a}{2} \right)^2 \right]^{\frac{1}{2}} \quad (3.1)$$

where k_x and k_y are the x and y components of the wave vector \vec{k} , with $a = 2.46\text{\AA}$, the lattice constant and $\gamma_0 = 2.9\text{eV}$ is the C-C tight-binding overlap integral [108]. Fig. 3.2 shows this energy dispersion relation and the first Brillouin zone on the left. It is interesting to note that the conduction and valence bands are degenerate at every K-point of the Brillouin zone. At these points, around the Fermi level, the electronic states form a dispersion

CHAPTER 3. STM INDUCED POINT DEFECTS IN SINGLE-WALLED CARBON NANOTUBES

cone whose expression is:

$$E_K(\vec{k}) = \pm \frac{3\gamma_0 a_{C-C}}{2} |\vec{k}| \quad (3.2)$$

with $a_{C-C} = \frac{a}{\sqrt{3}}$, the nearest distance between two carbon neighbours.

Let us now consider a vector connecting two equivalent atoms of a graphene sheet such that $\vec{C} = n\vec{a}_1 + m\vec{a}_2$, with \vec{a}_1 and \vec{a}_2 the lattice vectors of graphene and (n, m) a pair of integers. If both ends of the vector \vec{C} are joined, the result is a carbon nanotube whose geometry is uniquely linked to the (n, m) couple. Regarding the electronic properties, this tubular geometry makes a periodic boundary condition that induces a quantization of the electron wavevector in the direction along \vec{C} .

The wavevector \vec{k} can be expressed with 2 components, one in the SWCNT's axis direction and the other transversal (see Fig. 3.2)

$$\vec{k} = k_{//}\vec{e}_{//} + k_{\perp}\vec{e}_{\perp} \quad (3.3)$$

Thus, the transverse part of the wavevector is quantized as follows:

$$k_{\perp}\vec{e}_{\perp} \cdot \vec{C} = 2\pi q \quad (3.4)$$

with q an integer.

The dispersion relation of SWCNTs thus forms a set of 1D sub-bands cut in the 2D dispersion relation of graphene. For a nanotube to be metallic, this set of sub-bands must pass through a K point of graphene. If $n - m$ is a multiple of 3, then the condition is fulfilled. Writing $n - m = 3q + p$, p being an integer, one obtains

$$k_{\perp}(p) = 2\pi \frac{(m - n)/3 + p}{\pi d} \quad (3.5)$$

where $\pi d = |\vec{C}|$ is the perimeter of the nanotube.

When the wavevector (eq. (3.3) with eq. (3.5)) is injected in the dispersion relation (3.2), one gets the 1D bandstructure of a SWCNT around E_F which is drawn in Fig. 3.3:

$$E_K(\vec{k}_{//}) = \pm \frac{3\gamma_0 a_{C-C}}{d} \sqrt{\left(\frac{m - n}{3} + p\right)^2 + \left(\frac{k_{//}d}{2}\right)^2} \quad (3.6)$$

- If $m - n$ is a multiple of 3, then the lowest 1D sub-bands are:

$$E_K(\vec{k}_{//}) = \pm \frac{3\gamma_0 a_{C-C}}{d} \left(\frac{k_{//}d}{2}\right) \quad (3.7)$$

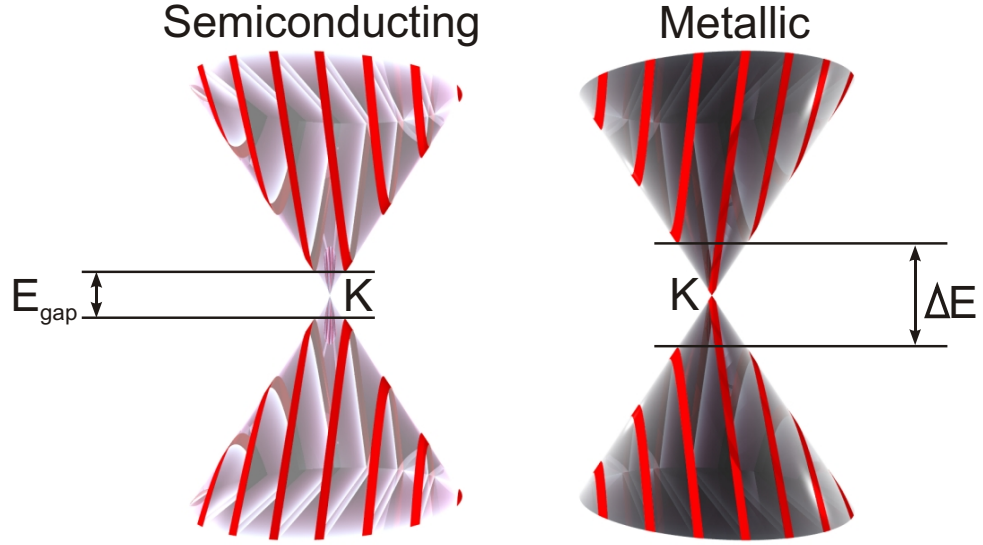


Figure 3.3: Energy dispersion relation of SWCNT around the point K at low energies. On the left, the nanotube is semiconducting because no 1D band (red stripes) crosses the K point. On the right, $m - n$ is a multiple of 3, the valence and conduction bands are degenerate in K: the nanotube is metallic.

but as they are degenerate in zero (the nanotube is metallic), one needs the second set of sub-bands:

$$E_K(\vec{k}_{//}) = \pm \frac{3\gamma_0 a_{C-C}}{d} \sqrt{1 + \left(\frac{k_{//}d}{2}\right)^2} \quad (3.8)$$

which define a low-conductivity zone between their extrema:

$$\Delta E = \frac{6\gamma_0 a_{C-C}}{d} \quad (3.9)$$

- If $m - n$ is not a multiple of 3, then the lowest 1D sub-bands are:

$$E_K(\vec{k}_{//}) = \pm \frac{3\gamma_0 a_{C-C}}{d} \sqrt{\left(\frac{1}{3}\right)^2 + \left(\frac{k_{//}d}{2}\right)^2} \quad (3.10)$$

Which give a semiconducting bandstructure with an energy gap of:

$$E_{gap} = \frac{2\gamma_0 a_{C-C}}{d} \quad (3.11)$$

Fig. 3.3 shows the difference between the metallic and the semiconducting bandstructure of SWCNTs. The extrema of the 1D sub-bands are called Van Hove singularities.

CHAPTER 3. STM INDUCED POINT DEFECTS IN SINGLE-WALLED CARBON NANOTUBES

In 1998, Odom et al. [109] and Wildöer et al. [110] demonstrated experimentally the link between the geometry of SWCNTs and their electronic properties by means of STM and STS. Thus they opened the way to study well defined systems.

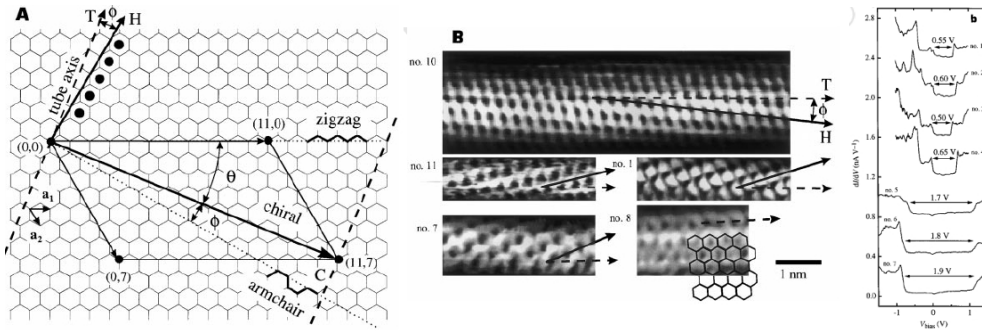


Figure 3.4: Explanations on the determination of the chiral vector of a SWCNT. Data taken from [110]

In fact, by STM, one measures the diameter d and the wrapping angle Φ that are equivalent to the (n, m) couple. d is deduced from STS by measuring the distance between the first Van Hove singularities (see expressions above) and Φ is determined by the topography images as shown in Fig. 3.4: Φ is the angle of the armchair direction compared to the CNT axis.

Because of the curvature of the CNT, the tip is not always over the atom it scans: the imaged atom is the closest one to the tip. As a result, the aspect of the nanotube seen by STM is deformed along its axis. Fig. 3.5 illustrates this distortion and shows that a factor can be applied in order to correct the tip-nanotube convolution [108].

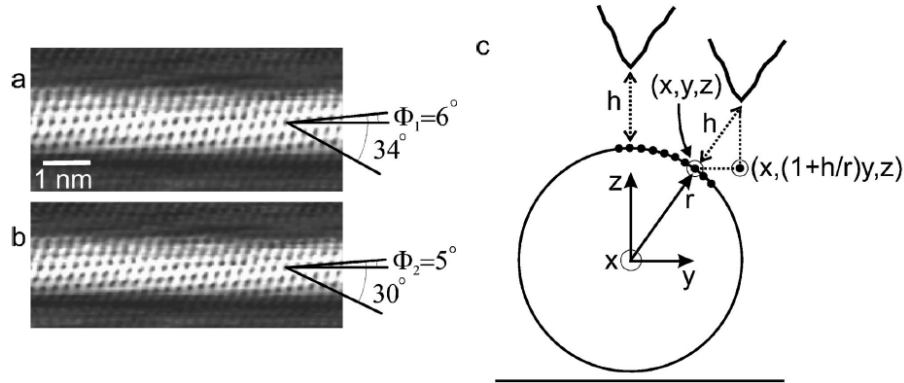


Figure 3.5: STM images of SWCNTs are distorted (a) because of the convolution between the shape of the tip and the nanotube. A factor can be applied on the direction perpendicular to the axis of the SWCNT to determine the true wrapping angle Φ . Data taken from Venema et al. [108]

3.1.2 Preparation of the samples

The experiments were conducted on single-walled carbon nanotubes (SWCNTs) deposited on Au(111) samples. We used electrochemically etched PtIr and W tips, cleaned in ultra-high vacuum (UHV) by heating and electron bombardment.

The gold samples are prepared as follows:

1. Mica sheets are carefully cleaved by hand and deposited on a copper plate. The copper plate is set into a High-Vacuum chamber (Base pressure $P = 1.10^{-6}T$) on a resistive heater. A shutter separates the samples from the gold evaporation source. The gold evaporation source is a basket made of a tungsten filament in which gold wires are put.
2. The temperature of the mica sheets (future samples) is set to $350^{\circ}C$, it is measured thanks to a Cr-Al thermocouple. The evaporation source is degassed while the shutter is kept closed.
3. A quartz micro-balance measures the evaporation rate. Once it is stable (1nm/min), the shutter is opened and left open for one hour.
4. The shutter is closed, the evaporation source is stopped. The samples are left one more hour at $350^{\circ}C$ for a better Au(111) surface morphology.
5. The samples are taken out in air and annealed with a H_2 flame.

HiPCO [111] SWCNTs dissolved in chloroform and 1-2-dichloroethane were used at a concentration of $1\mu\text{g}/10\text{mL}$, the solution was ultrasonicated

CHAPTER 3. STM INDUCED POINT DEFECTS IN SINGLE-WALLED CARBON NANOTUBES

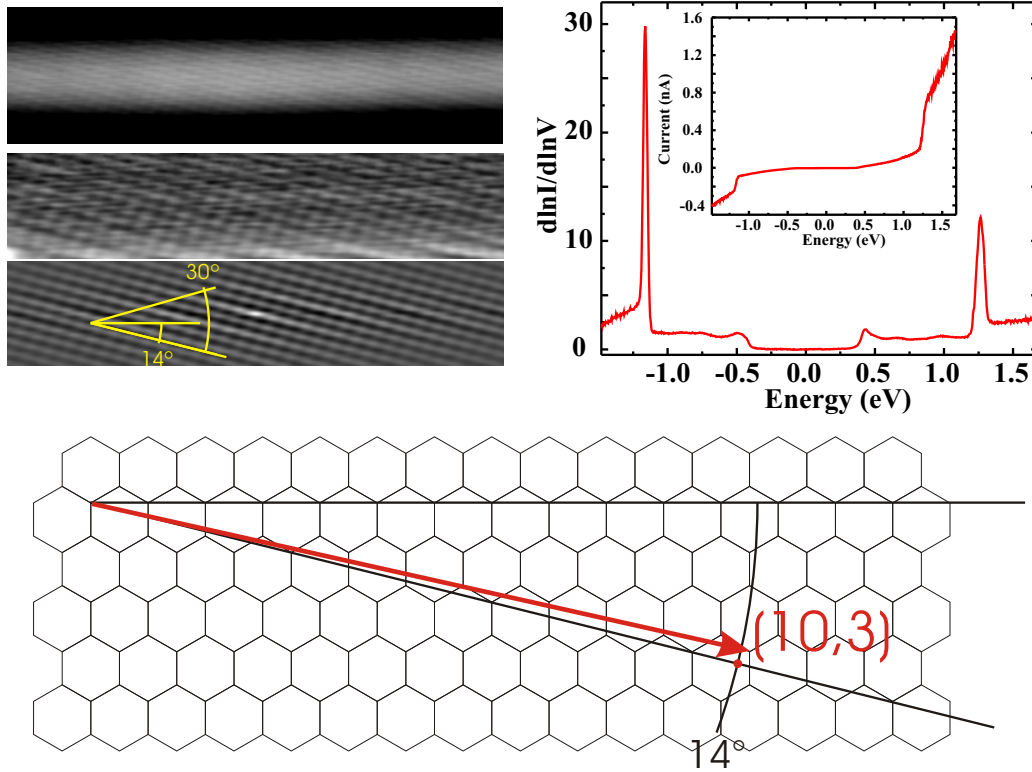


Figure 3.6: Top left: STM image of a SWCNT deposited on Au(111) ($10 \times 2.5 \text{ nm}^2$, $V_{bias} = -0.5 \text{ V}$; $I_{tunnel} = 100 \text{ pA}$, $T = 4 \text{ K}$); Middle left: zoom on the top of the CNT; Lower left: high pass filtered image corresponding to the zoomed area on top of the SWCNT in order to unambiguously identify the wrapping angle: $\Phi = 14^\circ$. The measured angle of 30° shows that the lattice of the SWCNT is not distorted (see Fig. 3.5); Top right: spectroscopy on the same SWCNT ($f_{lock-in} = 1 \text{ kHz}$, $V_{osc} = 10 \text{ mV rms}$) shows the 1D transport properties of the nanotube. The first Van-Hove singularities give the energy gap $E_{gap} = 0.9 \text{ eV}$ and thus the diameter is deduced $d = 0.92 \text{ nm}$; Bottom: The wrapping angle and the perimeter are drawn on a graphene lattice in order to measure the (n, m) coordinates of the nanotube. The red dot indicates the measured coordinates and the red arrows is the most probable chiral vector which corresponds to a $(10, 3)$ SWCNT. This nanotube is semiconducting.

for more than one hour in order to obtain individual nanotubes. After ultrasonication, one drop was deposited by spin coating on the freshly prepared and annealed Au(111) sample. The samples were then introduced into UHV and degassed before the experiments.

3.1.3 Identification of SWCNT atomic structure

The SWCNTs deposited on the sample were characterized by STM following the method described above. Fig. 3.6 shows a STM image of a SWCNT to be identified. The differential conductance curve against energy is zero around the Fermi level energy. So it shows that the nanotube is semiconduct-

3.2 Creation and removal of defects on SWCNTs

ing. As seen previously, the energy gap is formed by the separation between the first 1D sub-bands and its width is in our case $0.9eV$. This characteristics corresponds to a SWCNT with a diameter $d = 0.92nm$. The chiral angle has also been measured: $\Phi = 14^\circ$. The couple (d, Φ) can be linked to the (n, m) indices of the SWCNT as they both define the chiral vector in different coordinate systems. The chiral vector has been drawn on an hexagonal lattice thanks to (d, Φ) , Fig. 3.6, and corresponds to $(n, m) = (10, 3)$. The value of $m - n$, not multiple of 3, confirms that the nanotube is semiconducting.

Thus the system Au(111)/SWCNT/STM Tip is an example of double barrier tunnel junction DBTJ. In this case, the frontier between the nanotube and the gold surface is very thin. As a result, the potential of the sample can be considered the same in the SWCNT. Since the value of the current around 0V is zero and the STS measurements reveal the 1D character of the SWCNT, the coupling of the nanotube states with the surface states of gold can be considered weak. As a result, if a localized state is created in the nanotube, associated with a point defect for example, this state will be decoupled from the gold surface states and could be investigated by scanning tunneling spectroscopy.

3.2 Creation and removal of defects on SWCNTs

The experimental procedure to create a defect on the surface of a SWCNT is sketched in Fig. 3.7(a) and can be described as follow: after having identified the geometric properties of a CNT from its wrapping angle and its energy gap (for semiconducting CNTs) or low-conductivity zone (for metallic CNTs) [108] the STM tip is immobilized on a defect-free location on the SWCNT. A voltage ramp is additionally applied on the sample bias used to image a SWCNT as shown by the curve labeled V_{bias} . The typical sweep time is $0.1s/V$. During the voltage ramp, the feedback loop is kept closed and as a result, the tip-sample distance Z increases in order to keep the tunneling current I_{tunnel} constant. At certain bias, a sharp step appears on Z indicating an additional backward shift of the tip from the nanotube. This step is the response of the piezo controlling the tip height to a pulse observed in the tunneling current while the sample voltage increases. After the voltage sweep, the tip starts again scanning the nanotube. Fig. 3.7 (b) shows the modification of the nanotube when a negative sample voltage ramped is applied to a defect-free SWCNT. At a voltage of $-5.8 V$, an abrupt change in the linear behaviour of the $Z(V)$ curve occurs. After this event, a deforma-

CHAPTER 3. STM INDUCED POINT DEFECTS IN SINGLE-WALLED CARBON NANOTUBES

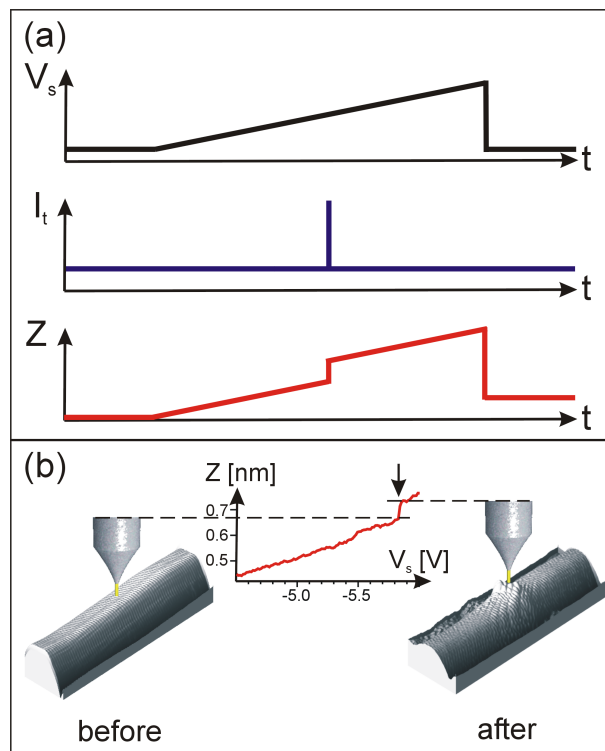


Figure 3.7: (a) Experimental scheme used to create a defect on a SWNT. The STM tip is first immobilized over a defect-free position at the surface of a SWNT. While maintaining the feedback loop close (I_{tunnel} constant), the sample voltage V_{bias} is usually ramped up to $\pm 8V$ and both the tunneling current I_{tunnel} and the tip height Z are recorded. At the time of the defect creation, a sharp peak occurs on the tunneling current as well as a sudden retraction of the tip away from the surface. (b) STM images of a SWNT before and after the defect creation along with a portion of the experimental $Z(V)$ curve showing a sudden backward shift of the tip, signature of the defect creation (Feedback parameters : $V_{bias} = -0.4V$, $I_{tunnel} = 200pA$, $T = 4K$). This retraction of the tip is indicated by a vertical arrow.

3.2 Creation and removal of defects on SWCNTs

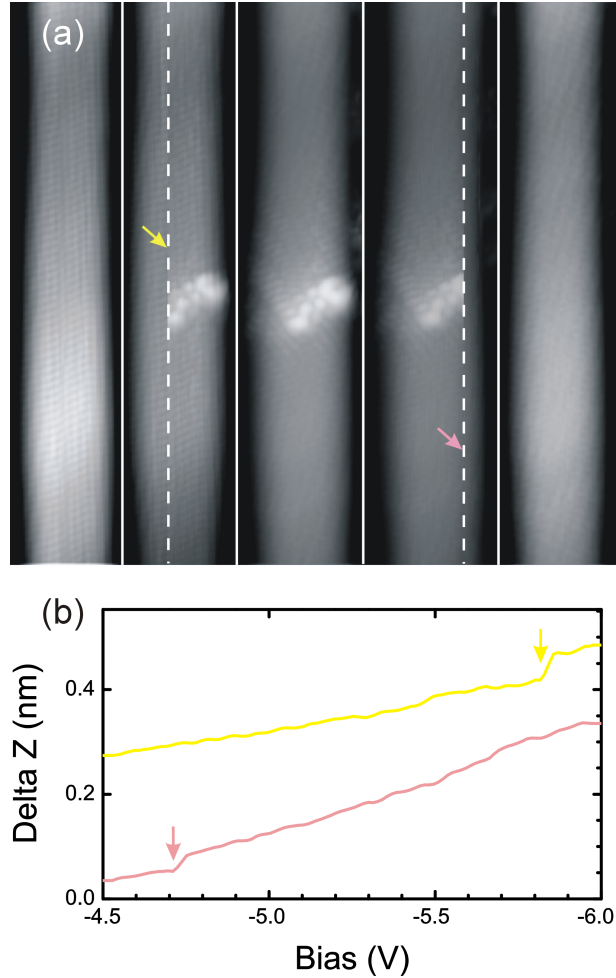


Figure 3.8: (a) from left to right: series of successive STM topography images ($3.3 \times 16 \text{ nm}^2$, $V_{bias} = -0.4 \text{ V}$; $I_{tunnel} = 200 \text{ pA}$) taken at 4K at the same place on a (9,5) CNT before the creation of a defect, during the creation of the defect, with the created defect, during the removal of the defect and after the annihilation of the defect. The scan direction for each image is from left to right. The dashed lines and the arrows indicate respectively when and where the voltage ramp was applied during scanning. (b) Portion of $Z(V)$ curves showing the characteristic step, indicated by a vertical arrow, and related to the local modification of the SWCNT. The upper curve (yellow) corresponds to the voltage ramp used for the creation of the defect, the lower one (pink) for its annihilation.

tion on the nanotube wall is clearly visible at the position where the voltage ramp was performed.

A similar protrusion is better seen in Fig. 3.8(a), where the same method was applied. In this example, a defect-free nanotube is first imaged and the voltage ramp is then turned on (upper curve in Fig. 3.8(b)). After the voltage is reset to its initial value, a protrusion is visible in the middle of the nanotube. The protrusion structure consists of a pattern superimposed to the nanotube lattice, with a shape resembling those observed by STM images

CHAPTER 3. STM INDUCED POINT DEFECTS IN SINGLE-WALLED CARBON NANOTUBES

for point defects found on the wall of SWCNTs. By applying a second voltage ramp to the nanotube, the protrusion disappears. Although the characteristic step in the $Z(V)$ curve does not occur at the same voltage used for the creation of the protrusion, the nanotube recovers its initial crystallographic structure, as shown in the last STM image of Fig. 3.8(a). Interestingly, the example in Fig. 3.8 illustrates that the creation or removal of a defect does not always occur at the position where the voltage sweep is applied, but a few nanometer apart.

3.3 Identification of the defect

Although the voltage onset to create or annihilate the protrusion varies from one nanotube to another, the local modification of the SWCNT has been found to be independent of the tip and the conformation of the nanotube. From these results, we suggest that the protrusion involves only materials from the nanotube and that the number of atoms of defect-containing and defect-free CNTs must be the same. In other words, the defect is not a result of the removal of some carbon atoms from the nanotube neither a result of the adsorption of some gas molecules or the release of adsorbate from the tip onto the side wall of the nanotube. Therefore, we attribute the protrusion to a point defect such as a Stone-Wales defect [112] or a vacancy-adatom defect [113].

Because the STM topographic images are the convolution between topography and multiple electronic effects including the scattering induced by a defect on the CNT [114], it is hardly possible to directly identify the atomic structure of a defect from the STM image alone. In order to determine the nature of the defects, spatially resolved spectroscopic measurements were therefore performed on SWCNTs and the results are shown in Fig. 3.9 for the nanotube observed in Fig. 3.8. Fig. 3.9(a) shows the differential conductance image at 0.4 V in the area of the defect. To get a better insight into the local variation of the SWCNT electronic structure, the variations of the differential conductance are plotted as a function of the voltage along a line running through the defect. As seen in Fig. 3.9(b), while the band gap of the nanotube is measured to be 1.13eV in the defect-free region deduced from most external horizontal dashed lines, the dI/dV profile measured on the defect clearly shows intense signal in the bandgap region of the nanotube at energies of at -0.45eV and at +0.26eV. Those peaks, visible in Fig. 3.9(c) are quite localized along the main axis of the nanotube and attributed to the defect states. The electronic structure of the defect agrees very well with a Stone-Wales defect that has heptagon donors and pentagon acceptors [115].

3.3 Identification of the defect

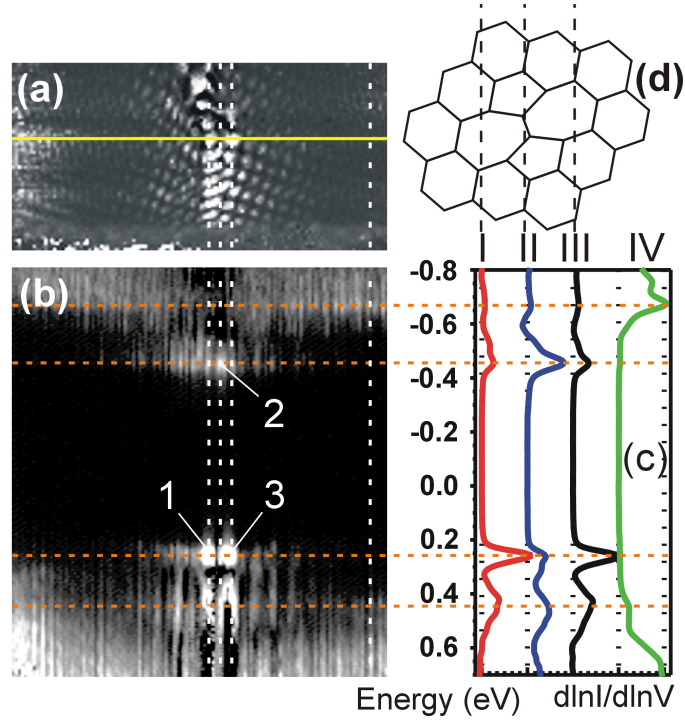


Figure 3.9: (a) dI/dV image ($f_{lock-in} = 1kHz$, $V_{osc} = 10mV_{rms}$) acquired at $V_{bias} = +0.4V$ on the defect of the SWCNT shown in Fig. 3.8. The image is rotated by 90° with respect to the STM images of Fig. 3.8. Feedback parameters $V_{bias} = -0.9V$, $I_t = 200pA$, $T = 4K$. Image size : $10nm \times 5nm$. (b) Spatial variation of dI/dV as a function of the sample voltage acquired along the horizontal line in (a). The four horizontal dashed lines indicate characteristic energy positions in the dI/dV curves: the upper and lower ones correspond to the band gap of the nanotube and the line in between corresponding to the defect states (areas 1, 2 and 3); (c) dI/dV curves corresponding respectively to the four vertical dashed lines running through the defect states (I to III from left to right) and a defect-free region (IV - upmost to the right) in (a) and (b).

Three orientations are possible for the defect as shown in Fig. 3.10. From the grid of the dI/dV curve with respect to the orientation of the nanotube, we deduce the most probable orientation for the defect in Fig. 3.9(d). This orientation is consistent with the theoretical pictures shown in Ref. [116].

CHAPTER 3. STM INDUCED POINT DEFECTS IN SINGLE-WALLED CARBON NANOTUBES

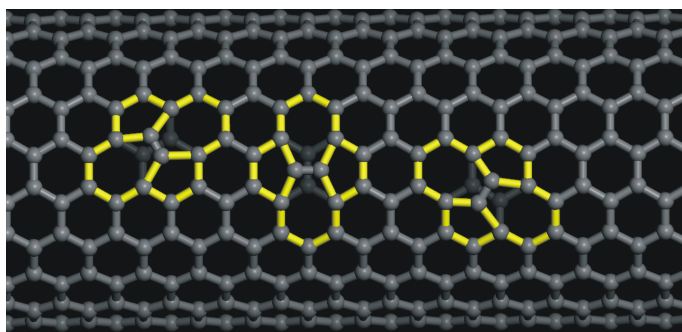


Figure 3.10: Schematics of the three possible orientations of a Stone-Wales defect on a CNT.

3.4 Statistics of the defect creation and annihilation

We have observed that the Stone-Wales defects are stable for days if we do not apply a second voltage sweep to the nanotube and that it did not disappear due to thermal fluctuations event at RT. To further understand the creation and annihilation reaction discussed above, we examined the voltage dependence of the reaction rates. For this purpose, similar voltage ramps were applied on many nanotubes with different STM tips. The sample bias was swept from $\pm 1.0V$ to $\pm 8.0V$ with increasing absolute value of the bias voltage in 1.2 second. During the voltage ramp, the tip-sample distance was feedback-controlled with the reference tunnel current at 1.0 nA. All experiments were performed at 77K. The histograms of the voltage onsets at which the creation or annihilation events occur are shown in Fig. 3.11.

In this figure, the observed points scattered over a wide range of bias voltages, in particular, for the creation reaction. Since there is no clear voltage threshold or sharp peak, the creation and removal of a defect is not related to a resonant electronic excitation of a carbon bond just under the tip. This is confirmed by the observation of defects created or removed far away from the tip. Although we do not know the mechanism(s) at the origin of their formation or annihilation, we can compare these thresholds to the energies used by other techniques to induce point defects in SWCNTs.

The energy for the removal of a carbon atom from a SWCNT is estimated to be 10 to 20 eV [117]. Moreover, usually, for an accelerated electron to give this amount of energy to a CNT, electrons must be accelerated up to 100 keV [117]. In contrast, the amount of energy needed to rotate the bond to form a Stone-Wales defect is compatible with our experiments. Indeed, the energy barrier for the rotation of a C-C bond on graphene is expected to be

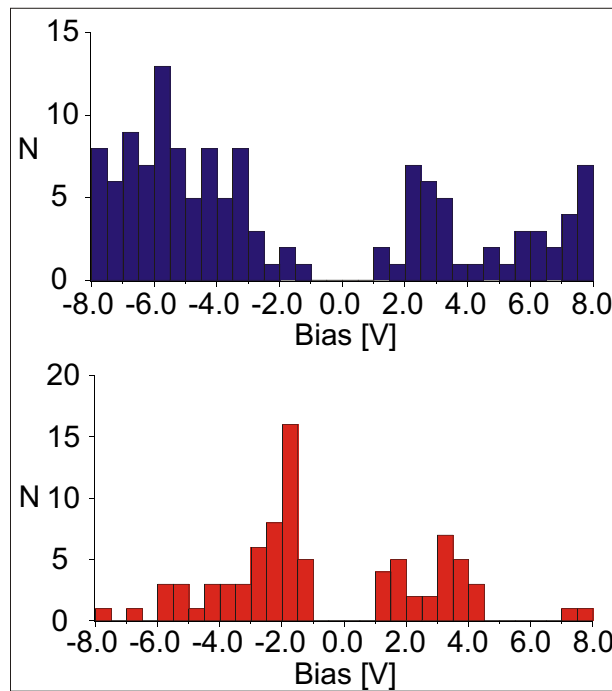


Figure 3.11: Upper and lower histograms: numbers of creation and annihilation events, respectively, with respect to the voltage bias

between 6 and 7eV [118], [119]. Since CNTs are rolled-up graphene sheets, the energy needed for the same action on a CNT may be lowered because of a curvature-induced strain [119] [120], which is consistent with the obtained results.

3.5 Conclusion

We have shown that we can not only probe the electronic structure of Single-Walled Carbon Nanotubes by Scanning Tunneling Spectroscopy but also the electronic structure of point defects. The type of defect that we created has been identified as a Stone-Wales defect, and was created via the rotation of C-C bonds on the wall of the CNT. Our method to create point defects is efficient and reproducible, and spectroscopic data clearly shows how the gap of the CNTs was tuned. Because the two states (defect-including; defect-free) are stable, such a technique opens the way for the creation of molecular switches based on the use of SWCNTs in a Double Barrier Tunnel Junction configuration. The advantage of this technique is that the conductivity of the device can be tuned by voltage pulses applied on one electrode with the hope that a true gate could replace the STM tip

CHAPTER 3. STM INDUCED POINT DEFECTS IN SINGLE-WALLED CARBON NANOTUBES

to create or annihilate the point defect.

Chapter 4

Running current through an isolated localized state in silicon

4.1 Introduction

In our study of electronic transport through isolated quantum objects, electron transport through a Double Barrier Tunneling Junction (DBTJ) made of a molecule placed between two metallic electrodes, a gold sample and a tungsten tip, was previously investigated (cf Fig. 4.1(left)). The molecule used was a Single Walled Carbon Nanotube, whose characteristic 1D transport property clearly influenced the flow of electrons from one electrode to the other one. Indeed, metallic electrodes are perfect to investigate resonant electronic transport through DBTJ setups: when the Fermi level of one electrode enters in resonance with an electronic state of the nanostructure this state acts as a bridge that carries the electrons to the empty states of the other electrode. Nevertheless, the efficiency of resonant transport has its drawback: it makes difficult to study inelastic processes which inherently take part into the transport but have a small contribution. For example, the characterization of inelastic processes in the transport through a single point defect in the SWCNT could give us the opportunity to understand the generation or annihilation of the defects in single-walled carbon nanotubes.

Thus, if one wishes to significantly alter the elastic transport, the DBTJ should be designed with at least one electrode being partially insulating. A semiconducting material can be used for example, in order that no electron can cross the DBTJ if its energy is below a certain value called the bandgap energy.

CHAPTER 4. RUNNING CURRENT THROUGH AN ISOLATED LOCALIZED STATE IN SILICON

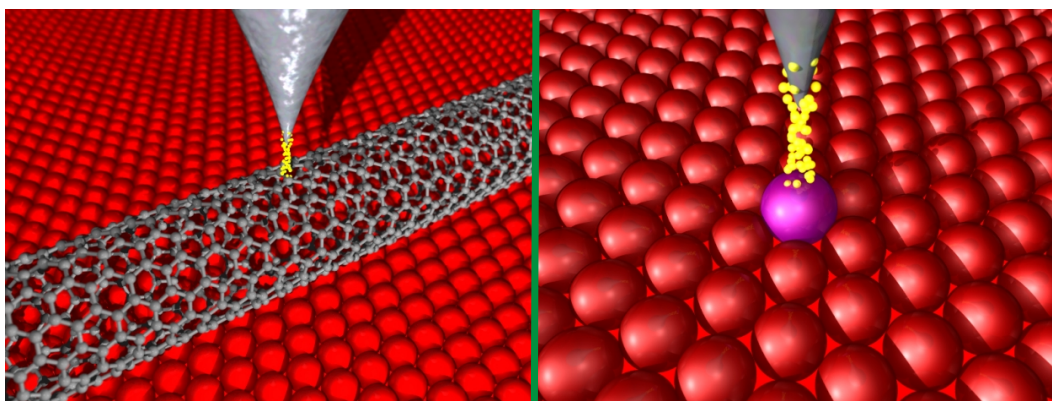


Figure 4.1: Scanning tunneling microscopy experiments on nanostructures: (left) on a single-walled carbon nanotube, (right) on a single atom

As a consequence, an electron transferred by the metallic electrode to a nanostructure bearing an electronic state energetically localized within the bandgap of the other electrode will have no other choice than staying in the nanostructure until it finds a way to relax. The electron can gain an amount of energy, by the absorption of light –photons– for instance, that helps it to finally tunnel into the empty states of the semiconducting electrode.

Another possibility is the recombination of the electron with a hole of the nanostructure, leading to the emission of a certain quantity of light or vibrations. The latter case will be the subject of our investigations in the present chapter. The gold electrode of the previous chapter will therefore be replaced by a silicon electrode, which is the most commonly used semiconducting material.

In this chapter, we will see that the (111) surface of silicon, bearing one Dangling Bond (DB) for each surface atom, can be almost perfectly passivated. Almost, but not entirely: a small residual concentration of defects, holding unpassivated DB states lying in the bandgap of the semiconductor (cf Fig. 4.1(right)), are able to support currents higher than the nano-Ampere! We will therefore take advantage of the atomic resolution provided by the Low Temperature STM to understand the transport mechanism through a single atom on silicon.

4.2 Electronic structure of the $\text{Si}(111)-(\sqrt{3} \times \sqrt{3})R30^\circ\text{-B}$ surface

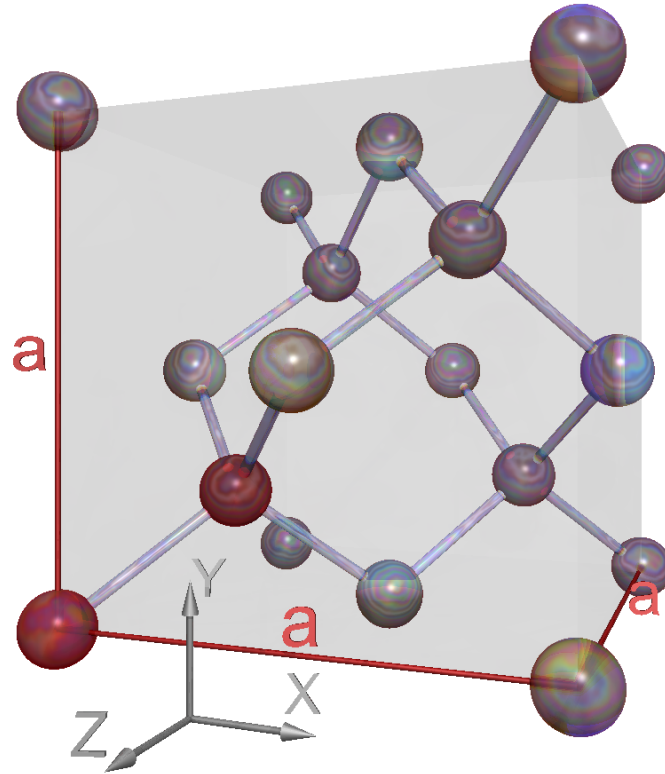


Figure 4.2: Crystalline Diamond structure of Silicon. It is made of two face-centered cubic (fcc) lattices translated of $a \frac{\sqrt{3}}{4} = 235\text{pm}$ ($a = 543\text{pm}$) in the direction of the main diagonal of the cube. The two red atoms in the lower left corner represent the base cell of the crystal.

4.2 Electronic structure of the $\text{Si}(111)-(\sqrt{3} \times \sqrt{3})R30^\circ\text{-B}$ surface

4.2.1 The Silicon(111) surface

Silicon is the second most abundant element on earth's surface after oxygen. It is not found naturally pure but mostly on the form of silicon dioxide, SiO_2 . It is the most used material for semiconductor devices because it is stable at high temperature and also because silicon dioxide is easily grown on it and is a good dielectric.

For use in electronic devices, the material is purified and crystallized in order to obtain a pure silicon monocrystal. Crystalline silicon has a diamond

CHAPTER 4. RUNNING CURRENT THROUGH AN ISOLATED LOCALIZED STATE IN SILICON

structure, with a lattice parameter of $a = 543\text{pm}$ (see Fig. 4.2).

The diamond structure is made of two intricately fcc lattices, one at the origin and the second shifted by $\left(\frac{a}{4}, \frac{a}{4}, \frac{a}{4}\right)$ as can be seen in fig 4.2 in the lower left corner. The distance between these two atoms is thus $a\frac{\sqrt{3}}{4} = 235\text{pm}$.

4.2.2 Reconstructions of the Si(111) surface

When the (111) surface of silicon is cleaved in UHV, it naturally forms the 2×1 reconstruction [121] [122]. This reconstruction was imaged in 1986 by Stroscio et al. [123] but is not stable at high temperature, where it becomes the well known 7×7 reconstruction, imaged in the early times of STM by Binnig et al. [4].

Though 7×7 reconstruction is the most common reconstruction of Si(111), the presence of Boron dopants at a high concentration induces a $(\sqrt{3} \times \sqrt{3})R30^\circ$ reconstruction. The first observation of this reconstruction was made by RHEED [124].

The unreconstructed Si(111) surface is made of two layers as seen in Fig. 4.3, all the atoms of the top layer bear an unpassivated Dangling Bond (DB). When a Boron-doped silicon crystal is heated, the dopants migrate and stabilize in the subsurface layer at the substitutional position S_5 [125] until saturation occurs, at $1/3$ ML, as seen in Fig. 4.3. The surface has two preferred adsorption sites: a threefold hollow site H_3 and a threefold occupied site T_4 , which is on top of a subsurface atom. In our case, silicon adatoms adsorb at the T_4 position where they passivate the three underneath Si DB. This process leads to charge transfer from the Si adatoms to the substitutional B atoms, making the last adatom's DB state passivated [126]. Silicon atoms form a new surface layer on top of the Boron atoms with the so-called Si(111)- $(\sqrt{3} \times \sqrt{3})R30^\circ$ -B reconstruction.

4.2 Electronic structure of the $\text{Si}(111)-(\sqrt{3} \times \sqrt{3})R30^\circ\text{-B}$ surface

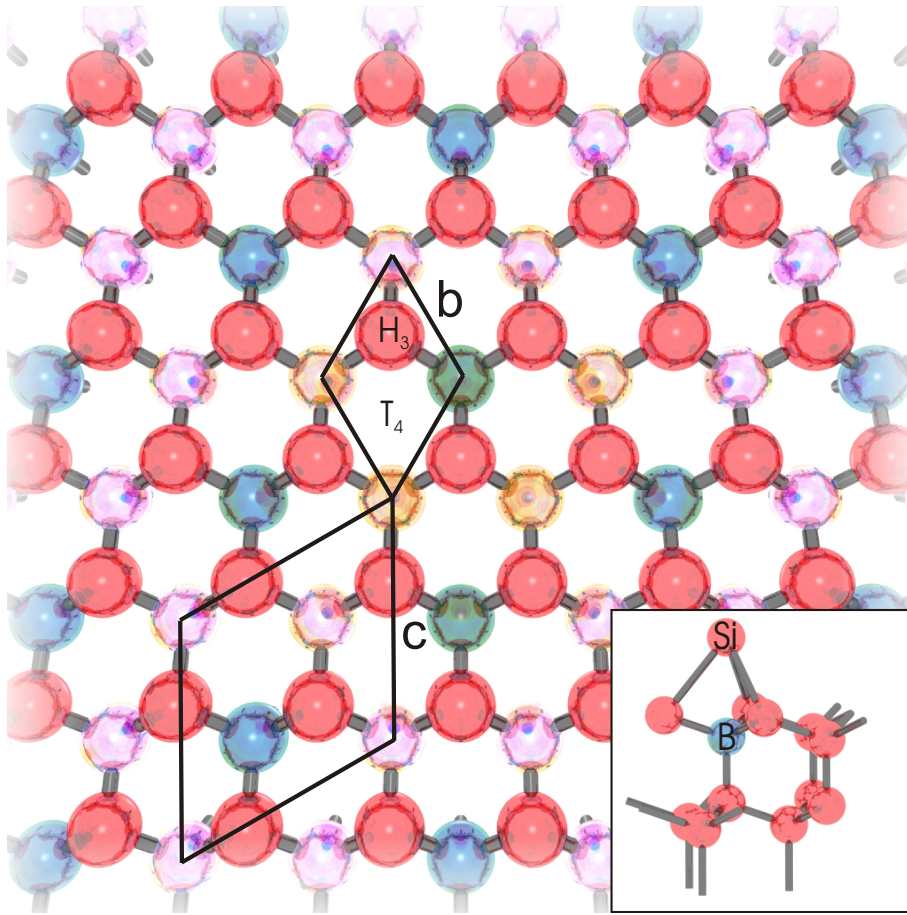


Figure 4.3: Top view of the unreconstructed $\text{Si}(111)$ surface. The (111) surface is made of two layers presented here with three different colors. The red atoms form the top layer whereas the pink and blue ones form a subsurface layer. The small rhombus delimits the primitive mesh of the surface which has two preferred adsorption sites called H_3 and T_4 . The distance between two atoms of the same layer is $b = a\frac{\sqrt{2}}{2} = 384\text{pm}$, with $a = 543\text{pm}$ the lattice parameter of bulk silicon. The blue atoms indicate which substitutional sites can be occupied by Boron atoms when the reconstruction $\text{Si}(111)-(\sqrt{3} \times \sqrt{3})R30^\circ\text{-B}$ is formed, these positions are usually labeled S_5 . The large rhombus indicates the primitive mesh of this reconstruction, it is rotated of 30° compared to the cell of the unreconstructed $\text{Si}(111)$ and one side measures $c = b\sqrt{3} = 665\text{pm}$. The Bottom right image shows a perspective view of one cell of the reconstructed $\text{Si}(111)-(\sqrt{3} \times \sqrt{3})R30^\circ\text{-B}$ with the surface silicon adatom labeled Si and the Boron substitutional atom labeled B. All the other atoms are silicon.

4.2.3 Sample preparation

The sample preparation is done by heating the sample by Joule effect (a dc current is established through the sample) with the following sequence, the temperature being checked by a pyrometer:

1. The sample is slowly heated to 950°C in 12h with a pressure kept lower than $5 \times 10^{-10}\text{T}$. This step aims at degassing the sample and removing the native oxide layer;

CHAPTER 4. RUNNING CURRENT THROUGH AN ISOLATED LOCALIZED STATE IN SILICON

2. Several flashes at $1220^{\circ}C$ for 5 seconds are done in order to remove Carbon contaminants and to reconstruct the surface;
3. The temperature is kept at $950^{\circ}C$ for several hours in order to allow the segregation of Boron dopants to the surface;
4. The temperature is slowly decreased from $950^{\circ}C$ to $700^{\circ}C$ in 2h in order to keep a sufficient adatom mobility during the reconstruction of the surface. After this step, the temperature can be decreased faster.

By controlling the duration of the third step, the number of substitutional B atoms can be tuned. In the following, we will only concentrate on the case where an almost saturation of the S_5 sites is reached, so that only a few sites without B atom are left.

4.2.4 The Si(111)- $(\sqrt{3} \times \sqrt{3})R30^{\circ}$ -B surface investigated by STM

Fig. 4.4 shows a constant-current STM image of a B-doped Si(111) surface with the characteristic $(\sqrt{3} \times \sqrt{3})R30^{\circ}$ reconstruction. Even though the 30° rotation of the lattice compared to Si(111) cannot be verified by STM, the distance between two surface adatoms is clearly consistent with the $(\sqrt{3} \times \sqrt{3})$ as we measure in the three directions a mean separation of $0.671nm$, $0.657nm$ and $0.660nm$, where the theoretical value is $a\frac{\sqrt{2}}{2} \times \sqrt{3} = 0.665nm$. The unreconstructed Si(111) network from Fig. 4.3 has been superimposed on the STM image, it represents the subsurface layer with the Boron atoms situated in position T4, directly under the surface silicon adatoms.

In order to unambiguously identify the nature of the surface, Scanning Tunneling Spectroscopy (STS) was done on the adatoms.

Fig 4.5 shows the spectrum acquired above a dark adatom site, it presents the Fermi level E_F positioned close to the top of the valence band, consistent a p-type semiconductor. Two distinct features demonstrate that the adatoms are electronically passivated silicon Dangling Bonds (DB):

- The occurrence of a 1.3 eV gap;
- The presence of a strong peak positioned 0.4 eV above the bottom of the conduction band (CB) marked with an arrow. Indeed, Fig. 4.6 shows the electronic structure of the surface from concurring experimental and simulated data by Higashiyama et al. [127], Grehk et al. [128] and Shi et al. [125]: an unoccupied surface state (open and square triangles) is lying $0.4eV$ above the minimum of the conduction band at

4.2 Electronic structure of the Si(111)-($\sqrt{3} \times \sqrt{3}$)R30°-B surface

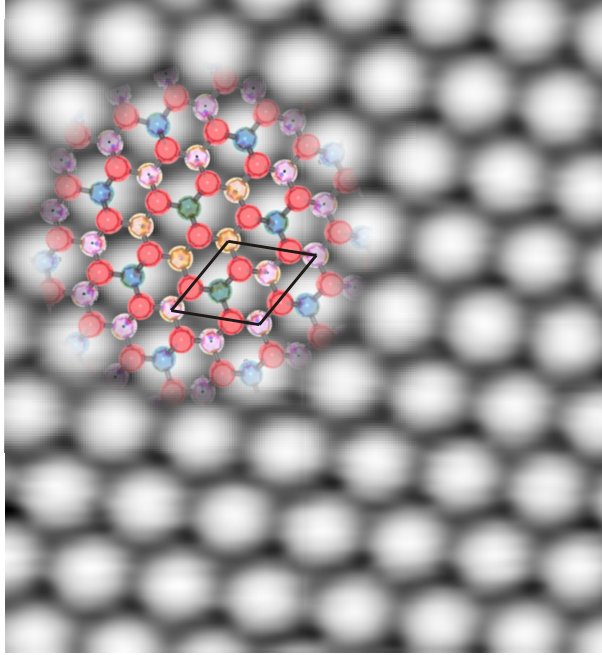


Figure 4.4: Visualization of the Si(111)-($\sqrt{3} \times \sqrt{3}$)R30°-B surface observed at 5 K. $V_{bias} = 1.5V$, $I_{tunnel} = 1nA$, $4.6 \times 5.0nm^2$. On the upper left corner, the unreconstructed Si(111) network from Fig. 4.3 has been superimposed and the primitive mesh is indicated by a rhombus.

the Γ point, region of the k-space where STM is the most sensitive. The peak measured in Fig. 4.5 is thus in agreement with the formation of an unoccupied band resonant with the conduction band due to charge transfer from Si to B [128].

4.2.5 Conclusion

We have seen that the Si(111)-($\sqrt{3} \times \sqrt{3}$)R30°-B surface forms a semi-conducting surface with a gap of $1.3eV$ free of electronic states, with a Fermi energy corresponding to the top of the valence band, consistent with a highly doped p-type semiconductor. Indeed, segregation of the boron dopants during the sample preparation passivates all the surface dangling bonds of the unreconstructed Si(111) surface and the metallic character of the surface is annihilated.

We will see in the next part that this property is crucial to our study since it allows to measure the concentration of dopants several layers below the surface.

CHAPTER 4. RUNNING CURRENT THROUGH AN ISOLATED LOCALIZED STATE IN SILICON

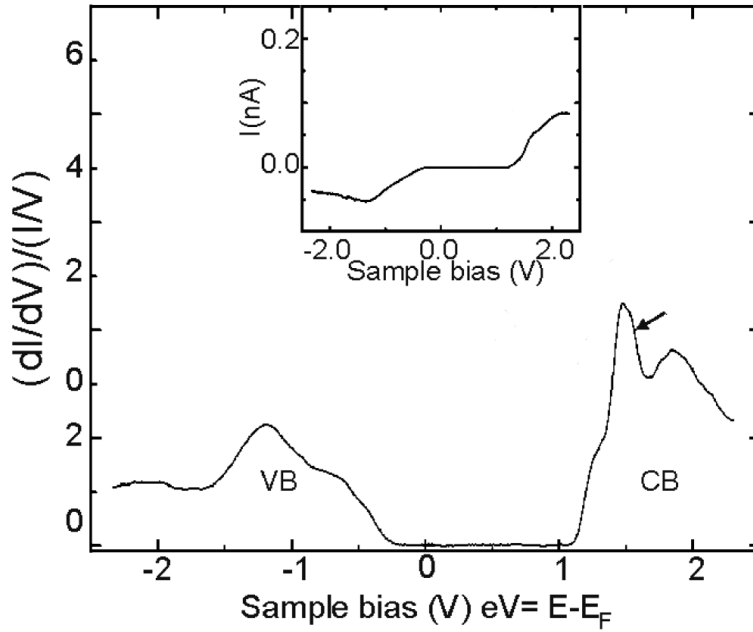


Figure 4.5: Normalized conductivity spectra obtained on Si(111)- $(\sqrt{3} \times \sqrt{3})R30^\circ$ -B adatom sites at a temperature of 5 K. The conduction and valence bands are respectively labeled CB, and VB. The arrow points toward the peak related to the surface state band of the passivated dangling bonds. The tip height is fixed at the feedback conditions $V_{bias} = +2.3V$, $I_{tunnel} = 80pA$.

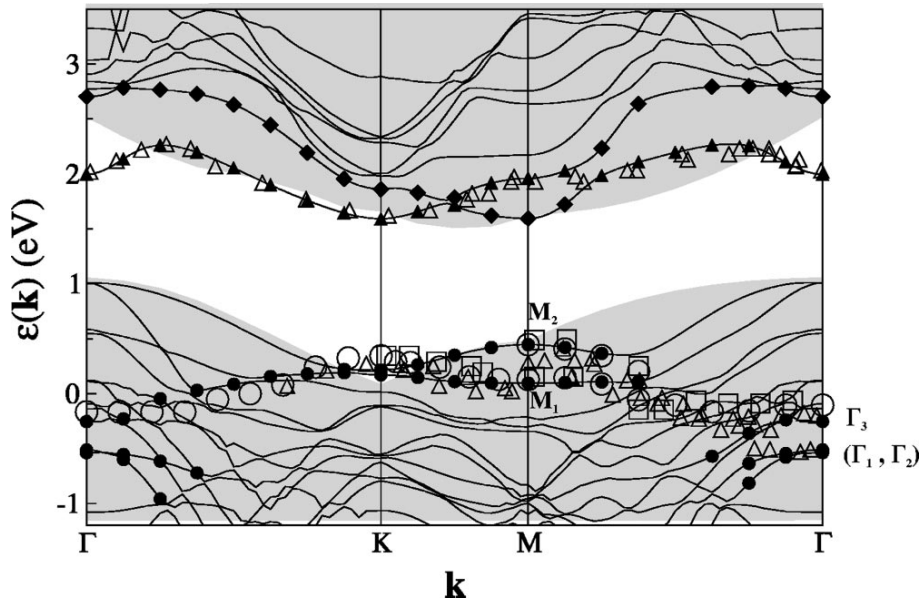


Figure 4.6: The electronic structure of the B(S5) configuration for the Si(111)- $(\sqrt{3} \times \sqrt{3})R30^\circ$ -B surface. The solid circles, triangles, and diamonds indicate the theoretically predicted electronic surface states. The open circles and squares represent the experimental data of Higashiyama et al. [127]. The open triangles indicate the experimental results of Grekh et al. [128]. Figure taken from ref. [125]

4.3 Identification of subsurface acceptors

Fig 4.7(a) shows an image of the empty electronic states of Si(111)- $(\sqrt{3} \times \sqrt{3})R30^\circ$ -B. The surface appears free of defects, nevertheless faint dark depressions can be observed. Fig. 4.7(b) corresponds to the same area, but is a filled states image. The dark depressions turn into bright protrusions, superimposed to the atomic corrugation of the Si adatoms. Due the high concentration of these features and a voltage-dependent signature which is similar to the acceptors observed in the cleaved (110) GaAs surface by STM [129] [130], we attribute these features to subsurface B dopants.

Indeed, boron dopants act as charged impurities in the silicon crystal. Because the $(\sqrt{3} \times \sqrt{3})R30^\circ$ -B reconstruction passivates the surface, only a weak charge screening is expected and as a result, the dopants can be imaged through the local effect of their screened Coulomb potential. As the electronic states associated to Boron lie near the Fermi level of the sample, they can be clearly seen while imaging at negative bias. At positive bias, a local charge-induced band bending causes the presence of darker features over the dopants.

The bulk concentration of dopants is a well known value from the beginning. As the sample preparation involves a segregation of Boron, the concentration near the surface is not known anymore. Nevertheless, on STM pictures, the dopants appear with different contrasts (variable apparent intensity of protrusions), associated with their depth in the bulk [131]: the relative local influence of their associated screened Coulomb potential on the STM contrast decreases with the depth.

Such electrically active impurities are lying at least four layers below the surface plane. Indeed, the surface layer is made of silicon adatoms and Boron atoms present in the three following layers are involved in the passivation of the surface. Since in these four layers, B impurities are located in symmetrical positions with respect to the adatoms, analyzing the corrugation profile across the protrusions allows the counting of the impurities in each layer [131].

Fig 4.8 gives STM images of individual dopants located in the 5th to 9th subsurface, associated with schematic representation of the protrusion intensity of the silicon atoms in STM images. The first line is the STM topographic image, the second line shows a top view of the surface, and the third line gives the depth of the dopant in a side view. In the schematics, some atoms are magnified to guide the eye as a comparison with the STM intensity.

As seen in Fig. 4.8, the STM dopant signature of layers 5 to 8 has the same shape with six possible orientations identifying the lateral position of

CHAPTER 4. RUNNING CURRENT THROUGH AN ISOLATED LOCALIZED STATE IN SILICON

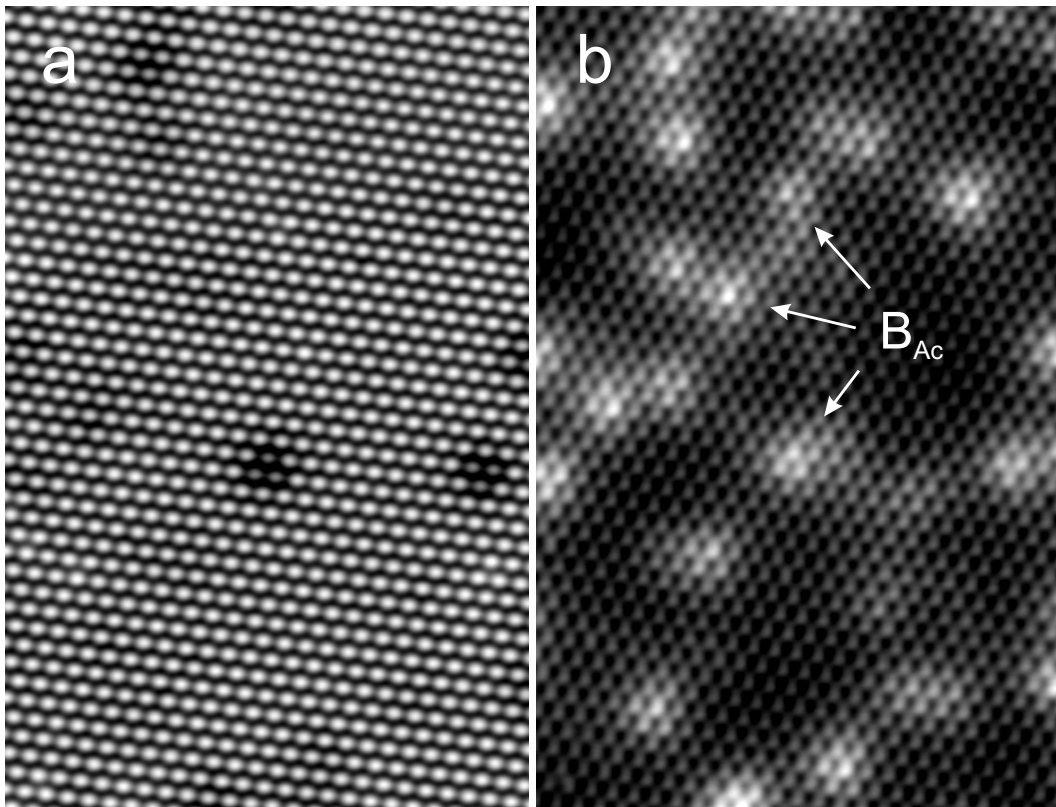


Figure 4.7: Voltage-dependent STM images ($16.8 \times 25.8 \text{ nm}^2$) of the Si(111)-($\sqrt{3} \times \sqrt{3}$)R30°-B surface acquired simultaneously with (a) $V_{bias} = +2V$, (b) $V_{bias} = -0.4V$. $I_{tunnel} = 1 \text{ nA}$. The arrows indicate protrusions associated with subsurface B acceptors (B_{Ac}) in the filled state image.

4.3 Identification of subsurface acceptors

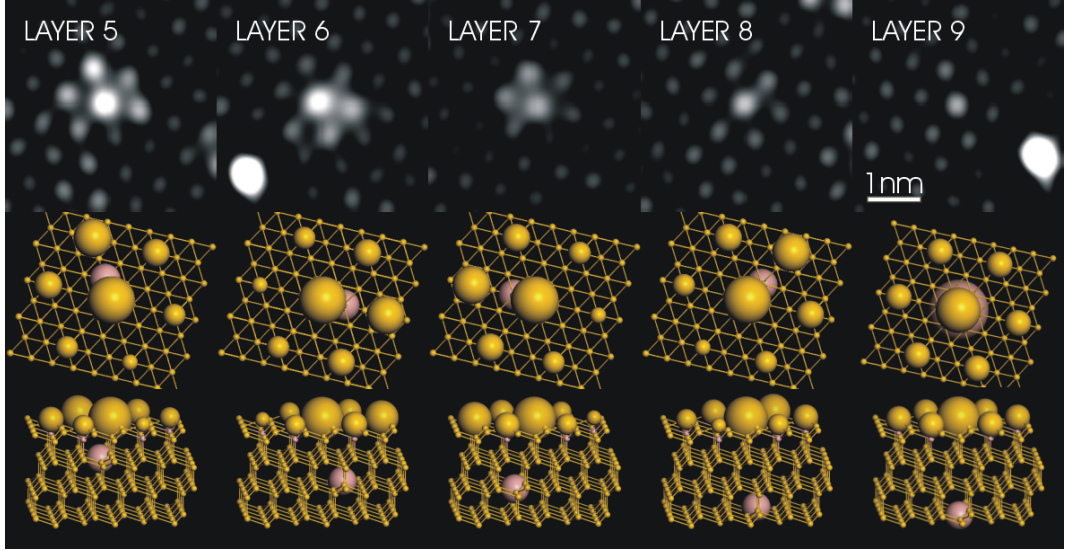


Figure 4.8: STM images of individual dopants situated in the 5th to 9th sub-surface layers. STM parameters are: $V_{gap} = -0.5V$, $I_{tunnel} = 80pA$, $T = 4K$, $5 \times 5nm^2$.

the dopant compared to the most intense surface atom. Nevertheless, the geometry of the silicon lattice allows only 3 orientations (1 possibility modulo $\pi/3$) for each previously mentioned layer. This will help for the following unambiguous identification of the depth of each dopant.

Indeed, between the image of dopants coming from successive layers between 5 and 8, there are two possibilities:

1. The lateral positions of the atoms of layer 5 respectively of layer 6 are the same. As a result, Dopants situated in layer 5 or layer 6 will induce rhombuses having the same orientation modulo $\pi/3$ radian. The same case applies for layer 7 and layer 8;
2. The relative lateral position of atoms in layer 6 and layer 7 corresponds to a rotation of the lattice of $\pi/6$, then the rhombuses seen on the surface must have the same orientation (modulo $\pi/3$) + $\pi/6$ radian.

One can note that we do not mention dopants of the 9th layer because they do not have a rhombus shape (Fig. 4.8) and thus are already unambiguously identified. Using these geometric deductions and the table below, where the angle of rhombuses in successive images are measured, it becomes clear that the 2nd and 3rd images respectively correspond to layers 6 and 7 and then logically, the 1st and 4th image are those of a dopant in the 5th and in the 8th layers.

CHAPTER 4. RUNNING CURRENT THROUGH AN ISOLATED LOCALIZED STATE IN SILICON

Successive Layers	Rotation angle (radian)
5 th to 6 th	$\frac{2\pi}{3}$
6 th to 7 th	$\frac{\pi}{3} + \frac{\pi}{6}$
7 th to 8 th	$\frac{2\pi}{3}$

Finally, we have analyzed the protusion intensity of the silicon atoms of the surface under coulombic influence of the bore atom located in the 5th to 8th sub-surface layer. There is always one central atom surrounded by 6 atoms, as illustrated in the onset of the Fig. 4.9. In that figure, we have plotted the STM intensity of the atoms versus their distance to the sub-layer associated dopant. In a first-order approximation, this intensity is proportional to the local Coulomb potential associated with the dopant and varies as the inverse of the distance from the dopant to the considered surface atom.

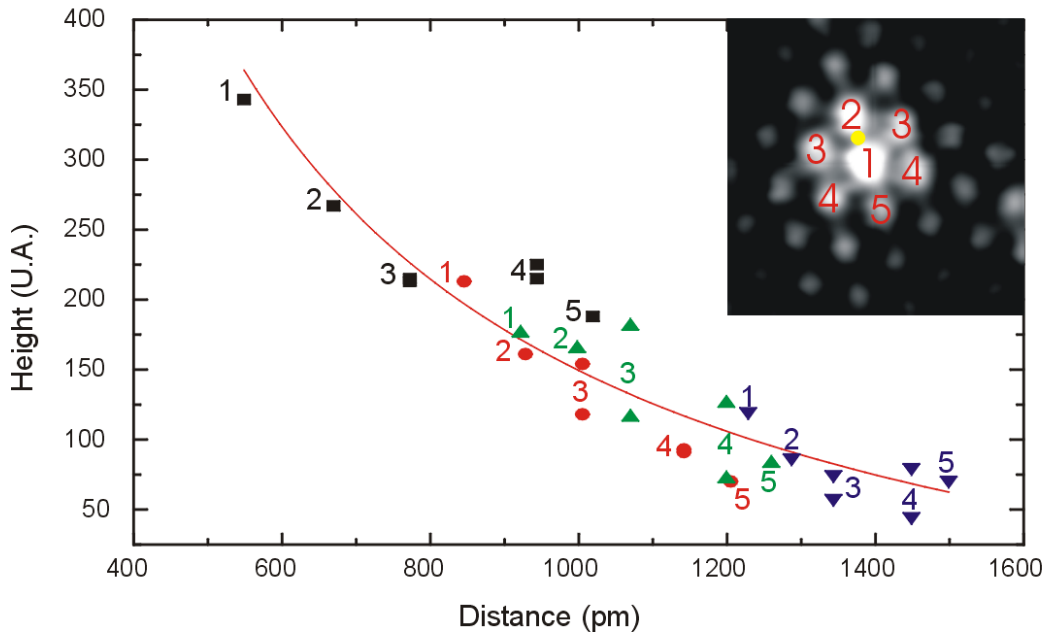


Figure 4.9: STM intensity of protusion associated with silicon surface atoms versus their distance to boron dopant located from the 5th to the 8th sub-surface layer. (square: 5th layer, round: 6th layer, upstanding triangle: 7th layer, downstanding triangle: 8th layer). The atoms are labelled from 1 to 6 and have the same figure when they are at the same distance far from the main protusion.

We observe that the STM intensity can indeed be fitted with a law varying as the inverse of the distance R from dopant to silicon surface atom, in agreement with the observation of local effect associated with a weakly screened Coulomb potential. For the 8th sub-surface layer, the variation is

4.4 Running current through an unpassivated silicon dangling bond

weak versus the distance because the lateral distance d from the central atom becomes negligible with respect to the absolute depth h of the dopant (the distance R equals $R = \sqrt{h^2 + d^2}$).

Below the sixth layer, we estimate a concentration of $5.1 \times 10^{19} \text{cm}^{-3}$. Such a concentration allows the formation of a degenerate band of acceptor states positioned at the top of the valence band.

4.4 Running current through an unpassivated silicon dangling bond

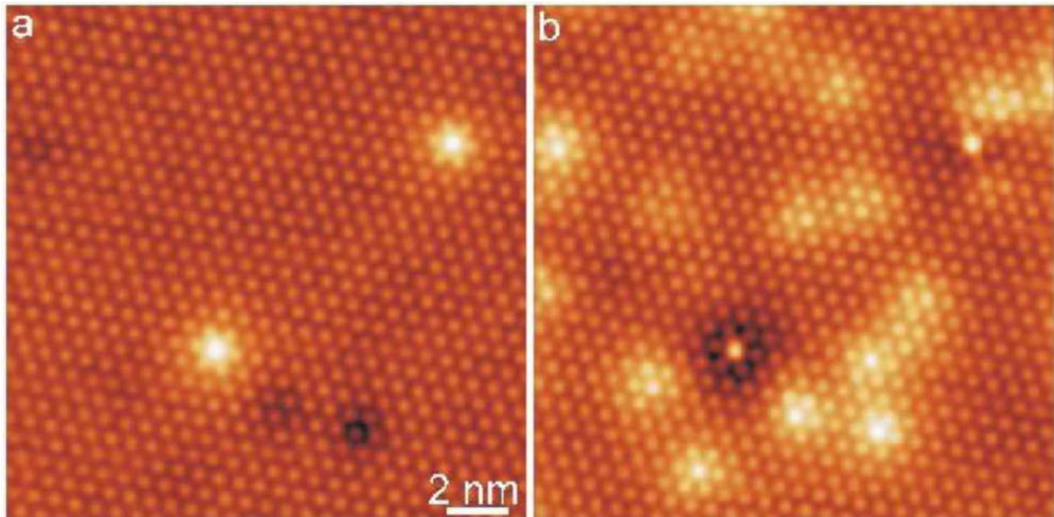


Figure 4.10: Visualization of passivated and isolated Si dangling bonds on the $\text{Si}(111)-(\sqrt{3} \times \sqrt{3})R30^\circ$ surface observed at 5 K. (a) Empty state STM image. The majority of the adatoms appears dark (adatoms with B atoms underneath). Unlike these adatoms, two Si adatoms appear much brighter and correspond to a configuration with a Si atom underneath. The height difference between the dark and bright adatoms is 0.6 \AA ($V_{bias} = +1.8V$). (b) Filled state STM image of the same area ($V_{bias} = -0.4V$). The numerous bright protrusions, which show a more or less dark contrast in the empty state image, correspond to subsurface B dopants, located at least 4 atomic layers below the surface.

Additionally to the dopants, which are imaged as protrusions in the filled states images and as depressions in the empty states images, when large scale STM images are acquired, a small concentration of adatoms appear brighter both in the empty and filled states images. Fig. 4.10 shows STM images of the $\text{Si}(111)-(\sqrt{3} \times \sqrt{3})R30^\circ\text{-B}$ surface where two of these bright adatoms are present.

To establish a direct link between the adatom contrast and their electronic nature, differential-conductance spectroscopy measurements were done on

CHAPTER 4. RUNNING CURRENT THROUGH AN ISOLATED LOCALIZED STATE IN SILICON

bright adatoms and compared to the spectra acquired on the dark adatom sites, Fig. 4.11.

In contrast to the dark adatoms, the spectrum on a bright adatom exhibits a distinct feature in the band gap region. A peak is now visible at an energy of 0.6 eV and is related to the contribution to the current of a non resonant DB state associated to a Si adatoms that is not passivated by the subsurface boron (B) layer [126]. Such a strong peak in the band gap explains the topographical contrast between the two types of Si adatoms in the empty state images of Fig. 4.10(a). Their electronic structure corresponds to a dangling-bond (DB) state energetically localized in the energy gap of the B-doped Si(111)-($\sqrt{3} \times \sqrt{3}$) $R30^\circ$ surface.

Nevertheless, as the electronic state of a bright adatom is lying in the bandgap, it is electronically decoupled from any other state and should not be able to carry a current. Surprisingly, the isolated DB state can hold an electron current bigger than 1 nA at a temperature of 5 K. This finding is at odds with the above picture of a DB state in the surface band gap.

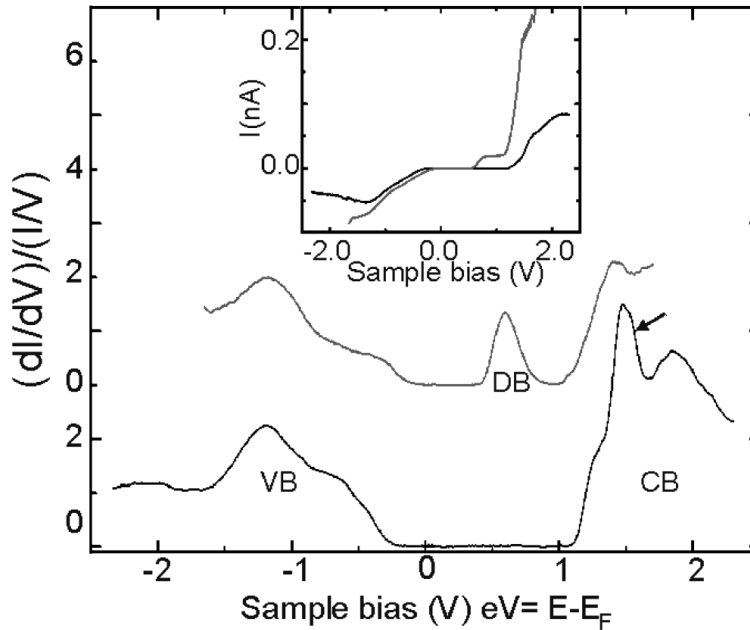


Figure 4.11: Normalized conductivity spectra obtained on dark (black line) and bright (gray line) adatom sites at a temperature of 5 K. The peak related to the localized dangling-bond state, the conduction, and valence bands are respectively labeled DB, CB, and VB. The arrow points toward the peak related to the surface state band of the passivated dangling bonds. The tip height is fixed at the feedback conditions (black line) $V_{bias} = +2.3V$, $I_{tunnel} = 80pA$ and (gray line) $V_{bias} = +1.7V$, $I_{tunnel} = 250pA$

4.4 Running current through an unpassivated silicon dangling bond

4.4.1 Establishing a current through an isolated dangling bond state

In order to explain the experimental large current through the DB state, several mechanisms can be invoked [132]:

1. Hopping of the electron among the different DB states; however, as hopping is a tunneling process, this is not possible due to the small concentration of bright adatoms on the surface (see Fig. 4.10). Indeed, the distance between bright adatoms is typically of 5 to 10nm;
2. Thermal excitation of the electron towards the CB by phonon absorption; yet, this process can be ruled out at 5 K because lattice vibrations are quenched;
3. As a result, only processes involving the recombination of the electron with a hole from the acceptor band are possible if the excess electron energy is absorbed by either photon emission or atomic vibrations.

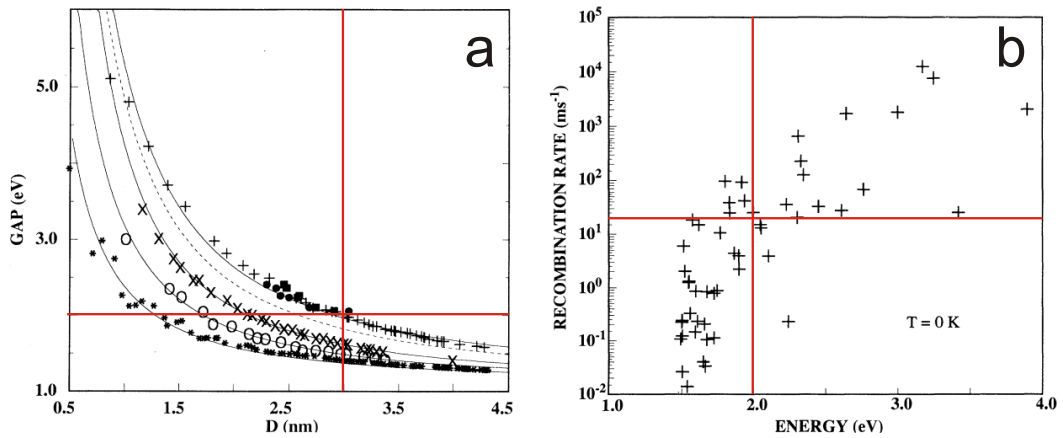


Figure 4.12: (a) Calculated optical band-gap energies for various silicon crystallites (+) or wires (100 : x; 110 : *; 111 : o) with respect to their diameter d . The continuous lines are an interpolation and an extrapolation of these results by a d^{-n} law. The black dots and squares are the experimental results of ref. [133]. The dashed line is the band-gap energy for the crystallites including the Coulomb interaction between the electron and the hole. (b) Calculated recombination rate (ms^{-1}) of an excited electron-hole pair in silicon crystallites (crosses) with respect to the photon energy at 5K. The spin degeneracy is not included: its inclusion would divide the calculated recombination rates by a factor of 2. (a) and (b) are data taken from [134]. The red crosses indicate the diameter and recombination rate of a crystallite of energy $E = 2eV$

Photon emission The recombination rate for a radiative recombination can be roughly estimated from the work of Delerue et al. [134] on the radiative recombination of electron-hole pairs in silicon crystallites.

CHAPTER 4. RUNNING CURRENT THROUGH AN ISOLATED LOCALIZED STATE IN SILICON

Let us take a crystallite whose energy gap is $E_g = 2.0eV$. The diameter of the crystallite is given by Fig. 4.12(a): $d = 3nm$, then its volume is

$$V = \frac{4\pi}{3} \left(\frac{d}{2}\right)^3 = 1.4 \times 10^{-20} cm^3 \quad (4.1)$$

Now using Fig. 4.12(b), the recombination rate of an electron-hole pair in the crystallite is $\frac{1}{\tau} = 11 \times 10^{3\pm 1} s^{-1}$, with a precision of one order of magnitude.

Considering a hole concentration of $5 \times 10^{19} cm^{-3}$ deduced from the concentration of boron dopants measured in section 4.3 on page 89, there is one hole every $2 \times 10^{-20} cm^3$. By a simple rule of three, the radiative recombination rate of an electron-hole pair in our sample yields $7.7 \times 10^{3\pm 1} s^{-1}$ (again with an uncertainty of one order of magnitude) which corresponds to a current

$$I = \frac{-e}{\tau} = 1.2 \times 10^{-6\pm 1} nA \quad (4.2)$$

This rate is however many orders of magnitude too small to account for the measured currents that are in the range of 10 pA to 1 nA. We will then investigate the possibility of an electron-phonon coupling to absorb the excess electron energy so that a hole could be efficiently captured by the DB state thanks to multi-emission of vibrations.

Atomic vibrations In order to describe the transfer of the electron, the configuration coordinate diagram, which is a graphical representation of the electronic energy against the lattice coordinate Q of the dangling bond, is introduced, Fig. 4.13.

1. When a DB changes its charge state, the Si adatom is displaced [135] [136], thus two equilibrium adatom positions can be drawn on the configuration coordinate diagram (Fig. 4.13):
 - When the DB is not charged, the position of the adatom is $Q = 0$;
 - When an electron is added to the DB, the adatom moves from $Q = 0$ to $Q = Q^-$ by Coulombic repulsion.

The description of the adatom's energy in each charge state can be described on the configuration coordinate diagram by quantum harmonic oscillator potentials centered on each equilibrium position $Q = 0$ and $Q = Q^-$.

4.4 Running current through an unpassivated silicon dangling bond

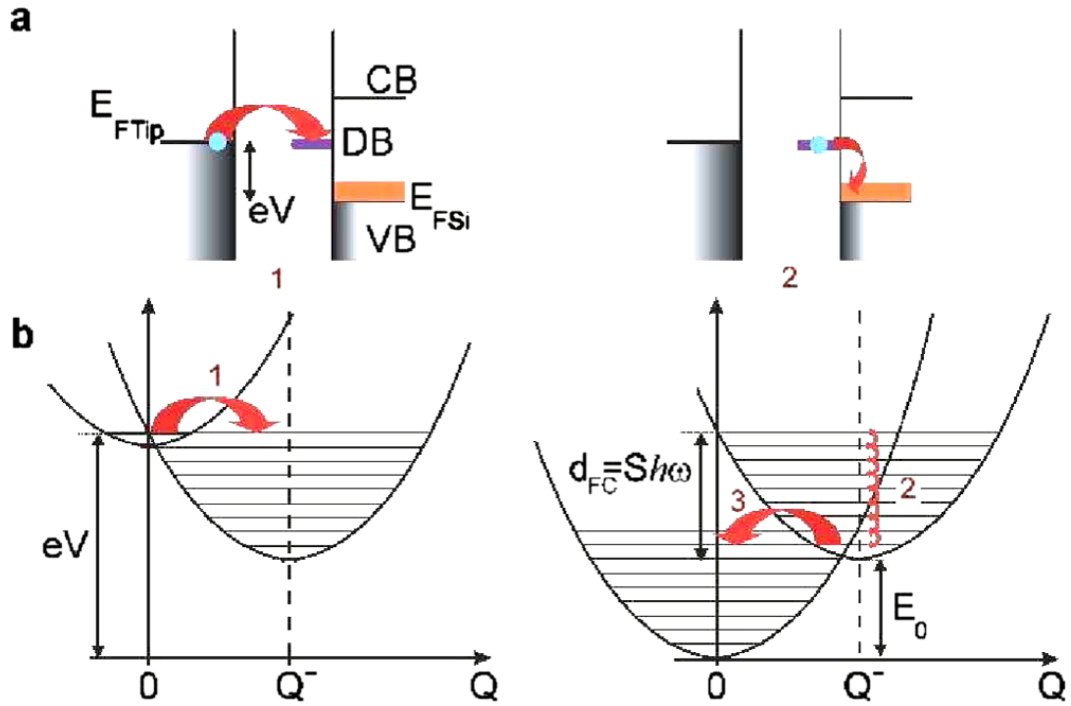


Figure 4.13: (a) Energy diagrams sketching the two step transport process: (1) the energy, eV , of the electron in the tip is tuned via the STM bias voltage, to become resonant with the dangling-bond state (DB) at a given vibrational state; (2) when sufficient energy has been transferred to the adatom, the probability of nonradiative transfer into the partially empty band of Boron impurities becomes high enough. The conduction and valence bands are, respectively, labeled by CB and VB, the tip and silicon Fermi levels by E_{FTip} and E_{FSi} . (b) Total energy curves as a function of the vibrational coordinate, Q , of the dangling-bond. On the left graph (process 1), the adatom in its ground state (top parabola) changes its charge state and its total energy corresponds to the bottom parabola, centered at $Q = Q^-$. On the second diagram, the adatom in the excited state (top parabola) may dissipate up to S quanta of vibration of energy $\hbar\omega$, corresponding to the Franck-Condon shift $d_{FC} = S\hbar\omega$ (process 2). Finally, the electron is transferred into the degenerated band of Boron impurities, leaving the adatom in a vibrationally excited state about its initial position (process 3).

2. The electron releases some of its energy through the vibration of the adatom.
3. The release of the electron energy provides enough energy to the dangling bond so that a hole of the acceptor band is captured to recombine non radiatively with the electron. Thus, the adatom returns to its neutral oscillator state, centered at $Q = 0$, in a highly excited vibrational state.

There is not only one possible energy at which the electron can be transferred, but a band of all the possible transitions centered on the energy $eV = E_0 + S\hbar\omega$ of Fig. 4.13, where E_0 is the ionization energy and $S\hbar\omega$ is the relaxation energy (details will be given below). This energy corre-

CHAPTER 4. RUNNING CURRENT THROUGH AN ISOLATED LOCALIZED STATE IN SILICON

sponds to the strongest coupling of the vibrational states at the position $Q = 0$ and $Q = Q^-$.

Fig 4.11 shows a broad peak corresponding to the DB state in the differential conductance curve. We will show in the next section that its width is directly related to the contribution of the vibronic states.

4.4.2 Shape of the differential conductance in the case of a strong electron-vibration coupling

In order to evaluate the shape of the differential conductance curve, let us investigate the transfer of electrons in the case of a strong coupling with the vibrations of the adatom.

Separation of the different contributions The current is proportional to the probability per unit time that an electron of the tip is captured by the DB at $T = 0K$. It is given by Fermi's golden rule:

$$W = \frac{2\pi}{\hbar} \sum_n |\langle \psi_{i,n} | V_{tunnel} | \psi_{f,n} \rangle|^2 \delta(E_{i,n} - E_{f,n}) \quad (4.3)$$

$\psi_{i,n}$ and $\psi_{f,n}$ are the states (electronic and vibrational) of the system respectively before and after the transfer of the electron of energy $E_{i,n}$ and $E_{f,n}$.

- The initial state is described by the curve centered on $Q = 0$ in Fig. 4.13: a neutral DB in its ground state, at $T = 0K$. Thus only $\psi_{i,0}$ contributes to the current.
- The final state corresponds to the curve centered on $Q = Q^-$ in Fig. 4.13: a negatively charged DB state in the p^{th} vibrationally excited state around the new equilibrium $Q = Q^-$.

Electrons can tunnel each time an initial and a final state are resonant, then the differential conductance should look like a sum of peaks with a spacing of $\hbar\omega$ (ω is the frequency of the vibrational mode) and its amplitude is proportional to $|\langle \psi_{i,n} | V_{tunnel} | \psi_{f,n} \rangle|^2$.

Following the Born-Oppenheimer approximation, one can split $|\psi_{i,0}\rangle$ and $|\psi_{f,n}\rangle$ into electronic and vibrational states centered around the equilibrium position of their nucleus:

$$|\psi_{i,0}\rangle = |\varphi_{tip}\rangle |\chi_{i,0}\rangle \quad (4.4)$$

$$|\psi_{f,n}\rangle = |\varphi_{DB}\rangle |\chi_{f,p}\rangle \quad (4.5)$$

4.4 Running current through an unpassivated silicon dangling bond

As a result, and if we consider that $\langle \varphi_{tip} | V_{tunnel} | \varphi_{DB} \rangle$ is independent of Q because we make the assumption that the vibrational excitation is much longer than the lifetime of the electron in the DB (Condon approximation), we get:

$$|\langle \psi_{i,n} | V_{tunnel} | \psi_{f,n} \rangle|^2 = |\langle \varphi_{tip} | V_{tunnel} | \varphi_{DB} \rangle|^2 |\langle \chi_{i,0} | \chi_{f,p} \rangle|^2 \quad (4.6)$$

Where $|\langle \varphi_{tip} | V_{tunnel} | \varphi_{DB} \rangle|^2$ is the tunnel probability of transmission for the electron and $|\langle \chi_{i,0} | \chi_{f,p} \rangle|^2$ is the overlap between two harmonic oscillators. The shape of this overlap against energy will explain the broadening of the differential conductance peak of the DB state.

Overlap between two harmonic oscillators In order to calculate

$$F_{0,p} = \langle \chi_{i,0} | \chi_{f,p} \rangle \quad (4.7)$$

that reflects the vibrational overlap between the ground state $|\chi_{i,0}\rangle$ of the harmonic oscillator centered on $Q_i = 0$ and the p^{th} excited state $|\chi_{f,p}\rangle$ of the harmonic oscillator centered on $Q_f = Q_-$, let us introduce the operators a_k^+ and a_k of each oscillator ($k=i$ or f) such that:

$$\begin{aligned} a_k^+ &= \frac{-\hbar(d/dQ) + M\omega(Q - Q_k)}{\sqrt{2M\hbar\omega}} \\ a_k &= \frac{+\hbar(d/dQ) + M\omega(Q - Q_k)}{\sqrt{2M\hbar\omega}} \end{aligned} \quad (4.8)$$

with M the mass of the electron and ω the vibrational pulsation.

These operators are called creation and annihilation operators because they provide a simple link between the energy states of the harmonic oscillator. They were introduced by Dirac in order to simplify the calculations and have the following properties:

$$\begin{aligned} \forall n \in \mathbb{N}, \\ a_k^+ a_k |\chi_{k,n}\rangle &= n |\chi_{k,n}\rangle \\ a_k a_k^+ &= 1 + a_k^+ a_k \\ |\chi_{k,n}\rangle &= n^{-1/2} a_k^+ |\chi_{k,n-1}\rangle = (n!)^{-1/2} (a_k^+)^n |\chi_{k,0}\rangle \\ |\chi_{k,n-1}\rangle &= n^{-1/2} a_k |\chi_{k,n}\rangle \end{aligned} \quad (4.9)$$

One can deduce from equation 4.9:

$$a_f^+ - a_i^+ = a_f - a_i = -\sqrt{\frac{M\omega}{2\hbar}}(Q_f - Q_i) \quad (4.10)$$

CHAPTER 4. RUNNING CURRENT THROUGH AN ISOLATED LOCALIZED STATE IN SILICON

Moreover, the relaxation energy $S\hbar\omega$ [137] can be expressed as (see Fig. 4.13, remember that the curves are parabolas)

$$\frac{1}{2}M\omega^2(Q_f - Q_i)^2 = S\hbar\omega \quad (4.11)$$

where S is the Huang-Rhys factor and corresponds to the number of phonons yielding the highest probability for the electronic transition. The relaxation energy $S\hbar\omega$ is equivalent to the Franck-Condon shift used to describe electronic transitions in optical absorption experiments.

As a result, equation 4.10 becomes

$$a_f^+ - a_i^+ = a_f - a_i = -\sqrt{S} \quad (4.12)$$

Thanks to these useful relations, one can rewrite equation (4.7) with the help of the third expression of 4.10:

$$F_{0,p} = \frac{1}{\sqrt{p!}} \langle \chi_{i,0} | (a_f^+)^p | \chi_{f,0} \rangle \quad (4.13)$$

thus:

$$F_{0,p} = \frac{1}{\sqrt{p!}} \langle \chi_{i,0} | (a_i^+ - \sqrt{S})^p | \chi_{f,0} \rangle \quad (4.14)$$

This expression can be expanded in powers of a_i^+ . However, any $\langle \chi_{i,0} | (a_i^+)^m$ is the conjugate of $(a_i)^m | \chi_{i,0} \rangle$ which equals zero, except if $m=0$. Then:

$$F_{0,p} = \frac{(-\sqrt{S})^p}{\sqrt{p!}} F_{0,0} \quad (4.15)$$

At last, let us calculate $F_{0,0}$, it is easily done with:

$$\sum_{p=0}^{\infty} |F_{0,p}|^2 = \sum_{p=0}^{\infty} \langle \chi_{i,0} | \chi_{f,p} \rangle \langle \chi_{f,p} | \chi_{i,0} \rangle = 1 \quad (4.16)$$

and in parallel, by inserting equation 4.15:

$$\sum_{p=0}^{\infty} |F_{0,p}|^2 = \sum_{p=0}^{\infty} \frac{(-S)^p}{p!} |F_{0,0}|^2 = |F_{0,0}|^2 \exp(S) \quad (4.17)$$

thus:

$$F_{0,0} = \exp\left(-\frac{S}{2}\right) \quad (4.18)$$

$$F_{0,p} = \frac{(-\sqrt{S})^p}{\sqrt{p!}} \exp\left(-\frac{S}{2}\right) \quad (4.19)$$

4.4 Running current through an unpassivated silicon dangling bond

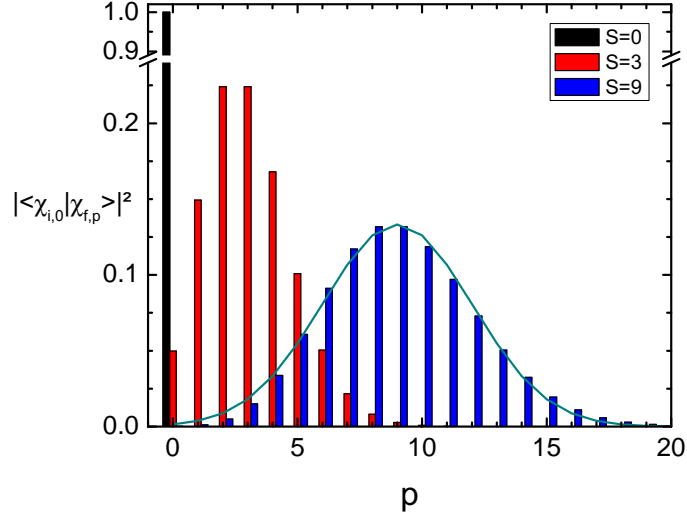


Figure 4.14: Simulation of the shape of the differential conductance in the case of (black, $S=0$) no electron-vibration coupling, (red, $S=3$) a weak electron-vibration coupling and (blue, $S=9$) a strong electron-vibration coupling.

and:

$$|\langle \chi_{i,0} | \chi_{f,p} \rangle|^2 = \frac{S^p}{p!} \exp(-S) \quad (4.20)$$

with (see equ. 4.11):

$$S = \frac{M\omega}{2\hbar} (Q^-)^2 \quad (4.21)$$

The shape of the differential conductance with respect to the strength of the electron-vibration coupling is illustrated in Fig. 4.14:

- When no coupling is possible: $S=0$, the shape is a delta function
- For a small electron-vibration coupling, the shape of the differential conductance becomes a bell-like function that is truncated on the lowest energy side.
- When the electron-vibration coupling is strong, the vibrational overlap is equivalent to a Gaussian function centered on $p=S$:

$$\frac{S^p}{p!} \exp(-S) \approx \exp\left[-\frac{(p-S)^2}{2S}\right] \quad (4.22)$$

CHAPTER 4. RUNNING CURRENT THROUGH AN ISOLATED LOCALIZED STATE IN SILICON

Indeed, the Gaussian function can be written as the limit of a binomial probability distribution with a number n of events:

$$\exp\left[-\frac{(p-S)^2}{2S}\right] = \lim_{n \rightarrow \infty} \frac{n!}{(n-p)!p!} \left(\frac{S}{n}\right)^p \left(1 - \frac{S}{n}\right)^{n-p} \quad (4.23)$$

Moreover, when the number of events is large and S remains constant, it is easily shown that the limit of a binomial distribution is the law of Poisson, or the law of rare events:

$$\begin{aligned} & \lim_{n \rightarrow \infty} \frac{n!}{(n-p)!p!} \left(\frac{S}{n}\right)^p \left(1 - \frac{S}{n}\right)^{n-p} \\ &= \lim_{n \rightarrow \infty} \binom{n}{n-p} \binom{n-p}{n-p-1} \binom{n-p-1}{n-p-2} \cdots \binom{n-p+1}{n-p} \left(\frac{S^p}{p!}\right) \left(1 - \frac{S}{n}\right)^n \left(1 - \frac{S}{n}\right)^{-p} \\ &= \frac{S^p}{p!} \exp(-S) \end{aligned} \quad (4.24)$$

Therefore, the broadening of the differential conductance is explained by a sum of peaks whose envelope is a Gaussian shape.

4.4.3 Experimental evidence for the strong electron-phonon coupling

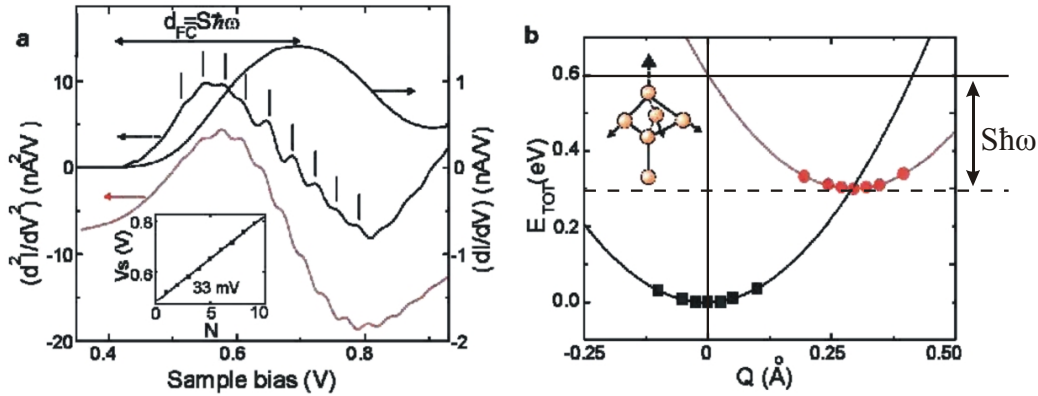


Figure 4.15: (a) Experimental (upper) and calculated (lower) d^2I/dV^2 spectra, shifted for clarity and obtained on a bright adatom. The vertical lines indicate the position of equally spaced peaks in the spectrum. The Franck-Condon shift $d_{FC} = S\hbar\omega$ is deduced from the width at half maximum of the dI/dV peak. The curves were acquired with feedback parameters $V_{bias} = +1.5V$ and $I_{tunnel} = 500pA$ at 5 K. Inset: Plot of the peak energy versus the peak number N for the vibronic progression, yielding the energy of the vibrational mode. (b) Total energy of a neutral (lower) and a negative charge (upper) dangling-bond, calculated by density functional theory, versus the lattice coordinate Q of the adatom (top atom in the atomic structure) for the stretching mode.

4.4 Running current through an unpassivated silicon dangling bond

To prove this mechanism, we measured d^2I/dV^2 spectra on bright adatoms. Figure 4.15(a) shows dI/dV and d^2I/dV^2 spectra acquired concurrently in the energy range of the peak labeled DB, in Fig. 4.11. In the d^2I/dV^2 curve, equidistant peaks are observed, suggesting the vibrational excitation of the adatom, when electrons tunnel into the DB state [138]. From measurements obtained on different bright adatoms, the peak spacing is found to be $31 \pm 3\text{meV}$, showing that a single vibrational mode is mainly involved in the transport.

The peak of the dI/dV curve in Fig. 4.15(a) has central value $E_{peak} = 0.7\text{eV}$ and a $fwhm = 0.84 - 0.57 = 0.27\text{eV}$. We deduce the value of the Franck-Condon shift: $d_{FC} = fwhm = 0.27\text{eV}$. Given the quantum of vibration $\hbar\omega = 31 \pm 3\text{meV}$, it is thus possible to determine experimentally strength of the electron-phonon coupling:

$$S = \frac{d_{FC}}{\hbar\omega} = 8.7 \pm 0.6 \quad (4.25)$$

Since the peak related to the DB state is positioned at an energy of 0.7 eV, and this energy corresponds to the sum of the Frank-Condon shift $d_{FC} = S\hbar\omega$ plus the ionization energy E_0 , we deduce E_0 to be 0.4 eV.

4.4.4 Comparison with theory

In order to confirm our results, we worked with Christophe Delerue, and Nicolas Lorente and his team who made first-principles calculations [139] to simulate the behaviour of a DB state with and without an extra electron. In order to simulate the vibronic tunnelling current based on the tunnelling of an electron through a single site coupled to vibrations [140] [141], they determined both the electronic and vibrational structures of the bright adatoms.

Thanks to the calculations, all the local vibrational modes of the adatom could be investigated; it was found that only the stretching mode gives a strong electron-vibration coupling. The computed configuration coordinate diagram for this mode of vibration, where the adatom oscillates in a direction normal to the (111) is drawn on Fig. 4.15(b); the Huang-Rhys factor, S , is evaluated as the linear term of the harmonic fit to the total energy as a function of the configuration coordinate, Q . The value is $S = 9.6$. For this mode, a quantum of vibration of $\hbar\omega = 32.5\text{meV}$ is found.

The simulations are in very good agreement with our experimental value of S . Furthermore the current has been calculated and, on its second derivative part, a succession of equidistant peaks is visible in Fig. 4.15(a)(red curve), fully consistent with the experimental curve.

CHAPTER 4. RUNNING CURRENT THROUGH AN ISOLATED LOCALIZED STATE IN SILICON

4.4.5 Conclusion

In summary, by using a scanning tunnelling microscope (STM) tip as an electrode and a passivated B-doped Si(111)-($\sqrt{3} \times \sqrt{3}$) $R30^\circ$ surface as the other electrode at 5 K, the conductance of an unpassivated Si adatom was measured. The electronic structure of this adatom corresponds to a DB state energetically localized in the energy gap of the surface. Hence, this state is electronically decoupled from any other electronic state. Yet, we found large currents on the adatom DB that can be rationalized in a two-step picture: a tunnelling of the electron into the DB state and then its nonradiative recombination with a hole from the boron band. Our main finding is that the latter process is possible only if the adatom can absorb the electron excess energy by becoming vibrationally excited. This process is efficient enough only in the presence of a large electron-vibration coupling, giving rise to a polaronic-like conduction.

Going further, if the tip is approached closer to the non-passivated adatom the current will increase until no more hole can recombine with the electrons. It was shown above in this chapter that the concentration of holes below the surface can be determined by the concentration of subsurface B dopants, thanks to STM topographic images. Knowing the saturation value of the current and the concentration of holes, it could then be possible to evaluate the capture coefficient of a single DB.

4.5 Probing the hole capture rate of a single Si dangling bond

So far, a common approach to study the probability per unit of time of carrier capture and emission has relied on the use of junction space charge techniques, such as (photo)current and capacitance techniques [142]. These techniques were first applied to point defects and interface states, generally referred as “deep level” due to the position of the energy level far apart from both band edges [143] [144]. But they require the formation of a space charge region, which is not always compatible with the current dimensions of single nanostructures. Due to the size of the space charge regions, junction techniques also inherently involve the integration of data over a large set of energy levels. Therefore, probing the carrier dynamics of a single deep level is still a challenge.

In this part, we report a direct method to probe the hole capture rate of single deep levels with atomic scale resolution using scanning tunnelling microscopy. By saturating the injection of inelastic electrons into the non res-

4.5 Probing the hole capture rate of a single Si dangling bond

onant localized state of a Si adatom in the B-doped Si(111)-($\sqrt{3} \times \sqrt{3}$)R30° surface, we are able to measure the hole capture rate of a Si dangling bond state and estimate its cross section. Its magnitude is found to be consistent with the localization of the wave function, obtained from the spatial mapping of the differential conductance. Furthermore, by probing a large set of dangling bonds, significant variations in the capture rates are observed and related to the position of the B dopants below the surface. Such result demonstrates the importance of the potential fluctuations induced by the random distribution of charged impurities on the carrier capture rate of single quantum levels.

4.5.1 STS at high tunneling currents

By further increasing the current setpoint on a bright adatom in comparison with the tunneling current used in section 4.4, the spectroscopic measurements reveal an increasing negative differential resistance (NDR) on the I(V) curve (Fig. 4.16(a)) and a broad peak on the $dI(V)/dV$ curve (Fig. 4.16(c)) in the Si band gap region. Surprisingly, with increasing tunneling current setpoints (ie decreasing tip-sample distances), the NDR peak intensity becomes saturated at 15 nA whereas one would expect an exponential growth of the tunneling current.

In the previous section, we have proved that the transport through this non resonant dangling bond state requires two processes [145], here we analyse their respective contributions [132]:

1. Tunneling of electrons between tip states and the localized DB state at the energy E_0 generates a current I_1 ; let us define W the probability per unit time for the tunneling of an electron between the tip and the DB. As the electron can tunnel only if the defect is empty, f being the probability of an occupied DB, the current is:

$$I_1 = -e(1 - f)W \quad (4.26)$$

2. A permanent current I is possible only if the DB exchanges carriers with the bands by emission or capture of electrons or holes. If p and n are the hole and electron concentrations, the probability per unit time of hole capture and electron capture are respectively $c_p p$ and $c_n n$. The probability per unit time of hole emission and electron emission are: e_p and e_n . As illustrated in Fig. 4.18, the current between the defect and the bands is:

$$I_2 = -e [f(e_n + c_p p) - (1 - f)(e_p + c_n n)] \quad (4.27)$$

CHAPTER 4. RUNNING CURRENT THROUGH AN ISOLATED LOCALIZED STATE IN SILICON

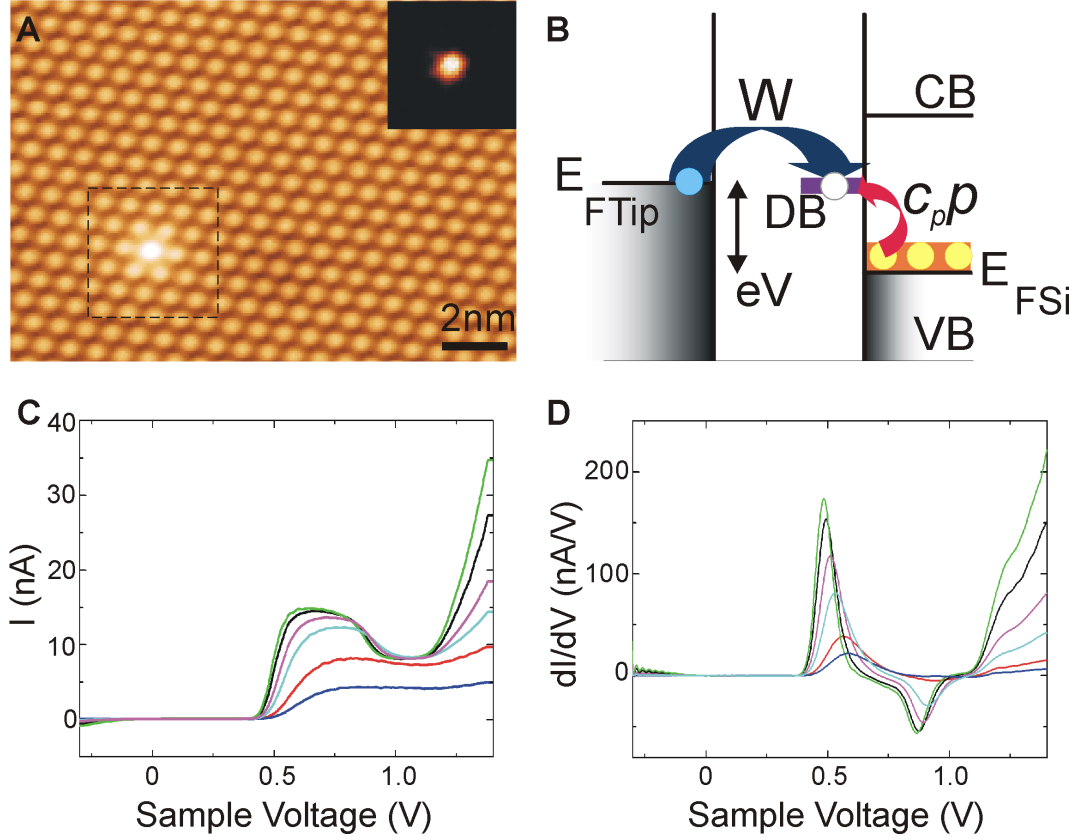


Figure 4.16: Saturation of the tunnelling current through a single non resonant dangling bond state. (A) STM image of the Si(111)-($\sqrt{3} \times \sqrt{3}$)R30 $^\circ$ -B surface observed at 77 K, showing a single non passivated bright Si adatom (Sample voltage $V_{bias} = +1.4V$, setpoint current $I_{tunnel} = 1nA$). Inset : differential conductance images recorded at $V_{bias} = +0.6V$ ($V_{mod} = 15mV$; $f_{mod} = 2kHz$). (B) Transport through the dangling bond state (DB) of the non passivated Si adatom at the energy eV . The transport processes are indicated by the tunneling rate W for the electron (blue particle) and the capture rate $c_p p$ of a hole (orange particle) from the degenerated band of Boron impurities, where c_p and p are the capture coefficient and the hole concentration respectively. The conduction and valence bands are respectively labelled V_B and C_B , the tip and silicon Fermi levels E_{FTip} and E_{FSi} . (C) Tunneling current spectra measured on a non passivated Si adatom for different setpoint currents at a sample voltage $V_{bias} = +1.4V$. (D) Corresponding differential conductance spectra measured with a lock-in amplifier ($V_{mod} = 15mV$; $f_{mod} = 2kHz$).

In our case, an electron is injected on the DB state, thus $e_p = 0$ and $c_p p = 0$. Moreover the temperature ($T = 4K$) does not allow the emission e_n of an electron to the conduction band. We have shown in a previous section (section 4.4.1, page 91) that the electron follows a non radiative recombination process with a hole from the valence band. Thus:

$$I_2 = -efc_p p \quad (4.28)$$

This second process is assisted by the mechanical vibration of the adatom and it is the contribution of vibronic states to the current

4.5 Probing the hole capture rate of a single Si dangling bond

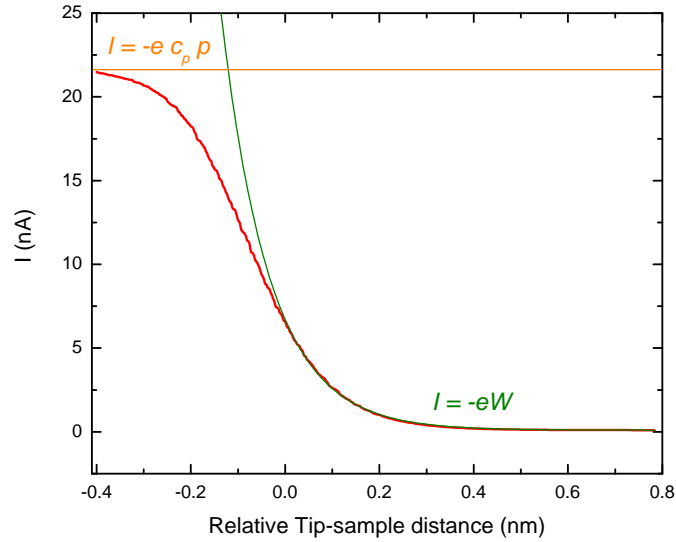


Figure 4.17: Saturation of the tunnelling current through a single non resonant dangling bond state through a Current vs Distance (I-Z) curve (red curve). $V_{bias} = 0.7V$, $T = 77K$. Extrem behaviours are shown by the green exponential (the limiting factor is the electron transfer rate from tip to DB) and orange constant (the transfer rate from a DB to the valence band is limiting)

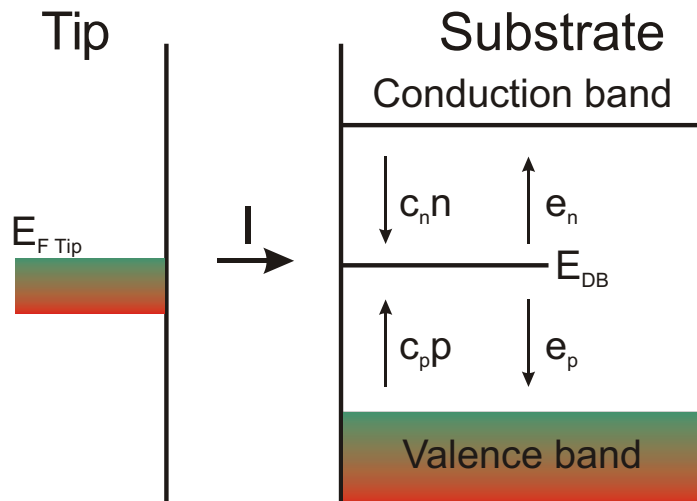


Figure 4.18: Tunneling current I through a DB state. The emission and capture coefficients of electrons and holes are respectively e_n , e_p , $c_n n$, $c_p p$.

which causes the significant broadening of the NDR peak [146].

In the permanent regime, the current corresponding to the tunneling rate

CHAPTER 4. RUNNING CURRENT THROUGH AN ISOLATED LOCALIZED STATE IN SILICON

I_1 (eq. 4.26) must be equal to the current due to the hole capture rate I_2 (eq. 4.28) by the Si dangling bond state, yielding thus, by elimination of f :

$$I = -e \frac{W c_p p}{W + c_p p} \quad (4.29)$$

Two asymptotical behaviours can be extracted from the above formula and are illustrated in Fig. 4.17:

1. When the tunneling rate is much lower than the capture rate (the tip-sample distance Z is large, corresponding to small current setpoints), $W \ll c_p p$, the tunneling current is proportional to the tunneling rate:

$$I = -eW \quad (4.30)$$

2. While approaching the tip closer to the DB, the probability of tunnel transfer increases exponentially (see 2.2.1, page 40). When the tunneling rate becomes higher than the capture rate (higher current setpoints), $W \gg c_p p$, the capture rate limits the current driven through the dangling bond state:

$$I = -e c_p p \quad (4.31)$$

As a result, the current becomes nearly saturated at the energy where the tip Fermi level is resonant with the dangling bond state.

Typically, the first behaviour corresponds to current setpoints lower than $5nA$, and the second one appears when the current is higher than $10nA$, at a tip energy resonant with the DB state, as can be seen on Fig. 4.17.

4.5.2 Saturation of the current through I-Z spectroscopy

Since a precise determination of the saturation current intensity requires higher and higher tunneling current setpoints, which can lead sometimes to a modification of the surface, we have adopted another approach to directly measure the capture rate. By recording $I(Z)$ curves in the band gap region up to the bottom of the conduction band, we observe in Fig. 4.19, that the variation of the current intensity deviates from a characteristic exponential increase [147] [80] [81], with the exception of the $I(Z)$ curves acquired with voltages higher than +1.2 V. For these voltages, an exponential increase is seen after a first plateau and corresponds to the contribution of conduction band states to the tunneling current, due to a stronger downward band bending when the tip becomes closer to the surface [130]. But, at lower voltages,

4.5 Probing the hole capture rate of a single Si dangling bond

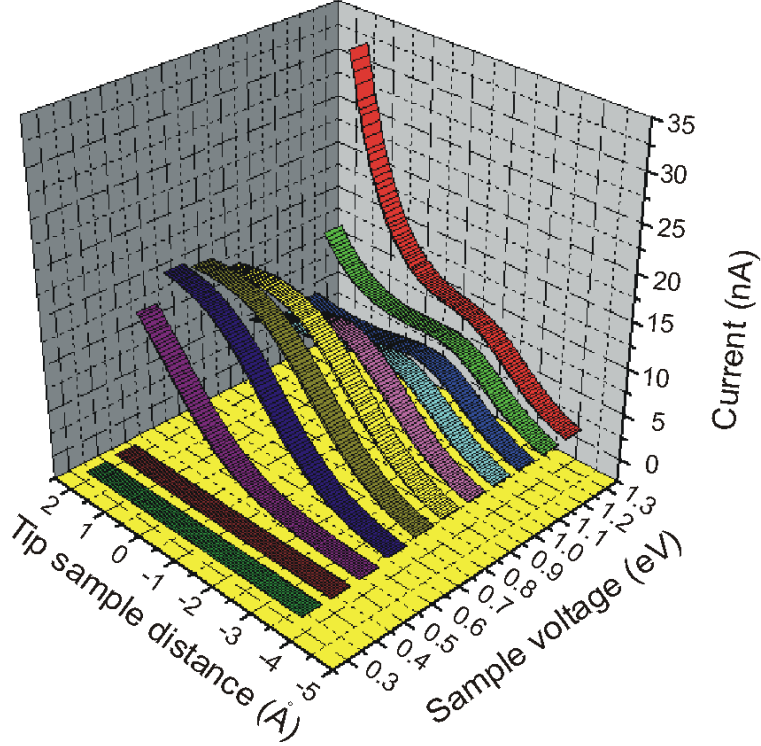


Figure 4.19: Tunneling current versus tip displacement at different V_{bias} . The feedback loop ($V_{bias} = +1.5V$; $I_{tunnel} = 5nA$) was first opened, V_{bias} was set to a voltage between $+1.3V$ and $+0.3V$ and the tip was displaced away from the surface by 3.7\AA , then moved forth and back by 6.0\AA (corresponding to the data shown) and finally returned to its initial position.

the downward band bending is not strong enough and transport occurs only through the vibronic states of the Si dangling bond down to $+0.5V$.

For these voltages, the current reaches a maximum value confirming the saturation observed in Fig. 4.19(a). The highest current intensity of $15nA$ is found for a voltage of $+0.6eV$. From this saturation value and the degenerate concentration of B dopants ($5^{+19}B.cm^{-3}$) in the sample (section 4.3, page 89), we estimate the capture coefficient (derived from eq. 4.31):

$$c_p = \frac{I}{-ep} \quad (4.32)$$

and find a value $c_p \approx 10^{-9}cm^3.s^{-1}$.

Although the capture coefficient is the meaningful physical quantity, it is rather common to introduce the capture cross-section to characterize the carrier trapping efficiency of a deep level [142]:

$$\sigma_p = \frac{c_p}{v} \quad (4.33)$$

CHAPTER 4. RUNNING CURRENT THROUGH AN ISOLATED LOCALIZED STATE IN SILICON

v describes the mobility of the trapped hole in the valence band, it is generally taken as the average thermal velocity v_{th} . Its expression is given by:

$$v_{th} = \frac{\int v(E)n(E)(1 - f(E)) dE}{\int n(E)(1 - f(E)) dE} \quad (4.34)$$

where $1 - f(E)$ is the probability of finding a hole at the energy E , at the temperature T , described by the distribution of Fermi-Dirac; $n(E)$ is the density of states and $v(E)$, the velocity of a hole at an energy E which is assumed to be only related to kinetic energy. In the effective mass approximation, the density of states of a 3D system is proportional to \sqrt{E} and:

$$v_{th} = \sqrt{\frac{8k_B T}{\pi m_p^*}} \quad (4.35)$$

with m_p^* the effective mass of a hole.

A cross-section of $1.1 \times 10^{-16} \text{cm}^2$ is thus obtained and is quite in agreement with the theoretical prediction for the capture cross-section of a dangling bond in silicon [148]. Such value belongs also to the order of magnitude usually found experimentally for the capture cross-sections of deep levels in semiconductors [149, 150], like the Pb center, which consists of a dangling bond located at the $Si(111) - SiO_2$ interface and where σ_p was measured by deep level transient spectroscopy (DLTS) [151].

As σ_p is related to the extension of the deep level wave function when the level crosses the valence band to capture a hole while the lattice vibrates [149, 150], it is interesting to spatially resolve the square of the deep level wave function to compare its extent with σ_p . Assuming that the dangling bond can be modeled by a square well potential with spherical symmetry, due to the position of $E_0 = 0.4 \text{eV}$ far above the top of the valence band, the radius of the bound state is given by :

$$a = \sqrt{\frac{\hbar^2}{2m^*} E_0} \quad (4.36)$$

Taking $m^* = 0.36m_o$, we find $2a = 10.2 \text{\AA}$ for the diameter, in good agreement with the experimental value (Fig. 4.16(a)(inset)), indicating thus a strong localization of the state, as expected from the small magnitude of σ_p .

In contrast to the DLTS technique, which yields an average capture rate for all the deep levels of a space charge region, STM can readily probe individual deep levels. As shown in Fig. 4.20(a), three bright adatoms are visible. By performing spatial mapping of $I(Z)$ curves, we observe that the current intensity does not vary in the same manner for these three dangling

4.5 Probing the hole capture rate of a single Si dangling bond

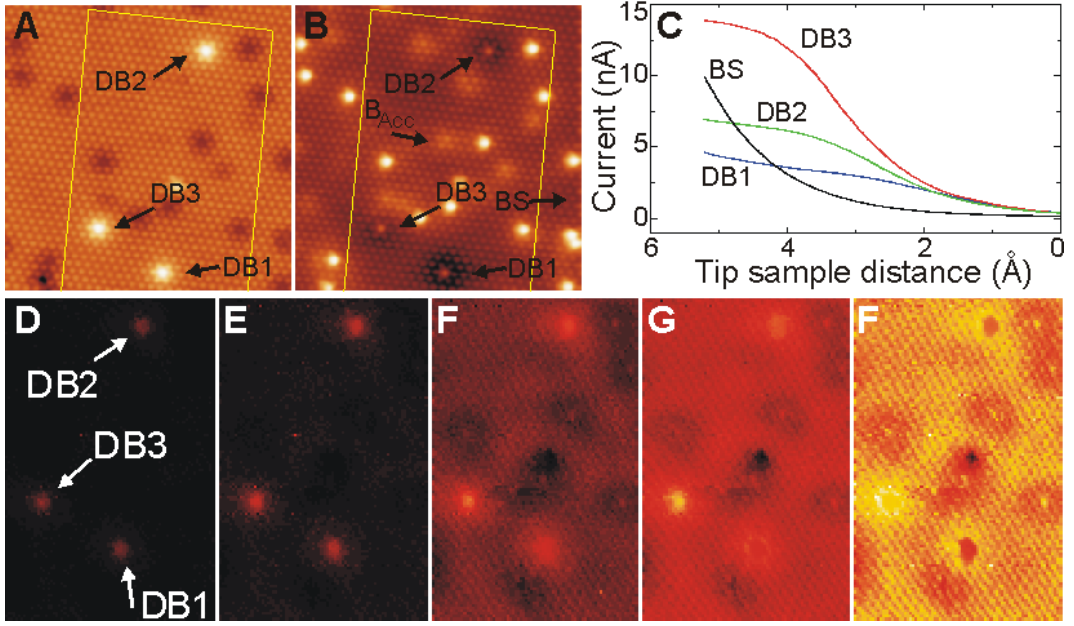


Figure 4.20: Variation in the saturation current for three non passivated bright Si adatoms labeled DB1, DB2 and DB3. (A) Empty state STM image ($V_{bias} = +1.4V$; $I_{tunnel} = 1nA$). (B) Filled state STM ($V_{bias} = -0.3V$; $I_{tunnel} = 1nA$), where a faint protrusion related to a subsurface B_{Acc} acceptor is indicated, as well as a passivated adatom BS away from any defects or subsurface dopant atoms. (C) Tunneling current versus tip displacement for the three Si bright adatoms and a passivated Si adatom of the bare surface (BS) at $V_{bias} = +1.2V$. (D) to (F) Spatial maps of the tunneling current versus tip displacement for distances of 1.07Å, 1.89Å, 3.05Å, 3.86Å, 5.17Å at $V_{bias} = +1.2V$ (feedback parameters $V_{bias} = +1.4V$; $I_{tunnel} = 1nA$).

bonds, as it is seen in the sequence of Fig. 4.20(d) to (h), corresponding to current intensity maps obtained at different tip-surface distances. For the dangling bonds labeled DB1 and DB2, their contrast begins to saturate after the tip has moved towards the surface by 3.05Å and 3.86Å respectively, while a halo, sign of saturation, is seen at a higher tip displacement for dangling bond DB3.

The saturation of the current intensity for the three dangling bonds is obtained from the plot of the $I(Z)$ curves in Fig. 4.19(c). We find that the current intensity at saturation is four times higher on DB1 than on DB3.

To avoid tip crash on regions of the sample where there is no state in the bandgap (passivated adatoms), spatial mapping of the $I(Z)$ curves can not be recorded at the energy E_0 , but at the edge of the conduction band. However, similar variations are found when single $I(Z)$ spectra are measured on different dangling bonds at the energy E_0 . Such results indicate thus that the capture rate depends on the environment of the dangling bond.

To understand such variations of the capture rate, Fig. 4.20(b) was acquired simultaneously with Fig. 4.20(a). In this filled state image, the three

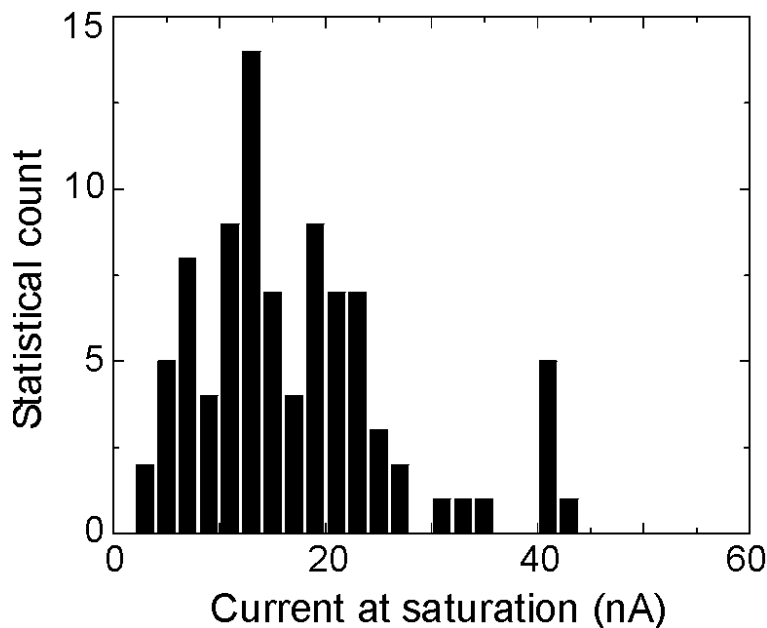


Figure 4.21: Distribution of the current intensity at saturation.

dangling bonds appear bright, but they are surrounded by a dark region, with different spatial extensions and depths. These regions are the signature of the Coulomb interaction between the charged dangling bonds and the free holes. The strength of this interaction is intimately related to the distribution of subsurface charged acceptors. As shown in section 4.3, the acceptors appear as bright protrusions superimposed to the atomic corrugation of the Si adatoms in the filled state STM image (Fig. 4.20(b)). Remarkably, two acceptors are found to be quite close from DB3, while no acceptor is visible around DB1. Such a distribution is quite consistent with the variation of the saturated current measured between the three dangling bonds and demonstrates that the potential fluctuations caused by the random distribution of B dopant atoms dramatically change the hole capture rate of a dangling bond.

By measuring similar $I(Z)$ curves over 90 dangling bonds, we found a distribution of the current intensities at saturation which is centred at 16 nA (Fig. 4.21). However, a few dangling bonds can bare currents with intensity higher than 40 nA, although the dangling bond states are electronically decoupled from any other state. While the result above demonstrates that the potential fluctuations caused by the random distribution of B dopant atoms can dramatically change the capture rate of a dangling bond, further work is needed to understand the interplay between variations in the potential landscape and the probability that the energy level of the dangling bond crosses

a hole band state and indeed captures a hole.

4.6 Conclusion

The electron transfer process from the tip of a STM to a silicon sample *via* a dangling bond state was characterized in this chapter. We found that the system is an atomic double barrier tunnel junction with a particular property: the DB state in which the electron transits is not resonant with any electronic state of the sample.

It was thus shown that the transport properties of the system are totally dependent on the vibrations of the adatom bearing the DB state which absorbs the energy of the electron thanks to its harmonic oscillations.

The process is made of two steps that were clearly identified:

1. When the energy of the tip is resonant with a vibrationally excited DB state, an electron is transferred from the tip to the surface adatom.
2. The electron in the adatom then recombines non-radiatively with a hole which was captured from the valence band thanks to the energy released by the electron through vibrations.

Moreover, this second step was found to be very interesting because, when the tip is approached very close to the surface, the tunneling current becomes saturated by the finite concentration of holes. The value of the saturation indeed gives directly the value of the hole capture rate of an individual silicon dangling bond state. Such a precision was never reached before.

While the capture rate is measured in the case of a non radiative recombination process involving the emission of vibrations, this new method is expected to be valid for the direct measurements of a wide range of carrier dynamic processes between a bound state and a continuum of states. It should be thus quite suitable to explore the capture and relaxation of charge carriers for semiconductor quantum confined systems such as quantum dots and nanotubes.

Conclusion

The goal of this thesis was to investigate the electronic transport through nanoscopic systems by means of STM and STS.

The first chapter gave the principles of electron tunneling devices and reviewed the current advances in this field. After a demonstration of the principle of the DBTJ, a review of the experimental setups and results has shown that up to now, double barrier tunneling experiments performed on nanostructures involved only metallic electrodes. In order to keep the strong electron confinement in the nanostructures, they are often decoupled from the electrodes by a vacuum gap or an insulating layer. Nevertheless, resonant electron tunneling remained the major means of transfer for the electrons and inelastic tunneling –electron transport involving an energy transfer from the electron to the nanostructure– could be observed only as a marginal phenomenon. Among the different setups, STM showed great advantages because it combines topographic abilities, able to localize nanostructures at the atomic scale, with a spectroscopic mode, useful for local characterization of electronic transport.

STM relies on the tunneling effect, which is also the main effect allowing electron transport in nanodevices. The spatial dependence of the tunnel current allowed to image the matter at the atomic scale and to address single nanostructures with a sub-nanometric precision. Details on the STM principle of operation in both topographic and spectroscopic modes were described in the second chapter.

The spatial and spectroscopic abilities of the STM have then been demonstrated in the case of a first study where a single-walled carbon nanotube was inserted between a Au(111) sample and the STM tip. While STM images and spectra allowed to clearly identify the geometry and electronic properties of the system, we saw that an increased energy of the electrons can modify the structure of the SWCNTs. We thus investigated the creation and annihilation of defects on the wall of the SWCNTs in order to tune their electronic transport properties. The process of creation/annihilation was simply realized in-situ by applying voltage ramps on the tip-sample bias while

CONCLUSION

keeping the feedback loop of the STM closed. While the process is efficient, further investigations are required in order to identify the mechanism of creation/annihilation.

In a last chapter, transport experiments through a silicon dangling bond state lying in the energy gap of a semiconducting silicon sample were done. In this particular case, one could have expected an electron, tunneling from the tip to the dangling bond, not to be able to escape this isolated state. Astonishingly, we could measure very high tunneling currents through the dangling bond state. Inelastic electron tunneling spectroscopic measurements revealed a strong coupling of the electrons with the vibrational states of the silicon atom bearing a dangling bond state. The energy given by the electron to the atom could then allow the capture of a hole from the sample and its non radiative recombination with the electron. These experiments show that single atoms are able to carry a very high density of current: $15 \times 10^{-9} A$ in the area defined by the dangling bond wave function $1 \times 10^{-12} mm^2$ yields a density of current of $15 kA.mm^{-2}$! Moreover, we have shown that we can control the amount of inelastic current until saturation by changing the tip-atom distance. These results show that it is indeed possible to design highly efficient structures at the nanoscale.

While this experiment gave the evidence that an exclusively inelastic electron transport is possible in a well designed system, we want to apply this principle to more applicable systems like molecules or nanocrystals. We saw in the third chapter that molecules may be altered by high biases, but the effect of current can be the same. In order to evaluate the performances of such systems, we have recently investigated the growth of silicon nitride on a Si(111) surface to form a test sample for inelastic tunneling experiments on weakly coupled nanostructures.

Ultra-thin layers of Silicon Nitride (SiN) can be grown on Si(111) by exposition of the hot sample ($T = 830^\circ C$) to N^+ ions [152]. At low coverages, SiN forms triangles whose size and number depends on the annealing time of the sample. Fig. 4.22 shows a STM image of the surface obtained after nitridation. The SiN areas present a wide bandgap of approximately $4eV$, as shown in Fig. 4.23, consistent with the bandgap of Si_3N_4 [153, 154]. This wide bandgap is useful for the formation of a decoupling layer for the adsorption of nanostructures on the Si(111)- 7×7 which otherwise would be chemically reactive because of a high concentration of silicon dangling bonds [155].

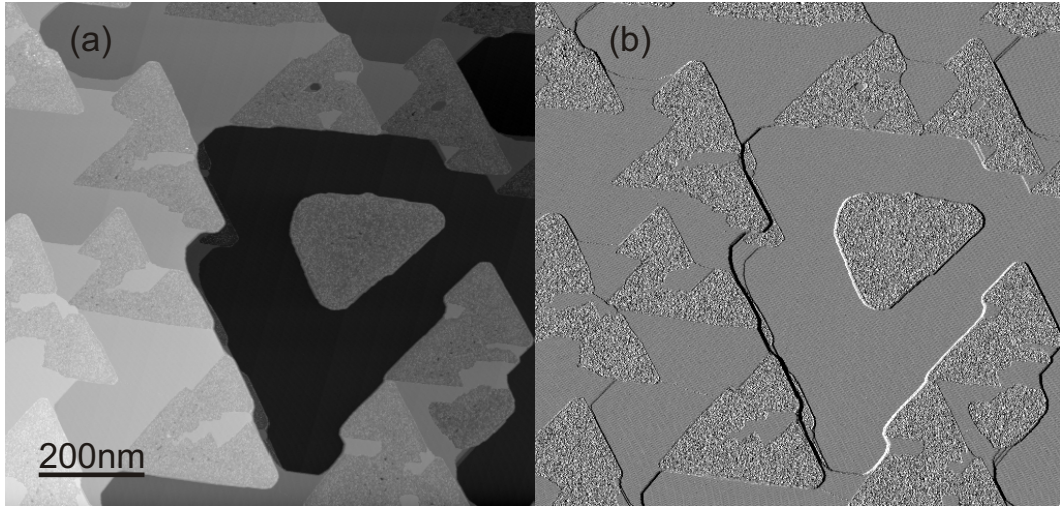


Figure 4.22: Large scale ($1000 \times 950 \text{nm}^2$) STM image of a Si(111) surface exposed to N^+ ions. (a) topography image; (b) current image. Noisy triangles appear at the edge of the atomic steps, they correspond to silicon nitride ultra-thin layers whereas the flat surface corresponds to the 7×7 reconstruction. $V_{bias} = -2.5V$, $I_{tunnel} = 10pA$.

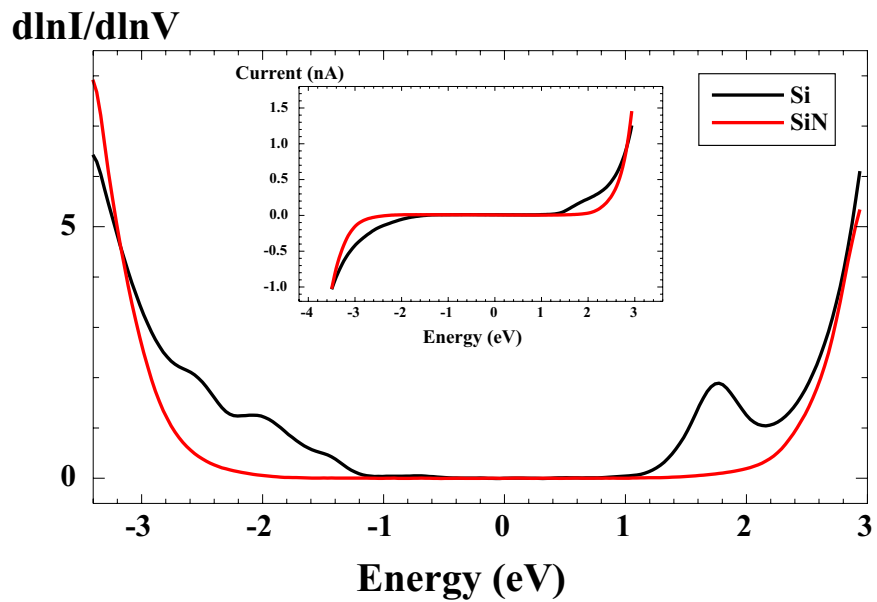


Figure 4.23: Normalized conductivity spectra obtained on Si(111)- 7×7 and on nitrogenated Si(111) at a temperature of 77 K. The tip height is fixed at the feedback conditions $V_{bias} = -3.5V$, $I_{tunnel} = 1nA$. Lock-in parameters: $V_{mod} = 12mV_{rms}$, $f = 2kHz$.

CONCLUSION

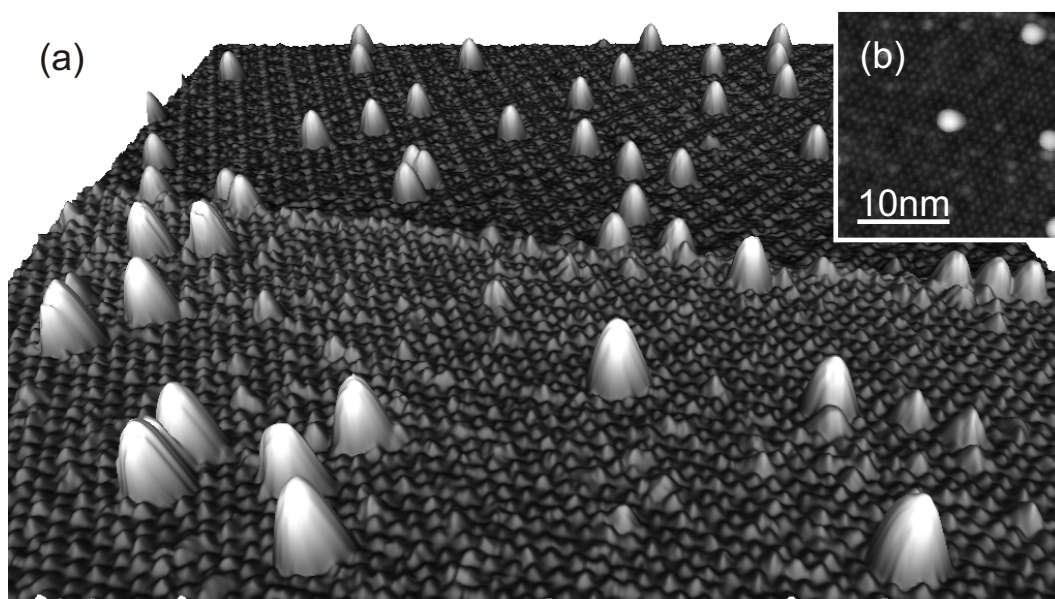


Figure 4.24: (a) STM topography image ($66 \times 66 \text{nm}^2$) of a silicon nitride ultra-thin layer (foreground) on Si(111) and of Si(111)- 7×7 (background). The white protrusions correspond to C_{60} molecules evaporated onto the surface at a submonolayer coverage. (b) Zoom ($25 \times 25 \text{nm}^2$) on the silicon nitride area, three C_{60} molecules are visible on the surface. $V_{bias} = -3V$, $I_{tunnel} = 1 \text{nA}$.

C_{60} molecules were deposited onto the sample at a sub-monolayer coverage as shown on Fig. 4.24 in order to make spectroscopic experiments on the single molecules. On this figure, one can see the Si(111)- 7×7 surface coexisting with the nitrated surface (foreground). On both surfaces, the molecules are imaged as spheric protrusions, as expected.

While the molecules were found to be stable on the bare silicon surface, their stability on nitride areas is less evident. Indeed STM images always show well defined spheres associated to the molecules while imaging the silicon surface but on SiN, the spheres can appear fuzzy.

Such sample should be suitable to study other nanostructures. It would offer an interesting opportunity to pursue the investigation of SWCNTs: in this case, the parts of SWCNTs that would lie on the SiN areas would increase the probability of charging effects and allow the observation of STM-induced luminescence.

Appendix A

Résumé de la thèse

Introduction

De l'invention du tube à vide au transistor, et du transistor au microprocesseur, l'augmentation des performances des composants électroniques a toujours été liée à leur consommation énergétique. Encore maintenant, la miniaturisation des parties actives de composants électroniques permet d'augmenter les performances et leur taille atteint l'échelle du nanomètre.

La réduction des dimensions n'a cependant pas que des avantages car des effets parasites naissent des faibles dimensions des composants et de leur faible séparation. Par exemple, la nature ondulatoire des électrons leur permet de traverser des barrières diélectriques de taille nanométriques. Ce phénomène cause des pertes par effet tunnel qui sont de moins en moins négligeables car elles augmentent au fur et à mesure de la réduction des dimensions. Une telle perturbation pourrait donc limiter les futurs projets de miniaturisation.

Inversement, l'exploitation de l'effet tunnel est aussi une grande opportunité, qui rend accessible la mesure du transport électronique quantique, dans des circuits nano-électroniques. La première exploitation du transport électronique quantique est due à L. Esaki, qui développa la diode tunnel en 1958 [1], et qui obtint le prix Nobel pour sa découverte en 1973. De tels composants reposaient sur des jonctions planaires d'épaisseur nanométrique, mais dont les dimensions latérales n'étaient pas nanoscopiques. La rapidité de ces composants pouvant atteindre plusieurs centaines de GHz, il est tout de même très encourageant de penser à leur évolution.

Mais l'exploitation de l'effet tunnel dans des systèmes dont les dimensions sont nanométriques dans plus d'une direction n'est pas facilement applicable. En effet, la fiabilité de systèmes tels une molécule ou un édifice fait d'un

nombre fini d'atomes n'a pas encore été caractérisée et l'on peut se demander la quantité de courant admissible avant leur destruction, si cette quantité est comparable aux systèmes actuels, et quels mécanismes seraient à l'origine du flux d'électrons. Le but de mon travail de recherche est d'explorer le transport électronique induit par l'effet tunnel dans de petits édifices pour répondre à ces questions.

Grâce aux avancées en techniques expérimentales, notamment l'invention du microscope à effet tunnel (STM) [2, 3, 4], il est devenu possible d'étudier le transport électronique au travers de structures dont les dimensions sont comparables au nanomètre. L'observation du confinement des électrons dans deux, voire trois dimensions a révélé les propriétés quasi-atomiques de certaines nanostructures [5], et permis l'espoir de façonner la matière à sa plus petite échelle. L'exploitation des propriétés de telles nanostructures donne un aperçu de l'avenir probable de l'électronique.

Quatre chapitres composent cette thèse, le premier rappelle les bases du transport électronique à travers les nanostructures et analyse les expériences déjà effectuées. Cette partie est suivie d'un chapitre donnant les détails sur les outils utilisés et montrant leur capacité à mesurer les propriétés électroniques de la matière à l'échelle atomique. Les troisième et quatrième chapitres sont dédiés à l'étude du transport à travers deux types de nanostructures et en conclusion, les premières tentatives d'utilisation d'un substrat permettant un fort découplage des nanostructures par rapport aux électrodes seront décrites.

Chapitre 1: Transport électronique dans des nanostructures faiblement couplées aux électrodes

Rappels théoriques

Le domaine du transport électronique à travers les systèmes quantiques étant en pleine effervescence, la première partie de cette étude (page 15) est consacrée à l'analyse de l'effet tunnel à travers des nanostructures. Cette partie a pour but de mettre en valeur la possibilité d'exaltation des propriétés électroniques intrinsèques d'une nanostructure si elle est convenablement découplée des électrodes. En effet, lorsqu'un nano-objet est isolé des deux électrodes, ce que l'on appelle une jonction tunnel double barrière (DBTJ) est formée. La partie 1.2, page 16 décrit de façon théorique le comportement d'un tel système. La Figure 1.1 (a), page 16, donne une représentation unidi-

mentionnelle de la DBTJ, où les électrons incidents, réfléchis et transmis sont représentés par des ondes planes progressives d'amplitudes respectives A_1 , B_1 et A_5 . Le coefficient de transmission des électrons à travers le système en fonction de leur énergie est donné par l'expression (1.11) et représenté dans la figure 1.2, page 19. Cette illustration montre une forte résonance à l'énergie E_0 qui constitue un canal privilégié pour le passage des électrons.

Le calcul du courant tunnel, en tenant compte de la température non nulle, est expliqué dans la section 1.2.2, page 19. Son expression est donnée par l'expression (1.16), avec le coefficient de transmission de l'expression (1.26), et donne une caractéristique en forme d'escalier visible dans la figure 1.4, page 23. Il est visible dans cette caractéristique que la forme en escaliers s'estompe lorsque la température augmente, rendant nécessaires les mesures à faible température. De plus, lorsque la température est suffisamment basse (inférieure à 100K), il est possible d'observer une résistance différentielle négative, c'est-à-dire une décroissance du courant alors que la polarisation augmente. Cette caractéristique est utile pour la conception d'oscillateurs par exemple.

En modélisant la DBTJ par le circuit électronique de la figure 1.5, page 25, il est aussi possible d'expliquer les phénomènes de charge. En effet, la section 1.2.3, page 24, montre que des interactions coulombiennes apparaissent lorsque la nanostructure est faiblement couplée à son environnement.

Caractérisation expérimentale d'une DBTJ

La partie 1.3, page 26, analyse des résultats expérimentaux déjà obtenus sur des configurations de type DBTJ. La conception d'électrodes séparées par un espace de taille nanométrique par lithographie [12], puis l'insertion de nanostructures entre ces électrodes est la façon la plus facilement intégrable de créer une DBTJ. Cependant, le dépôt de nanostructures dans l'espace restreint entre les électrodes manque de reproductibilité [11, 13] et l'épaisseur des barrières tunnel n'est pas réglable.

Par contre, l'utilisation de la sonde mobile d'un microscope à effet tunnel, même si elle est plus difficilement intégrable dans un circuit, permet de localiser des nanostructures déposées sur un substrat et d'étudier le transport électronique à travers celles-ci avec une reproductibilité atteignant 100%. Pour obtenir une structure de type DBTJ, le substrat est d'une importance primordiale car il doit être (semi)conducteur tout en n'étant que faiblement couplé à la nanostructure, pour ne pas en masquer les propriétés.

La solution communément adoptée est de faire croître une couche isolante ultra-mince sur le substrat afin de créer une barrière tunnel entre celui-ci et la nanostructure, la deuxième barrière étant constituée par l'espace séparant

APPENDIX A. RÉSUMÉ DE LA THÈSE

la sonde du microscope et la nanostructure. La largeur de cette deuxième barrière est configurable à souhait en modifiant l'intensité du signal de contre-réaction. Des exemples récents de substrats possédant une couche isolante sont donnés dans la section 1.3.3, page 28. Le substrat supportant la couche isolante peut être métallique ou semi-conducteur.

Il a été montré que quelques couches atomiques d'un matériau isolant suffisent pour obtenir une couche isolante à la surface d'un métal [41] et les meilleurs résultats obtenus jusqu'à maintenant sont la croissance de Al_2O_3 sur $NiAl(110)$ [29, 58, 59] et $NaCl$ sur $Cu(111)$ [60, 61]. Sur de tels systèmes,

- *Repp et al.* ont démontré l'observation d'orbitales moléculaires non perturbées de molécules individuelles de pentacene par STM à basse température [61]. La figure 1.6(a), page 30, montre les images obtenues comparées aux calculs théoriques de la forme des orbitales. Des spectres montrent de plus les pics attribués à ces orbitales.
- *Qiu et al.* ont étudié la fluorescence de molécules [29], toujours à basse température par STM grâce à un découplage du substrat métallique. La figure 1.6(b) montre des molécules individuelles déposées sur la surface $Al_2O_3/NiAl(110)$ et leur conformation respective. Au contraire, les molécules adsorbées sur la surface métallique $NiAl(110)$, aucune émission lumineuse n'est détectée.

Cependant, le caractère métallique du substrat sous-jacent privilégie le transport élastique des électrons, c'est-à-dire le transfert sans perte d'énergie des états pleins d'une électrode vers les états vides de l'autre électrode lorsque l'énergie des électrons entre en résonance avec les états de la nanostructure, voir la figure 1.8(a), page 33. Des contributions inélastiques au courant ont déjà été mesurées [29, 58], mais elle représentent une infime proportion des électrons. La maîtrise des procédés inélastiques est tout de même importante, car ils mettent en œuvre des propriétés intrinsèques à chaque molécule telles que la luminescence.

Pour ce faire, l'une des électrodes doit ne pas être métallique afin d'empêcher le transfert élastique des électrons à certaines énergies. La figure 1.8(b), page 33 montre un diagramme de cette configuration avec un substrat semi-conducteur sur lequel est présente une couche isolante. Cependant, aucune expérience n'a encore été menée sur des nanostructures déposées sur de tels substrats.

Pour certains types de nanostructures, il est même possible d'utiliser une barrière de vide entre la nanostructure et le substrat, c'est le cas des nanostructures unidimensionnelles (1D) tels les nanotubes de carbone [78].

Dans les chapitres suivants, l'étude des propriétés de transport de deux nanostructures sera donc menée à l'aide d'un STM. L'observation de phénomènes relevant d'un faible couplage entre la nanostructure et les électrodes est un des premiers objectifs de cette thèse.

Chapitre 2:

Microscopie et spectroscopie à effet tunnel (STM et STS)

L'effet tunnel

Dans le deuxième chapitre de ce mémoire (page 37), le principe sur lequel repose le STM à basse température est exposé. La première partie de ce chapitre est donc dédiée à l'effet tunnel, phénomène rendu possible par le comportement ondulatoire des particules, qui donne aux électrons la possibilité de traverser une barrière énergétique d'amplitude plus élevée que leur propre énergie. L'expression (2.7) donne la probabilité de transmission pour les électrons, dont le comportement est exponentiel en fonction de l'épaisseur de la barrière, comme illustré par la figure 2.2, page 39.

Le microscope à effet tunnel (STM)

La partie 2.2, page 40, donne le principe de fonctionnement du STM, microscope permettant d'observer la matière à l'échelle atomique. Le microscope est constitué d'une pointe conductrice, jouant le rôle de sonde, que l'on place en face de l'échantillon à analyser. Lorsque la séparation entre la pointe et la surface de l'échantillon est très réduite (de l'ordre du nanomètre, voir l'illustration 2.3, page 41), un courant tunnel est établi. Son expression, donnée par l'équation (2.12), montre la dépendance exponentielle du courant en fonction de la distance pointe surface et prouve que cela constitue un très bon signal de contre-réaction: une variation de 1Å change le courant d'un facteur 10. Mais la résolution verticale du STM ne serait rien sans sa résolution latérale, qui fut estimée à $\Delta x \approx 1.4\sqrt{R}$ par Tersoff et Hamann [83], avec R le rayon de courbure de la pointe. Cette estimation donne en fait une limite haute de la résolution atteignable car on sait aujourd'hui expliquer des résolutions expérimentales bien supérieures [84].

Le microscope utilisé dans cette thèse est un STM à basse température de la société Omicron. C'est un système opérant dans l'ultra-vide, dont la pression de base est $5 \times 10^{-11}T$, composé de trois chambres indépendantes:

APPENDIX A. RÉSUMÉ DE LA THÈSE

- un sas d'introduction permet d'entrer les matériaux dans le STM;
- une chambre de préparation permet le chauffage et le bombardement ionique des échantillons et des pointes;
- enfin, une chambre STM permet l'observation et la caractérisation des échantillons. Cette chambre possède deux cryostats pouvant être remplis d'azote liquide ou d'hélium liquide afin de faire des expériences respectivement à 77K ou 4K.

La spectroscopie à effet tunnel (STS)

Le STM offre aussi la possibilité de caractériser les propriétés électroniques locales des échantillons grâce au mode spectroscopique [86]. Ce mode d'opération est décrit en détails dans la partie 2.3, page 50. Il existe différents types de spectroscopie, mais la plus utilisée est la mesure du courant tunnel en fonction de la polarisation $I(V)$.

La spectroscopie $I(V)$ et la mesure conjointe de sa dérivée première (appelée conductance différentielle) grâce à une détection synchrone ("Lock-in technique", voir 2.3.2, page 55) donne des informations sur la densité locale d'états électroniques (LDOS) de l'échantillon étudié à l'échelle atomique, comme indiqué par l'équation (2.22), indépendamment du coefficient de transmission des électrons tunnel [87]. La valeur calculée s'appelle conductance différentielle normalisée. Pour éviter la divergence de la conductance différentielle normalisée sur les bords de bandes des semi-conducteurs, il est nécessaire d'effectuer encore un traitement décrit par l'équation (2.23) [89].

L'intérêt de la basse température en spectroscopie est décrit par la figure 2.8 qui montre que les spectres sont élargis à cause de l'agitation thermique des électrons à température non nulle. La résolution spectroscopique est donc directement reliée à la température de l'échantillon: la largeur minimale à mi-hauteur d'un pic vaut $fwhm = 3.2k_B T$, avec k_B la constante de Boltzmann et T la température de l'échantillon.

En plus de la dérivée première du courant, il est intéressant d'en mesurer la dérivée seconde qui donne des informations sur les transitions inélastiques lors du transfert des électrons entre la pointe et l'échantillon [91]. Cette mesure est appelée IETS pour Inelastic Electron Tunneling Spectroscopy et est illustrée par la figure 2.10, page 58. Dans ce cas, la température est un facteur encore plus important puisque la largeur à mi-hauteur d'un pic vaut $fwhm = 5.44k_B T$.

Il est à noter que l'utilisation de la détection synchrone amène, elle aussi, une diminution de la résolution des spectres de conductance différentielle et

des spectres IETS respectivement de $fwhm = 2eV_{mod}$ et $fwhm = 1.22eV_{mod}$, où V_{mod} est l'amplitude de la modulation appliquée au signal de polarisation.

Ces propriétés font du STM un outil majeur en nanotechnologie, qui offre l'avantage unique d'observer la matière dans l'espace direct et d'en mesurer les propriétés électroniques et vibrationnelles à l'échelle atomique. Le fonctionnement à basse température donne de plus accès à une spectroscopie de haute résolution énergétique, mise à profit dans les chapitres suivants.

Chapitre 3:

Défauts individuels dans les nanotubes de carbone simple-paroi

Dans le troisième chapitre (page 61), la caractérisation d'une nanostructure unidimensionnelle (1D) –le nanotube de carbone simple paroi (SWCNT)– inséré dans une jonction tunnel est expliquée, la première électrode étant la pointe métallique d'un STM et la seconde électrode étant un échantillon d'or plan.

Les nanotubes de carbone simple paroi (SWCNT)

Les SWCNT sont des molécules pouvant atteindre plusieurs micromètres de longueur avec un diamètre de l'ordre du nanomètre, la figure 3.1, page 62, en montre des images par microscopie électronique en transmission. Elles sont composées d'atomes de carbone arrangés suivant un réseau hexagonal et leur construction peut s'expliquer par l'enroulement d'une feuille de graphène, en joignant des points équivalents du réseau. De ce fait, la structure électronique d'un SWCNT est dérivée de la structure électronique du graphène (Fig. 3.2, page 63), en prenant en compte la direction d'enroulement qui impose une condition de périodicité sur le vecteur d'onde des électrons. Par conséquent, la structure de bandes des SWCNTs est unidimensionnelle (Fig. 3.3, page 65), elle indique un caractère conducteur ou semi-conducteur en fonction de la direction d'enroulement et du diamètre du SWCNT.

La figure 3.4 (a), page 66 [110], montre que la façon d'enrouler une feuille de graphène pour obtenir un nanotube peut être décrite de façon équivalente par l'angle d'enroulement Φ et le diamètre d du CNT ou par le couple (n,m) de coordonnées sur le réseau de graphène. Ces paramètres peuvent être identifiés par STM et STS [109, 110]. Le caractère métallique ou semi-conducteur d'un SWCNT peut être identifié grâce à ce couple (n,m) de la façon suivante : si $m - n$ est multiple de 3, alors le SWCNT est métallique,

APPENDIX A. RÉSUMÉ DE LA THÈSE

et dans le cas contraire, il est semi-conducteur. La bande interdite d'un tel SWCNT est donnée par l'expression (3.11).

Création et retrait de défauts sur les SWCNTs

La partie 3.2, page 69, montre qu'il est possible de modifier de façon réversible la structure locale d'un SWCNT à l'aide d'un STM. La figure 3.7, page 70, décrit la procédure suivie pour la création d'un défaut:

- la pointe du STM est immobilisée sur une partie exempte de défaut d'un SWCNT caractérisé auparavant;
- une rampe de tension est appliquée en plus de la polarisation entre la pointe et la surface, comme indiqué sur la courbe $V_s(t)$. Pendant cette rampe, la boucle de contre-réaction est maintenue, de ce fait la distance pointe-surface augmente afin de conserver un courant tunnel constant;
- à une certaine valeur de polarisation, un retrait brusque de la pointe est enregistré, il se traduit par un pic sur la courbe du courant $I_t(t)$ et une marche sur la hauteur de la pointe $Z(t)$;
- après cette rampe, la pointe continue d'imager le SWCNT et l'on observe une modification locale de la topographie du SWCNT (Fig. 3.7(a)).

La procédure suivie pour le retrait d'un défaut est identique et l'on peut voir une séquence d'images illustrant la création et le retrait successifs d'un défaut sur la paroi d'un SWCNT dans la figure 3.8, page 71.

Identification des défauts

Dans la partie 3.3, page 72, le type de défaut créé sur la paroi des SWCNTs grâce à la pointe du STM est analysé. Quelle que soit la pointe STM utilisée, quel que soit le SWCNT testé, quel que soit l'endroit où l'on applique la rampe de tension, la procédure est efficace et réversible (les défauts créés peuvent être supprimés), donc ce type de défaut ne doit pas provenir de l'inclusion ou du retrait d'atomes ou de molécules venant de l'extérieur mais doit conserver le même nombre de composants.

D'après des mesures spectroscopiques résolues spatialement (Fig. 3.9, page 73), des pics correspondant au caractère électronique du défaut sont identifiables dans la bande interdite du SWCNT.

Statistique de la création et du retrait de défauts

La figure 3.11, page 75 montre deux histogrammes représentant le nombre de défauts créés (en bleu) et le nombre de défauts annihilés (en rouge) en fonction de la polarisation entre la pointe et le SWCNT, obtenus sur une population de SWCNTs. Ces graphes montrent que l'énergie nécessaire à la création ou à l'annihilation d'un défaut est faible (inférieure à 10 eV) et comparable à l'énergie nécessaire pour induire la rotation d'une liaison carbone-carbone. Ces résultats sont donc en accord avec des défauts de type Stone-Wales.

En conclusion de ce chapitre, il a été montré que le transport électronique dans un tel système est dicté par la structure de bandes 1D du SWCNT. L'utilisation du STM comme outil de manipulation de la matière à l'échelle atomique a été démontré à travers la création et l'annihilation de défauts sur la paroi du SWCNT. L'influence des défauts sur les propriétés de transport du SWCNT a été directement observée. Ces expériences ouvrent la voie de la création d'interrupteurs moléculaires, dont la conductivité pourrait être modifiée par des rampes de tension.

Chapitre 4: Courant à travers un état localisé isolé dans le Silicium

Après avoir exploré les propriétés de transport électronique d'une nanostructure constituée d'une molécule faiblement couplée aux électrodes, dans un système où le transport résonant reste tout de même dominant, le quatrième chapitre (4, page 77) s'intéresse au cas où l'une des électrodes n'est plus métallique mais semiconductrice afin d'empêcher les phénomènes élastiques. En effet, si l'on considère un électron transféré de l'électrode métallique vers une nanostructure, sur un état électronique énergétiquement situé dans la bande interdite de l'électrode semiconductrice, il ne pourra quitter cette nanostructure que lorsqu'il aura trouvé un moyen de gagner ou perdre de l'énergie afin de se relaxer avec un état de l'électrode semiconductrice.

Un atome de silicium portant un état électronique énergétiquement découplé de tout autre état sur une surface Si(111) est l'objet de l'étude menée dans ce chapitre. Ce système possède les propriétés évoquées ci-dessus, le STM est donc exploité pour déterminer la façon dont le courant est établi.

Structure électronique de la surface Si(111)-($\sqrt{3} \times \sqrt{3}$)R30°-B

Le silicium, substrat le plus utilisé dans la fabrication de composants semi-conducteurs, possède la structure diamant (Fig. 4.2, page 79). La partie 4.2, page 79, décrit la surface du silicium suivant le plan (111).

Plus particulièrement, la reconstruction ($\sqrt{3} \times \sqrt{3}$)R30°-B de cette surface a été étudiée. Cette reconstruction peut être obtenue en chauffant un substrat de silicium fortement dopé par des atomes de bore, accepteurs d'électrons (dopage de type P). Le chauffage provoque une ségrégation des impuretés dans une couche atomique sous le plan (111) de surface jusqu'à saturation (1/3 de monocouche) comme illustré par la figure 4.3, page 81 (les atomes bleus représentent les atomes de bore, les atomes roses sont les atomes de silicium de la même couche, les atomes rouges sont les atomes de silicium de la couche supérieure, représentant la surface non-reconstruite.). La surface reconstruite, visible par STM dans la figure 4.4, page 83, est constituée d'un atome de silicium adsorbé sur chaque site T4 : au dessus de chaque atome de bore.

Chaque atome de la surface reconstruite est lié aux trois atomes de silicium sous jacents et, le silicium possédant quatre électrons de valence, un transfert de charge avec les atomes de bore achève de passiver les liaisons pendantes de cette surface. Elle est donc chimiquement non-réactive et se pollue lentement. Les spectres STS acquis sur la surface (Fig 4.5, page 84) confirment les hypothèses précédentes :

- la conductance différentielle normalisée présente les états de la bande de valence à gauche et les états de la bande de conduction à droite, le gap de 1,3 eV est vide d'état et le niveau de Fermi est situé près de la bande de valence, ce qui correspond à un substrat dopé P;
- la présence d'un pic 0,4 eV au dessus du minimum de la bande de conduction concorde avec les résultats théoriques et expérimentaux obtenus dans d'autres laboratoires [127, 128, 125] (Fig. 4.6, page 84) et correspond à une bande d'états vides résonante avec la bande de conduction à cause du transfert de charge de Si vers B.

Identification d'accepteurs sous la surface

Grâce à la passivation de la surface décrite précédemment, le potentiel de Coulomb créé par la charge portée par chaque dopant dans le substrat n'est que faiblement écranté. De ce fait, les dopants peuvent être imagés par STM par l'influence locale de leur potentiel de Coulomb écranté. La figure 4.7,

page 86, montre deux images STM à des polarisations différentes où l'on voit les dopants. Grâce à leur forme et à leur intensité, il est possible de connaître la profondeur de chaque dopant situé entre cinq et neuf couches atomiques sous la surface et d'en calculer la concentration (Fig. 4.8, page 87). La concentration de dopants à partir de la sixième couche sous la surface a été évaluée à $5,1 \times 10^{19} \text{cm}^{-3}$ et forme une bande dégénérée d'états accepteurs proche du maximum de la bande de valence.

Passage du courant à travers une liaison pendante de silicium non passivée

Sur les images STM de plus grande dimension, en plus des dopants, il existe une petite quantité d'ad-atomes plus clairs que les autres. La figure 4.10, page 89, montre deux de ces ad-atomes dans une image STM. La partie 4.4, page 89, est consacrée à l'identification des mécanismes permettant le passage du courant à travers ces ad-atomes clairs.

Contrairement aux ad-atomes sombres, les mesures spectroscopiques effectuées sur les ad-atomes brillants révèlent la présence d'un état électronique dans la bande interdite du semi-conducteur (Fig. 4.11, page 90). Un tel pic reflète la contribution au courant tunnel d'un état de liaison pendante de silicium non passivé par un atome de bore. Même si l'intensité du pic explique le caractère plus brillant de ce type d'ad-atomes sur les images topographiques, il est étonnant d'observer un courant aussi intense (plusieurs nano-Ampères) à travers un état découplé de tous les autres puisqu'il est dans la bande interdite.

L'explication d'un tel courant et de la forme gaussienne du spectre associé à cet état vient d'une forte excitation vibrationnelle de l'ad-atome isolé quand sa position d'équilibre est perturbée par le transit d'un électron. En effet, lorsqu'un électron vient charger l'ad-atome portant une liaison pendante, celui-ci se déplace vers une nouvelle position d'équilibre en se comportant comme un oscillateur harmonique. L'absorption de l'énergie de l'électron par l'amortissement des vibrations de l'ad-atome permet la capture d'un trou de la bande d'accepteurs et la recombinaison de l'électron avec ce trou. La figure 4.15, page 98, montre un spectre IETS mesuré sur un ad-atome portant une liaison pendante; la série de pics visible sur la dérivée seconde correspond aux niveaux d'énergie de l'oscillateur harmonique quantique associé à l'ad-atome. L'espace entre chaque pic et la comparaison des résultats à des simulations montre un couplage fort des électrons avec un mode de vibration de l'ad-atome dans la direction normale au plan (111).

Le passage du courant à travers un ad-atome de silicium portant une

liaison pendante sur la surface Si(111)- $(\sqrt{3} \times \sqrt{3})R30^\circ$ -B nait donc de la possibilité de faire vibrer cet ad-atome grâce à un fort couplage électron-phonon. Pour aller plus loin, la partie suivante s'intéresse à la maîtrise de ce courant purement inélastique.

Efficacité de capture des trous par une liaison pendante de silicium unique

La partie 4.5, page 100 s'intéresse au contrôle du courant inélastique en faisant varier la distance pointe-surface du STM. En effet, lorsque la pointe, en résonance avec l'état de liaison pendante associé à un ad-atome, est approchée progressivement, le courant augmente exponentiellement puis atteint une valeur de saturation (Fig. 4.17, page 103). En décomposant le processus de passage d'un électron de la pointe vers le substrat en deux étapes, l'évolution du courant et le phénomène de saturation peuvent être expliqués:

- le transfert d'un électron de la pointe sur la liaison pendante est lié à la probabilité de transmission tunnel et dépend exponentiellement de la distance pointe-surface. Lorsque la pointe est loin de la surface, le courant est faible et dicté par ce processus;
- au fur et à mesure de l'approche de la pointe, le passage des électrons sur la liaison pendante est de plus en plus rapide. Pour qu'un courant soit possible, les électrons se recombinaient avec des trous capturés par la liaison pendante, cependant, il ne peut excéder un maximum qui dépend de la concentration d'accepteurs p sous la surface et du taux de capture de trous c_p .

La concentration d'accepteurs p est une valeur connue puisqu'elle a été déterminée ci-dessus, mais le taux de transfert c_p n'a jamais pu être mesuré sur une liaison pendante unique. La figure 4.21, page 108, est un graphe de la distribution des valeurs de saturation du courant sur 90 liaisons pendantes qui montre une valeur moyenne de 16 nA. Grâce à cette valeur du courant et à la concentration p , le taux de capture c_p d'une liaison pendante a été déduit et est en accord avec des résultats obtenus par le passé sur des jonctions planaires incluant un nombre infini de liaisons pendantes [148, 149, 150, 151].

Cette nouvelle méthode a été appliquée dans cette thèse à un processus de recombinaison non-radiative sur un seul atome, mais elle pourrait aussi être employée sur d'autres systèmes confinés tels des nanofils ou des nanocristaux pour en étudier la dynamique des porteurs.

Conclusion

Dans l'espoir d'appliquer la technique développée au chapitre précédent à une plus grande variété de nanostructures, le développement de substrats semi-conducteurs comportant une couche isolante ultra-mince a été étudié. La figure 4.24, page 114, montre par exemple un substrat Si(111)-7x7 semi-conducteur (arrière-plan) sur lequel une couche isolante de nitrure de silicium a été fabriquée (premier plan). Les dômes blancs visibles sur cette image sont des molécules C_{60} qui ont été déposées sur le substrat en vue de tester leurs propriétés de transport inélastique.

Appendix B

List of publications

- Electron Transport via Local Polarons at Interface Atoms
M. Berthe, A. Urbieto, L. Perdigão, B. Grandidier, D. Deresmes, C. Delerue, D. Stiévenard, R. Rurali, N. Lorente, L. Magaud, and P. Ordejón
Physical Review Letters 97, 206801 (2006)
- Anisotropic Free-Electron-Like Dispersions and Standing Waves Realized in Self-Assembled Monolayers of Glycine on Cu(100)
K. Kanazawa, Y. Sainoo, Y. Konishi, S. Yoshida, A. Taninaka, A. Okada, M. Berthe, N. Kobayashi, O. Takeuchi, and H. Shigekawa
Journal of the American Chemical Society 129, 740 (2007)
- Reversible Defect Engineering of Single-Walled Carbon Nanotubes using Scanning Tunneling Microscopy
M. Berthe, S. Yoshida, Y. Ebine, K. Kanazawa, A. Okada, A. Taninaka, O. Takeuchi, N. Fukui, H. Shinohara, S. Suzuki, K. Sumimoto, Y. Kobayashi, B. Grandidier, D. Stiévenard, and H. Shigekawa
NanoLetters 7, 3623 (2007)
- Probing the carrier capture rate of a single quantum level
M. Berthe, R. Stiufiuc, B. Grandidier, D. Deresmes, C. Delerue, and D. Stiévenard
Science Express Reports, December 13, 2007 (Online publication)
Science 319, 436 (2008)

Electron Transport via Local Polarons at Interface Atoms

M. Berthe,¹ A. Urbietta,¹ L. Perdigão,¹ B. Grandidier,¹ D. Deresmes,¹ C. Delerue,¹ D. Stiévenard,¹ R. Rurali,²
N. Lorente,^{2,*} L. Magaud,³ and P. Ordejón⁴

¹*Institut d'Electronique, de Microélectronique, et de Nanotechnologie, IEMN (CNRS, UMR 8520), Département ISEN,
41 bd Vauban, 59046 Lille Cédex, France*

²*LCAR (UMR 5589), Université Paul Sabatier, 118 route de Narbonne, 31062 Toulouse, Cédex France*

³*Laboratoire d'Etude des Propriétés Electroniques des Solides (LEPES-CNRS), BP 166, 38042 Grenoble Cédex 9, France*

⁴*Institut de Ciència de Materials de Barcelona CSIC, 08193, Barcelona, Spain*

(Received 17 March 2006; published 13 November 2006)

Electronic transport is profoundly modified in the presence of strong electron-vibration coupling. We show that in certain situations, the electron flow takes place only when vibrations are excited. By controlling the segregation of boron in semiconducting Si(111)- $\sqrt{3} \times \sqrt{3}R30^\circ$ surfaces, we create a type of adatom with a dangling-bond state that is electronically decoupled from any other electronic state. However, probing this state with scanning tunnelling microscopy at 5 K yields high currents. These findings are rationalized by *ab-initio* calculations that show the formation of a local polaron in the transport process.

DOI: [10.1103/PhysRevLett.97.206801](https://doi.org/10.1103/PhysRevLett.97.206801)

PACS numbers: 73.43.Jn, 63.22.+m, 68.37.Ef, 73.63.-b

Electronic transport through atomic systems determines the way that devices behave on the atomic scale. This has important consequences in the development of molecular electronics [1]. Hence, the field of electronic transport on the atom scale is subject to great recent activity [1,2]. These efforts have permitted to understand how electronic current flows according to the geometry and the nature of the atomic components of the studied systems. Landauer theory has proven to be of great value in the rationalization of the many careful experiments addressing transport through a few systems [2]. However, this type of understanding needs to be revisited when vibrations affect electron transport.

The role of vibrations in electronic transport is thus attracting a lot of interest. Indeed, recent theoretical work [3] has shown that the coupling between electrons and vibrations can efficiently suppress the electron flow leading to a Franck-Condon blockade regime. This transport regime can have tremendous impact in the device's shot noise and the avalanche-like type of electron flow [4]. Interesting physics has been explored when combining electron-electron and electron-vibration interactions [5,6]. Regarding the electron-vibration strong-coupling regime, great theoretical interest has been devoted to the description of polarons as electronic excitations coupled with atomic vibrations [7,8]. Recently, using the lowest-order expansion (LOE) on the electron-vibration coupling, simulated inelastic electron tunnelling spectra have been successfully compared with experimental work [9]. Also at the *ab-initio* level, a detailed theory-experiment comparison within the LOE has been undertaken for a group of hydrocarbon molecules connected to gold electrodes [10]. A first all-order calculation at the *ab-initio* level [11] has permitted to gain insight in the intricacies of vibration excitation in ballistic conductance experiments [12]. Yet,

it is desirable to extend these studies to the strong-coupling limit where the above effects may take place.

Unfortunately, there are few conduction experiments dealing with the physical regimes explored in the limit of strong electron-vibration coupling. Wu and coworkers [13] have been able to explore the region of medium electron-vibration coupling by going into the limit of very weak molecule-electrode couplings. They show the dramatic signature of vibrations in electronic transport. To our knowledge, there is one only transport experiment where the regime of strong electron-vibration coupling has been attained. Repp *et al.* [14] give experimental evidence that the conductance dependence with voltage is modified by the electron-vibration interactions in such a way that the effect of the electronic structure behind the conductance behavior is not directly identifiable.

The present work addresses the physics treated in the above references [3–6] by providing electronic transport measurements in the presence of strong electron-vibration coupling in the basically ideal case of transport through a single atomic state, decoupled from other electronic states. The measurements are performed by using a scanning tunnelling microscope (STM) tip as an electrode and a passivated boron-doped Si(111)- $\sqrt{3} \times \sqrt{3}R30^\circ$ surface as the other electrode at 5 K. When a Si adatom is not passivated by the subsurface boron (B) layer, its electronic structure corresponds to a dangling-bond (DB) state energetically localized in the energy gap of the B-doped Si(111)- $\sqrt{3} \times \sqrt{3}R30^\circ$ surface. Hence, the electron current should be zero until the STM tip enters in mechanical contact with the adatom. Surprisingly, far before contact, the current easily reaches 1 nA. This is possible because of the large electron-vibration coupling on the adatom, leading to the formation of a local polaron. In the present case, not only does the electron-vibration coupling modify the

conductance spectrum, but it is strictly required to establish the current.

When a B-doped Si(111) crystal is heated, B dopants diffuse to the surface and replace Si atoms just under the adatom position. This process leads to charge transfer from the Si adatoms to the substitutional B atoms, making the adatom's DB state passivated [15]. By controlling the heating of the Si crystal, the number of substitutional B atoms can be tuned, so that only a few Si DB, bearing a localized state, are left.

Figure 1(a) shows a constant-current STM image of a B-doped Si(111) surface with the characteristic $\sqrt{3} \times \sqrt{3}R30^\circ$ reconstruction. The measurements have been performed at a temperature of 5 K. Most of the Si adatoms appear dark, consistent with the passivation of the DB states [15]. However, two isolated bright adatoms can be seen. Their corresponding DB wave functions are localized into the region defined by the six first surface neighbors of the adatom, giving rise to a bright flowerlike shape.

Superimposed to the contrast of the passivated DBs, faint dark depressions are observed in Fig. 1(a). They turn into protrusions when flipping the voltage sign to image filled states, Fig. 1(b). These features are the signature of subsurface dopant atoms [16,17]. They result from the local screened Coulomb potential-induced band bending surrounding the charged B impurities. Such impurities are lying at least four layers below the surface plane. Since in these four layers B impurities are located in symmetrical positions with respect to the adatoms, analyzing the corrugation profile across the protrusion allows the counting of the impurities in each layer [18]. Below the sixth layer, we estimate a concentration of $5.1 \times$

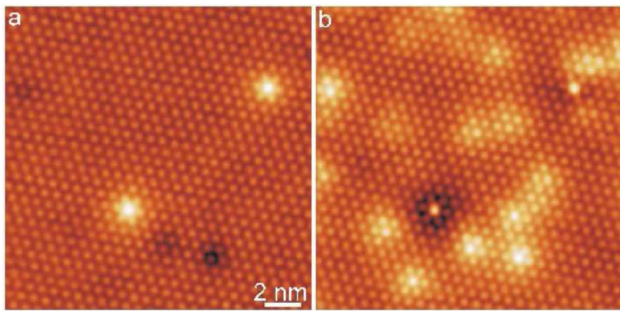


FIG. 1 (color online). Visualization of passivated and isolated Si dangling bonds on the Si(111) $\sqrt{3} \times \sqrt{3}R30^\circ$ -B surface observed at 5 K. (a) Empty state STM image. The majority of the adatoms appears dark (adatoms with B atoms underneath). Unlike these adatoms, two Si adatoms appear much brighter and correspond to a configuration with a Si atom underneath. The height difference between the dark and bright adatoms is 0.6 Å ($V_{\text{sample}} = +1.8$ V). (b) Filled state STM image of the same area ($V_{\text{sample}} = -0.4$ V). The numerous bright protrusions, which show a more or less dark contrast in the empty state image, correspond to subsurface B dopants, located at least 4 atomic layers below the surface.

10^{19} cm $^{-3}$, thus permitting the formation of a degenerated band of acceptor states positioned at the top of the valence band.

To establish a direct link between the adatom contrast and their electronic nature, differential-conductance spectroscopy measurements were done on dark and bright adatoms, Fig. 2. The spectrum acquired above a dark adatom site presents the Fermi level E_F positioned close to the top of the valence band, consistent with the formation of the just mentioned acceptor band. Two distinct features demonstrate that the dark Si DBs are electronically passivated: (i) the occurrence of a 1.3 eV gap and (ii) the presence of a strong peak positioned 0.4 eV above the bottom of the conduction band (CB) marked with an arrow, in agreement with the formation of an unoccupied band resonant with the conduction band due to charge transfer from Si to B [19]. In contrast, the spectrum on a bright adatom exhibits a distinct feature in the band gap region with respect to the dark adatom sites. A peak is now visible at an energy of 0.6 eV and is related to the contribution to the current of the non resonant DB state of the bright adatom. Such a strong peak in the band gap explains the topographical contrast between the two types of Si adatoms in the empty state images of Fig. 1(a).

Surprisingly, the isolated DB state can hold an electron current bigger than 1 nA at a temperature of 5 K. This finding is at odds with the above picture of a DB state in the surface band gap. In order to explain the experimental large current through the DB state, several mechanisms can be

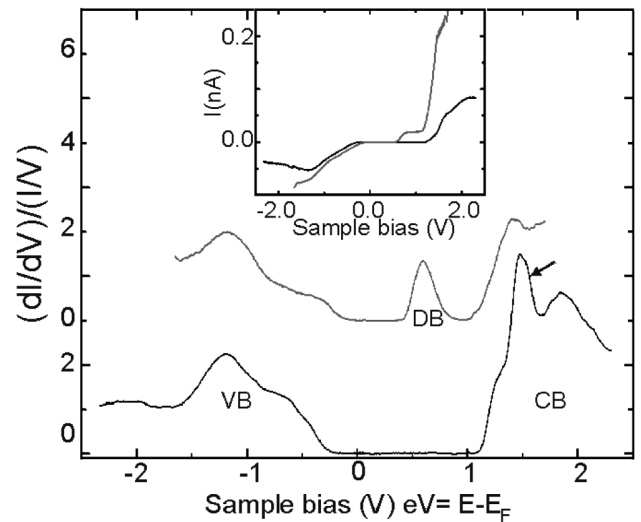


FIG. 2. Normalized conductivity spectra obtained on dark (black line) and bright (gray line) adatom sites at a temperature of 5 K. The peak related to the localized dangling-bond state, the conduction, and valence bands are, respectively, labeled DB, CB, and VB. The arrow points toward the peak related to the surface state band of the passivated dangling bonds. The tip's height is fixed at the feedback conditions (black line) +2.3 V, 80 pA and (gray line) +1.7 V, 250 pA.

invoked [20]: (i) hopping of the electron among the different DB states; however, this is not possible due to the small concentration of *bright* adatoms on the surface; (ii) thermal excitation of the electron towards the CB by phonon absorption; yet, this process can be ruled out at 5 K; (iii) as a result, only processes involving the recombination of the electron with a hole from the acceptor band are possible if the excess electron energy is absorbed by either photon emission or atomic vibrations. Considering a hole concentration of $5 \times 10^{19} \text{ cm}^{-3}$, a rough estimation of the recombination rate [21] for a radiative recombination yields 5 ms^{-1} . This rate is however many orders of magnitude too small to account for the measured currents that are in the range of 10 pA to 1 nA. Rather, the electron transfer takes place because the excess energy is given to local vibrations.

When a DB changes its charge state, the Si adatom is displaced [22,23]: its configuration coordinate, Q , varies from $Q = 0$ to $Q = Q^-$, Fig. 3. Since the electron transfer is much faster than the adatom relaxation, the negatively charged adatom is left in a vibrationally excited state. Next, the electron is transferred to an empty state of the acceptor band to recombine non radiatively with a hole. Thus, the

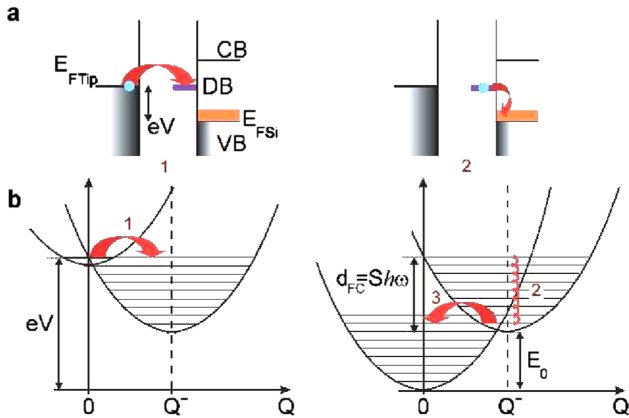


FIG. 3 (color online). (a) Energy diagrams sketching the two-step transport process: (1) the energy, eV , of the electron in the tip is tuned via the STM bias voltage, to become resonant with the dangling-bond state (DB) at a given vibrational state; (2) when sufficient energy has been transferred to the adatom, the probability of nonradiative transfer into the partially empty band of Boron impurities becomes high enough. The conduction and valence bands are, respectively, labeled by CB and VB, the tip and silicon Fermi levels by $E_{F\text{Tip}}$ and $E_{F\text{Si}}$. (b) Total energy curves as a function of the vibrational coordinate, Q , of the dangling-bond. On the left graph (process 1), the adatom in its ground state (top parabola) changes its charge state and its total energy corresponds to the bottom parabola, centered at $Q = Q^-$. On the second diagram, the adatom in the excited state (top parabola) may dissipate up to S quanta of vibration of energy $\hbar\omega$, corresponding to the Franck-Condon shift $d_{\text{FC}} = S\hbar\omega$ (process 2). Finally, the electron is transferred into the degenerated band of Boron impurities, leaving the adatom in a vibrationally excited state about its initial position (process 3).

adatom returns to its neutral oscillator state, centered at $Q = 0$, in a highly excited vibrational state. Eventually, the vibrational damping of the adatom can change the intermediate vibrational state.

To prove this mechanism, we measured d^2I/dV^2 spectra on bright adatoms. Figure 4(a) shows dI/dV and d^2I/dV^2 spectra acquired concurrently in the energy range of the peak labeled DB, in Fig. 2. In the d^2I/dV^2 curve, equidistant peaks are observed, suggesting the vibrational excitation of the adatom, when electrons tunnel into the DB state

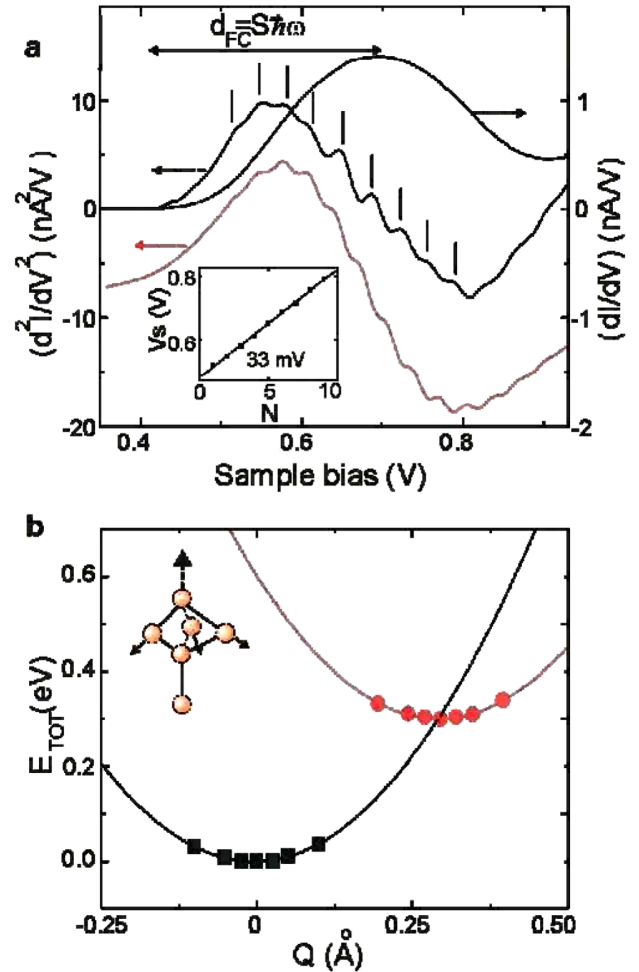


FIG. 4 (color online). (a) Experimental (upper) and calculated (lower) d^2I/dV^2 spectra, shifted for clarity and obtained on a bright adatom. The vertical lines indicate the position of equally spaced peaks in the spectrum. The Franck-Condon shift $d_{\text{FC}} = S\hbar\omega$ is deduced from the width at half maximum of the dI/dV peak. The curves were acquired with feedback parameters $V_{\text{sample}} = +1.5 \text{ V}$ and $I = 500 \text{ pA}$ at 5 K. Inset: Plot of the peak energy versus the peak number N for the vibronic progression, yielding the energy of the vibrational mode. (b) Total energy of a neutral (lower) and a negative charge (upper) dangling-bond, calculated by density functional theory, versus the lattice coordinate Q of the adatom (top atom in the atomic structure) for the stretching mode.

[13]. From measurements obtained on different bright adatoms, the peak spacing is found to be 31 ± 3 meV.

First-principles calculations [24] were used to determine both the electronic and vibrational structures of the bright adatoms that enter the simulation of the vibronic tunnelling current based on the tunnelling of an electron through a single site coupled to vibrations [25,26]. The calculations are performed for a DB state with and without an extra electron. The Huang-Rhys factor, S , is evaluated as the linear term of the harmonic fit to the total energy as a function of the configuration coordinate, Q , Fig. 4(b). Among all the local vibrational modes studied, only the stretching mode gives a strong electron-vibration coupling where $S = 9.6$. For this mode, a quantum of vibration of $\hbar\omega = 32.5$ meV is found. The lifetime of the electron in the dangling-bond is derived from Ref. [27]. The capture rate $W = 1/\tau$ is written as $W = pc_0R(T, E_0)$. The hole concentration p is obtained from the observed concentration of subsurface dopant atoms. We assume the capture coefficient c_0 to be close to its value for the Pb defect [28], i.e., the dangling-bond defect at the Si-SiO₂ interface. Finally, $R(T, E_0)$ is a dimensionless function which is explicitly given in Ref. [28] and depends on the temperature T and the ionization energy, E_0 , of the DB. Since the peak related to the DB state is positioned at an energy of 0.7 eV, and this energy corresponds to the sum of the Frank-Condon shift $d_{FC} = S\hbar\omega$ plus the ionization energy E_0 , we deduce E_0 to be 0.4 eV. An estimation of the electron lifetime in the DB yields a lifetime of the order of 10^{-12} s at 5 K leading to currents of 1 nA. Taking into account these values, the calculation of the d^2I/dV^2 spectrum was performed, with excellent agreement with experiment, supporting the assignment of the peaks in Fig. 4(a) to vibronic states.

In summary, by using a scanning tunnelling microscope (STM) tip as an electrode and a passivated B-doped Si(111) $\sqrt{3} \times \sqrt{3}R30^\circ$ surface as the other electrode at 5 K, the conductance of an unpassivated Si adatom was measured. The electronic structure of this *adatom* corresponds to a DB state energetically localized in the energy gap of the surface. Hence, this state is electronically decoupled from any other electronic state. Yet, we found large currents on the adatom DB that can be rationalized in a two-step picture: a tunnelling of the electron into the DB state and then its nonradiative recombination with a hole from the boron band. Our main finding is that the latter process is possible only if the adatom can absorb the electron excess energy by becoming vibrationally excited. This process is efficient enough only in the presence of a large electron-vibration coupling, giving rise to a polaronic-like conduction.

This work was supported by the European Community's Human Potential Programme under contract No. HPRN-CT-2001-00320, NANOSPECTRA, by DGES-Spain's No. BFM2003-03372-C03, by the Generalitat de

Catalunya (No. 2005 SGR 683) and by the French-Spanish bilateral programme PICASSO. R.R. acknowledges the financial support of the Generalitat de Catalunya (NANOTEC). Computational resources at the Centre Informatique National de l'Enseignement Supérieur and the Centre de Calcul Midi-Pyrénées are gratefully acknowledged.

*Corresponding author: Electronic mail: lorente@irsamc.ups-tlse.fr

- [1] A. Nitzan and M. A. Ratner, *Science* **300**, 1384 (2003).
- [2] N. Agraït, A. Levy Yeyati, and J.M. van Ruitenbeek, *Phys. Rep.* **377**, 81 (2003), and references therein.
- [3] J. Koch and F. von Oppen, *Phys. Rev. Lett.* **94**, 206804 (2005).
- [4] J. Koch, M.E. Raikh, and F. von Oppen, *Phys. Rev. Lett.* **95**, 056801 (2005); *Phys. Rev. Lett.* **96**, 056803 (2006).
- [5] P.S. Cornaglia, H. Ness, and D.R. Grempel, *Phys. Rev. Lett.* **93**, 147201 (2004).
- [6] Jens Paaske and Karsten Flensberg, *Phys. Rev. Lett.* **94**, 176801 (2005).
- [7] W. Koller, A.C. Hewson, and D.M. Edwards, *Phys. Rev. Lett.* **95**, 256401 (2005).
- [8] H. Ness and A.J. Fisher, *Phys. Rev. Lett.* **83**, 452 (1999).
- [9] M.-L. Bocquet, H. Lesnard, and N. Lorente, *Phys. Rev. Lett.* **96**, 096101 (2006).
- [10] M. Paulsson, T. Frederiksen, and M. Brandbyge, *Nano Lett.* **6**, 258 (2006); *Phys. Rev. B* **72**, 201101(R) (2005).
- [11] T. Frederiksen *et al.*, *Phys. Rev. Lett.* **93**, 256601 (2004).
- [12] N. Agraït *et al.*, *Phys. Rev. Lett.* **88**, 216803 (2002).
- [13] S. Wu *et al.*, *Phys. Rev. Lett.* **93**, 236802 (2004).
- [14] J. Repp *et al.*, *Phys. Rev. Lett.* **95**, 225503 (2005).
- [15] I.-W. Lyo, E. Kaxiras, and Ph. Avouris, *Phys. Rev. Lett.* **63**, 1261 (1989).
- [16] P. Ebert, *Surf. Sci. Rep.* **33**, 121 (1999).
- [17] G. Mahieu *et al.*, *Phys. Rev. Lett.* **94**, 026407 (2005).
- [18] R.M. Feenstra, J.M. Woodall, and G.D. Pettit, *Phys. Rev. Lett.* **71**, 1176 (1993).
- [19] T.M. Grehk, P. Mårtensson, and J.M. Nicholls, *Phys. Rev. B* **46**, 2357 (1992); H.Q. Shi, M.W. Radny, and P.V. Smith, *Phys. Rev. B* **66**, 085329 (2002).
- [20] X. de la Broise *et al.*, *Phys. Rev. B* **61**, 2138 (2000).
- [21] C. Delerue, G. Allan, and M. Lannoo, *Phys. Rev. B* **48**, 11 024 (1993).
- [22] W.A. Harrison, *Surf. Sci.* **55**, 1 (1976).
- [23] M. Lannoo and P. Friedel, *Atomic and Electronic Structure of Surfaces* (Springer Verlag, New York, 1991).
- [24] J. Soler *et al.*, *J. Phys. Condens. Matter* **14**, 2745 (2002); <http://www.uam.es/siesta/>.
- [25] G.D. Mahan, *Many-particles Physics* (Plenum, New York, 2000).
- [26] M. Lannoo and J. Bourgoin, *Point Defects in Semiconductors* (Springer Verlag, Berlin, 1983).
- [27] C. Delerue, G. Allan, and M. Lannoo, *Phys. Rev. B* **48**, 11 024 (1993).
- [28] D. Goguenheim and M. Lannoo, *J. Appl. Phys.* **68**, 1059 (1990).

Anisotropic Free-Electron-Like Dispersions and Standing Waves Realized in Self-Assembled Monolayers of Glycine on Cu(100)

Ken Kanazawa, Yasuyuki Sainoo, Yasuaki Konishi, Shoji Yoshida, Atsushi Taninaka, Arifumi Okada, Maxime Berthe, Nobuhiko Kobayashi, Osamu Takeuchi, and Hidemi Shigekawa*

Institute of Applied Physics, CREST-JST, 21st Century COE, University of Tsukuba, Tsukuba 305-8573, Japan

Received August 31, 2006; E-mail: hidemi@ims.tsukuba.ac.jp

Knowledge and control of the self-organization of materials are the essential foundations not only for understanding the mechanism of the phenomenon but also for the development of functional materials and devices for practical applications. In fact, among the recent developments in nanoscale science and technology, the realization of new functions via self-organization is the basis of many brilliant innovations and is one of the main goals of researchers. Efficient use of the multifold characteristics of organic materials plays important roles.^{1–12}

The formation of nanostructures is achieved, in general, by controlling the direct and indirect interactions between building blocks, originating from, for example, electronic and conformational structures, strains, and chemical reactions. Recently, a selective supramolecular assembly of adsorbed molecules, for example, has been successfully produced through the chemical modification of functional groups.¹ For the further advance of the nanostructure-based functional devices, the understanding and control of the electronic properties of self-organized structures based on such a modification of interactions are key factors for success.

Here, we demonstrate a two-dimensional (2D) anisotropic electronic structure produced through the formation of a self-assembled monolayer (SAM) of glycine molecules on a Cu(100) surface. A standing wave originating from the 2D electronic structure was visualized, for the first time, for the SAM of organic molecules, and the anisotropic dispersion relations reflecting the structure of the SAM were obtained.

Glycine is the simplest amino acid and does not have any active functional groups except for the carboxyl and amino groups, which are common to all amino acids, and one of the fundamental components of biological molecules such as proteins and peptides. Glycine molecules are evaporated in a neutral form ($\text{NH}_2\text{CH}_2\text{COOH}$). When the substrate is maintained at room temperature (RT), the hydrogen atom in the carboxyl group is removed from the surface and glycine molecules are adsorbed in a glycinate form ($\text{NH}_2\text{CH}_2\text{COO}^-$).^{12,13} The two oxygen atoms in the carboxylate group and the nitrogen atom in the amino group, which are located on the top sites of Cu(100), are bonded to the Cu atoms, where the carboxyl and amino groups are negatively and positively polarized, respectively. Among the amino acids, glycine is the only molecule that does not have chirality, but enantiomeric isomers are observed on the Cu surface depending on the directional relationship of the two groups in the adsorbed form, as schematically shown in Figure 1c. The adsorption properties of this system are well characterized, indicating the importance of this material for understanding and application of the basic mechanism of the self-organization of a polarized molecule with chirality.

In addition to sample preparation, scanning tunneling microscopy and spectroscopy (STM/STS) measurements were performed under ultrahigh vacuum conditions (base pressure $< 1 \times 10^{-8}$ Pa). A Cu(100) clean surface was obtained after three cycles of Ar^+ ion

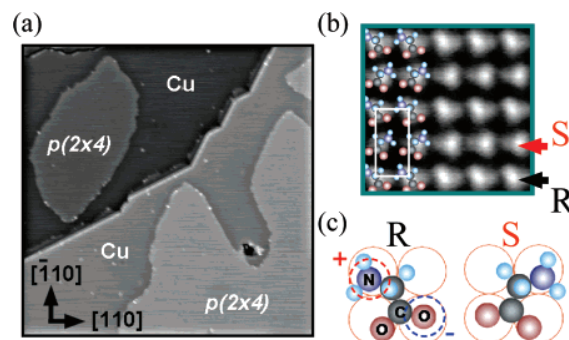


Figure 1. (a) STM image obtained at 5 K ($V_s = -100$ mV, $I_t = 1.0$ nA, 0.4 ML, 150×150 nm²). (b) Magnification of a $p(2 \times 4)$ area with molecular arrangement. (c) Two conformations of an adsorbed glycine molecule.

bombardment and annealing at 820 K. After the glycine source was outgassed by heating the Al_2O_3 crucible at 330 K for 5 h, glycine molecules were adsorbed on the substrate, where the source and Cu sample temperatures were maintained at 370 K and RT, respectively. Then STM/STS measurements were performed at 5 K using a tungsten tip.

Figure 1a is an STM image observed at 5 K of the surface prepared by the adsorption of 0.4 monolayer (ML) glycine. As illustrated in the magnified image (Figure 1b), there is a phase with a $p(2 \times 4)$ periodicity. While the $p(2 \times 4)$ structure is unstable at RT, isolated molecules are stable when the molecules are adsorbed at 5 K. Therefore, the $p(2 \times 4)$ phase structure is formed during the cooling of the sample after molecular deposition.¹⁴ The $p(2 \times 4)$ structure consists of alternately ordered two molecular rows along the [110] direction, which have two different molecular conformations as indicated by red (S) and black (R) arrows in Figure 1c, showing the existence of heterochirality for this structure.

This result indicates that the $p(2 \times 4)$ phase has the pseudo-(2×2) structure.¹⁵ As presented in Figure 1b, the STM image of molecular arrangement is in good agreement with that predicted by the theoretical simulation, and the molecular arrangement is shown (Figure 1b).

Figure 2a shows the $I-V$ (inset) and its derivative spectra obtained for a bare Cu substrate and the $p(2 \times 4)$ structure at 5 K. The $p(2 \times 4)$ structure exhibits a sharp peak near +130 mV. In order to investigate the origin of this signal, we measured the dI/dV images over the area presented in Figure 1a (lock-in modulation = 8 mV, 2.74 kHz, scan speed = 3 ms/pixel, 512×512 pixels).

As shown in the images in Figure 2b, a modulated local density of states (LDOS) is observed, which has a clear bias dependence.

From the bias dependence of the autocorrelations of the modulated LDOS (Figure 3a,b), we obtained nearly free-electron-like dispersion relations, as plotted in Figure 3c. Unlike the substrate symmetry, the dispersion relations are anisotropic, and the effective

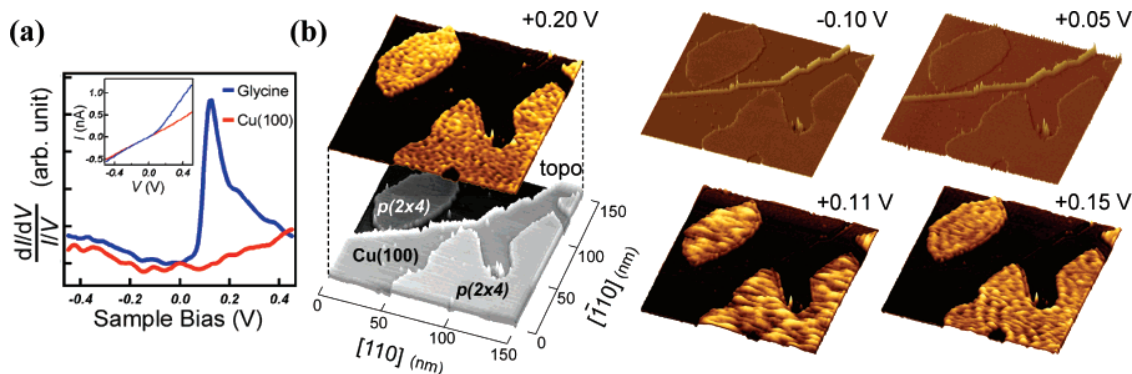


Figure 2. (a) I - V and STS spectra for the glycine $p(2 \times 4)$ structure and bare Cu(100) surfaces obtained at 5 K. (b) STM topographic and dI/dV images obtained at different bias voltages over the same area (set point: $V_s = -100$ mV, $I_t = 1$ nA, 150×150 nm²).

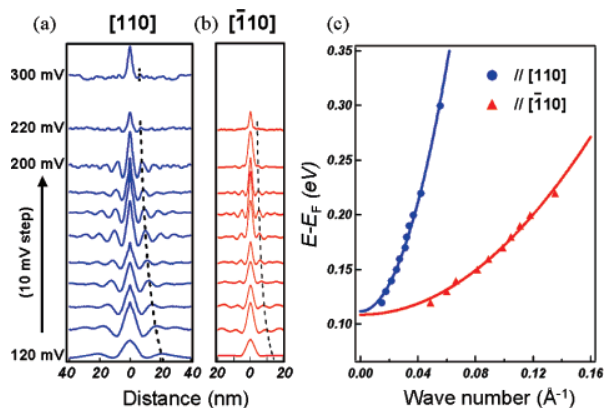


Figure 3. (a) Autocorrelations along (a) $[110]$ and (b) $[-110]$ directions, obtained from the 2D autocorrelation of the dI/dV images. (c) Dispersion relations obtained from the autocorrelations in (a) and (b).

masses obtained from the dispersion relations are $(0.061 \pm 0.002)m_e$ for $[110]$ and $(0.61 \pm 0.04)m_e$ for $[-110]$ directions.

The observed electronic structures are different from those that may be caused by the Cu(100) substrate, such as simple resonance. Therefore, the observed modulated LDOS can be attributed to the standing wave produced by the electronic states originating from the interaction between the glycine SAM and the Cu substrate. As have been observed, for example, on the (111) surface of noble metals, standing wave, the long-range modulation of LDOS, originates from the quantum interference of low-dimensional free electrons.^{16,17} However, this is the first result that demonstrates the formation of an anisotropic 2D electronic structure in the SAM of an organic material, reflecting the characteristics of the molecular arrangement.

The 10-fold difference in the effective masses is attributed to the anisotropy of the molecular interactions in the SAM; that is, the interaction along the molecular rows in the $[110]$ direction is stronger than the interaction between the molecular rows. In fact, although it is not shown here, the $p(2 \times 4)$ arrangement exhibited some phase defects formed by the substitution of a molecular row of one chirality with a molecular row of the other chirality (appearance of SSS or RRR ordering instead of SRS or RSR as in Figure 1b). This is likely because of a larger overlap of electronic states in molecules along the $[110]$ direction, originating from the carboxyl or amino groups in the molecules (Figure 1b).

The ability to control the electronic structures through chemical modification, for example, by changing functional groups and side chains, is a significant improvement in the design of interactions for producing desired electronic structures.

In summary, an anisotropic 2D electronic structure was formed using the self-organization of glycine molecules on a Cu(100) surface. From the analysis of the standing wave, observed for the first time in the SAM of organic molecules, anisotropic dispersion relations originating from the structure of molecular rows were successfully obtained.

Acknowledgment. This work was supported by a Grant-in-Aid for Scientific research from the Ministry of Education, Culture, Sports, Science, and Technology of Japan. We thank Ms. Rie Yamashita, in our group, for her help in preparing this paper.

Supporting Information Available: Procedure of the standing wave analysis. This material is available free of charge via the Internet at <http://pubs.acs.org>.

References

- (1) Yokoyama, T.; Yokoyama, S.; Kamikado, T.; Okuno, Y.; Mashiko, S. *Nature* **2001**, *413*, 619–621.
- (2) Harada, A. *Acc. Chem. Res.* **2001**, *34*, 456–464.
- (3) Barth, J.; Costantini, G.; Kern, K. *Nature* **2005**, *437*, 671–679.
- (4) Troisi, A.; Ratner, M. *Small* **2006**, *2*, 172–181.
- (5) Ulman, A. *Chem. Rev.* **1996**, *96*, 1533–1554.
- (6) Piva, P.; DiLabio, G.; Pitters, J.; Zikovskiy, J.; Rezaei, M.; Dogel, S.; Hofer, W.; Wolkow, R. *Nature* **2005**, *435*, 658–661.
- (7) Joachim, C.; Gimzewski, J.; Aviram, A. *Nature* **2000**, *408*, 541–548.
- (8) Rosei, F.; Schunack, M.; Naitoh, Y.; Jiang, P.; Gourdon, A.; Laegsgaard, E.; Stensgaard, I.; Joachim, C.; Besenbacher, F. *Prog. Surf. Sci.* **2003**, *71*, 95–146.
- (9) Lehn, J.; Atwood, J.; Davies, J.; Macnicol, D. *Comprehensive Supramolecular Chemistry*; Elsevier Science Ltd.: Oxford, 1996.
- (10) Xu, B.; Li, S.; Xiao, X.; Sakaguchi, H.; Tao, N. *Nano. Lett.* **2005**, *5*, 1491–1495 and references therein.
- (11) Tour, J. *Molecular Electronics*; World Scientific: River Edge, NJ, 2003.
- (12) Kang, J.; Toomes, R.; Polcik, M.; Kitterl, M.; Hoefl, J.; Efstathiou, V.; Woodruff, D.; Bradshaw, A. *J. Chem. Phys.* **2003**, *118*, 6059–6071.
- (13) Chen, Q.; Frankel, F.; Richardson, N. *Surf. Sci.* **2002**, *497*, 37–46.
- (14) In the initial stage of adsorption, two phases with $c(2 \times 4)$ or $p(2 \times 4)$ periodicity are observed at step edges of the Cu surface. However, the $p(2 \times 4)$ domains are selectively grown to form islands for higher amount of adsorption.
- (15) Mae, K.; Morikawa, Y. *Surf. Sci.* **2004**, *553*, L63–L67.
- (16) Park, J.; Ham, U. D.; Kahng, S.; Kuk, Y.; Miyake, K.; Shigekawa, H. *Phys. Rev. B* **2000**, *62*, R16341–R16344 and references therein.
- (17) Ono, M.; Nishigata, Y.; Nishio, N.; Eguchi, T.; Hasegawa, Y. *Phys. Rev. Lett.* **2006**, *96*, 16801 and references therein.

JA066318U

Reversible Defect Engineering of Single-Walled Carbon Nanotubes Using Scanning Tunneling Microscopy

Maxime Berthe,^{†,||} Shouji Yoshida,[†] Yuta Ebine,[†] Ken Kanazawa,[†] Arifumi Okada,[†] Atsushi Taninaka,^{††} Osamu Takeuchi,[†] N. Fukui,[§] H. Shinohara,[§] S. Suzuki,[§] K. Sumimoto,[§] Y. Kobayashi,[§] Bruno Grandidier,^{||} Didier Stiévenard,^{||} and Hidemi Shigekawa^{*,†}

Institute of Applied Physics, Crest, University of Tsukuba, Tsukuba, 305-8573, Japan, Department of Chemistry, Nagoya University, Nagoya, 464-86,2, Japan, NTT Basic Research Laboratories, NTT Corporation, Atsugi, Kanagawa 243-0198, Japan, and Institut d'Electronique, de Microélectronique, et de Nanotechnologie, IEMN (CNRS, UMR 8520), Département ISEN, 41 bd Vauban, 59046 Lille Cédex, France

Received July 28, 2007; Revised Manuscript Received October 15, 2007

ABSTRACT

The experimental creation and annihilation of defects on single-walled carbon nanotubes (SWCNT) with the tip of a scanning tunneling microscope are reported. The technique used to manipulate the wall structure of a nanotube at the atomic scale consists of a voltage ramp applied at constant tunneling current between the tip and the nanotube adsorbed on a gold substrate. While topographic images show an interference pattern at the defect position, spatially resolved tunneling spectroscopy reveals the presence of localized states in the band gap of the nanotube. Removal of the defect by the same procedure demonstrates the reversibility of the process. Such a precise control in the local modification of the nanotube wall opens up new opportunities to tailor SWCNT electronic properties at will.

Owing to their unique aspect ratio, single-walled carbon nanotubes (SWCNTs) have attracted considerable attention in the study of transport across one-dimensional systems.¹ The way they are wrapped not only determines their geometric properties but also their electronic structure: semiconductive or metallic. Such properties allow SWCNTs to be used as functional devices like transistors.² Recent studies have focused on the engineering of SWCNT properties such as the exploitation of intramolecular junctions³ or the modification of their band gap by the insertion of impurities: ions⁴ or molecules.⁵ Atomic defects are also investigated as good candidates for tailoring the electronic properties of SWCNTs; for example, Lee et al. observed deep and shallow levels associated with vacancy-atom and pentagon-heptagon defects,⁶ and Park et al. modulated the electron transmission probability of a defect by an electric field.⁷ Until now, several types of defects, like Stone-Wales defects,⁸ vacancies,⁹ ad-dimers,¹⁰ or H–C complex¹¹ could be introduced on SWCNTs by electron or ion sputtering.^{9,11,12} But the incorporation of defects in the nanotube generally

relies on macroscopic processes, which inherently involve the creation of several defects in the same nanotube with a large dispersion on their spatial distribution. Therefore no precise control of the creation or even removal of defects in a single nanotube has been achieved so far.

Because of the nanometer size of SWCNTs, scanning tunneling microscopy (STM) is a quite suitable technique for the investigation of the SWCNTs properties.¹³ It has been widely used to study their electronic structure as well as identify and characterize individual defects on their surface.¹⁴ More remarkably, it can also be used to manipulate SWCNT by locally cutting the tube for example.¹⁵ But to date this technique has not yet been proved to tailor the properties of SWCNTs without destroying them.

In this paper, we describe a method to selectively modify the electronic properties of semiconductor SWCNTs by the creation and destruction of point defects on their surface with an STM tip. The fabrication of the defects is detected from the measurements of the tip height variation when the sample voltage is increased to a few volts maintaining the tunneling current constant. The investigation of the defect nature by STM topographic images shows the formation of interference patterns on the nanotube wall, and spatially tunneling spectroscopic measurements reveal that this pattern is related

* Corresponding author. Website: <http://dora.ims.tsukuba.ac.jp>.

[†] University of Tsukuba.

^{††} Nagoya University.

[§] NTT Corporation.

^{||} IEMN (CNRS, UMR 8520).

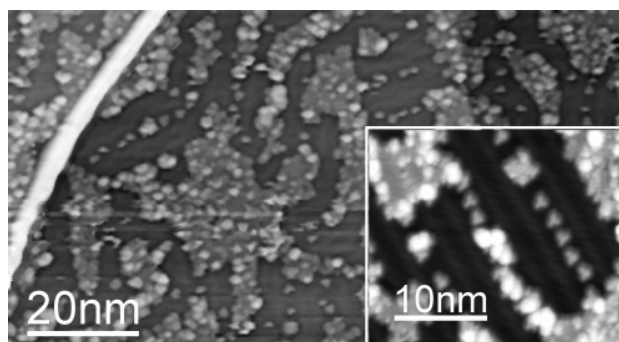


Figure 1. STM image of SWCNT deposited by the spin coating on a freshly cleaned Au(111) surface (sample voltage $V_s = -1$ V, tunneling current setpoint $I_t = 100$ pA, $T = 4$ K). Inset: High-resolution STM image of a smaller area partially covered with molecular species from the solvent ($V_s = 1.0$ V, $I_t = 100$ pA, $T = 4$ K).

66 to the presence of localized states in the band gap of the
 67 nanotube. Because the defects are removed by applying a
 68 similar voltage ramp, the controlled formation of localized
 69 states in the band gap of the nanotube indicates that the
 70 atomic scale modification of its electronic structure is fully
 71 reversible, providing new pathways to tailor SWCNT
 72 electronic properties.

73 The experiments were conducted with an Omicron LT-
 74 STM operated at 77 and 4 K on SWCNTs deposited by spin
 75 coating on freshly prepared and flame-annealed Au(111)
 76 samples. We used electrochemically etched PtIr and W tips,
 77 cleaned in ultrahigh vacuum (UHV) by heating and electron
 78 bombardment. HiPCO¹⁶ SWCNTs dissolved in chloroform
 79 and 1-2-dichloroethane were used at a concentration of 1
 80 $\mu\text{g}/10$ mL. Then the solution was ultrasonicated for more
 81 than 1 h to obtain individual nanotubes. After ultrasonication,
 82 one drop was deposited by spin coating on the freshly cleaned
 83 Au(111) sample. The samples were then introduced into
 84 UHV and degassed before the experiments.

85 Figure 1 shows a large scale STM image obtained after
 86 the deposition of SWCNTs on a Au(111) surface. A SWCNT
 87 is clearly visible on the left of the image, running along
 88 the edge of an atomic terrace. We note that the terraces are
 89 partially covered with molecules from the solvent. The
 90 observation of single molecules self-aligned in the face-
 91 centered cubic region of the herringbone reconstruction in
 92 the inset of Figure 1 reveals a ternary symmetry, suggesting
 93 the adsorption of chloroform molecules of the solvent during
 94 the deposition of SWCNTs.

95 After having identified the geometric properties of a CNT
 96 from its wrapping angle and its energy gap (for semiconducting
 97 CNTs) or low-conductivity zone (for metallic CNTs)
 98 based on established procedures,¹⁷ the STM tip was im-
 99 mobilized on a defect-free location on the SWCNT. The
 100 creation of protrusions on the nanotube wall was then
 101 performed using the method described in Figure 2. A voltage
 102 ramp was additionally applied on the sample voltage used
 103 to image a SWCNT, as shown by the curve labeled V_s . The
 104 typical sweep time was 0.1 s/V. During the voltage ramp,
 105 the feedback loop was kept closed and as a result, the tip-
 106 sample distance Z increased to keep the tunneling current I_t

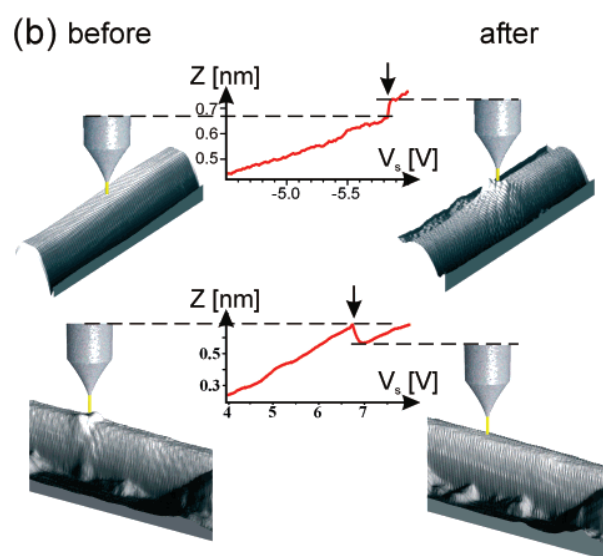
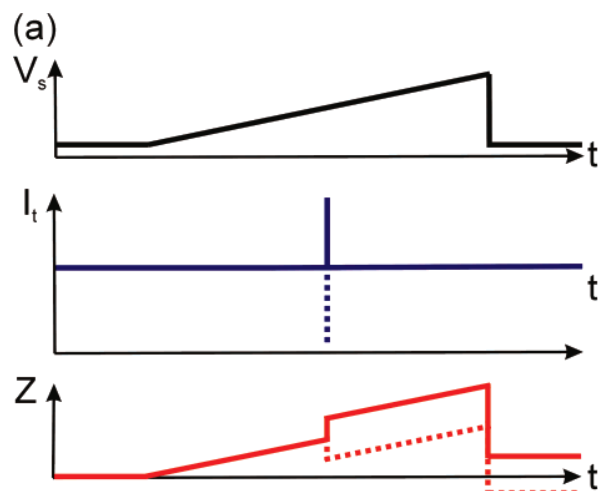


Figure 2. (a) Experimental scheme used to create a defect on a SWNT. The STM tip is first immobilized over a defect-free position at the surface of a SWNT. While maintaining the feedback loop close (I_t constant), the sample voltage V_s is usually ramped up to ± 8 V and both I_t and the tip height Z variation are recorded. At the time of the defect creation or annihilation, a sharp peak occurs on the tunneling current as well as a sudden shift of the tip height, away from the surface for the creation (continuous line), closer to the surface for the annihilation (dotted line). (b) STM images of a SWNT before and after the defect creation (top) or annihilation (bottom) along with a portion of the experimental $Z(V)$ curves showing a sudden shift of the tip height (vertical arrow), signature of the defect creation or annihilation (Feedback parameters: $V_s = -0.4$ V, $I_t = 200$ pA, $T = 4$ K).

constant. At certain bias, a sharp step appeared on Z 107
 indicating an additional backward shift of the tip from the 108
 nanotube. This step is the response of the piezo controlling 109
 the tip height to a pulse observed in the tunneling current 110
 while the sample voltage increases. After the voltage sweep, 111
 the tip started again scanning the nanotube. Figure 2b shows 112
 the modification of the nanotube when a negative sample 113
 voltage ramped is applied to a defect-free SWCNT. At a 114
 voltage of -5.8 V, an abrupt change in the linear behavior 115
 of the $Z(V)$ curve occurs. After this event, a deformation on 116

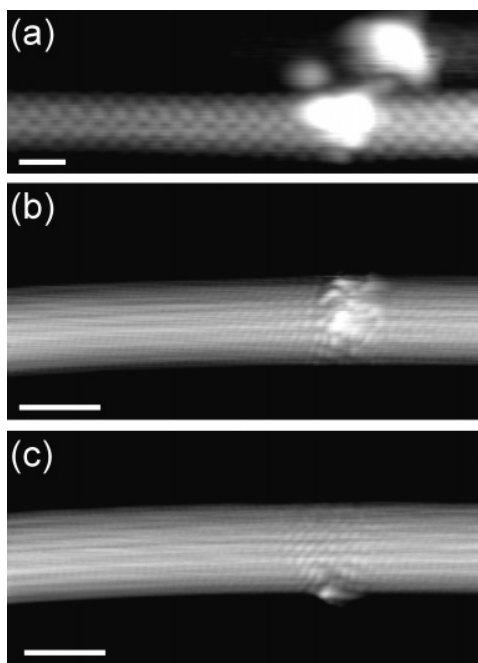


Figure 3. Examples of protrusions created by the tip and observed on the nanotube wall in topographic STM images. Protrusions are divided in (a) type A protrusions associated with adsorbates ($V_s = 1.0$ V, $I_t = 200$ pA, and (b,c) type B protrusions associated with point defects. ($V_s = -0.5$ V/ -0.8 V, $I_t = 100$ pA). Scale bar: 1 nm.

117 the nanotube wall is clearly visible at the position where the
118 voltage ramp was performed.

119 Similarly, applying a voltage ramp at constant current on a
120 protrusion created by the tip leads to the annihilation of
121 the protrusion and restores the defect-free structure of the
122 nanotube wall, as shown in Figure 2. We note that the voltage
123 threshold required to modify the nanotube varies and that
124 multiple events can sometimes occur in a single voltage
125 ramp, indicating both the creation and removal reactions
126 during the same voltage ramp.

127 The protrusions, which are created by this method, exhibit
128 different shapes that are visible in Figure 3. They can be
129 divided in two categories: protrusions that show an unper-
130 turbed structure of the nanotube lattice surrounding the
131 protrusion (type A) and protrusions which involve strong
132 distortion of the nanotube lattice (type B). An example of
133 type A protrusion is seen in Figure 3a, and we associated it
134 with the adsorption of a molecule onto the wall of the
135 nanotube.¹⁸ This molecule may diffuse from the Au(111)
136 surface to adsorb on the nanotube or may have been picked
137 up by the tip during scanning and is released on the nanotube
138 during the voltage ramp. In contrast, type B protrusions show
139 a lower contrast (see Supporting Information, Figure S4),
140 and the protrusions resemble those generally attributed to
141 point defects in the nanotube.^{6,14} They are found either on
142 top of the nanotube (Figure 3b) or on the sidewall (Figure
143 3c). As the interference pattern observed for these protrusions
144 suggests an electronic origin with the expectation of a strong
145 modification of the local density of states at the position of
146 the defect, we focus the rest of the paper onto type B
147 protrusions.

Nano Lett.

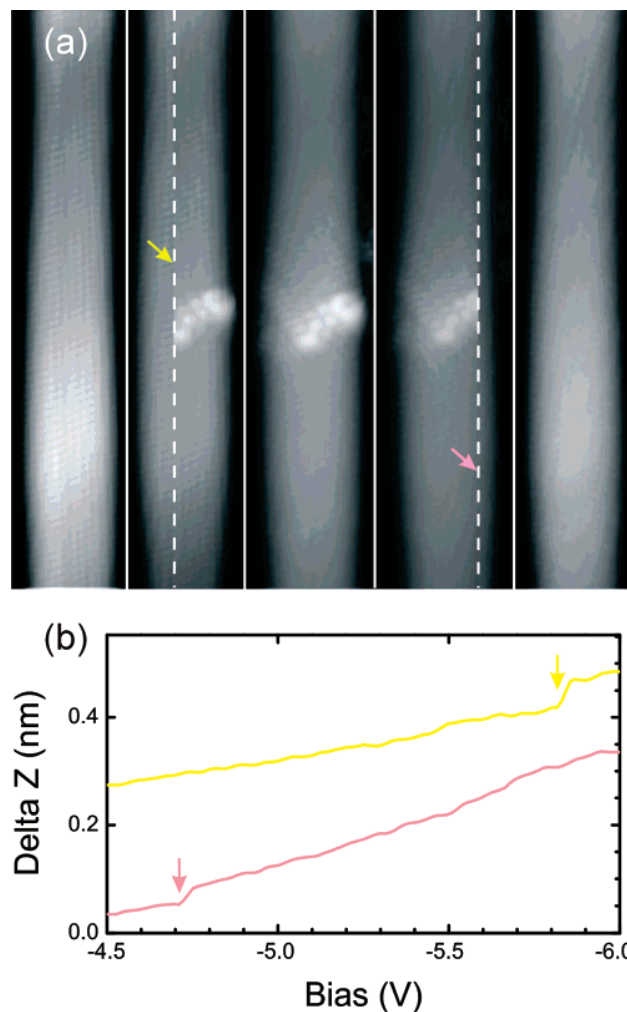


Figure 4. (a) From left to right: series of successive STM topography images (5×16 nm², $V_s = -0.4$ V; $I_t = 200$ pA) taken at $T = 4$ K at the same place on a (9,5) CNT before the creation of a defect, during the creation of the defect, with the created defect, during the removal of the defect, and after the annihilation of the defect. The scan direction for each image is from right to left. The dashed lines and the arrows indicate, respectively, when and where the voltage ramp was applied during scanning. (b) Portion of $Z(V)$ curves showing the characteristic step, indicated by a vertical arrow, and related to the local modification of the SWCNT. The upper curve corresponds to the voltage ramp used for the creation of the defect, and the gray one is for its annihilation.

148 Central to the work reported here is our ability to create
149 and subsequently remove a type B protrusion. An example
150 is given in Figure 4, where a defect-free nanotube is first
151 imaged and the voltage ramp is then turned on (upper curve
152 in Figure 4b). After the voltage is reset to its initial value,
153 a protrusion is visible in the middle of the nanotube. By
154 applying a second voltage ramp to the nanotube, the
155 protrusion disappears. Although the characteristic step in the
156 $Z(V)$ curve does not occur at the same voltage used for the
157 creation of the protrusion (lower curve in Figure 4b), the
158 nanotube recovers its initial crystallographic structure, as
159 shown in the last STM image of Figure 4a. Interestingly,
160 the example in Figure 4 illustrates that the creation or
161 removal of a defect does not always occur at the position

C

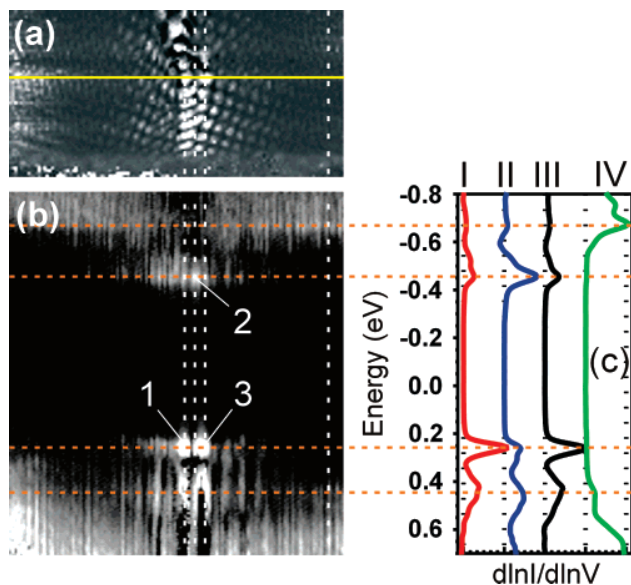


Figure 5. (a) dI/dV image acquired at $V_s = +0.4$ V in the region of the defect shown in Figure 4. The image is rotated by 90° with respect to the STM images of Figure 4. Feedback parameters $V_s = -0.9$ V, $I_t = 200$ pA, $T = 4$ K. Image size: 10 nm \times 5 nm. (b) Spatial variation of dI/dV as a function of the sample voltage acquired along the horizontal line in panel a. The four horizontal dashed lines indicate characteristic energy positions in the dI/dV curves: the upper and lower ones correspond to the band gap of the nanotube and the line in between corresponding to the defect states (areas 1, 2, and 3). (c) dI/dV curves corresponding respectively to the four vertical dashed lines running through the defect states (I–III from left to right) and a defect-free region (IV, upmost to the right) in panels a,b.

where the voltage sweep is applied, but a few nanometer apart. In that case, the annihilation of the defects might take place with a backward step of the Z piezo, instead of a decrease of the tip–sample distance as shown in Figure 2b.

Because the lattice distortion is likely to be caused by a local modification of the nanotube electronic structure, spatially resolved spectroscopic measurements were performed on the nanotube shown in Figure 4 between the creation and annihilation processes. Figure 5a shows the differential conductance imaged at 0.4 V in the area of the defect, where an interference pattern is clearly seen wrapping the nanotube, but spatially localized along the main axis of the nanotube. To get a better insight into the local variation of the SWCNT electronic structure, the variations of the differential conductance are plotted as a function of the voltage along a line running through the defect. As seen in Figure 5b, while the band gap of the nanotube is measured to be 1.13 eV in the defect-free region deduced from most external horizontal dashed lines, the dI/dV profile measured on the defect clearly shows intense signal in the band gap region of the nanotube at energies of at -0.45 and $+0.26$ eV. Those peaks, visible in Figure 5c, are quite localized along the main axis of the nanotube and are consistent with the position of the deep levels generally found for point defects related to vacancy–adatom pair or adatom–adatom complex in a nanotube.^{6,19,20} Although theoretical support is required to determine the precise nature of the defect created

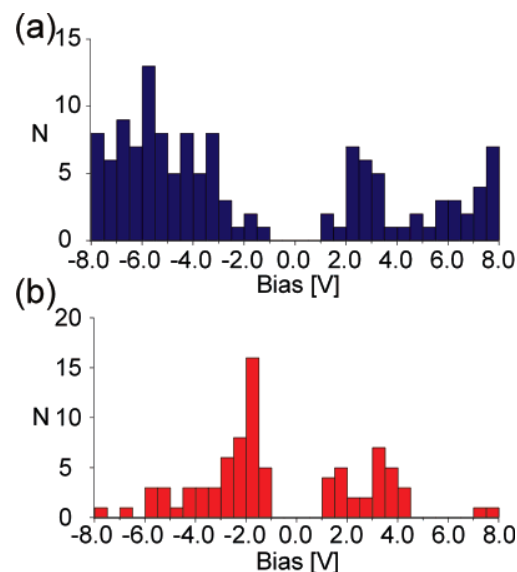


Figure 6. Distribution of the voltage thresholds for (a) creation and (b) annihilation events.

on this (9,5) nanotube, the spectroscopic measurements indicate that the creation of a type B protrusions causes a significant modification of the nanotube electronic structure, spatially localized at the location of the defect.

We have observed that the type B protrusions are stable for days if we do not apply a second voltage sweep to the nanotube and that it did not disappear due to thermal fluctuations event at room temperature. To further understand the creation and annihilation reaction discussed above, we examined the bias-voltage dependence of the reaction rates. For this purpose, the voltage ramps were applied on many nanotubes with different STM tips. The sample voltage was swept from ± 1.0 to ± 8.0 V with increasing absolute value of V_s in 1.2 s. During the voltage ramp, the tip–sample distance was feedback controlled with the reference tunnel current at 1.0 nA. All experiments were performed at 77 K. The histograms of the sample voltage thresholds at which the creation or annihilation events occur are shown in Figure 6.

The distribution of the voltage thresholds for the creation events does not mark a clear onset, although the creation of a defect is lower for smaller voltages. Conversely, the probability to produce an annihilation event is the highest at small voltages indicating therefore that the energy barrier height for the annihilation process is lower than the one for the creation process. Furthermore, it is worth pointing out that the measured voltage thresholds are smaller compared with the barrier energy for the removal of a carbon atom from a SWCNT, which was estimated to be 10 to 20 eV.²¹ Usually, for an accelerated electron to give this amount of energy to a CNT, electrons must be accelerated up to 100 keV.²¹ In contrast, the amount of energy needed to rotate a C–C bond in a nanotube wall or to create a point defect induced by a hydrogen ion is found to be compatible with the range of voltage thresholds shown in Figure 6.^{22,23} Although we cannot rule out that hydrogen ions may be produced by the voltage ramp due to their desorption from

226 molecular species in the vicinity of the nanotube and their
 227 further adsorption on the nanotube wall, the reproducibility
 228 of the defect shape for several successive creation events
 229 on the same nanotube favors the formation of defects related
 230 to the rotation of C–C bonds (see Supporting Information).
 231 Variability of the threshold voltages is also consistent with
 232 the variation of the energy barrier to create or annihilate point
 233 defects induced by different rotation of C–C bonds, whose
 234 formation energy depends on the helicity of the nanotubes.²⁴

235 In a conclusion, we propose a method to form point defects
 236 on the wall of a nanotube based on the application of a
 237 voltage ramp while the tunneling current is kept constant
 238 between the STM tip and the nanotube. The defects show
 239 localized states in the band gap of the nanotube, and
 240 spectroscopic studies as well as the analysis of the energetic
 241 distribution for the defect formation suggest the creation of
 242 defects induced by the rotation of C–C bonds, such as Stone-
 243 Wales defects. Remarkably, the defects are removed by the
 244 same methods, allowing the nanotube wall to recover its
 245 initial structure. Such a reversible manipulation of the
 246 nanotube wall should open the way to create confined regions
 247 within SWCNTs.

248 **Acknowledgment.** This work was supported in part by
 249 a Grant-in-Aid for Scientific research from the Ministry of
 250 Education, Culture, Sports, Science, and Technology of
 251 Japan.

252 **Supporting Information Available:** Figures showing
 253 different sequences of creation and annihilation events. This
 254 material is available free of charge via the Internet at [http://](http://pubs.acs.org)
 255 pubs.acs.org.

256 **References**

257 (1) (a) Iijima, S. *Nature* **1991**, *354*, 56. (b) Saito; R.; Fujita; M.;
 258 Dresselhaus, G.; Dresselhaus, M. S. *Appl. Phys. Lett.* **1992**, *60*, 2201.
 259 (c) Hamada, N.; Sawada, S. I.; Oshiyama, A. *Phys. Rev. Lett.* **1992**,

68, 1579. (d) Tans, S. J.; Devoret, M. H.; Dai, H.; Thess, A.; Smalley, R. E.; Geerligs, L. J.; Dekker, C. *Nature* **1997**, *386*, 474. 260
 261
 (2) Tans, S. J.; Verschueren, A. R. M.; Dekker, C. *Nature* **1998**, *393*, 262
 49. 263
 (3) Yao, Z.; Postma, H. W. Ch.; Balents, L.; Dekker, C. *Nature* **1999**, 264
 402, 273. 265
 (4) Zhou, C.; Kong, J.; Yenilmez, E.; Dai, H. *Science* **2000**, *290*, 1552. 266
 (5) Lee, J.; Kim, H.; Kahng, S. J.; Kim, G.; Son, Y. W.; Ihm, J.; Kato, 267
 H.; Wang, Z. W.; Okazaki, T.; Shinohara, H.; Kuk, Y. *Nature* **2002**, 268
 415, 1005. 269
 (6) Lee, S.; Kim, G.; Kim, H.; Choi, B. Y.; Lee, J.; Jeong, B. W.; Ihm, 270
 J.; Kuk, Y.; Kahng, S. J. *Phys. Rev. Lett.* **2005**, *95*, 166402. 271
 (7) Park, J.-Y. *Appl. Phys. Lett.* **2007**, *90*, 023112. 272
 (8) Stone, A. J.; Wales, D. J. *Chem. Phys. Lett.* **1986**, *128*, 501. 273
 (9) Smith, B. W.; Luzzi, D. E. *J. Appl. Phys.* **2001**, *90*, 3509. 274
 (10) Orlikowski, D.; Nardelli, M. B.; Bernholc, J.; Roland, C. *Phys. Rev. 275*
Lett. **1999**, *83*, 4132. 276
 (11) Nikitin, A.; Osagawara, H.; Mann, D.; Denecke, R.; Zhang, Z.; Dai, 277
 H.; Cho, K.; Nilsson, A. *Phys. Rev. Lett.* **2005**, *95*, 225507. 278
 (12) Krashennnikov, A. V.; Nordlund, K.; Keinonen, J. *Phys. Rev. B* **2002**, 279
65, 165423. 280
 (13) (a) Wildöer, J. W. G.; Venema, L. C.; Rinzler, A. G.; Smalley, R. 281
 E.; Dekker, C. *Nature* **1998**, *391*, 59. (b) Odom, T. W.; Huang, J.- 282
 L.; Kim, P.; Lieber, C. M. *Nature* **1998**, *391*, 62. 283
 (14) Ishigami, M.; Choi, H. J.; Aloni, S.; Louie, S. G.; Cohen, M. L.; 284
 Zettl, A. *Phys. Rev. Lett.* **2004**, *93*, 196803. 285
 (15) Rubio, A.; Apell, S. P.; Venema, L. C.; Dekker, C. *Eur. Phys. J. B* 286
2000, *17*, 301. 287
 (16) Martell, R.; Schmidt, T.; Shea, H. R.; Hertel, T.; Avouris, Ph. *Appl.* 288
Phys. Lett. **1998**, *73*, 2447. 289
 (17) Venema, L. C.; Meunier, V.; Lambin, Ph.; Dekker, C. *Phys. Rev. B* 290
2000, *61*, 2991. 291
 (18) Graupner, R.; Abraham, J.; Wunderlich, D.; Vencelova, A.; Lauffer, 292
 P.; Röhrl, J.; Hundhausen, M.; Ley, L.; Hirsch, A. *J. Am. Chem.* 293
Soc. **2006**, *128*, 6683. 294
 (19) Kim, H.; Lee, J.; Lee, S.; Kuk, Y.; Park, J.-Y.; Kahng, S. J. *Phys.* 295
Rev. B **2005**, *71*, 235402. 296
 (20) Buchs, G.; Krashennnikov, A. V.; Ruffieux, P.; Gröning, P.; Foster, 297
 A. S.; Nieminen, R. M.; Grönnig, O. *New. J. Phys.* **2007**, *9*, 275. 298
 (21) Banhart, F. *Rep. Prog. Phys.* **1999**, *62*, 1181. 299
 (22) Nardelli, M. B.; Yacobson, B. I.; Bernholc, J. *Phys. Rev. B* **1998**, 300
57, R4277. 301
 (23) Buchs, G.; Ruffieux, P.; Gröning, P.; Grönnig, O. *Appl. Phys. Lett.* 302
2007, *90*, 013104. 303
 (24) Zhou, L. G.; Shi, S.-Q. *Appl. Phys. Lett.* **2003**, *83*, 1222. 304
 NL071845C 305



Probing the Carrier Capture Rate of a Single Quantum Level

M. Berthe, *et al.*

Science **319**, 436 (2008);

DOI: 10.1126/science.1151186

The following resources related to this article are available online at www.sciencemag.org (this information is current as of January 25, 2008):

Updated information and services, including high-resolution figures, can be found in the online version of this article at:

<http://www.sciencemag.org/cgi/content/full/319/5862/436>

Supporting Online Material can be found at:

<http://www.sciencemag.org/cgi/content/full/1151186/DC1>

This article **cites 19 articles**, 3 of which can be accessed for free:

<http://www.sciencemag.org/cgi/content/full/319/5862/436#otherarticles>

This article appears in the following **subject collections**:

Physics

<http://www.sciencemag.org/cgi/collection/physics>

Information about obtaining **reprints** of this article or about obtaining **permission to reproduce this article** in whole or in part can be found at:

<http://www.sciencemag.org/about/permissions.dtl>

Probing the Carrier Capture Rate of a Single Quantum Level

M. Berthe, R. Stiuftuc,* B. Grandidier,† D. Deresmes, C. Delerue, D. Stiévenard

The performance of many semiconductor quantum-based structures is governed by the dynamics of charge carriers between a localized state and a band of electronic states. Using scanning tunneling spectroscopy, we studied the transport of inelastic tunneling electrons through a prototypical localized state: an isolated dangling-bond state on a Si(111) surface. From the saturation of the current at an energy resonant with this state, the hole capture rate by the dangling bond was determined. By further mapping the spatial extension of its wave function, the localized nature of the level was found to be consistent with the small magnitude of its cross section. This approach illustrates how the microscopic environment of a single defect critically affects its carrier dynamics.

A localized state in the band gap of a semiconductor is known to exchange carriers by the emission or capture of electrons/holes with conduction or valence bands, respectively. Because of the limited scale in the size of materials used in nanotechnology, such as quantum dots, nanocrystallites, and nanowires, developments in semiconductor devices critically depend on the ability to probe and understand the carrier dynamics between confined electronic states and the states in the bands of the semiconductor materials (1–3). So far, a common approach to study the probability (per unit of time) of carrier capture and emission has relied on the use of junction space-charge techniques, such as photocurrent and capacitance techniques (4). These techniques were first applied to point defects and interface states, which are generally referred to as “deep level” because the position of the energy level is far apart from both band edges (5, 6). But such techniques require the formation of a space-charge region, which is not always compatible with the current dimensions of single nanostructures. As a result of the size of the space-charge regions, junction techniques also inherently involve the integration of data over a large set of energy levels. Therefore, probing the carrier dynamics of a single deep level is still a challenge.

We report on the use of scanning tunneling microscopy (STM) to probe the hole capture rate of single deep levels with atomic-scale resolution. By saturating the injection of inelastic electrons into the deep level of a Si adatom in the boron-doped Si(111) ($\sqrt{3} \times \sqrt{3}$)R30° surface, we are able to measure the hole capture rate of a Si dangling-bond state and estimate its capture

cross section. Its magnitude is found to be consistent with the localization of the deep-level wave function, obtained from the spatial mapping of the differential conductance. Furthermore, by probing a large set of dangling bonds, significant variations in the capture rates are observed and related to the position of the B dopants below the surface. Such a result demonstrates the importance of the potential fluctuations induced by the random distribution of charged impurities on the carrier capture rate of single quantum levels.

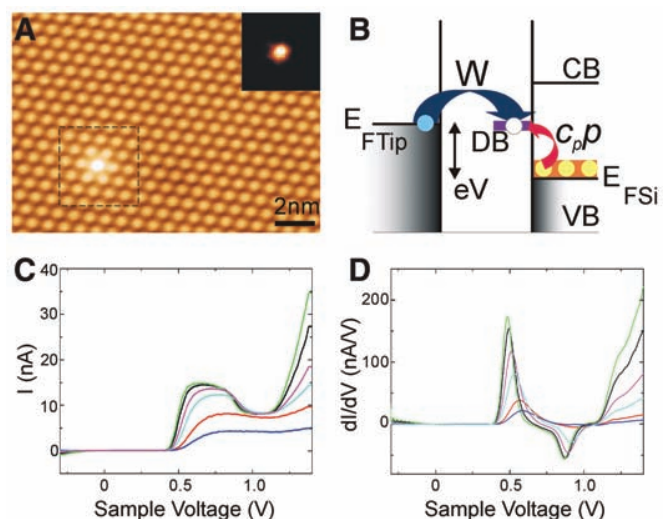
The experiments were carried out on a boron-doped Si(111) surface with a scanning tunneling microscope working at 77 K. As a result of the segregation of B atoms during the surface preparation at temperatures higher than 900°C, B impurities substitute for most Si atoms located just under the Si adatom position, causing the passivation of the adatom dangling-bond states

(7). However, for a few minority sites, the substitution does not take place, leaving their dangling-bond states localized in the band gap region of Si. Such an adatom appears bright in the empty-state STM image (Fig. 1A) (corresponding to a positive sample voltage), in contrast to the darker passivated adatoms (8). Performing spectroscopic measurements on a bright adatom with tunneling current setpoints lower than 10 nA reveals a negative differential resistance (NDR) on the current-voltage [$I(V)$] curve (Fig. 1C) and a broad peak on the $dI(V)/dV$ curve (Fig. 1D) in the Si band gap region, which is a signature of the tunneling of electrons through a localized state (9). Unexpectedly, with increasing tunneling current setpoints, the NDR peak intensity becomes saturated at 15 nA.

It was recently shown that the transport through this nonresonant dangling-bond state requires two processes (Fig. 1B): a tunneling of an electron between a tip state and the localized state at the energy E_0 , and the nonradiative recombination process of the electron with a hole from the valence band (8). This second process is assisted by the mechanical vibration of the adatom, and it is the contribution of vibronic states to the current that causes the significant broadening of the NDR peak (10). In the steady-state regime, the current corresponding to the tunneling rate W must be equal to the current due to the hole capture rate $c_p p$ by the Si dangling-bond state, thus yielding $I = -\frac{ec_p p W}{c_p p + W}$, where e is the magnitude of the electronic charge, c_p is the hole capture coefficient of the dangling bond, and p is the hole concentration (11).

When the tunneling rate is much lower than the capture rate (i.e., the tip-sample distance Z is large, corresponding to small current setpoints),

Fig. 1. Saturation of the tunneling current through a single nonresonant dangling-bond state. **(A)** STM image of the boron-doped Si(111) ($\sqrt{3} \times \sqrt{3}$)R30° surface, showing a single nonpassivated bright Si adatom (tunneling setpoint $V_S = +1.4$ V; $I = 1$ nA; temperature $T = 77$ K). The inset shows a differential conductance image recorded at $V_S = +0.6$ V from inside the dashed square of the topographic image ($V_{\text{mod}} = 15$ mV; $f_{\text{mod}} = 2$ kHz). **(B)** Schematic illustrating the transport through a dangling-bond state (DB) at the energy eV , with a tunneling rate W for the tip electron and a capture rate $c_p p$ for the valence band (VB) hole. E_{FTip} and E_{FSi} denote the tip and Si Fermi levels, and CB denotes the conduction band. **(C)** Tunneling current spectra measured on a nonpassivated Si adatom for different setpoint currents at $V_S = +1.4$ V. **(D)** Corresponding differential conductance spectra measured with a lock-in amplifier ($V_{\text{mod}} = 15$ mV; $f_{\text{mod}} = 2$ kHz).



Institut d'Electronique, de Microelectronique et de Nanotechnologie (IEMN), CNRS Unité Mixte de Recherche 8520, Département ISEN, 41 Boulevard Vauban, 59046 Lille Cedex, France.

*Present address: University Babeş-Bolyai, 400084 Cluj-Napoca, Romania.

†To whom correspondence should be addressed. E-mail: bruno.grandidier@isen.fr

the tunneling current is proportional to the tunneling rate. But, when the tunneling rate increases (higher current setpoints) and becomes higher than the capture rate, the capture rate limits the current driven through the dangling-bond state ($I = -ec_p p$). As a result, the current becomes nearly saturated at the energy where the tip Fermi level is resonant with the dangling-bond state.

Because a precise determination of the saturation current intensity requires increasingly higher tunneling current setpoints, which can sometimes lead to a modification of the surface, we have adopted another approach to directly measure the capture rate. By recording $I(Z)$ curves in the band gap region up to the bottom of the con-

duction band, we observe (Fig. 2) that the variation of the current intensity deviates from a characteristic exponential increase (12–14), with the exception of the $I(Z)$ curves acquired with voltages higher than +1.2 V. For these voltages, an exponential increase is seen after an initial plateau and corresponds to the contribution of conduction band states to the tunneling current, resulting from a stronger downward band bending when the tip comes closer to the surface (15). But, at lower voltages, the downward band bending is not strong enough, and transport occurs only through the vibronic states of the Si dangling bond down to +0.5 V. For these voltages, the current reaches a maximum value, confirming the saturation observed in Fig. 1A. The

highest current intensity of 15 nA is found for a voltage of +0.6 eV, thus yielding a hole capture rate for the dangling-bond state of $c_p p = 10^{11} \text{ s}^{-1}$.

From the degenerate concentration of B dopants ($10^{20} \text{ B}\cdot\text{cm}^{-3}$) in the sample (8), we can estimate c_p and find a value of $10^{-9} \text{ cm}^3 \text{ s}^{-1}$. Although the capture coefficient is the meaningful physical quantity, it is common to introduce the capture cross section $\sigma_p = c_p/v_{\text{th}}$ (with v_{th} being the average thermal velocity of the trapped carrier) to characterize the carrier trapping efficiency of a deep level (2). A cross section of $1.1 \times 10^{-16} \text{ cm}^2$ is thus obtained and agrees with the theoretical prediction for the capture cross section of a dangling bond in Si (16). Such a value also belongs to the order of magnitude usually found experimentally for the capture cross sections of deep levels in semiconductors (17), like the so-called P_b center, which consists of a dangling bond located at the Si(111)-SiO₂ interface and where σ_p was measured by deep-level transient spectroscopy (DLTS) (18).

Because σ_p is related to the spatial extent of the deep level when the level crosses the valence band to capture a hole while the lattice vibrates (17), it is interesting to spatially resolve the square of the deep-level wave function to compare its extent with σ_p . From the spatial mapping of the wave function in the dI/dV image recorded at the energy of the dangling-bond state (Fig. 1A, inset), we measure an average spatial extent of 10 Å. Assuming that the dangling bond can be modeled by a square well potential with spherical symmetry, resulting from the position of $E_0 = 0.4 \text{ eV}$ far above the top of the valence band, the radius of the bound state is given by $a = \sqrt{\hbar^2/2m^*E_0}$, where \hbar is Planck's constant h divided by 2π . Taking $m^* = 0.36 m_0$ (where m_0 is the free-electron mass, $9.1 \times 10^{-31} \text{ kg}$), we find a spatial extent of $2a = 10.2 \text{ Å}$, which is in good agreement with the experimental value, thus indicating a strong localization of the state, which is as expected from the small magnitude of σ_p .

In contrast to the DLTS technique, which yields an average capture rate for all the deep levels of a space-charge region, STM can readily

Fig. 2. Tunneling current I_T versus tip displacement at different V_S . The feedback loop ($V_S = +1.5 \text{ V}$; $I_T = 5 \text{ nA}$) was first opened; V_S was set to a voltage between +1.3 and +0.3 V; and the tip was displaced away from the surface by 3.7 Å, then moved back and forth by 6.0 Å (corresponding to the data shown), and finally returned to its initial position.

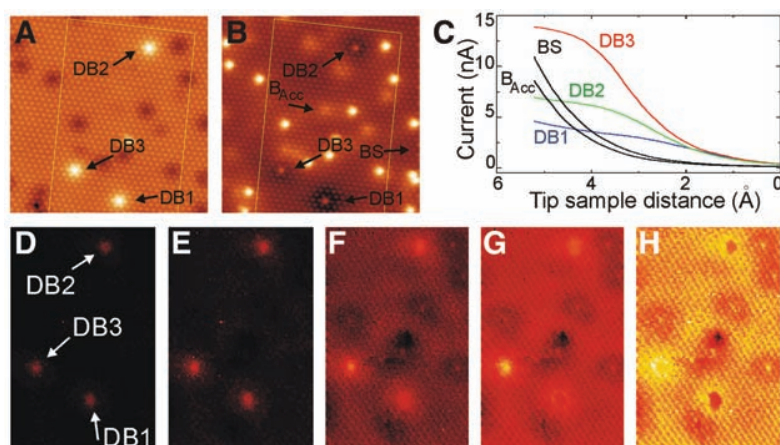
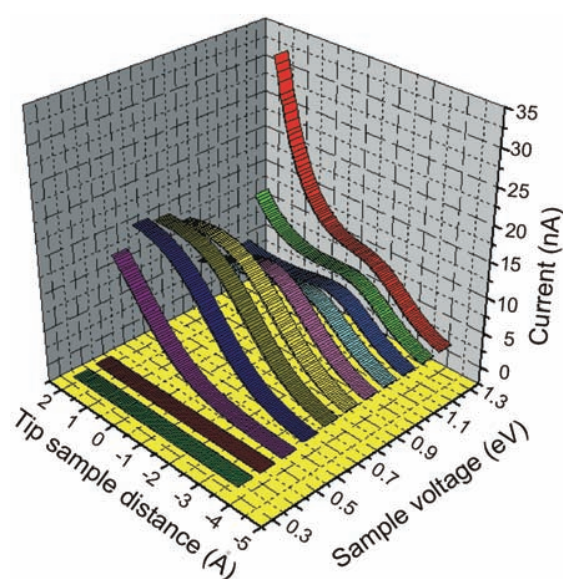


Fig. 3. Variation in the saturation current for three nonpassivated bright Si adatoms labeled DB1, DB2, and DB3. (A) Empty-state STM image ($V_S = +1.4 \text{ V}$; $I_T = 1 \text{ nA}$). (B) Filled-state STM image ($V_S = -0.3 \text{ V}$; $I_T = 1 \text{ nA}$), where a faint protrusion related to a passivated Si adatom located above a subsurface acceptor (B_{Acc}) is indicated, as well as a passivated adatom of the bare surface (BS) that is away from any defects or subsurface dopant atoms. (C) Tunneling current versus tip displacement for the three bright Si adatoms, BS, and B_{Acc} at $V_S = +1.2 \text{ V}$. (D–H) Spatial maps of the tunneling current versus tip displacement for distances of 1.07, 1.89, 3.05, 3.86, and 5.17 Å, respectively, at $V_S = +1.2 \text{ V}$ (feedback parameters $V_S = +1.4 \text{ V}$; $I_T = 1 \text{ nA}$).

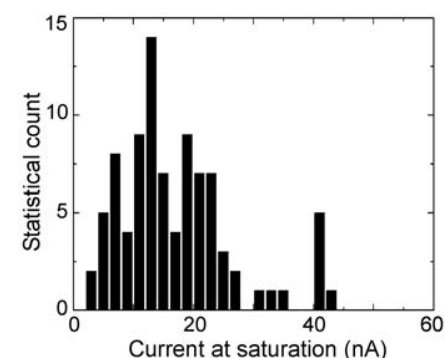


Fig. 4. Distribution of the current intensity at saturation.

probe individual deep levels. As shown in Fig. 3A, three bright adatoms are visible. By performing spatial mapping of $I(Z)$ curves, we observe that the current intensity does not vary in the same manner for these three dangling bonds, as seen in the sequence of Fig. 3, D to H, corresponding to current intensity maps obtained at different tip-surface distances. For the dangling bonds labeled DB1 and DB2, their contrast begins to saturate after the tip has moved toward the surface by 3.05 Å (Fig. 3F) and 3.86 Å (Fig. 3G), respectively, whereas a halo, a sign of saturation, is seen at a higher tip displacement for dangling bond DB3 (Fig. 3H).

The saturation of the current intensity for the three dangling bonds is obtained from the plot of the $I(Z)$ curves in Fig. 3C. We find that the current intensity at saturation is four times higher on DB1 than on DB3. Although the spatial mapping of the $I(Z)$ curves cannot be recorded at the energy E_0 (19), similar variations are found when single $I(Z)$ spectra are measured on different dangling bonds at the energy E_0 , as illustrated in fig. S1 (20). Thus, such a result indicates that the capture rate depends on the environment of the dangling bond.

To understand such variations of the capture rate, we acquired the image in Fig. 3B simultaneously with that in Fig. 3A. In this filled-state image, the three dangling bonds appear bright, but they are each surrounded by a dark region, with different spatial extents and depths. These regions are the signature of the Coulomb interaction between the charged dangling bonds and the free holes. The strength of this interaction is intimately related to the distribution of subsurface charged acceptors. As shown in (8), the acceptors appear as bright protrusions superimposed to the atomic corrugation of the Si adatoms in the filled-state STM image (Fig. 3B). Notably, two acceptors are found to be quite close from DB3, whereas no acceptor is visible around DB1. Such a distribution is quite consistent with the variation of the saturated current measured between the three dangling bonds and demonstrates that the potential fluctuations caused by the random distribution of B dopant atoms dramatically change the capture rate of a dangling bond.

By measuring similar $I(Z)$ curves for more than 90 dangling bonds, we found a distribution of the current intensities at saturation that is centered at 16 nA with a SD of 9 nA (Fig. 4). To explain this deviation, we analyzed the $I(Z)$ curves that were measured away from the bright Si adatoms. From the exponential tunneling behavior of these $I(Z)$ curves (see curves labeled BS and B_{Acc} in Fig. 3C), the spatial variations of the apparent barrier height are extracted (21) and yield a potential fluctuation range of 25 meV. Such fluctuations are expected to affect both the capture coefficient and the hole concentration. At 77 K, the capture cross section has a thermally activated behavior (22), and we estimate that the potential fluctuations induce a

variation of the capture cross section by a factor of 1.4 (at most). Furthermore, the heavy doping of the Si sample yields a narrowing of the band gap of 130 meV. The potential fluctuations lead to a modification of the band gap narrowing, causing substantial variations of the hole concentration, which we estimate to range between 0.6×10^{20} and 1.7×10^{20} hole-cm⁻³ (23, 24). Such variations of the capture cross section and hole concentration agree well with the measured distribution of the current intensities at saturation.

Although the capture rate is measured for a nonradiative recombination process involving the emission of vibrations, this new method is expected to be valid for the direct measurements of a wide range of carrier dynamic processes between a bound state and a continuum of states. It should be suitable to explore the capture and relaxation of charge carriers by the bound states of quantum dots or by point-defect states in nanostructures, such as nanowires, nanotubes, and single atomic sheets.

References and Notes

- K. H. Schmidt, G. Medeiros-Ribeiro, M. Oestreich, P. M. Petroff, G. H. Dohler, *Phys. Rev. B* **54**, 11346 (1996).
- C. Delerue, G. Allan, M. Lannoo, *Phys. Rev. B* **48**, 11024 (1993).
- S. Coe, W. K. Woo, M. Bawendi, V. Bulovic, *Nature* **420**, 800 (2002).
- S. M. Sze, *Physics of Semiconductor Devices* (Wiley, New York, ed. 2, 1981).
- J. Bourgoin, M. Lannoo, *Point Defects in Semiconductors, Volume II: Experimental Aspects* (Springer-Verlag, Berlin, 1983).
- H. G. Grimmeiss, C. Ovren, *J. Phys. E Sci. Instrum.* **14**, 1032 (1981).
- I.-W. Lyo, E. Kaxiras, Ph. Avouris, *Phys. Rev. Lett.* **63**, 1261 (1989).
- M. Berthe et al., *Phys. Rev. Lett.* **97**, 206801 (2006).
- I.-W. Lyo, Ph. Avouris, *Science* **245**, 1369 (1989).
- J. Repp, G. Meyer, S. Paavilainen, F. E. Olsson, M. Persson, *Phys. Rev. Lett.* **95**, 225503 (2005).
- X. de la Broise, C. Delerue, M. Lannoo, B. Grandier, D. Stiévenard, *Phys. Rev. B* **61**, 2138 (2000).
- I.-W. Lyo, Ph. Avouris, *Science* **253**, 173 (1991).
- L. Limot, J. Kröger, R. Berndt, A. Garcia-Lekue, W. A. Hofer, *Phys. Rev. Lett.* **94**, 126102 (2005).
- N. Néel et al., *Phys. Rev. Lett.* **98**, 065502 (2007).
- G. Mahieu et al., *Phys. Rev. Lett.* **94**, 026407 (2005).
- D. Goguenheim, M. Lannoo, *Phys. Rev. B* **44**, 1724 (1991).
- C. H. Henry, D. V. Lang, *Phys. Rev. B* **15**, 989 (1977).
- N. M. Johnson, D. J. Bartelink, J. P. McVittie, *J. Vac. Sci. Technol.* **16**, 1407 (1979).
- Because there is no state in the band gap region when the tip is above the passivated adatoms, closing the feedback loop between two $I(Z)$ spectra leads to a tip crash for sample voltages below +1 V.
- Additional results obtained at a temperature of 5 K are available as supporting material on Science Online.
- The apparent barrier height is given by $\Phi \approx 0.95 \left(\frac{d \ln I}{d \ln Z}\right)^2$.
- D. Goguenheim, M. Lannoo, *J. Appl. Phys.* **68**, 1059 (1990).
- J. Wagner, *Phys. Rev. B* **29**, 2002 (1984).
- J. Wagner, J. A. del Alamo, *J. Appl. Phys.* **63**, 425 (1988).
- R.S. acknowledges the financial support of the Institut de Recherche sur les Composants Logiciels et Matériels pour l'Information et la Communication Avancée.

Supporting Online Material

www.sciencemag.org/cgi/content/full/1151186/DC1
Figs. S1 and S2

1 October 2007; accepted 3 December 2007

Published online 13 December 2007;

10.1126/science.1151186

Include this information when citing this paper.

Spin Conservation Accounts for Aluminum Cluster Anion Reactivity Pattern with O₂

R. Burgert,¹ H. Schnöckel,^{1*} A. Grubisic,² X. Li,² S. T. Stokes,² K. H. Bowen,² G. F. Ganteför,³ B. Kiran,⁴ P. Jena⁵

The reactivity pattern of small (~10 to 20 atoms) anionic aluminum clusters with oxygen has posed a long-standing puzzle. Those clusters with an odd number of atoms tend to react much more slowly than their even-numbered counterparts. We used Fourier transform ion cyclotron resonance mass spectrometry to show that spin conservation straightforwardly accounts for this trend. The reaction rate of odd-numbered clusters increased appreciably when singlet oxygen was used in place of ground-state (triplet) oxygen. Conversely, monohydride clusters Al_nH⁻, in which addition of the hydrogen atom shifts the spin state by converting formerly open-shell structures to closed-shell ones (and vice versa), exhibited an opposing trend: The odd-*n* hydride clusters reacted more rapidly with triplet oxygen. These findings are supported by theoretical simulations and highlight the general importance of spin selection rules in mediating cluster reactivity.

Metal-atom clusters occupy a broad middle ground between small molecules and extended solids. Early mass spectrometric studies revealed certain atomic compositions that exhibited unusual stability and were therefore termed “magic.” A framework analo-

gous to the atomic shell-filling model has been successful in rationalizing many of these observations on the basis of electronic structure considerations; i.e., the valence electrons are governed by an average potential created by the residual positive charges. The result is a jellium-



www.sciencemag.org/cgi/content/full/1151186/DC1

Supporting Online Material for

Probing the Carrier Capture Rate of a Single Quantum Level

M. Berthe, R. Stiuftuc, B. Grandidier,* D. Deresmes, C. Delerue, D. Stiévenard

*To whom correspondence should be addressed. E-mail: bruno.grandidier@isen.fr

Published 13 December 2007 on *Science Express*

DOI: 10.1126/science.1151186

This PDF file includes:

Figs. S1 and S2

Probing the carrier capture rate of a single quantum level

M. Berthe, R. Stiuftuc, B. Grandidier, D. Deresmes, C. Delerue, D. Stiévenard

Institut d'Electronique, de Microélectronique et de Nanotechnologie, IEMN, (CNRS, UMR 8520)

Département ISEN, 41 bd Vauban, 59046 Lille Cedex, France

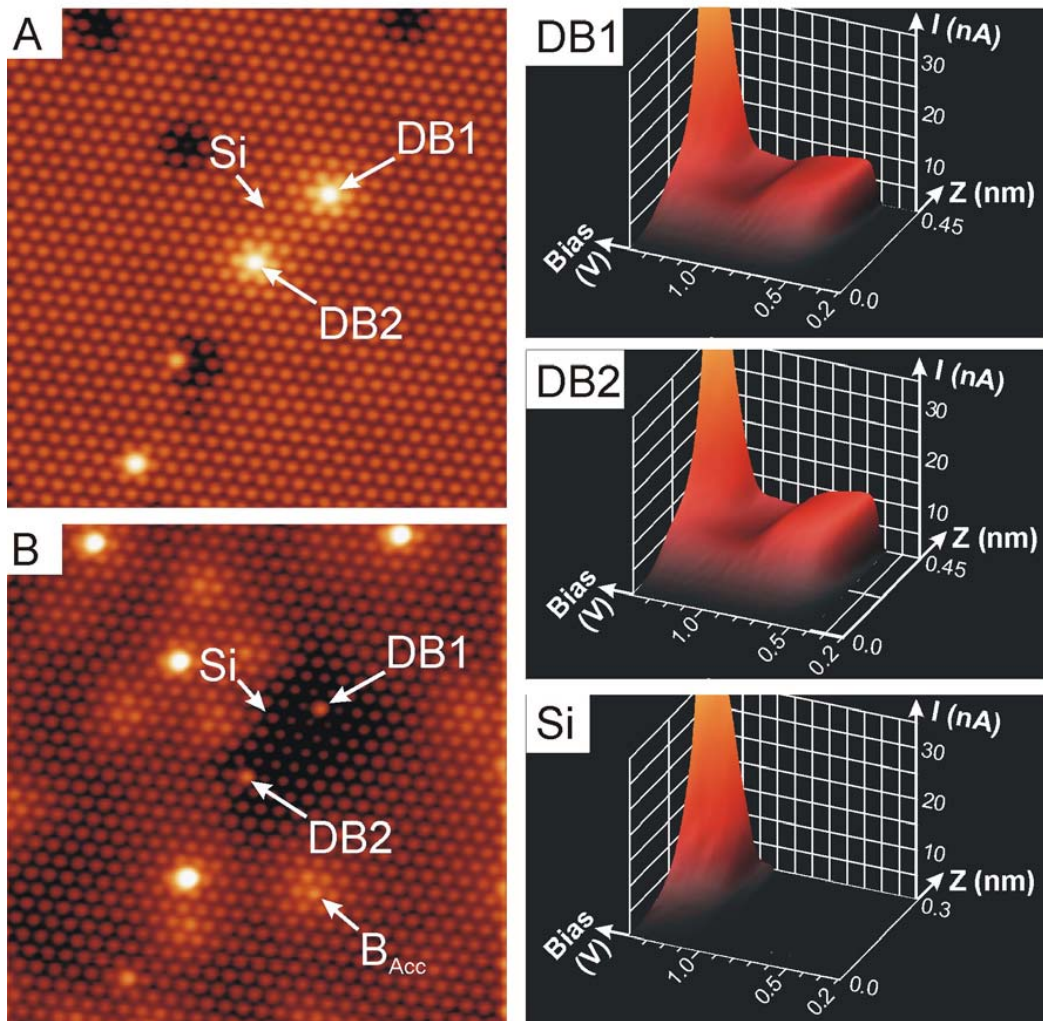


Figure S1. Variation in the saturation current for two non passivated bright Si adatoms labeled DB1 and DB2 at $T = 5\text{K}$. **(A)** Empty state STM image, where arrows point to two bright Si adatoms DB1 and DB2 and a passivated Si adatom ($V_S = +1.4\text{ V}$; $I_T = 1\text{ nA}$). **(B)** Filled state STM ($V_S = -0.3\text{ V}$; $I_T = 1\text{ nA}$), where a subsurface B_{Acc} acceptors is also indicated. **(DB1, DB2, Si)** 3 dimensional $I(V,Z)$ plots measured on the adatoms labelled DB1, DB2 and Si. The feedback loop was $V_S = +1.4\text{ V}$; $I_T = 1\text{ nA}$. Resolutions along the voltage axis and the tip displacement axis are respectively 20 mV and 6 pm .

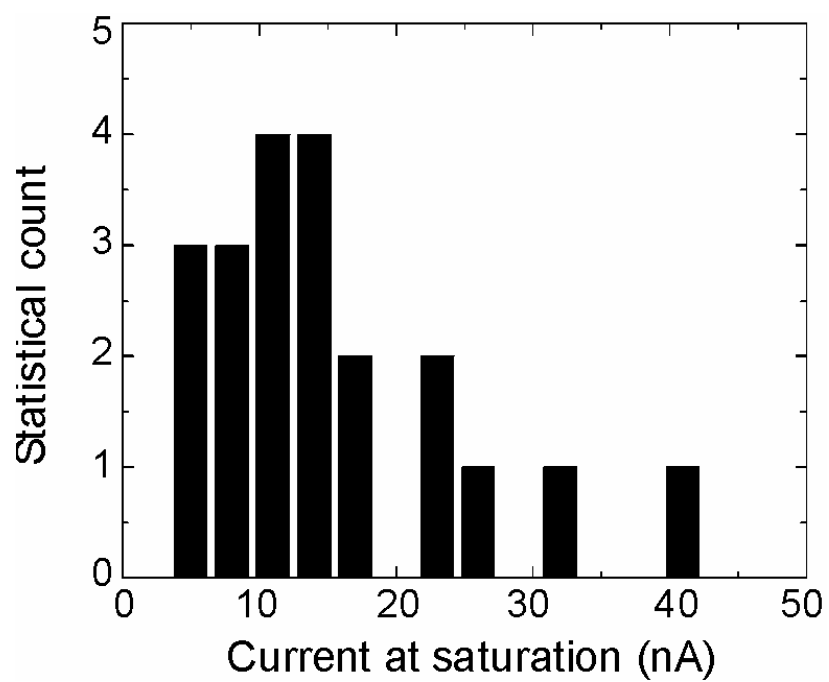


Figure S2. Distribution of the current intensity at saturation at a temperature of 5 K.

Bibliography

- [1] L. Esaki. New phenomenon in narrow germanium p-n junctions. *Phys. Rev.*, 109:603, 1958.
- [2] G. Binnig, H. Rohrer, Ch. Gerber, and E. Weibel. Surface Studies by Scanning Tunneling Microscopy. *Phys. Rev. Lett.*, 49:57, 1982.
- [3] G. Binnig, H. Rohrer, Ch. Gerber, and E. Weibel. Tunneling through a controllable vacuum gap. *Appl. Phys. Lett.*, 40:178, 1982.
- [4] G. Binnig, H. Rohrer, Ch. Gerber, and E. Weibel. 7x7 Reconstruction on Si(111) Resolved in Real Space. *Phys. Rev. Lett.*, 50:120, 1983.
- [5] U. Banin, Y.W. Cao, D. Katz, and O. Millo. Identification of atomic-like electronic states in indium arsenide nanocrystal quantum dots. *Nature*, 400:542, 1999.
- [6] L. Esaki. Long journey into tunneling. *Rev. Mod. Phys.*, 46:237, 1974.
- [7] I. Giaever. Electron tunneling and superconductivity. *Rev. of Mod. Phys.*, 46:245, 1974.
- [8] B. D. Josephson. The discovery of tunneling supercurrents. *Rev. of Mod. Phys.*, 46:251, 1974.
- [9] R. H. Davis and H. H. Hosack. Double barrier in thin-film triodes. *J. Appl. Phys.*, 34:864, 1963.
- [10] R.L. Kronig and WG Penney. Quantum Mechanics of Electrons in Crystal Lattices. *Proc. R. Soc. London, Ser. A*, 130:499–513, 1931.
- [11] H. Park, J. Park, A.K.L. Lim, E.H. Anderson, A.P. Alivisatos, and P.L. McEuen. Nanomechanical oscillations in a single-C₆₀ transistor. *Nature*, 407:57, 2000.

BIBLIOGRAPHY

- [12] H. Park, A.K.L. Lim, A.P. Alivisatos, J. Park, and P.L. McEuen. Fabrication of metallic electrodes with nanometer separation by electromigration. *Appl. Phys. Lett.*, 75:301, 1999.
- [13] K. Shibata, C. Buizert, A. Oiwa, K. Hirakawa, and S. Tarucha. Lateral electron tunneling through single self-assembled InAs quantum dots coupled to superconducting nanogap electrodes. *Appl. Phys. Lett.*, 91:112102, 2007.
- [14] R. Smoluchowski. Anisotropy of the Electronic Work Function of Metals. *Phys. Rev.*, 60:661, 1941.
- [15] Z. Q. Zou, Z. C. Dong, A. S. Trifonov, and H. Nejo. Atomic resolution imaging of a single-crystal Cu(100) surface by scanning tunneling microscopy in ultrahigh vacuum at room temperature. *J. Vac. Sci. Technol. B*, 20:1567, 2002.
- [16] R. J. Hamers, R. M. Tromp, and J. E. Demuth. Surface Electronic Structure of Si(111)-(7x7) Resolved in Real Space. *Phys. Rev. Lett.*, 56:1972, 1986.
- [17] P. S. Weiss and D. M. Eigler. Site dependence of the apparent shape of a molecule in scanning tunneling microscope images: Benzene on Pt(111). *Phys. Rev. Lett.*, 71:3139, 1993.
- [18] X. Lu, M. Grobis, K. H. Khoo, Steven G. Louie, and M. F. Crommie. Spatially Mapping the Spectral Density of a Single C₆₀ Molecule. *Phys. Rev. Lett.*, 90:096802, 2003.
- [19] A. J. Maxwell, P. A. Brühwiler, D. Arvanitis, J. Hasselström, M. K.-J. Johansson, and N. Mårtensson. Electronic and geometric structure of C₆₀ on Al(111) and Al(110). *Phys. Rev. B*, 57:7312, 1998.
- [20] B. W. Hoogenboom, R. Hesper, L. H. Tjeng, and G. A. Sawatzky. Charge transfer and doping-dependent hybridization of C₆₀ on noble metals. *Phys. Rev. B*, 57:11939, 1998.
- [21] H. Yanagi, D. Schlettwein, H. Nakayama, and T. Nishino. Site-specific physisorption and chemical reaction of subphthalocyanine molecules on silicon(111)-7x7. *Phys. Rev. B*, 61:1959, 2000.
- [22] R.J. Hamers, S.K. Coulter, M.D. Ellison, J.S. Hovis, D.F. Padowitz, and M.P. Schwartz. Cycloaddition Chemistry of Organic Molecules with Semiconductor Surfaces. *Acc. Chem. Res.*, 33:617, 2000.

- [23] C. Silien, N. A. Pradhan, W. Ho, and P. A. Thiry. Influence of adsorbate-substrate interaction on the local electronic structure of C_{60} studied by low-temperature STM. *Phys. Rev. B*, 69:115434, 2004.
- [24] Th. Bertrams, A. Brodde, and H. Neddermeyer. Tunneling through an epitaxial oxide film: Al_2O_3 on NiAl(110). *J. Vac. Sci. Technol. B*, 12:2122, 1993.
- [25] A. Wiltner, A. Rosenhahn, J. Schneider, C. Becker, P. Pervan, M. Milun, M. Kralj, and K. Wandelt. Growth of copper and vanadium on a thin Al_2O_3 -film on Ni₃Al(111). *Thin Solid Films*, 400:71, 2001.
- [26] T. Maroutian, S. Degen, C. Becker, K. Wandelt, and R. Berndt. Superstructures and coincidences of a thin oxide film on a metallic substrate: A STM study. *Phys. Rev. B*, 68:155414, 2003.
- [27] R. Franchy, J. Masuch, and P. Gassmann. The oxidation of the NiAl(111) surface. *Appl. Surf. Sci.*, 93:317, 1996.
- [28] M. Baumer and H.J. Freund. Metal deposits on well-ordered oxide®lms. *Prog. Surf. Sci.*, 61:127, 1999.
- [29] XH Qiu, GV Nazin, and W. Ho. Vibrationally Resolved Fluorescence Excited with Submolecular Precision. *Science*, 299:542, 2003.
- [30] SC Street, C. Xu, and DW Goodman. The physical and chemical properties of ultrathin oxide films. *Annu. Rev. Phys. Chem.*, 48:43, 1997.
- [31] Ch. Dietrich, H.-G. Boyen, and B. Koslowski. Characterization of ultrathin insulating Al_2O_3 films grown on Nb(110)/sapphire(0001) by tunneling spectroscopy and microscopy. *J. Appl. Phys.*, 94:1478, 2003.
- [32] M. Baumer, D. Cappus, H. Kuhlenbeck, H.J. Freund, G. Wilhemi, A. Brodde, and H. Neddermeyer. The structure of thin NiO(100) films grown on Ni(100) as determined by Low-Energy-Electron Diffraction and Scanning Tunneling Microscopy. *Surf. Sci.*, 253:116, 1991.
- [33] T. Bertrams and H. Neddermeyer. Growth of NiO(100) layers on Ag(100): Characterization by scanning tunneling microscopy. *J. Vac. Sci. Technol. B*, 14:1141, 1996.

BIBLIOGRAPHY

- [34] I. Sebastian, T. Bertrams, K. Meinel, and H. Neddermeyer. Scanning tunnelling microscopy on the growth and structure of NiO (100) and CoO (100) thin films. *Faraday Discuss.*, 114:129, 1999.
- [35] Ch Hagendorf, R. Shantyr, K. Meinel, KM Schindler, and H. Neddermeyer. Scanning tunneling microscopy and spectroscopy investigation of the atomic and electronic structure of CoO islands on Ag (001). *Surf. Sci.*, 532:346, 2003.
- [36] J. van Elp, J. L. Wieland, H. Eskes, P. Kuiper, G. A. Sawatzky, F. M. F. de Groot, and T. S. Turner. Electronic structure of CoO, Li-doped CoO, and LiCoO₂. *Phys. Rev. B*, 44:6090, 1991.
- [37] EL Lopes, GJP Abreu, R. Paniago, EA Soares, VE de Carvalho, and H.D. Pfannes. Atomic geometry determination of FeO(001) grown on Ag(001) by low energy electron diffraction. *Surf. Sci.*, 601:1239, 2007.
- [38] FM Pan, LK Verheij, R. David, and R. Franchy. Temperature dependence of the growth of gallium oxide on CoGa(100). *Thin Solid Films*, 400:22, 2001.
- [39] U. Berner and K. Schierbaum. Cerium oxide layers on Pt(111): a scanning tunneling microscopy study. *Thin Solid Films*, 400:46, 2001.
- [40] H. Nörenberg and G. A. D. Briggs. Surface structure of CeO₂(111) studied by low current STM and electron diffraction. *Surf. Sci.*, 402:734, 1998.
- [41] S. Schintke, S. Messerli, M. Pivetta, F. Patthey, L. Libiouille, M. Stengel, A. De Vita, and W.-D. Schneider. Insulator at the Ultrathin Limit: MgO on Ag(001). *Phys. Rev. Lett.*, 87:276801, 2001.
- [42] M. Klaua, D. Ullmann, J. Barthel, W. Wulfhekel, J. Kirschner, R. Urban, TL Monchesky, A. Enders, JF Cochran, and B. Heinrich. Growth, structure, electronic, and magnetic properties of MgO/Fe(001) bilayers and Fe/MgO/Fe(001) trilayers. *Phys. Rev. B*, 64:134411, 2001.
- [43] H. Oh, S. B. Lee, Jikeun Seo, H. G. Min, and J.-S. Kim. Chemical structure of the interface between MgO films and Fe(001). *Appl. Phys. Lett.*, 82:361, 2003.
- [44] M.C. Wu, J.S. Corneille, C.A. Estrada, J.W. He, and D.W. Goodman. Synthesis and characterization of ultra-thin MgO films on Mo(100). *Chem. Phys. Lett.*, 182:472, 1991.

- [45] M.C. Wu, J.S. Corneille, J.W. He, C.A. Estrada, and D.W. Goodman. Preparation, characterization, and chemical properties of ultrathin MgO films on Mo(100). *J. Vac. Sci. Technol. A*, 10:1467, 1992.
- [46] MC Gallagher, MS Fyfield, JP Cowin, and SA Joyce. Imaging insulating oxides: Scanning tunneling microscopy of ultrathin MgO films on Mo (001). *Surf. Sci.*, 339:909, 1995.
- [47] S. Altieri, LH Tjeng, and GA Sawatzky. Electronic structure and chemical reactivity of oxide-metal interfaces: MgO(100)/Ag (100). *Phys. Rev. B*, 61:16948, 2000.
- [48] U. Schönberger, OK Andersen, and M. Methfessel. Bonding at metal-ceramic interfaces; ab initio density-functional calculations for Ti and Ag on MgO. *Acta metall. mater.*, 40:1, 1992.
- [49] C. Li, R. Wu, A. J. Freeman, and C. L. Fu. Energetics, bonding mechanism, and electronic structure of metal-ceramic interfaces: Ag/MgO(001). *Phys. Rev. B*, 48:8317, 1993.
- [50] E. Heifets, EA Kotomin, and R. Orlando. Hartree-Fock simulation of the Ag/MgO interface structure. *J. Phys. Cond. Matt.*, 8:6577–6584, 1996.
- [51] W. Hebenstreit, J. Redinger, Z. Horozova, M. Schmid, R. Podloucky, and P. Varga. Atomic resolution by STM on ultra-thin films of alkali halides: experiment and local density calculations. *Surf. Sci.*, 424:321, 1999.
- [52] I. Mauch, G. Kaindl, and A. Bauer. Formation of NaCl stripes on Cu(100). *Surf. Sci.*, 522:27, 2003.
- [53] R. Bennowitz, A. S. Foster, L. N. Kantorovich, M. Bammerlin, Ch. Loppacher, S. Schär, M. Guggisberg, E. Meyer, and A. L. Shluger. Atomically resolved edges and kinks of NaCl islands on Cu(111): Experiment and theory. *Phys. Rev. B*, 62:2074, 2000.
- [54] S. Fölsch, A. Helms, S. Zöphel, J. Repp, G. Meyer, and K. H. Rieder. Self-Organized Patterning of an Insulator-on-Metal System by Surface Faceting and Selective Growth: NaCl/Cu(211). *Phys. Rev. Lett.*, 84:123, 2000.
- [55] J. Repp, S. Fölsch, G. Meyer, and K. H. Rieder. Ionic Films on Vicinal Metal Surfaces: Enhanced Binding due to Charge Modulation. *Phys. Rev. Lett.*, 86:252, 2001.

BIBLIOGRAPHY

- [56] S. Fölsch, A. Riemann, J. Repp, G. Meyer, and K. H. Rieder. From atomic kinks to mesoscopic surface patterns: Ionic layers on vicinal metal surfaces. *Phys. Rev. B*, 66:161409, 2002.
- [57] S. Schintke and W. D. Schneider. Insulators at the ultrathin limit: electronic structure studied by scanning tunnelling microscopy and scanning tunnelling spectroscopy. *J. Phys. Cond. Mat.*, 16:R49, 2004.
- [58] X. H. Qiu, G. V. Nazin, and W. Ho. Vibronic States in Single Molecule Electron Transport. *Phys. Rev. Lett.*, 92:206102, 2004.
- [59] G. Mikaelian, N. Ogawa, X. W. Tu, and W. Ho. Atomic scale control of single molecule charging. *J. Chem. Phys.*, 124:131101, 2006.
- [60] J. Repp and G. Meyer. Controlling the Charge State of Individual Gold Adatoms. *Science*, 305:493, 2004.
- [61] J. Repp, G. Meyer, S. M. Stojkovic, A. Gourdon, and C. Joachim. Molecules on Insulating Films: Scanning-Tunneling Microscopy Imaging of Individual Molecular Orbitals. *Phys. Rev. Lett.*, 94:026803, 2005.
- [62] N. Nilius, T. M. Wallis, and W. Ho. Influence of a Heterogeneous Al_2O_3 Surface on the Electronic Properties of Single Pd Atoms. *Phys. Rev. Lett.*, 90:046808, 2003.
- [63] A. Stierle, F. Renner, R. Streitel, H. Dosch, W. Drube, and B. C. Cowie. X-ray Diffraction Study of the Ultrathin Al_2O_3 Layer on NiAl(110). *Science*, 303:1652, 2004.
- [64] G. Kresse, M. Schmid, E. Napetschnig, M. Shishkin, L. Kohler, and P. Varga. Structure of the Ultrathin Aluminum Oxide Film on NiAl(110). *Science*, 308:1440, 2005.
- [65] Ph. Avouris and R. Wolkow. Scanning tunneling microscopy of insulators: CaF_2 epitaxy on Si(111). *Appl. Phys. Lett.*, 55:1074, 1989.
- [66] J. Viernow, D. Y. Petrovykh, F. K. Men, A. Kirakosian, J.-L. Lin, and F. J. Himpsel. Linear arrays of CaF_2 nanostructures on Si. *Appl. Phys. Lett.*, 74:2125, 1999.
- [67] J. Viernow, D. Y. Petrovykh, A. Kirakosian, J.-L. Lin, F. K. Men, M. Henzler, and F. J. Himpsel. Chemical imaging of insulators by STM. *Phys. Rev. B*, 59:10356, 1999.

- [68] H. Rauscher, TA Jung, JL Lin, A. Kirakosian, FJ Himpsel, U. Rohr, and K. Mullen. One-dimensional confinement of organic molecules via selective adsorption on CaF_1 versus CaF_2 . *Chem. Phys. Lett.*, 303, 1999.
- [69] A. Klust, T. Ohta, A. A. Bostwick, E. Rotenberg, Q. Yu, F. S. Ohuchi, and M. A. Olmstead. Electronic structure evolution during the growth of ultrathin insulator films on semiconductors: From interface formation to bulklike $\text{CaF}_2/\text{Si}(111)$ films. *Phys. Rev. B*, 72:205336, 2005.
- [70] A. Klust, Q. Yu, M. A. Olmstead, T. Ohta, F. S. Ohuchi, M. Bierkanndt, C. Deiter, and J. Wollschlager. Contrast in scanning probe microscopy images of ultrathin insulator films. *Appl. Phys. Lett.*, 88:063107, 2006.
- [71] NS Sokolov, SM Sutturin, VP Ulin, L. Pasquali, G. Selvaggi, and S. Nannarone. Initial stages of MBE growth and formation of $\text{CaF}_2/\text{Si}(001)$ high-temperature interface. *Appl. Surf. Sci.*, 234:480, 2004.
- [72] L. Pasquali, S. D'Addato, G. Selvaggi, S. Nannarone, NS Sokolov, SM Sutturin, and H. Zogg. Formation of CaF_2 nanostructures on $\text{Si}(001)$. *Nanotechnology*, 12:403, 2001.
- [73] L. Pasquali, S. Sutturin, N. Sokolov, G. Selvaggi, S. D'Addato, and S. Nannarone. Electronic properties of CaF_2 nanodimensional islands on $\text{Si}(001)$: An MDS and UPS study. *Nucl. Instrum. Methods Phys. Res., Sect. B*, 193:474, 2002.
- [74] L. Pasquali, SM Sutturin, VP Ulin, NS Sokolov, G. Selvaggi, A. Giglia, N. Mahne, M. Pedio, and S. Nannarone. Calcium fluoride on $\text{Si}(001)$: Adsorption mechanisms and epitaxial growth modes. *Phys. Rev. B*, 72:45448, 2005.
- [75] L. Pasquali, S. M. Sutturin, A. K. Kaveev, V. P. Ulin, N. S. Sokolov, B. P. Doyle, and S. Nannarone. Interface chemistry and epitaxial growth modes of SrF_2 on $\text{Si}(001)$. *Phys. Rev. B*, 75:075403, 2007.
- [76] K. Glöckler, M. Sokolowski, A. Soukopp, and E. Umbach. Initial growth of insulating overlayers of NaCl on $\text{Ge}(100)$ observed by scanning tunneling microscopy with atomic resolution. *Phys. Rev. B*, 54:7705, 1996.
- [77] V. Zielasek, T. Hildebrandt, and M. Henzler. Measurement of $\text{NaCl}/\text{Ge}(001)$ interface states by inelastic low-energy electron scattering with high momentum resolution. *Phys. Rev. B*, 69:205313, 2004.

BIBLIOGRAPHY

- [78] B.J. LeRoy, SG Lemay, J. Kong, and C. Dekker. Electrical generation and absorption of phonons in carbon nanotubes. *Nature*, 432:371, 2004.
- [79] R. Young, J. Ward, and F. Scire. Observation of Metal-Vacuum-Metal Tunneling, Field Emission, and the Transition Region. *Phys. Rev. Lett.*, 27:922, 1971.
- [80] L. Limot, J. Kröger, R. Berndt, A. Garcia-Lekue, and W. A. Hofer. Atom Transfer and Single-Atom Contacts. *Phys. Rev. Lett.*, 94:126102, 2005.
- [81] N. Néel, J. Kröger, L. Limot, T. Frederiksen, M. Brandbyge, and R. Berndt. Controlled Contact to a C₆₀ Molecule. *Phys. Rev. Lett.*, 98:065502, 2007.
- [82] N. Néel, J. Kröger, L. Limot, K. Palotas, W. A. Hofer, and R. Berndt. Conductance and Kondo Effect in a Controlled Single-Atom Contact. *Phys. Rev. Lett.*, 98:016801, 2007.
- [83] J. Tersoff and D. R. Hamann. Theory of the scanning tunneling microscope. *Phys. Rev. B*, 31:805, 1985.
- [84] W. Sacks. Tip orbitals and the atomic corrugation of metal surfaces in scanning tunneling microscopy. *Phys. Rev. B*, 61:7656, 2000.
- [85] G. Binnig and H. Rohrer. *Helv. Phys. Acta.*, 55:726, 1982.
- [86] R. M. Feenstra, W. A. Thompson, and A. P. Fein. Real-space observation of π -bonded chains and surface disorder on Si(111)2x1. *Phys. Rev. Lett.*, 56:608, 1986.
- [87] RM Feenstra, JA Stroscio, and AP Fein. Tunneling spectroscopy of the Si(111) 2x1 surface. *Surf. Sci.*, 181:295, 1987.
- [88] P. Mårtensson and R. M. Feenstra. Geometric and electronic structure of antimony on the GaAs(110) surface studied by scanning tunneling microscopy. *Phys. Rev. B*, 39:7744, 1989.
- [89] R. M. Feenstra. Tunneling spectroscopy of the (110) surface of direct-gap III-V semiconductors. *Phys. Rev. B*, 50:4561, 1994.
- [90] J. Klein, A. Léger, M. Belin, D. Défourneau, and M. J. L. Sangster. Inelastic-Electron-Tunneling Spectroscopy of Metal-Insulator-Metal Junctions. *Phys. Rev. B*, 7:2336, 1973.

- [91] R. C. Jaklevic and J. Lambe. Molecular Vibration Spectra by Electron Tunneling. *Phys. Rev. Lett.*, 17:1139, 1966.
- [92] J. Lambe and R. C. Jaklevic. Molecular Vibration Spectra by Inelastic Electron Tunneling. *Phys. Rev.*, 165:821, 1968.
- [93] L.V. Radushkevich and V.M. Lukyanovich. O strukture ugleroda, obrazujucesja pri termiceskom razlozenii okisi ugleroda na zeleznom kontakte (Structure of the carbon produced in the thermal decomposition of carbon monoxide on an iron catalyst). *Zurn Fisic Chim*, 26:88, 1952.
- [94] S. Iijima. Helical microtubules of graphitic carbon. *Nature*, 354:56, 1991.
- [95] S. Iijima and T. Ichihashi. Single-shell carbon nanotubes of 1-nm diameter. *Nature*, 363:603, 1993.
- [96] D. S. Bethune, C. H. Klang, M. S. de Vries, G. Gorman, J. Savoy, R. and Vazquez, and R. Beyers. Cobalt-catalysed growth of carbon nanotubes with single-atomic-layer walls. *Nature*, 363:605, 1993.
- [97] M. Monthieux and V.L. Kuznetsov. Who should be given the credit for the discovery of carbon nanotubes. *Carbon*, 44:1621, 2006.
- [98] N. Hamada, S. Sawada, and A. Oshiyama. New one-dimensional conductors: Graphitic microtubules. *Phys. Rev. Lett.*, 68:1579, 1992.
- [99] R. Saito, M. Fujita, G. Dresselhaus, and MS Dresselhaus. Electronic structure of chiral graphene tubules. *Appl. Phys. Lett.*, 60:2204, 1992.
- [100] S.J. Tans, M.H. Devoret, H. Dai, A. Thess, R.E. Smalley, L.J. Geerligs, and C. Dekker. Individual single-wall carbon nanotubes as quantum wires. *Nature*, 386:474, 1997.
- [101] S.J. Tans, A.R.M. Verschueren, and C. Dekker. Room-temperature transistor based on a single carbon nanotube. *Nature*, 393:49, 1998.
- [102] A. Rubio. Spectroscopic properties and STM images of carbon nanotubes. *Appl. Phys. A*, 68:275–282, 1999.
- [103] L.C. Venema, J.W.G. Wildöer, J.W. Janssen, S.J. Tans, H.L.J.T. Tuinstra, L.P. Kouwenhoven, and C. Dekker. Imaging Electron Wave Functions of Quantized Energy Levels in Carbon Nanotubes. *Science*, 283:52–55, 1999.

BIBLIOGRAPHY

- [104] R. Saito, M. Fujita, G. Dresselhaus, and M. S Dresselhaus. Electronic structure of chiral graphene tubules. *Appl. Phys. Lett.*, 60:2204, 1992.
- [105] R. Saito, M. Fujita, G. Dresselhaus, and M. S. Dresselhaus. Electronic structure of graphene tubules based on C_{60} . *Phys. Rev. B*, 46:1804, 1992.
- [106] JW Mintmire, BI Dunlap, and CT White. Are fullerene tubules metallic? *Phys. Rev. Lett.*, 68:631, 1992.
- [107] P. R. Wallace. The Band Theory of Graphite. *Phys. Rev.*, 71:622, 1947.
- [108] LC Venema, V. Meunier, P. Lambin, and C. Dekker. Atomic structure of carbon nanotubes from scanning tunneling microscopy. *Phys. Rev. B*, 61:2991, 2000.
- [109] T.W. Odom, J.L. Huang, P. Kim, and C.M. Lieber. Atomic structure and electronic properties of single-walled carbonnanotubes. *Nature*, 391:63, 1998.
- [110] J.W.G. Wildoer, L.C. Venema, A.G. Rinzler, R.E. Smalley, and C. Dekker. Electronic structure of atomically resolved carbon nanotubes. *Nature*, 391:59, 1998.
- [111] R. Martel et al. Single- and multi-wall carbon nanotube field-effect transistors. *Appl. Phys. Lett.*, 73:2447, 1998.
- [112] AJ Stone and DJ Wales. Theoretical studies of icosahedral C_{60} and some related species. *Chem. Phys. Lett.*, 128:501, 1986.
- [113] G. Kim, B.W. Jeong, and J. Ihm. Deep levels in the band gap of the carbon nanotube with vacancy-related defects. *Appl. Phys. Lett.*, 88:193107, 2006.
- [114] D. Orlikowski, M. Buongiorno Nardelli, J. Bernholc, and C. Roland. Theoretical STM signatures and transport properties of native defects in carbon nanotubes. *Phys. Rev. B*, 61:14194, 2000.
- [115] S. Lee, G. Kim, H. Kim, B.Y. Choi, J. Lee, B.W. Jeong, J. Ihm, Y. Kuk, and S.J. Kahng. Paired Gap States in a Semiconducting Carbon Nanotube: Deep and Shallow Levels. *Phys. Rev. Lett.*, 95:166402, 2005.
- [116] V. Meunier and P. Lambin. Scanning tunnelling microscopy of carbon nanotubes: One contribution of 12 to a Theme 'Nanotechnology of carbon and related materials'. *Phil. Trans. R. Soc. London A*, 362:2187, 2004.

- [117] F. Banhart. Irradiation effects in carbon nanostructures. *Rep. Prog. Phys.*, 62:1181, 1999.
- [118] VH Crespi, LX Benedict, ML Cohen, and SG Louie. Prediction of a Pure-Carbon Covalent Metal. *Phys. Rev. B*, 53:13303, 1996.
- [119] M. Buongiorno Nardelli, BI Yakobson, and J. Bernholc. Mechanism of strain release in carbon nanotubes. *Phys. Rev. B*, 57:4277, 1998.
- [120] LG Zhou and S.Q. Shi. Formation energy of Stone–Wales defects in carbon nanotubes. *Appl. Phys. Lett.*, 83:1222, 2003.
- [121] K. C. Pandey. New π -Bonded Chain Model for Si(111)-(2x1) Surface. *Phys. Rev. Lett.*, 47:1913, 1981.
- [122] J. E. Northrup and M. L. Cohen. Reconstruction Mechanism and Surface-State Dispersion for Si(111)-(2x1). *Phys. Rev. Lett.*, 49:1349, 1982.
- [123] J. A. Stroscio, R. M. Feenstra, and A. P. Fein. Electronic Structure of the Si(111)2 x 1 Surface by Scanning-Tunneling Microscopy. *Phys. Rev. Lett.*, 57:2579, 1986.
- [124] H. Hirayama, T. Tatsumi, and N. Aizaki. Reflection high energy electron diffraction and Auger electron spectroscopic study on B/Si(111) surfaces. *Surf. Sci.*, 193:47, 1988.
- [125] H. Q. Shi, M. W. Radny, and P. V. Smith. Electronic structure of the Si(111) $\sqrt{3}\times\sqrt{3}$ R30°-B surface. *Phys. Rev. B*, 66:085329, 2002.
- [126] I.-W. Lyo, Efthimios Kaxiras, and Ph. Avouris. Adsorption of boron on Si(111): Its effect on surface electronic states and reconstruction. *Phys. Rev. Lett.*, 63:1261, 1989.
- [127] K. Higashiyama, S. Yamazaki, H. Ohnuki, and H. Fukutani. Surface states of boron-induced $\sqrt{3}\times\sqrt{3}$ structure on Si(111). *Solid state commun.*, 87:455, 1993.
- [128] T. M. Grehk, P. Mårtensson, and J. M. Nicholls. Occupied and unoccupied surface states on the Si(111) $\sqrt{3}\times\sqrt{3}$:B surface. *Phys. Rev. B*, 46:2357, 1992.
- [129] P. Ebert. Nano-scale properties of defects in compound semiconductor surfaces. *Surf. Sci. Rep.*, 33:121, 1999.

BIBLIOGRAPHY

- [130] G. Mahieu, B. Grandidier, D. Deresmes, J. P. Nys, D. Stiévenard, and Ph. Ebert. Direct Evidence for Shallow Acceptor States with Non-spherical Symmetry in GaAs. *Phys. Rev. Lett.*, 94:026407, 2005.
- [131] R. M. Feenstra, J. M. Woodall, and G. D. Pettit. Observation of bulk defects by scanning tunneling microscopy and spectroscopy: Arsenic antisite defects in GaAs. *Phys. Rev. Lett.*, 71:1176, 1993.
- [132] X. de la Broïse, C. Delerue, M. Lannoo, B. Grandidier, and D. Stiévenard. Theory of scanning tunneling microscopy of defects on semiconductor surfaces. *Phys. Rev. B*, 61:2138, 2000.
- [133] S. Furukawa and T. Miyasato. Quantum size effects on the optical band gap of microcrystalline Si:H. *Phys. Rev. B*, 38:5726, 1988.
- [134] C. Delerue, G. Allan, and M. Lannoo. Theoretical aspects of the luminescence of porous silicon. *Phys. Rev. B*, 48:11024, 1993.
- [135] W. Harrison. Surface Reconstruction on Semiconductors. *Surf. Sci.*, 55:1, 1976.
- [136] M. Lannoo and P. Friedel. *Atomic and electronic structure of surfaces: theoretical foundations*. Springer-Verlag, 1991.
- [137] K. Huang and A. Rhys. Theory of Light Absorption and Non-Radiative Transitions in F-Centres. *Proc. R. Soc. London, Ser. A*, 204:406, 1950.
- [138] S. W. Wu, G. V. Nazin, X. Chen, X. H. Qiu, and W. Ho. Control of Relative Tunneling Rates in Single Molecule Bipolar Electron Transport. *Phys. Rev. Lett.*, 93:236802, 2004.
- [139] J.M. Soler, E. Artacho, J.D. Gale, A. García, J. Junquera, P. Ordejón, and D. Sánchez-Portal. The SIESTA method for ab initio order-N materials simulation. *J. Phys. Cond. Mat.*, 14:2745, 2002.
- [140] G.D. Mahan. *Many-Particle Physics*. Springer, 2000.
- [141] M. Lannoo and J. Bourgoin. *Point Defects in Semiconductors*. Springer-Verlag New York, 1983.
- [142] S. M. Sze. *Physics of semiconductor devices /2nd edition/*. 1981.
- [143] JC Bourgoin and M. Lannoo. *Point Defect in Semiconductors: Experimental Aspects vol. 2*. Berlin: Springer, 1983.

- [144] HG Grimmeiss and C. Ovren. Fundamentals of junction measurements in the study of deep energy levels in semiconductors. *J. Phys. E Sci. Inst.*, 14:1032, 1981.
- [145] M. Berthe, A. Urbieto, L. Perdigo, B. Grandidier, D. Deresmes, C. Delerue, D. Stiévenard, R. Rurali, N. Lorente, L. Magaud, and P. Ordejón. Electron Transport via Local Polarons at Interface Atoms. *Phys. Rev. Lett.*, 97:206801, 2006.
- [146] J. Repp, G. Meyer, S. Paavilainen, F. E. Olsson, and M. Persson. Scanning Tunneling Spectroscopy of Cl Vacancies in NaCl Films: Strong Electron-Phonon Coupling in Double-Barrier Tunneling Junctions. *Phys. Rev. Lett.*, 95:225503, 2005.
- [147] I.W. Lyo and Ph. Avouris. Field-Induced Nanometer- to Atomic-Scale Manipulation of Silicon Surfaces with the STM. *Science*, 253:173, 1991.
- [148] Didier Goguenheim and Michel Lannoo. Theoretical calculation of the electron-capture cross section due to a dangling bond at the Si(111)-SiO₂ interface. *Phys. Rev. B*, 44:1724, 1991.
- [149] C. H. Henry and D. V. Lang. Nonradiative capture and recombination by multiphonon emission in GaAs and GaP. *Phys. Rev. B*, 15:989, 1977.
- [150] G L Miller, D V Lang, and L C Kimerling. Capacitance Transient Spectroscopy. *Annu. Rev. Mat. Sci.*, 7:377, 1977.
- [151] N. M. Johnson, D. J. Bartelink, and J. P. McVittie. Measurement of interface defect states at oxidized silicon surfaces by constant-capacitance DLTS. *J. Vac. Sci. Technol.*, 16:1407, 1979.
- [152] AG Schrott and SC Fain. Nitridation of Si(111) by Nitrogen Atoms. *Surf. Sci.*, 111:39, 1981.
- [153] H. Kurata, M. Hirose, and Y. Osaka. Wide Optical-Gap, Photoconductive α -Si_xN_{1-x}: H. *Jpn. J. Appl. Phys.*, 20, 1981.
- [154] VI Belyi, LL Vasilyeva, and AS Ginovker. Silicon Nitride in Electronics. *Elsevier Science Publishers B. V, Sara Bugerhartstraat 25, P. O. Box 211, 1000 AE Amsterdam, The Netherlands, 1988.*, 1988.
- [155] K. Takayanagi, Y. Tanishiro, M. Takahashi, and S. Takahashi. Structural analysis of Si (111)-7x7 by UHV-transmission electron diffraction and microscopy. *J. Vac. Sci. Technol. A*, 3:1502, 1985.

ABSTRACT

With the advent of nanotechnology, a broad range of materials can be shaped with nanometer scale dimensions involving different methods, and the integration of nanostructures into electronic devices needs to characterize their electronic structure. Scanning tunnelling microscopy is a well appropriate technique for such purpose because it allows a precise positioning of the probe above the nanostructures and has the ability to resolve their electronic structure.

Through this work, we report on the electronic transport of two nanostructures: single wall carbon nanotubes deposited on a gold surface and single Si atoms on a silicon substrate.

In the first study, the weak coupling of the nanotube with the gold substrate give access to the one-dimensional density of states of nanotubes and allows the formation of point defects, with localized states in the band gap of the nanotubes. Such an atomic scale, reversible, modification of the nanotube wall opens up opportunities to tailor single wall carbon nanotube electronic properties at will.

The second study aims at characterizing the carrier dynamics of an isolated Si dangling bond state on a Si(111) surface, which is energetically decoupled from any other electronic states. Analysis of the transport reveals an inelastic current involving the non radiative recombination of electrons from the tip with holes captured by the dangling bond state, thanks to the emission of vibrations. By further scanning tunnelling spectroscopy experiments, we show that it is possible to characterize the trapping efficiency of a single quantum state, knowing its energy level, wave function, capture cross-section and electron-phonon coupling.

RÉSUMÉ

Depuis l'avènement des nanotechnologies, une grande quantité de matériaux sont façonnés à l'échelle du nanomètre par des techniques diverses et l'intégration de ces nanostructures demande une caractérisation de leur structure électronique. La microscopie à effet tunnel est adaptée à ces études car elle permet l'adressage de nanostructures uniques pour mesurer leur structure électronique.

Nous rapportons ici l'étude du transport électronique dans deux types de nanostructures: des nanotubes de carbone simple paroi déposés sur une surface d'or et des atomes uniques de silicium sur un substrat de silicium.

Dans la première étude, le couplage faible entre un nanotube et le substrat permet d'accéder à la densité d'états unidimensionnelle des nanotubes et autorise la formation de défauts ponctuels, ayant des états localisés dans la bande interdite des nanotubes. Cette modification, réversible, de la structure atomique des nanotubes de carbone amène des opportunités concernant la modification contrôlée et à volonté de leurs propriétés électroniques.

La deuxième étude vise à caractériser la dynamique des porteurs dans une liaison pendante de silicium énergétiquement isolée de tout autre état électronique sur une surface Si(111). L'analyse du transport révèle un courant inélastique mettant en œuvre la recombinaison non radiative des électrons de la pointe avec des trous capturés par l'état de la liaison pendante, grâce à l'émission de vibrations. La spectroscopie à effet tunnel montre de plus que l'on peut caractériser l'efficacité de capture d'un état quantique unique, en connaissant son niveau d'énergie, sa fonction d'onde, sa section de capture et le couplage électron-phonon.